Fall 12-2010

Study of 3,3' vs. 4,4' DDS Isomer Curatives on Physical Properties and Phenyl Ring Motions of DGEBA Epoxy via Molecular Dynamics, Deuterium NMR, and Dielectric Spectroscopy

Samuel James Tucker
University of Southern Mississippi

The University of Southern Mississippi

STUDY OF 3,3' VS. 4,4' DDS ISOMER CURATIVES ON PHYSICAL PROPERTIES AND PHENYL RING MOTIONS OF DGEBA EPOXY VIA MOLECULAR DYNAMICS, DEUTERIUM NMR, AND DIELECTRIC SPECTROSCOPY

by

Samuel James Tucker

A Dissertation
Submitted to the Graduate School
of The University of Southern Mississippi
in Partial Fulfillment of the Requirements
for the Degree of Doctor of Philosophy

December 2010

ABSTRACT

STUDY OF 3,3' VS. 4,4' DDS ISOMER CURATIVES ON PHYSICAL PROPERTIES AND PHENYL RING MOTIONS OF DGEBA EPOXY VIA MOLECULAR DYNAMICS, DEUTERIUM NMR, AND DIELECTRIC SPECTROSCOPY

by Samuel James Tucker

December 2010

The purpose of this research is to develop a multiscale understanding of crosslinked amorphous matrices, connecting molecular level events to macroscopic properties. To accomplish this goal, our methodology was to identify network architectures that influence molecular level energy dissipation through mechanisms such as bond rotations, torsions, and ring flips and then relate those molecular motions to macroscopic properties. Studies were accomplished on two aerospace grade matrices: the epoxy, diglycidyl ether of bisphenol A (DGEBA) cured with two amines, 3,3'-diaminodiphenyl sulfone (33DDS) and 4,4'-diaminodiphenyl sulfone (44DDS). The 33DDS/DGEBA and 44DDS/DGEBA served both to provide a baseline for experimental testing of aerospace matrices and to enable the comparison of a meta-substituted vs. para-substituted diamine in chemically isotropic systems. The results presented in the first seven chapters of the dissertation focus on these two matrices.

Molecular Dynamics (MD) simulations provide a tool to quickly create networks with alterations in network architectures, such as crosslink density, aromaticity, sulfone content, pendant bulky groups, etc. MD can then be used to predict thermomechanical properties of these matrices and determine the effect of network architecture on properties. In this work, molecular dynamics simulations were used to accurately predict

thermomechanical properties of 33DDS/DGEBA and 44DDS/DGEBA. Additionally, modifications to these baseline matrices were made in order to study the effect of network architecture and chemical composition of matrices.

To bridge the gap in understanding between network architecture and ultimate matrix performance, molecular motions resulting from the network architecture and responsible for ultimate properties, must be understood. To analyze these molecular motions, various solid state Nuclear Magnetic Resonance (NMR) spectroscopic techniques, Dielectric Spectroscopy (DES), and Dynamic Mechanical Analysis (DMA) are employed.

Deuterium (^{2}H) NMR spin-lattice relaxation studies and lineshape analyses are powerful tools in determining the motional behavior of targeted chemical moieties within the glassy state. Solid state deuterium NMR studies were used to selectively study the phenyl ring motions of 33DDS, 44DDS, and DGEBA in 33DDS/DGEBA and 44DDS/DGEBA networks. Phenyl ring deuterated diglycidyl ether of bisphenol A (d8-DGEBA), 3,3'-diaminodiphenyl sulfone (d8-33DDS), and 4,4'-diaminodiphenyl sulfone (d8-44DDS) were all synthesized. Deuterated DGEBA was reacted with non-deuterated 33DDS and 44DDS to study the effect of the amine on the motions of the epoxy rings. Deuterated 33DDS and 44DDS were reacted with non-deuterated DGEBA to study the phenyl ring motions of the amines. Carbon NMR spectroscopy was also used to provide additional information about phenyl ring motions of the epoxies.

While solid state NMR techniques can be used to elucidate the motions of specific chemistries and architectures within the network, secondary, or sub-T_g, relaxations seen in dielectric spectroscopy and dynamic mechanical analysis are often associated with

mechanical properties, including modulus, toughness, and strength. The association of the chemistries responsible for specific motions and the contributions of these motions to secondary relaxations help connect the molecular scale to the macroscale. In this work, phenyl ring motions have been correlated with sub-T_g transitions observed with DES and DMA, furthering understanding of the relationship between chemical composition and mechanical properties in polymers. DES and DMA have also shown distinct differences in 33DDS/DGEBA and 44DDS/DGEBA.

Solid state NMR techniques were used to study the kinetics of reaction of 33DDS and 44DDS with DGEBA. The reaction of most primary amines before reaction of secondary amines was observed in 33DDS/DGEBA and 44DDS/DGEBA. This provides information on network architecture by showing that DDS/DGEBA systems form linear oligomers prior to crosslinking.

The effect of modification with an octafunctional polyhedral oligomeric silsesquioxane (POSS) on network properties of on an ambient cure epoxy was studied. The results show that POSS modification provides substantial increases in mechanical properties at ambient conditions and elevated temperatures.

Finally, the surface chemistry of industrially manufactured aerospace composites was analyzed to gain insight on preparing proper surfaces for bonding. Release agents used in the fabrication process were found in trace quantities on the surfaces. The presence of low surface energy release agents on surfaces is counterproductive to the bonding of those surfaces.

The University of Southern Mississippi

STUDY OF 3,3' VS. 4,4' DDS ISOMER CURATIVES ON PHYSICAL PROPERTIES AND PHENYL RING MOTIONS OF DGEBA EPOXY VIA MOLECULAR DYNAMICS, DEUTERIUM NMR, AND DIELECTRIC SPECTROSCOPY

by

Samuel James Tucker

A Dissertation
Submitted to the Graduate School
of The University of Southern Mississippi
in Partial Fulfillment of the Requirements
for the Degree of Doctor of Philosophy

Approved:

Jeffrey S. Wiggins .
Director

Robson Storey .

Kenneth Mauritz .

Sergei Nazarenko .

William Jarrett .

Steve Christensen .

Susan A. Siltanen .
Dean of the Graduate School

December 2010

DEDICATION

This dissertation is dedicated to my family for making me who I am today.

To my parents, Bill and Mary Tucker, for being excellent role models, teaching me by irreproachable example, and giving me their encouragement, strength, and love.

To my brothers and sister, Ben, Jon, and Rachel, for always being there for me, for their endless support and complete trust.

To my grandparents, Norman and Virginia Myers and Ralph and Orma Tucker and my Aunt Ray for their wisdom, kindness, and sense of humor.

For everyone, I am truly grateful.

ACKNOWLEDGMENTS

I would like to acknowledge my advisor, Dr. Jeffrey S. Wiggins, for being a great friend and mentor. I have learned a great deal from his professional and personal guidance, encouragement to strive for excellence, and dedication to the people around him. I would also like to acknowledge my committee members: Dr. Robson Storey, Dr. Kenneth Mauritz, Dr. Sergei Nazarenko, Dr. William Jarrett, and Steve Christensen. To Dr. Storey, Dr. Mauritz, and Dr. Nazarenko, I thank you for your persistence in the pursuit of scientific excellence and your guidance in becoming a better scientist. To Dr. Jarrett, I thank you for your patience, time, and effort in working through difficult problems, and I thank you for making it fun. To Steve, I thank you for your help understanding difficult concepts, your encouragement in pushing my understanding all the way back to first principles, and your patience in answering my never-ending questions.

I would like to acknowledge the Wiggins Research Group, Abdelwahed, Matt, Stephen, Travis, David, Kat, Jianwei, Sritama, Jinhai, Dave, and Lawrence for their help with research, and more importantly, for making this a fun place to work. I would like to thank Mohamed and Mukul for their scientific help. I would like to acknowledge the faculty and staff in Polymer Science for their support in everything I have asked. I thank my fellow graduate students and my first year class for their camaraderie. I thank the late Dr. Charles Hoyle for his joyful attitude, love of science, and dedication to his faith above all else. Finally, I thank all the close friends I have made in the program for their support and the great times we had together.

TABLE OF CONTENTS

LIST OF ILLUSTRATIONS

Figure

LIST OF TABLES

Table

CHAPTER I

INTRODUCTION

Since the Bronze Age, metals have set the standard for material strength, durability, and performance. As a result, large structural applications in major industries including construction, marine, and aerospace transitioned from wood to metal, leading to larger and more durable structures. One disadvantage of metals for use in large structural applications is specific weight. Over the years, engineers and scientists have strived to increase the strength-to-weight ratio for metals; through the use of lighter weight metals such as aluminum, titanium, and alloys, improvements have been achieved. Concurrently during the last half-century, society has witnessed the onset of another structural materials revolution with the development of fiber-reinforced polymer composites.

Scientists and engineers have gained a practical understanding of fiber reinforced polymer composite's advantages and limitations, and continue to advance the physical and thermal properties of these materials to broaden their application base. Increased strength, reduced weight, longevity, maintenance, environmental corrosion resistance, zero magnetic signature, improved design flexibility, and lifecycle economics are important driving forces for replacing metals. Limitations for composites are often associated with a lack of long-term performance data. Metals have been widely studied for many years in large structural applications leading to relatively high confidence for the prediction of behavior and response of these materials prior to failure. Composites do not have the abundance of historical data and design know-how in comparison to metals, and their complexity in construction and failure demands conservative decisions in structural application.

Advancing a multiscale understanding of composites which range in length and time scales from the quantum/molecular matrix level through the structural continuum will provide scientists confidence for incorporating composites into applications. In order to do so, it is necessary to increase knowledge of how glassy polymer network solids influence and control critical structural performance. Linking glassy polymer network chemistry to structural capabilities has been difficult due to the complexities of analyzing intractable, insoluble, and thermally stable polymer network solids. In particular, connecting matrix chemistry to strain induced structural failures is particularly complicated since fracture initiation and progression in fiber-reinforced composites is quite complex and involves numerous failure modes associated with interfacial delamination, fiber-matrix interfaces, matrix cracking, fiber-breakage, and etc.

To advance understanding of glassy amorphous thermosets used in composite applications, two aerospace-grade matrices will be the focus of this work. The industry standard diepoxy, the diglycidyl ether of bisphenol A (DGEBA) will be cured with the tetra-functional diamines 3,3'-diaminodiphenyl sulfone (33DDS) and 4,4'-diaminodiphenyl sulfone (44DDS); shown in Figure 1.1. In addition to using industrially prevalent matrices, the use of isomeric amines provides the opportunity to study the effect on properties of aromatic networks possessing meta-substitution versus a fully para-substituted network. Specific objectives of this research are as follows:

(1) In order to advance multiscale understanding of composite matrices, molecular dynamics simulations will be used to predict properties of matrices. Simulated properties will be compared to experimentally determined properties for 33DDS/DGEBA and 44DDS/DGEBA to determine accuracy of simulations.

Where simulations do not match experimental values, improvements to the simulation procedure will be made. Simulations will also be accomplished to determine the effects of meta-substitution in the backbone, varied crosslink density, aromatic and sulfone group content, and pendant bulky group incorporation.

(2) Polymer network glassy state (sub-T_g) molecular motions will be analyzed to gain an understanding of the chemical structures undergoing molecular motion and the types and rates of those motions using deuterium (^2H) and carbon (^{13}C) solid state NMR spectroscopy. Glassy state relaxations will be characterized with dielectric spectroscopy (DES) and dynamic mechanical analysis (DMA). The rates and types of motion seen in NMR spectroscopy will be related to the secondary transitions seen in DES and DMA for 33DDS/DGEBA and 44DDS/DGEBA matrices.

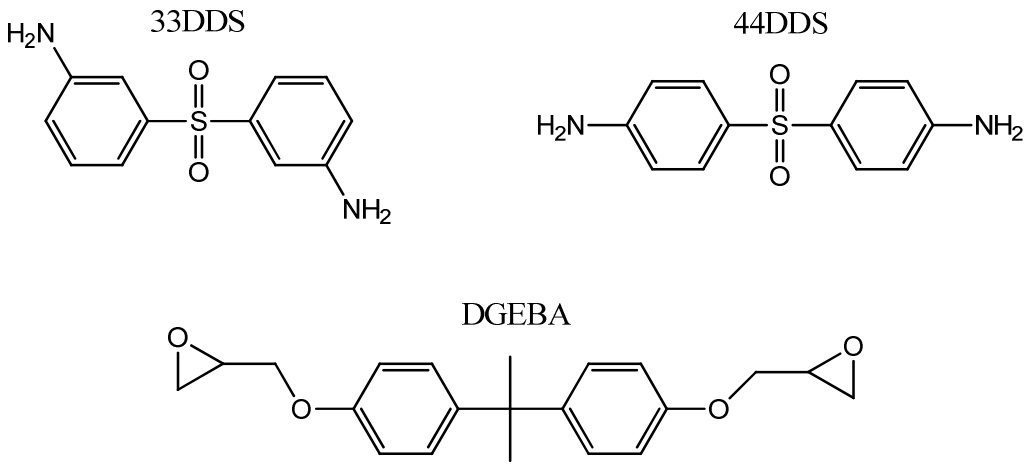

Figure 1.1. Structures of 44DDS, 33DDS, and DGEBA.

Epoxy Networks

Epoxy networks are formed through step-growth polymerization reactions where glycidyl rings open in the presence of strong nucleophiles. Tetra-functional aromatic and aliphatic diamines are commonly used as curing agents for epoxies due to their economics and performance. Network formation usually occurs through two isothermal reaction steps. The first step is generally conducted at a lower temperature condition which promotes the formation of linear step-growth oligomers through primary amine-oxirane reactions, sometimes referred to as "B-stage." The second step of the cure is performed at a higher temperature where secondary amine-oxirane crosslinking reactions drive the ultimate network formation. At some point of curing, dependent upon the flexibility of the molecules, reactive groups no longer possess the configurational freedom to come into contact with other reactive groups and form a bond. The network reaches its vitrified state when chemical reactions stop occurring, and crosslink density and network architecture remain constant. The extent of cure obtained during the post-cure drives the network into the vitrified state, thus giving the network its ultimate thermomechanical properties

Chemical compositions and crosslink densities are two factors that govern the thermal and physical properties of polymer networks.[1,2] Chemical composition refers to the chemical make-up of the polymer, including backbone features such as aromaticity, ethers, sulfones, etc and functional groups. In general, networks containing aromatic moieties show increased rigidity and thermal stability when compared to networks comprised from aliphatics. Hydroxyl groups form during the amine-oxirane ring opening reaction and contribute to network properties through hydrogen bonding with tertiary

amines and other hydroxyls.[3] A recent report demonstrated that increasing intermolecular interactions through a higher density of hydrogen bonding increased the low-deformation mechanical properties of epoxy networks at temperatures between secondary and primary relaxations.[4]

Crosslink density also has a significant effect on network properties. In general, a higher crosslink density results in a higher modulus,[5] and longer chain segments generally display higher degrees of local chain mobility and flexibility leading to a reduction in modulus.[6] The crosslink density of a network is dependent upon the molecular weight between crosslinks and the extent of reaction; higher conversion results in higher crosslink density. Quantitative conversion of functional groups in an epoxy is never attained due to network vitrification; the fully cured network architecture is comprised of tertiary and secondary amines. As a result, molecular weight of the monomers affects the average molecular weight between crosslinks, M_c, but does not precisely determine it.[7]

Multi-Scale Modeling

In multi-scale modeling, the goal is to predict the properties and behavior of complex structures across all relevant time-length scales starting from fundamental chemical and physical mechanisms. Macroscopic material properties and behaviors, such as strength and performance, are always associated with phenomena that occur on a smaller length scale including the localization of micro-defects. When sub-scale events are examined in detail, it is found that these events result from mechanisms that occur on finer time-length scales, with root analysis leading to quantum and molecular level events. When molecular dynamics models are more accurate, modeling frameworks

which capture dominant mechanisms across all time-length scales will offer more reliable predictive capabilities.

Despite extensive material research and development, high-modulus matrix resins used in advanced aerospace composites have historically been labeled as brittle. Whether or not this behavior is manifested will be dependent on the local strain environment. Advancements in molecular dynamics modeling provide insights to further study the physical deformations of glassy polymers. The mechanisms of glassy polymer distortions in response to applied strains are not well-understood, nor is there an accurate model that relates distortional capabilities of glassy polymers to specific structural chemistries. This deficiency is a key limitation for advancing reliable multi-scale models that relate matrix chemistry to ultimate composite performance.

Boeing Research and Technology has recently introduced the physics-based Onset Theory to reduce its dependence on empirical testing for the prediction of ultimate composite performance in advanced aerospace structures.[8] Onset Theory is a strain-based method, which uses invariant, scalar values to determine the onset of critical events that result in ultimate composite failure. Onset Theory predicts that composite matrix damage initiation is essentially controlled by two strain invariants, the first invariant of the strain tensor, J_1, associated with laminar transverse cracking failure dominated by volume increase of the matrix, and the von Mises strain, associated with equivalent strain and shape change of the matrix, a function of the second invariant of the strain deviator tensor, ε_{vm}. Invariants are terms for mathematical constructs which remain unchanged when certain types of transformations are applied. J_1 and ε_{vm} are invariant to rotation of the principle axis system, meaning they are invariant to the geometry of the sample or the

direction in which strain is applied. J_1 gives a measure of the dilational response of the material to an applied strain, while ε_{vm} measures the distortional response. Distortion and dilation will be further discussed in the following section within the introduction.

Onset Theory has shown that matrix fracture initiation, independent of structural designs and modes of loading, is associated with the effective critical volumetric or equivalent strains of the lamina. In composite lamina tensile tests, as the fiber angle within the composite increases, the method of failure changes from distortional to dilatational (Figure 1.2).[9] In composites, when critical volumetric or equivalent strains are reached, failure of the composite is imminent. Therefore, the most efficient approach to significantly improve performance of composite structures is to improve the von Mises strain of the matrix. Onset Theory will provide keys to:

- predict the strength of complex structures from basic properties
- reduce the number of durability tests
- link resin properties to composite properties
- simplify moisture and thermal degradations at the matrix molecular level[10]

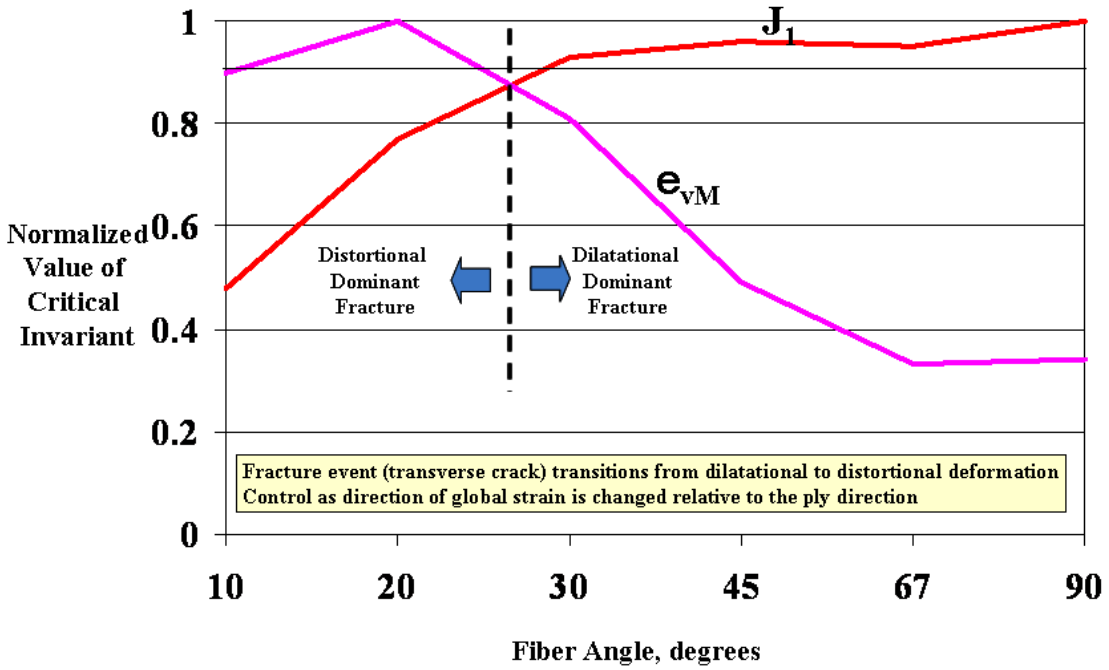

Figure 1.2. Invariant value vs. fiber angle for lamina tensile tests.

Polymer Dilatational and Distortional Deformations

Polymer deformation models have been the subject of intense physical polymer research for several decades.[11] The evolution of molecular modeling over the last decade has provided new opportunities for scientists to study the physical interactions of glassy polymers, and one of the most powerful methods to study these nanoscopic events is molecular dynamics modeling. Molecular systems are studied by applying laws of chemistry, physics, and mathematics to predict molecular behavior via computer simulation. Due to the complex nature of physical interactions between polymers and a lack of analytical methods sufficiently sensitive to measure molecular level stresses and strains, molecular dynamics simulations are providing new molecular-level insights

toward understanding the bulk property responses of polymers subjected to applied forces.[12]

In polymers, certain stress-field conditions may cause crazing. A craze is a narrow zone of highly deformed and voided polymer. The relevant criterion for craze formation proposed by Sternstein and Ongchin can be interpreted as a critical volume increase related to a critical polymer chain mobility induced by stress.[13] The development of cavitation is recognized as a leading energy dissipation process during the deformation of glassy polymers and largely controls their resistance to mechanical loading.[14] It has been shown that cavitation relieves hydrostatic tension in the matrix, increases deviatoric stresses, and promotes shear deformation.[15] The contribution of cavitation has proven to be essential to adequately model plasticity in zones of highly stressed fields including crack tips.

Condensed matter can deform in one of two ways: dilatation and distortion. At some amount of deformation, either dilatation or distortion becomes critical, and permanent deformation results. Materials are said to dilate when induced stress causes a deformation resulting in volume expansion in the material but not a change in shape as depicted in Figure 1.3. Equation 1.1 gives the definition of J_1, which accounts for over 98% of the dilational strain. If the volume expansion is small, the cohesive forces of the material will persevere, and the material will recover to its initial volume upon release of the applied stress. However, if the stress causes large molecular displacements and cohesive forces in the material are exceeded, an increase in volume of the material will occur due to the formation of nanoscopic cavities. Once formed, cavities become

permanent weaknesses within the material eventually leading to the onset of crack propagation and catastrophic failure.

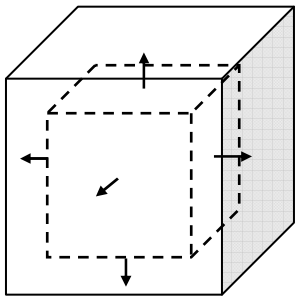

Figure 1.3. Pictorial representation of material dilation.

$$J_1 = \varepsilon_1 + \varepsilon_2 + \varepsilon_3$$

where: ε_1, ε_2, and ε_3 are the strains in the x, y, and z directions

Equation 1.1. Definition of the first invariant of the strain tensor, J_1.

Distortional deformation, depicted in Figure 1.4, is a molecular deformation mechanism that theoretically avoids cavitation by changing shape without undergoing a change in volume. Distortional deformation can be accurately measured by von Mises strain, ε_{vm}, defined in Equation 1.2. In distortional deformation net frictional forces do not change and the ultimate strength of the material remains intact. Although intermolecular forces of attraction may be overcome during distortional events, the net result is a torsional movement of the material followed by recovery of the attractive forces that prevent the formation of cavities and cohesively hold the molecules intact. For these reasons, it is logical to conclude that increasing the distortional capability of a

glassy polymer will lead to improved macroscale mechanics. Increasing the distortional capability of a polymer network involves enhancing the ability of the material to deform at the molecular level, and distortional deformation is dependent upon ability of the backbone to rotate through dihedral angles.[16,17,18] These rotations increase the ability of the system to respond to strain by means of plastic processes. Another way to reduce a polymer's resistance to plastic flow is to disperse toughening particles throughout the system, creating a cellular solid.[18] Particles are believed to increase the free-volume of the deformable material, increasing the uniformity of strain in the system, and ultimately augmenting the distortional capability of the network.[18]

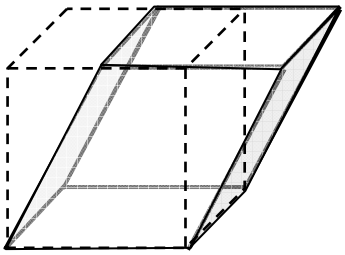

Figure 1.4. Pictorial representation of material distortion.

$$\varepsilon_{vm} = \sqrt{0.5 * [(\varepsilon_1 - \varepsilon_2)^2 + (\varepsilon_2 - \varepsilon_3)^2 + (\varepsilon_1 - \varepsilon_3)^2]}$$

where: ε_1, ε_2, and ε_3 are the strains in the x, y, and z directions

Equation 1.2. Definition of von Mises strain, ε_{vm}.

To better illustrate the molecular structure differences in dilational and distortional deformation behavior, well-known thermoplastic materials are good models

for the purpose of demonstration. Relatively tough polycarbonate (PC) and polysulfone (PSu) are thermoplastics that exhibit classic distortional deformation under applied stress states as compared to relatively brittle polystyrene (PS) that displays classic dilational behavior.[19] When stress is applied to PC or PSu, the material responds with a plastic response in which no change in volume is observed. Practically speaking, distortion is responsible for the necking behavior of these polymers when put under tension, and for their relatively high impact strengths. On the other hand, polystyrene reacts to stress with a dilational response, generally does not neck under tension, and exhibits a relatively low-energy catastrophic failure in similar tensile and impact scenarios. A further noteworthy example is the behavior of brittle PS in unidirectional tensile stress testing under hydrostatic pressure. In this case, the material will deform without volume change and display distortional deformation behavior by necking, similar to polycarbonate. This examination of thermoplastic models including the backbone chemistries and torsional conformations that favor distortional deformation capabilities of glassy polymers can be used to provide insights for developing improved distortional capabilities within aerospace composite networks.

Evaluating conformational rotations and molecular-level energy absorbing mechanisms by synthesizing model networks with controlled molecular level conformations is fundamental to this research. Controlled conformational positioning provides rotational mechanisms into the polymer backbone leading to variations in deformational and physical behaviors. For example, the meta-substituted dianiline link designed into the backbone of ULTEM® (Figure 1.5) allows the aromatic ether-imide

polymer to be a melt-processable thermoplastic with high distortional deformation capability.[20]

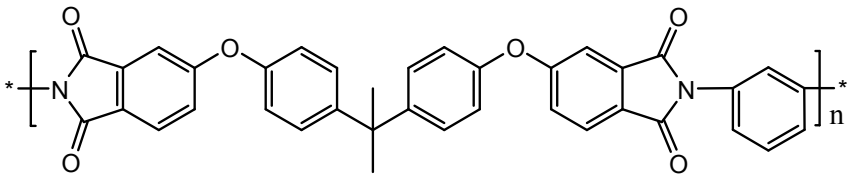

Figure 1.5. Polymeric structure of ULTEM®.

Cohesive forces in a material are governed by a balance between intermolecular attractions arising from Van der Waals forces and repulsions due to nearest neighbor effects[21]. Van der Waals forces describe the complex combinations of dipole and electron-cloud distribution forces between molecules including Keesom forces, Debye forces, and London dispersion forces, which create instantaneous attractions between molecules.[22,23,24] Pauli repulsions result from the overlapping of proximal electron clouds and are the primary repulsive forces between molecules. The balance between these attractive and repulsive forces significantly influences physical properties of a material and can be described using the Lennard-Jones (L-J) 6-12 potential energy function depicted in Figure 1.6. The zero net force balance between attraction and repulsion occurs at a radial separation of about 3.4Å, and attractive forces are strongest when atoms are separated by 3.8Å. The interactions between attractive and repulsive forces dictate the energy barriers for bond rotations, such as gauche- to trans-conformations. Energy barriers associated with changes in molecular level conformations can also be considered as molecular level energy absorbing and dissipating mechanisms that control dilational and distortional modes of deformation in amorphous glassy polymers.

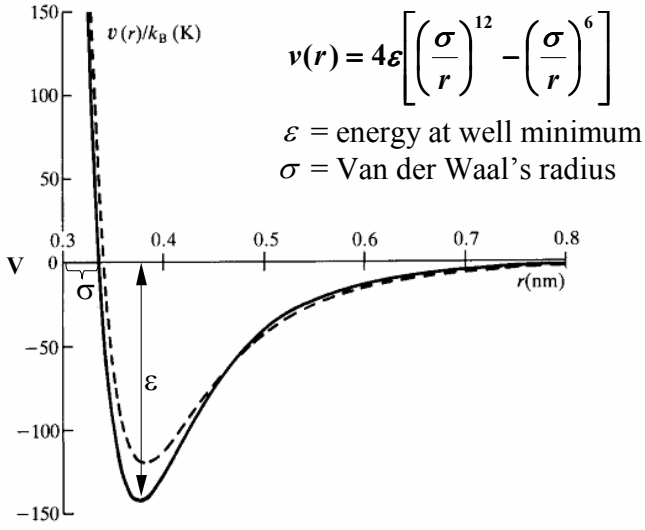

Figure 1.6. Lennard-Jones 6-12 Potential.

Molecular dynamics has shown that the initial response of a Lennard-Jones material streched between rigid walls is elastic due to intermolecular attractions. Molecular instability causes molecular level yielding behavior, ultimately resulting in cavitation within the material.[25] As shear strains are increased, local potential energy minima vanish, causing the system to become unstable and driving the system to relaxation at new minima.[26] Rather than a continuous process, plastic flow of the system consists of a series of discrete yielding or cavitation events separated by nearly elastic behavior. As the material is continually strained, cavities become larger, increasing in size from nanoscopic to microscopic and eventually to macroscopic, where a coalescence of the cavities occurs, causing a complete fracturing of the material. The Lennard-Jones potential facilitates molecular modeling by providing the maintenance of minimum particle spacing and an estimate of long-range cohesion through its weakly attractive tail section.[27]

Secondary Relaxations

Secondary relaxations are a broad term for relaxations in polymers other than the glass transition, which is termed the primary relaxation. Secondary relaxations are associated with short range sub-T_g molecular motions, meaning they occur at lower temperatures than the long range cooperative motions which signal the onset of the glass transition. Since secondary relaxations occur below T_g, the term sub-T_g relaxation is often used to refer to secondary relaxations. Secondary relaxations are usually attributed to simple motions such as methyl rotations, phenyl ring flips, or crankshaft motions of methylene sequences.[28] Secondary relaxations are of particular interest since applications based upon epoxy networks function in the glassy state, where simple, small scale molecular motion dominates polymer dynamics.

Secondary relaxations seen using dielectric spectroscopy (DES) and dynamic mechanical analysis (DMA) correlate with engineering properties such as tensile and compressive moduli, yield, fluid sensitivity, and electrical properties.[4,29,30,31] The mechanisms of secondary relaxations in glasses have been a topic of debate for the last several decades and are not completely agreed upon. In polymeric glasses, due to the complexity and heterogeneity in molecular structures, they are assumed to originate from different motions associated with varying length and time scales.[32,33]

Solid state NMR studies on molecular dynamics of typical model polymers have shed light on the origins of secondary relaxations. The sub-T_g relaxation of poly(alkyl methacrylate) has been studied and believed to be associated with main chain motions caused from librations of ester side moieties.[34,35] The term libration refers to a nondescript motion in the backbone of the polymer caused by other distinct motions, such

as the methyl rotations, phenyl ring flips, or crankshaft motions mentioned previously. Although speculated, it is not certain if the ester librations trigger main chain motions, or the reverse is true.[36] Inglefield demonstrated through deuterium echo delay line shape experiments that the sub-T_g relaxations observed in dynamic mechanical analysis for linear and crosslinked epoxy systems were composite motions of phenyl ring flips and trans-gauche isomerization of hydroxypropylether groups.[32] Ring flips were assigned as the faster motions contributing to mechanical loss in the low temperature region of the secondary relaxation, and the trans-gauche isomerization was assigned as the slower motions contributing to mechanical loss at the higher temperature region of the relaxation. The two motions mentioned above do not fully account for the sub-T_g transition of epoxy polymers. Although Inglefield indicates the existence of even slower motions than observed for epoxy polymers, he could not conclusively identify the specific architectural contributions.

Temperature dependence for the rate of the secondary relaxation obeys the Arrhenius Equation; when plotting τ_c vs. T the activation energy, E_a, and exponential (frequency) pre-factor, τ_0^{-1}, are calculated (Equation 1.3). [10]

$$\tau_c^{-1} = \tau_0^{-1} * e^{(\frac{-E_a}{RT})}$$

where: τ_c = correlation time

τ_0 = exponential pre-factor

E_a = activation energy

R = the universal gas constant

T = temperature

Equation 1.3. Arrhenius equation for calculating activation energy.

As discussed above, more complex motions can be associated with motional "cooperativity" of neighboring groups. This "cooperativity" tends to slow molecular motions and increase the activation energy of relaxations.[37] Intra- and inter-chain cooperativity in polymeric glasses is governed by molecular architecture including symmetry, rigidity, and steric hindrance.[38] Kremer, et al. incorporated cyclohexylene rings into the main-chains of PET and reported a cooperative secondary relaxation of ester group interactions with "chair-chair" conformational transitions.[39] Yee and coworkers reported the secondary relaxation in BPA-PC was associated with cooperative motions of chain lengths up to seven repeat units.[40] In contrast, BPA-polyformals containing methylene-diether groups represent more flexible polymers and show no evidence of cooperation larger than one repeat unit.[41] These observations suggest the extent of backbone rigidity controls the level of in-chain motional cooperativity.

Reports also suggest that simple relaxations have very little, or no, contribution to configurational entropy unless involved in cooperative motions.[42,43] Starkweather described a method for calculating configurational entropy as a thermodynamic criterion

to distinguish between simple and cooperative secondary relaxations, and proposed that activation energies of secondary relaxations are expressed as Equation 1.4:

$$E_a = RT * \left[1 + \ln\left(\frac{kT}{2\pi hf}\right)\right] + T\Delta S$$

where: E_a and R are the same as defined in Equation 1.3

k = Boltzman constant

h = Plank's constant

f = the frequency equal to τ_c^{-1}

ΔS = configurational entropy

T = the temperature at which the relaxation reaches its peak. [44]

Equation 1.4. Starkweather expression for cooperativity of motions.

Figure 1.7 depicts the application of Equation 2 for distinguishing relaxations with varying degrees of cooperativity. The line in Figure 1.7 was drawn using Equation 2 at $\Delta S = 0$, which defines the theoretical limit of activation energy for secondary relaxations. The figure includes activation energy data extracted from several references[32,45,46] and represents a range of cooperative motions. In general, as the activation energies on this diagram deviate from the theoretical limit, or simple motion line, a higher degree of cooperativity is assigned to the polymer secondary motions.

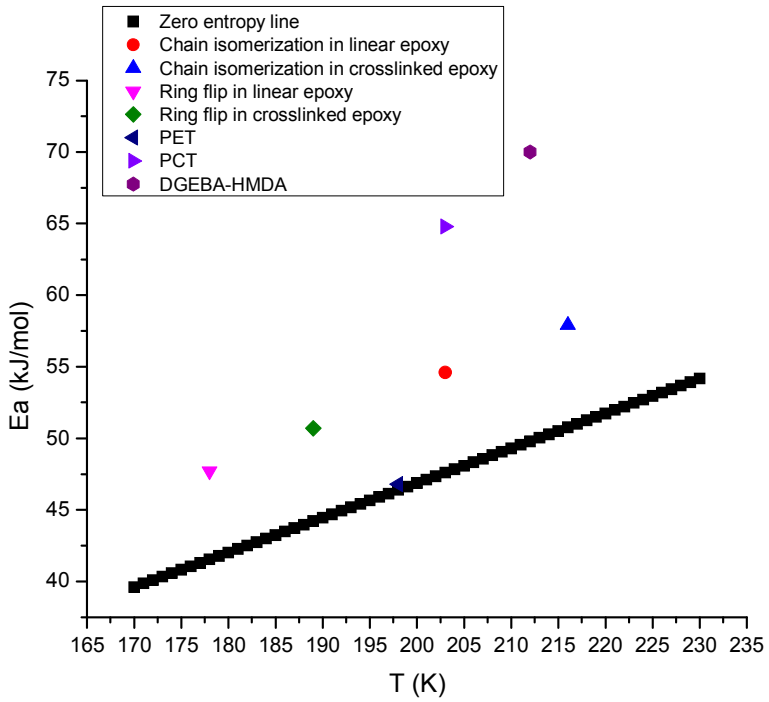

Figure 1.7. Starkweather plots of the E_a for several cooperative motions.

Johari and Goldstein discovered secondary relaxations in rigid small molecule glasses.[47,48] Since "local" motions are not possible for rigid molecules, this class of secondary relaxations is attributed to motions of the entire molecule. This principle suggests internal flexibility of molecules is not a requirement for the occurrence of secondary relaxations.[49,50] This class of secondary relaxations shows a temperature and pressure dependence, and is correlated to primary relaxations.[51] It was found that this class of secondary relaxations resembles primitive relaxations.[52,53,54,55] A primitive relaxation is a hypothetical local relaxation process for a small molecule or, in the case of polymers, a repeat unit. The similar characteristics of the special secondary relaxation and the primitive relaxation lead to a reasonable conclusion that the special secondary relaxation also functions as a precursor of the glass transition. To distinguish this

secondary relaxation from other secondary relaxations, it is commonly recognized as the Johari-Goldstein β-relaxation in honor of their pioneering work.[49]

The JG β-relaxation was found in a variety of glasses including small molecule, metallic, and polymeric.[56,57,58] The universality of JG β-relaxation in glasses has been discussed and accepted by numerous researchers.[59,60] In polymeric glasses, research has mainly focused on linear polymers.[61,62,63] Very little work has been reported on crosslinked polymeric glasses regarding the mechanism of the JG β-relaxation, factors that affect its thermodynamic properties, or its correlation with the primary relaxation. Johari[50] and Beiner[64] examined the evolution of relaxation times during different stages of epoxy amine reactions. Johari calculated an E_{act}=63.4 kJ/mol for the JG β-relaxation of 4,4'-diaminodicyclohexylamine and DGEBA, regardless of the extent of conversion.

Configurational Entropy

33DDS/DGEBA possesses more configurational entropy in the melt state than 44DDS/DGEBA. Due to the meta substitution, 33DDS/DGEBA possesses more configurations above T_g; therefore, a larger amount of cooling from the melt state is required to eliminate the configurational entropy and cross the glass transition into the glassy state. The para substituted 44DDS creates a network with DGEBA consisting of only para linkages, giving 44DDS/DGEBA a lower number of configurations above T_g, and a lower amount of cooling is needed to eliminate the configurational entropy and become a glass. This difference in configuration entropy has the effect of lowering the glass transition of 33DDS/DGEBA when compared to 44DDS/DGEBA.

This explanation for 33DDS/DGEBA possessing a lower T_g than 44DDS/DGEBA also explains the higher density and lower amount of free volume in the 33DDS epoxy.[65]

Polymer chains in epoxies cured with 33DDS possess a greater amount of flexibility due to the increased configurational entropy. This flexibility allows the chains to rearrange at lower temperatures, eliminating free volume to form more tightly packed amorphous networks than 44DDS epoxies.

The meta substitution also has an effect on the ability of the DDS rings to undergo ring-flipping, thus affecting secondary relaxations.[66] Phenyl rings in DGEBA and 44DDS can undergo facile rotation about the axis of symmetry comprised by the 1 and 4 phenyl ring bonds creating a phenyl ring π-flip (Figure 1.8).[67,68] The process requires the simultaneous rotation of two bonds: the bonds in the 1 and 4 positions of the phenyl ring.[69] Due to 33DDS's meta substitution, it does not possess an axis of symmetry through the phenyl ring, making it impossible for 33DDS rings to undergo ring flipping. Therefore, DDS ring flips, as a method of energy dissipation, are unavailable to the 33DDS/DGEBA network (Figure 1.8). When one of the bonds adjacent to the phenyl ring undergoes rotation, cooperative motions in the polymer backbone are necessary to relieve torsional strain.

Upon warming, the glass transition coincides with the onset of long-range segmental motions. In crosslinked aromatic systems, one bond rotations causing cooperative motions will result in long range segmental motions in the matrices. Therefore, the inability of 33DDS rings to undergo phenyl ring flips forces longer range cooperative motions as the result of a one bond rotation, having the effect of lowering T_g of 33DDS epoxies in comparison to 44DDS epoxies.

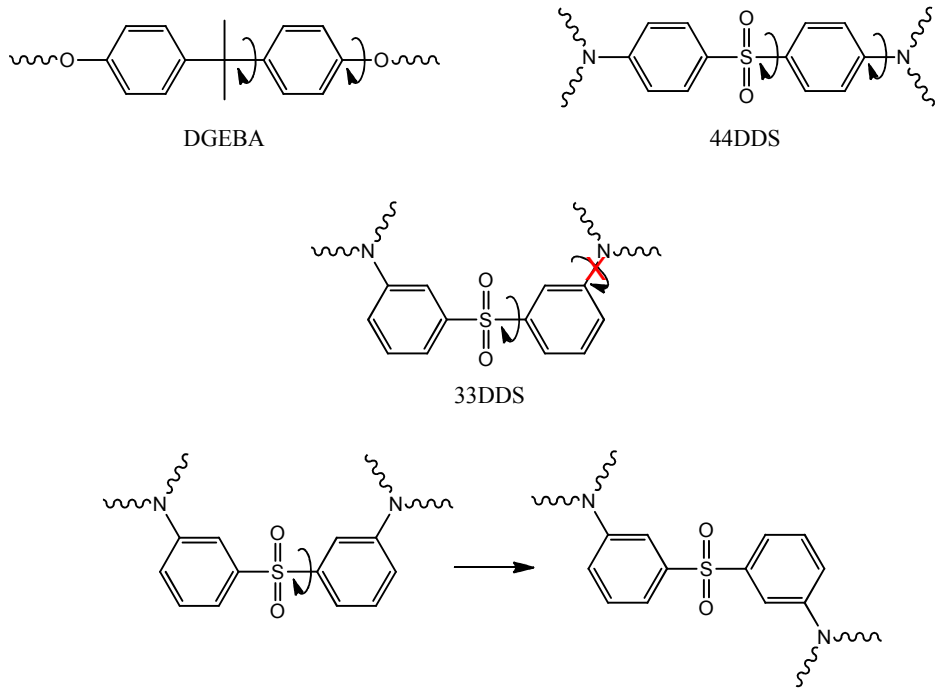

Figure 1.8. Phenyl ring π-flips in DGEBA and 44DDS are not possible in 33DDS forcing long range cooperative motion for a 33DDS phenyl ring rotation.

Viscoelastic Mechanical Properties

Viscoelastic mechanical properties influence the performance of polymers in deformation and control stress relaxation, creep, and hysteresis.[70] Macroscopic deformations of materials, distortion and dilation, can be coupled to viscoelasticity. Linking viscoelastic behavior to chemical composition and architecture in glassy polymer network solids is critical since a variety of relaxations, including secondary relaxations, are used to probe macroscopic mechanical behavior.[71]

Figure 1.9 shows a stress-strain curve of an epoxy network in uniaxial compression. Deformations of glassy polymer networks in compression are governed through elastic, viscoelastic, and plastic responses. In the elastic region polymer chains undergo spring-like affine deformations where the molecules are held intact by crosslinks

and intermolecular cohesive forces. Strain recovers linearly and instantaneously upon release of stress in the elastic state.[72] Strain deviates from linearity under stress when the polymer enters its viscoelastic regime. Due to the viscoelastic nature of polymer chains, energy is dissipated in molecular movements and residual strain recovers more slowly after release of stress (non-instantaneous) so a time dependant factor is introduced. Raising the temperature accelerates viscoelastic strain recovery, showing these relaxations are time-temperature sensitive. As a result, by obtaining sets of measurements from a polymeric material at different temperatures and times, and using an appropriate shift factor, α_T, it is possible to assemble the data sets into a single "master curve" that represents stress relaxation data over a vast range of timescales.

Theoretically all viscoelastic strain is recoverable once the polymer is heated to above its T_g.[73] In the plastic regime, irreversible deformation occurs, and part of the strain developed is not recoverable. This can be explained by the cavitation of molecules and large dissipation of energy of this cavitation event.[74] Experimental techniques have been employed for decades to study viscoelasticity of glassy polymer solids; however, the phenomena is still not sufficiently understood. Although the connection of molecular motions and secondary relaxation processes to macroscopic viscoelastic behavior is not made in this work, it is the overall goal of advancing multi-scale understanding.

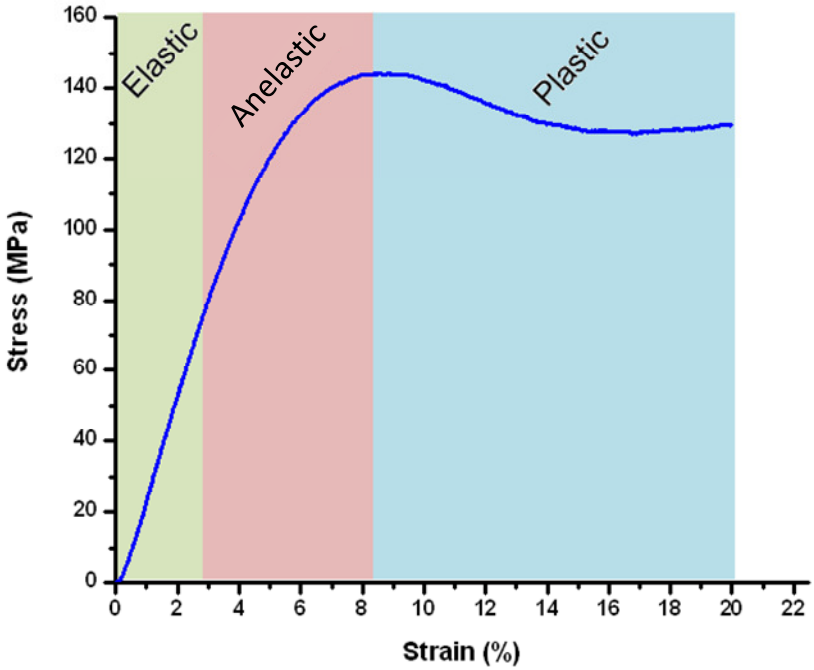

Figure 1.9. Uniaxial compression stress vs. strain plot.[65]

References

1. Lesser, A.J.; Calzia, K.J. *J. Polym. Sci.: Part B: Polym. Phys.,* **2004**, *42*, 2050.
2. Bershtein, V.A.; Peschanskaya, N.N.; Halary, J.L.; Monnerie, L. *Polymer,* **1999**, *40*, 6687.
3. Bellenger, V.; Verdu, J.; Francillette, J.; Hoarau, P.; Morel, E. *Polymer,* **1987**, *28*, 1079-1086.
4. Blanco, M.; Ramos, J.A.; Goyanes, S.; Rubiolo, G.; Salgueiro, W.; Somoza, A.; Mondragon, I. *J. Polym. Sci.: Part B: Polym. Phys*, **2009**, *47*, 1240.
5. Hiemenz, P.C.; Lodge, T.P. *Polymer Chemistry*, 2nd ed.; CRC Press: Boca Raton, FL, 2007; p. 404.
6. Heinz, S.R.; Wiggins, J.S. *SAMPE International Symposium Proceedings*, Salt Lake City, UT, October 2010.
7. Crosslinking. <http://web.mst.edu/~wlf/Coatings/crosslink.html> (accessed 08/10/2010).
8. Gosse, J.H. and Christensen, S., *American Institute of Aeronautics & Astronautics*, **2001**, 1184.
9. Christensen, S. *Explanation of Deformation*, Boeing Internal Report (Seattle, WA, 2001).
10. Kuraishi, A., Gosse, J.H., Wollschlager, J.A. and Townsley, J.L., "Methodology for Composite Durability Assessment" DARPA-NAVAIR Presentation (2005).
11. Seefeldt, M. *Advanced Material Science*; **2001**, *2*, 44.
12. Mott, P.H., Argon, A.S. and Suter, U. *Philosophical Magazine,* **1993**, *67*, 961.

13. Sternstein, S.S.; Ongchin, L. *ACS Poly. Prepr.*, **1969**, *10*, 1117.

14. Zebarjad, S.M.; Bagheri, R.; Seyed Reihani, M.; Lazzeri, A. *J. Appl. Poly. Sci.,* **2003**, *90*, 3767.

15. Fond, C.; Lobbrecht, A.; Schirrer, R. *International Journal of Fracture,* **1996**, *77*, 141.

16. Chui, C.; Boyce, M.C. *Macromolecules,* **1999**, *32,* 3795.

17. Capaldi, F.M.; Boyce, M.C.; Rutledge, G.C. *Physical Review Letters,* **2002**, *89,* 175505.

18. Argon, A.S.; Cohen, R.E. *Polymer,* **2003**, *44*, 6013.

19. Haward, R.N.; Young R.J. *The Physics of Glassy Polymers, 2nd ed.* London, UK: Chapman & Hall, 1997.

20. Hasegawa, M., Sensui, N., Shindo, Y., and Yokota, R. *Macromolecules,* **1999**, *32*, 387.

21. Hou, Y.; Bai, X.; Gao, J.; Pang, T. *Heilongjiang Daxue Ziran Kexue Xuebao.* **2002**, *22,* 781.

22. Morrison, R.T.; Boyd, R.N. *Organic Chemistry, 5th ed.* Newton, MA: Allyn and Bacon, Inc, 1987

23. Brown, T.L., LeMay, H.E., and Bursten, B.E. *Chemistry the Central Science, 6th ed.* Englewood Cliffs, NJ: Prentice Hall, 1994

24. Atkins, P. and de Paula, J. *Atkin's Physical Chemistry, 8th ed.* New York, NY: W.H. Freeman and Company, 2006.

25. Baljon, A.R.C.; Robbins, M.O. *Computational and Theoretical Polymer Science* **1999**, *9*, 35.

26. Malandro, D.L.; Lacks, D.J. *J. of Chemical Physics* **1999**, *110*, 4593.

27. Chui, D. and Boyce, M.C. *Macromolecules* **1999**, *32,* 3795.

28. Gedde, U.W. *Polymer Physics*, 1st ed.; Chapman & Hall: London, UK, 1995; p. 92.

29. Sun, N.; Liu, J.; Dull, T.; Yee, A.F. *J. Polym. Sci.: Part B: Polym. Phys.* **2007**, *45*, 1410.

30. Mijovic, J.; Zhang, H. *Macromolecules* **2003**, *36*, 1279.

31. Liu, J.; Yee, A.F. *Macromolecules* **1998**, *31*, 7865.

32. Shi, J.-F.; Inglefield, P.T.; Jones, A.A.; Meadows, M.D. *Macromolecules* **1996**, *29*, 605.

33. Bartolotta, A.; Carini, G.; Carini, G.; DiMarco, G.; Tripodo, G. *Macromolecules* **2010**, *43*, 4798.

34. Schimidt-Rohr, K.; Kulik, A.S.; Beckham, H.W.; Ohlemacher, A.; Pawelzik, U.; Boeffel, C.; Spiess, H.W. *Macromolecules* **1994**, *27*, 4733.

35. Kuebler, S.C.; Schaefer, D.J.; Boeffel, C.; Pawelzik, U.; Spiess, H.W. *Macromolecules* **1997**, *30*, 6597.

36. Vogel, M.; Medick, P.; Rossler, E.A. *Ann. Rep. on NMR Spec.* **2005**, *56*, 231.

37. Matsuoka, S.; Hale, A. *J. Appl. Polym. Sci.* **1997**, *64*, 77.

38. Fitz, B.; Andjelic, S.; Mijovic, J. *Macromolecules* **1997**, *30*, 5227.

39. Merenga, A.S.; Papadakis, C.M.; Kremer, F.; Liu, J.; Yee, A.F. *Colloid Polym. Sci.* **2001**, *279*, 1064.

40. Jho, J.Y.; Yee, A.F. *Macromolecules* **1991**, *24*, 1905.

41. Li, L.; Yee, A.F. *Macromolecules* **2002**, *35*, 425.

42. Starkweather, H.W. *Macromolecules* **1981,** *14,* 1277.

43. Pinto, S.S.; Moura-Ramos, J.J.; Diogo, H.P. *Euro. Polym. J.* **2009**, *45*, 2644.

44. Starkweather, H.W. *Macromolecules* **1988**, *21*, 1798.

45. Chen, L.P.; Yee, A.F.; Goetz, J.M.; Schaefer, J. *Macromolecules* **1998**, *31*, 5371.

46. Heux, L.; Halary, J.L.; Laupretre, F.; Monnerie, L. *Polymer* **1997**, *38*, 1767.

47. Johari, G.P.; Goldstein, M. *J. Chem. Phys.* **1970**, *53*, 2372.

48. Johari, G.P. *J. Chem. Phys.* **1973**, *58*, 1766.

49. Ngai, K.L.; Paluch, M. *J. Chem. Phys.* **2004**, **120**, 857.

50. Tombari, E.; Salvetti, G.; Johari, G.P. *J. Chem. Phys.* **2000**, *113*, 6957.

51. Kessairi, K.; Capaccioli, S.; Prevosto, D.; Lucchesi, M.; Sharifi, S.; Rolla, P.A. *J. Phys. Chem. B.* **2008**, *112*, 4470.

52. Bengtzelius, U.; Gotze, W.; Sjolander, A. *J. Phys. Solid State Phys.* **1984**, *C17*, 5915.

53. Gotze, W.; Sjogren, L. *Rep. Prog. Phys.* **1992**, *55*, 241.

54. Schilling, R. *Disorder Effects on Relaxational Processes*; Springer-Verlag: Berlin, 1994; p. 193.

55. Ngai, K.L. *J. Chem. Phys.* **1998**, *109*, 6982.

56. Brand, R.; Lunkenheimer, P.; Loidl, A. *J. Chem. Phys.* **2002**, *116*, 10386.

57. Hachenberg, J.; Bedorf, D.; Samwer, K. *Appl. Phys. Lett.* **2008**, *92*, 131911.

58. Pelletier, J.M.; Perez, J.; Duffrene, L.; Sekkat, A. *J. Non-Cryst. Solid.* **1999**, *258*, 119.

59. Thayyil, M.S.; Capaccioli, S.; Prevosto, D.; Ngai, K.L. *Philo. Mag.* **2008**, *88*, 4007.

60. Bogoslovov, R.B.; Hogan, T.E.; Roland, C.M. *Macromolecules* **2010**, *43*, 2904.

61. Roland, C.M.; Schroeder, M.J.; Fontanella, J.J.; Ngai, K.L. *Macromolecules* **2004**, *37*, 2630.

62. Casalini, R.; Roland, C.M. *Macromolecules* **2005**, *38*, 1779.

63. Kaminski, K.; Wlodarczyk, P.; Adrjanowicz, K.; Kaminska, E.; Wojnarowska, Z.; Paluch, M. *J. Phys. Chem. B* **2010**, *114*, 11272.

64. Beiner, M.; Ngai, K.L. *Macromolecules* **2005**, *38*, 7033.

65. Kauskik, M.; Jackson, M.; Heinz, S; Wiggins, J.S.; Nazarenko, S. *SAMPE International Symposium Proceedings*, Witchita, KS, 2009.

66. David, L.; Etienne, S. *Macromolecules,* **1992**, *25*, 4302-4308.

67. Cholli, A.L.; Dumais, J.J.; Engel, A.K.; Jelinski, L.W. *Macromolecules,* **1984**, 17, 2399-2404.

68. Schaefer, J.; *Macromolecules,* **1985**, 18, 368-373.

69. Sydney K. Brownstein and Michael D. Guiver, *Macromolecules,* **1992**, 25, 5181-5185.

70. Marano, C.; Rink, M. *Mech. Time-Dependent Mat.* **2005**, *9*, 1.

71. Viscoelasticity notes. <http://silver.neep.wisc.edu/~lakes/VEnotes.html> (accessed 8/29/2010).

72. Gedde, U.W. *Polymer Physics*, 1st ed.; Chapman & Hall: London, UK, 1995; p.41.

73. Lakes, R.S. *Viscoelastic Solids*; CRC Press: Boca Raton, FL, 1999.

74. G'Sell, C. *Mat. Sci. Eng. A,* **2001**, *309*, 539.

CHAPTER II

A MOLECULAR DYNAMICS APPROACH TO PREDICTING PROPERTIES OF CROSSLINKED AROMATIC POLYMERS, PART I

Introduction

Molecular Dynamics (MD) simulations are a useful tool to visualize network architecture, the process of crosslinking, and molecular interactions. MD simulations also provide a powerful technique for predicting thermomechanical properties of polymers. In this regard, MD simulations represent an expedient, multiscale technique, connecting interactions and properties on the atomistic time and size scale to macroscale properties of the material.

Molecular dynamics simulations have further use as a multiscale technique when considering composite property prediction. Composite properties are predicted using a Finite Element Analysis (FEA), a technique which operates in the continuum using constituative relations. FEA uses the physical properties of the individual components in a composite to calculate the ultimate properties of the composite. For example, in a matrix-fiber composite, FEA would combine the physical properties of the matrix with those of the fibers to calculate the properties of the fiber reinforced matrix composite. Using MD with FEA in a hierarchical or concurrent fashion creates a powerful simulation combination where the outputs of the molecular dynamics simulations (thermomechanical properties of polymers) become the inputs for finite element analysis. The ultimate goal is to design composites possessing a specific set of properties without having to complete the time-consuming and costly process of synthesizing the monomers, B-staging the matrix, incorporating the B-staged matrix into the fiber, curing the

composite, and finally completing dozens of different material properties tests. This goal has not yet been attained; however, we are able to predict matrix properties with steadily decreasing error.

In this research, atomistically explicit MD methods have been refined to continually improve the accuracy of simulations without substantially increasing the time or computing power needed to complete simulations. Increasing the accuracy and efficiency of MD has been accomplished through better understanding of the polymers involved, and specifically, an increased awareness of how chemical make-up and network architecture influence the simulations.

Objective

This first chapter provides a detailed description of the molecular dynamics simulation procedure and theory behind that procedure. Chapters II and III are based on the same general procedure and theory; however, we will adjust our approach to create more accurate simulations. Our reasoning for using MD simulations is twofold. First, we want to improve the accuracy of the simulations by comparing the simulated thermomechanical properties to experimentally obtained values and adjusting the simulation procedure where discrepancies are observed. Second, we want to use the simulations, where accurate, to understand the effect of the chemical and structural design of the network on thermomechanical properties. An example of chemical design is the introduction of additional sulfone or phenyl ring content, while network design could include a change in crosslink density. Even though some of the simulated properties may not exactly match experimental results, simulations giving values which are internally comparable are useful to show trends among polymers.

For the purpose of improving accuracy of simulations by comparison of the simulated properties to experimentally obtained properties, two amine / epoxy systems will be used: 3,3'-diaminodiphenyl sulfone (33DDS) / diglycidyl ether of bisphenol A (DGEBA) and 4,4'-diaminodiphenyl sulfone (44DDS) / DGEBA. The thermomechanical properties which will be compared are tensile modulus (E), shear modulus (G), glass transition temperature (T_g), density (ρ), and compression yield strain (ε_y). In addition to these properties, the simulations will report Poisson's ratio (ν), coefficient of thermal expansion in the glassy state (α), and the first invariant of the strain tensor (J_1).

To examine the effect of chemical and structural design on network properties, the two base systems (33DDS/DGEBA and 44DDS/DGEBA) will be compared with a third system (22DDS/DGEBA) to study the effect of para vs. meta vs. ortho amine group positioning. 33DDS and 44DDS will also be modified to contain more sulfones and phenyl rings, additional meta linkages in the middle of the diamine, and higher and lower crosslink densities. The epoxy (DGEBA) will be kept the same across all simulations such that the effects of changes in the diamines can be selectively studied.

Materials

3,3'-diaminodiphenyl sulfone and 4,4'-diaminodiphenyl sulfone were purchased from Sigma Aldrich and used as received. Diglycidyl ether of bisphenol A was purchased under the tradename EPON 825 from Hexion and used as received. The DGEBA was cured with both the 44DDS and 33DDS to make polymers for the experimental physical testing.

The simulated systems consist of a diepoxy cured with multifunctional amines. The epoxy is kept the same across all simulations (DGEBA), while the amine is changed to observe the effect on thermomechanical properties. The chemical structures for the amines and epoxy simulated in Chapter I are shown in Figure 2.1.

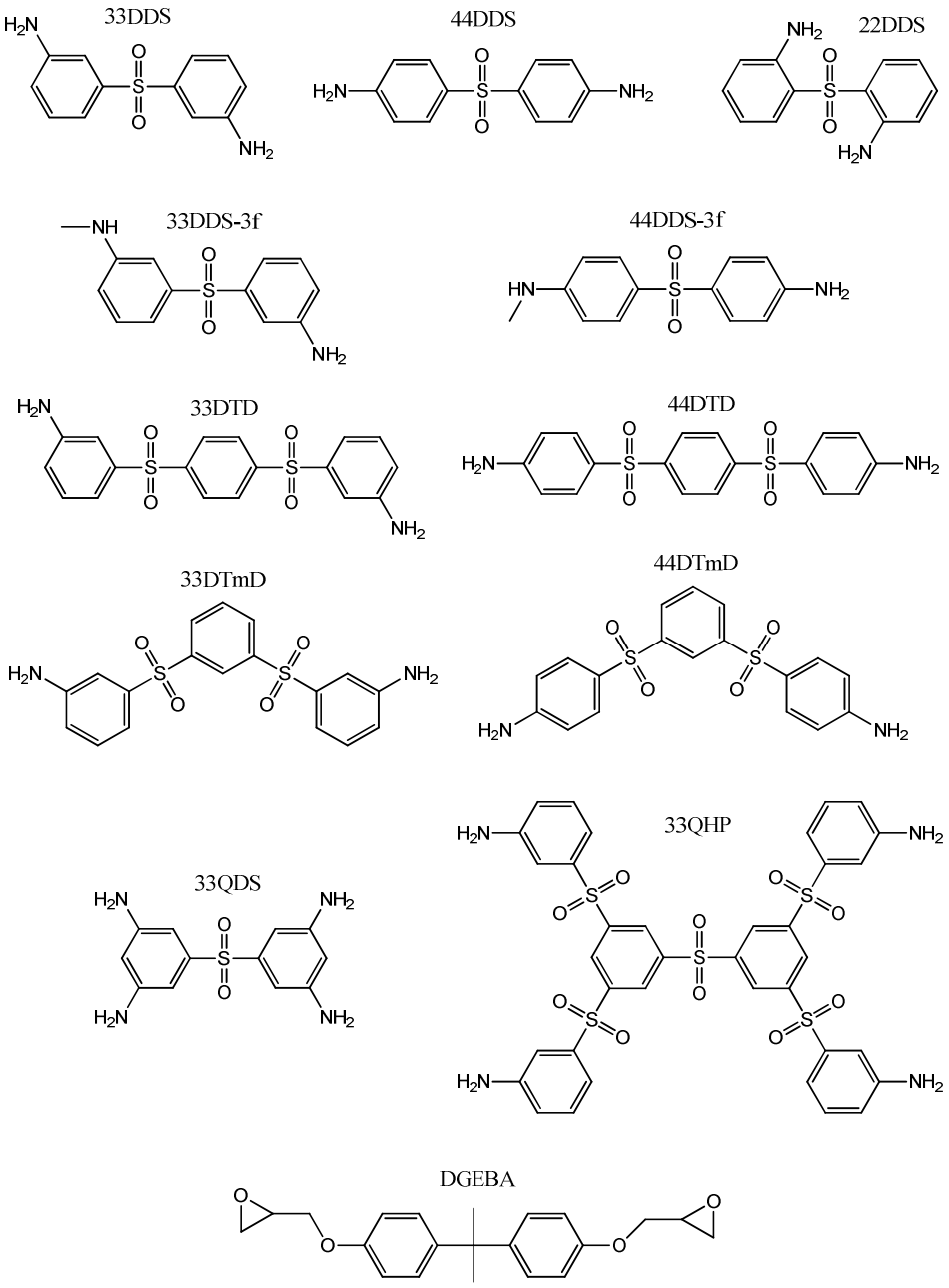

Figure 2.1. Simulated amines and epoxy.

The following table lists the chemical names for the amines and epoxy in the figure above (Table 2.1). The center column lists the commonly used industrial name or a name derived from industry naming and is the name from which the abbreviations are taken. The column on the right gives the Chemdraw® name for each molecule. My naming system for amines was modeled from the industrial names for 3,3' and 4,4'-diaminodiphenyl sulfone.

Table 2.1. Abbreviations and Names for Amines and Epoxy Used in Simulations.

Abbrev.	Industry/Author naming system	Chemdraw® name
33DDS	3,3'-diaminodiphenyl sulfone	3,3'-sulfonyldianiline
44DDS	4,4'-diaminodiphenyl sulfone	4,4'-sulfonyldianiline
22DDS	2,2'-diaminodiphenyl sulfone	2,2'-sulfonyldianiline
33DTD	3,3'-diaminotriphenyl disulfone	3,3'-(1,4-phenylenedisulfonyl)dianiline
44DTD	4,4'-diaminotriphenyl disulfone	4,4'-(1,4-phenylenedisulfonyl)dianiline
33DTmD	3,3'-diaminotriphenyl meta-disulfone	3,3'-(1,3-phenylenedisulfonyl)dianiline
44DTmD	4,4'-diaminotriphenyl meta-disulfone	4,4'-(1,3-phenylenedisulfonyl)dianiline
33QDS	3,3',5,5'-quattraminodiphenyl sulfone	5,5'-sulfonylbis(benzene-1,3-diamine)
33QHP	3,3',3",3'"-quattraminohexaphenyl pentasulfone	3,3',3",3'"-(5,5'-sulfonylbis (benzenedisulfonyl))tetraaniline
DGEBA	Diglycidyl ether of Bisphenol A	2,2'-(((propane-2,2-diylbis(4,1-phenylene)) bis(oxy))bis(methylene))bis(oxirane)

Methods

Matrix Preparation

To prepare 33DDS/DGEBA and 44DDS/DGEBA samples in the bulk, 33DDS and 44DDS must first be solubilized into DGEBA. 33DDS is fully solubilized at 110°C and 45 minutes, while 44DDS is dissolved at 125°C and 45 minutes. Both amines are solubilized using magnetic stirring and a vacuum to remove air and water which become defects in the cured networks. Once the amines are dissolved into DGEBA, the mixtures are poured into molds to create geometries needed for physical property determination,

and the samples are cured. To achieve cure without degradation, the 33DDS/DGEBA and 44DDS/DGEBA are cured for 5 hours at 125°C and 1 hour at 200°C.

Instrumental Analysis

Density is determined using the hydrostatic weighing method. By weighing a sample in and out of water, the Archimedes principle can be used to calculate density. A smooth matrix sample of approximate dimensions 10 X 10 X 4mm is weighed on an accurate balance. This same sample is then submerged in water and weighed. Density is calculated using Equation 2.1. The average of 5 samples is reported.

$$density\ of\ body = \frac{weight\ of\ body}{weight\ of\ body - weight\ of\ immersed\ body} * density\ of\ water$$

Equation 2.1. Density determination by hydrostatic weighing.

Dynamic mechanical analysis (DMA) is accomplished on a Thermal Analysis (TA) Q800® instrument using a tensile fixture. A strain of 0.05% and a frequency of 1Hz are used. Silicone molds used in DMA sample preparation create small rectangular strips, which have dimensions of approximately 5.0 X 1.7 X 61.0mm. TA Universal Analysis® software is used to analyze the DMA plots. Tensile modulus is determined as the storage modulus at 25°C and the T_g is determined as the tanδ maximum. The average of three samples is reported.

Shear modulus is determined using a TA ARES rheometer. Silicone molds used in rheometry sample preparation create rectangles, which have dimensions of approximately 10.0 X 4.0 X 46.0mm. A strain of 0.05% and frequency of 6.28 rad/sec (1Hz) is used. The average of 4 samples is reported.

Differential scanning calorimetry (DSC) is accomplished on a TA Q200 instrument at a temperature ramp of 10°C per minute. An initial heating to >25°C above T_g is accomplished to clear thermal history, and a subsequent cooling and heating ramp are run for each sample. T_g is calculated using the 'glass transition' analysis function in TA's Thermal Advantage software. For each sample, the second heating and cooling T_gs are averaged to give the reported T_g of that sample. The average of four samples is reported.

Compression yield strain is measured on an MTS 800 testing frame with a specially designed compression subpress according to ASTM D695. To obtain the precise cylindrical sample geometry necessary, samples are prepared in cylindrical Teflon molds. Once cured, the matrix cylinders are precisely lathed to a diameter of 0.50in. Then the cylinders are cut with a diamond edged saw to be 1.00 in. long and completely square (90° angles at the rim) to create a geometry in concordance with ASTM D695. The compression tests are run at a strain controlled compression rate of 0.05in./min. The average of two samples is reported.

Molecular Dynamics Simulation Procedure

All molecular dynamics calculations and simulations were accomplished in Accelrys Materials Studio 4.2® using the Condensed Phase Optimized Molecular Potentials for Atomistic Simulation Studies (COMPASS®) forcefield, group based cutoffs based on user assigned charge groups, and the "Medium" quality setting. The quality of the simulation is determined by four parameters: cutoff distance, spline width, buffer width, and relative dielectric. The cutoff distance determines the distance at which the nonbond forces (van der Waals and Coulombic interactions) will be included in the

summation. The spline width specifies the size of the region within which non-bond interactions are splined from their full value to zero. The buffer width defines the distance beyond cutoff at which non-bond interactions are zero.[1] Finally, the dielectric constant is adjusted relative to the permittivity of free space. The "Medium" quality summation sets the cutoff distance at 9.50Å, the spline width at 1.00Å, the buffer width at 0.50Å, and the relative dielectric at 1.00.

Build seed and structures. The molecules analyzed were built using Materials Studio's Dendrimer function. The Dendrimer function starts with a Seed molecule and builds Structure molecules onto that Seed as prescribed by the user. The Seed and Structure molecules are essentially monomers. The user determines the chemical structure and reactive sites of the Seeds and Structures.

Materials Studio® cannot predict a chemical reaction, such as the ring opening of an epoxide by an amine, so the Seeds and Structures used need to combine in a way that yields a bonded epoxy-amine system. Additionally, in order to save computing time and ensure that dipoles are not broken at the summation cutoff, the calculations are completed using group based cutoffs instead of atom based cutoffs, meaning the software will not consider each atom individually when performing calculations. Instead, groups of bonded atoms with a net charge of 0 will be assigned as charge groups, and MD calculations will be performed considering these charge groups.

To (1) create a chemically correct network and (2) create a method by which non-bond forces may be summed without splitting dipoles, the amine and epoxy Seeds and Structures are built in a specific fashion. The epoxies are built with epoxide groups that have already been opened and are missing a methyl group, and the amines are built with

two methyl groups bonded to each nitrogen atom (Figure 2.2). It may be noted that each opened epoxide is missing one methyl group because this group is included on the amine in order to make neutral charge groups. The H* atoms present on both the modified epoxy and amine are hydrogen atoms that function as connection points. When the modified epoxies and amines are bonded together, these H* atoms will disappear to leave a chemically correct epoxy-amine bond.

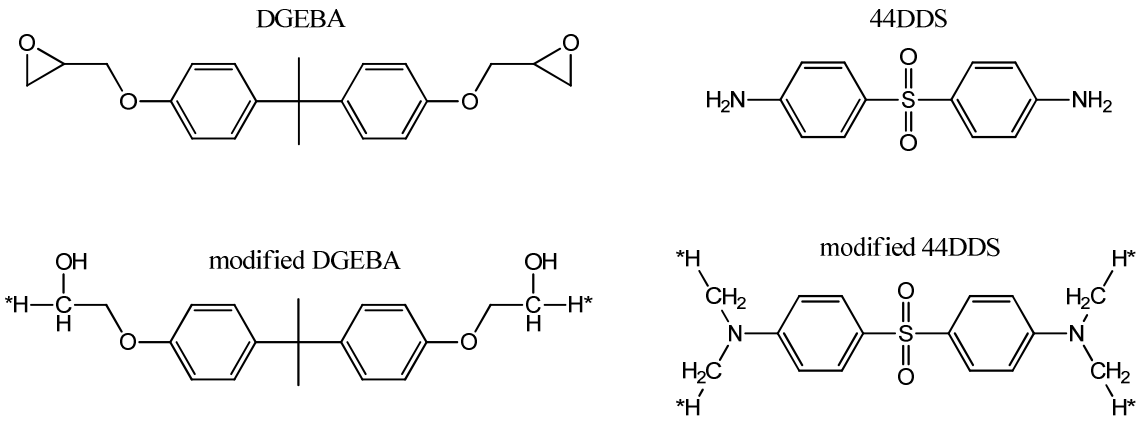

Figure 2.2. Modified DGEBA and 44DDS for use in MD simulations.

Build polymer and amorphous cell. For the purpose of this research, amines are always used as the Seed, and both amines and epoxies are used as Structures. The polymer is built in dendritic fashion, starting with an amine and adding first an epoxy, then an amine, then an epoxy, and so on. Dendrimers are built assuming full conversion of epoxies and amines until the dendrimer reaches ~3,500 atoms, at which point the appropriate number of epoxies or amines are added to balance the stoichiometry (2:1 epoxy:amine ratio). The dendrimers are relaxed using the Clean function to minimize

some of the energy in the structure, mostly by setting the bonds to the appropriate angles and lengths.

Before any of the remaining calculations can be performed, a periodic cell must be created from the dendrimer. The periodic Amorphous Cell is necessary to overcome the problem of surface effects. Periodic boundary conditions define a quantity of material in three dimensional space; as atoms move and leave that space, replacements come in.[2] The amorphous cell construction function is used to place a single dendrimer into 10 separate amorphous cells at a temperature of 298K. The density of the amorphous cell is ramped at 0.01g/cc to reach a final density of 0.4 g/cc. To optimize geometry and configuration of the amorphous cell, the maximum number of lookahead bonds (6) and lookahead configurations (48) are used. Ring catenations are identified, and the amorphous cell construction is restarted if ring catenation is found. A total of 1,000 dynamics steps are performed at the end of the construction.

Minimization and equilibration. The amorphous cell construction will attempt to return ten amorphous cells as specified. However, some of these jobs may fail for energetic reasons. Of the amorphous structures created, the three with the lowest final total energy are chosen to be further analyzed. Three structures are chosen to obtain statistically viable data and average out some of the error. These three structures are minimized using 2,500 iterations with the Discover Minimizer employing the Smart Minimizer method. The Smart Minimizer uses a combination of the steepest descent, conjugate gradient, and Newton energy minimization processes. To determine whether the structure is appropriately minimized, the maximum derivative of the energy is calculated. The closer the maximum derivative is to 0, the closer the structure is to the

bottom of the energy well, meaning the energy has been effectively minimized. The minimization process should yield a maximum derivative of ~10. If the maximum derivative is above 15, the structure is minimized again. For the minimization, both van der Waals and Coulombic forces are considered.

The three amorphous cells are further minimized using a previously written anneal script donated by Boeing Research and Technology. The annealing procedure uses a series of alternating NPT and NVT statistical mechanical ensembles that start at 650K and reduce in temperature by 150K stepwise to 300K. An NPT simulation keeps moles, pressure, and temperature constant over the course of the simulation while allowing other factors such as volume to change, while an NVT run keeps moles, volume, and temperature constant while allowing pressure to change. The anneal process should drastically reduce the energy in the amorphous cell and yield a system close to its energy minimum. The maximum derivative after this step must be less than 0.001. If the maximum derivative is above 0.001, the anneal process must be repeated. The anneal process uses the Andersen thermostat and barostat.

Calculation of molecular trajectories. The output file from the anneal process is taken through another NPT simulation to obtain trajectories through time. In this NPT process, the three amorphous cells are individually run through a series of 250,000 time steps of 1fs and a dynamics time of 250ps. In other words, frames were captured every 2.5ps for a total time of 0.25ns. To cut down on the excessive amount of data this yields, a cell at each of the 250,000 steps is not saved. Instead, a frame is saved every 2,500 steps to give a total of 100 frames. The NPT is completed at atmospheric temperature and pressure using the Andersen thermostat and the Berendsen barostat.

Analysis of Molecular Trajectories. After the NPT trajectories are completed, a series of tests are run to determine the physical properties of the material. Tensile modulus (E), shear modulus (G), and Poisson's ratio (ν) are all calculated on the output of the NPT simulation using the Discover Static Elastic Property Analysis tool. The last 10 frames of each of the three trajectories are analyzed, and the values obtained from the tests are averaged. The values for the three different trajectories are then averaged.

To calculate E, G, and ν, a total of twelve loading experiments are performed, in which six shear processes are accomplished and uniaxial tensile and compression stresses are applied stepwise along the x, y, or z directions.[3] For each loading direction, constant stress dynamics is performed as a series of up to 10 stages, each having a 1ps duration. At the end of each stage, values of the internal stress tensor and of the strain tensor are recorded. Before continuing on to the next stage, the applied (external) stress is incremented by a predefined amount (0.05 GPa, or 500 bar). An experiment for any given pulling direction stops when the strain in that direction exceeds 0.2, or when all 10 stages have been completed, whichever occurs first. When all three loading experiments are completed, the recorded stress-strain data are averaged for all three directions.

In isotropic systems, only two independent coefficients, referred to as Lamé coefficients, are needed to fully describe the stress-strain behavior. The stiffness matrix resulting from the constant stress dynamics experiment is shown in Equation 2.2. Tensile modulus and Poisson's ratio are calculated from a least-squares fit to the average tensile stress vs. strain data and the average lateral strain vs. tensile strain data generated by the program. Since these are isotropic systems, Young's modulus and Poisson's ratio can be

written in terms of the Lamé coefficients, shown in equations 3 and 4, respectively. The shear modulus is calculated directly from the stiffness matrix (Equation 2.5 and 2).

λ+2μ	Λ	λ	0	0	0
λ	λ+2μ	λ	0	0	0
λ	Λ	λ+2μ	0	0	0
0	0	0	μ	0	0
0	0	0	0	μ	0
0	0	0	0	0	μ

Equation 2.2. Stiffness matrix with Lamé coefficients.

$$E = \mu * \frac{3\lambda + 2\mu}{\lambda + \lambda}$$

Equation 2.3. Young's modulus expressed in terms of the Lamé coefficients.

$$\nu = \frac{\lambda}{2(\mu + \lambda)}$$

Equation 2.4. Poisson's ratio expressed in terms of Lamé coefficients.

$$G = \mu$$

Equation 2.5. Shear modulus calculated from Lamé coefficients.

Compression yield strain is calculated using a stress controlled compression script written for Materials Studio 4.2 by Boeing. Uniaxial loads are placed in the x, y, and z directions in separate simulations. Twenty uniaxial loads are applied to each cell starting at 0kPa and increasing up to 0.275kPa. The cell dimensions are recorded after each load,

and the corresponding axial strains are calculated from the average of the uniaxial compressions in the x, y, and z directions. A stress vs. strain curve is approximated by fitting the data to a second order polynomial. The compression yield strain is approximated from the maximum of the second order polynomial curve. Von Mises strain (ε_{vm}) is approximated by multiplying the compression yield strain (ε_y) by 1.5 (Equation 2.6).

$$\varepsilon_{vm} = 1.5 * \varepsilon_y$$

Equation 2.6. Approximation of von Mises strain.

To determine CTE (α), glass transition temperature (T_g), density (ρ), and the first invariant of the strain tensor (J_1), the temperature cycle in Amorphous Cell Protocols is employed. The pressure is kept constant at 0.0001GPa (1bar), the stage duration is set to the maximum of 40,000fs, and the averaging period is also maximized at 20,000fs. The temperature simulation cycles the temperature from 800K to 100K and back to 800K in these 40,000 time steps. Since a theoretical V vs. T plot should be obtained infinitely slowly, the values for the heating and cooling cycles are averaged to give an approximation of a slow process.

With the pressure held constant at atmospheric pressure, the volume will change as the temperature is cycled. Volume, temperature, and density data are recorded every 25K during heating and cooling. The density at room temperature for the heating and cooling cycles is averaged to yield the ambient condition density for the structure. The temperature and volume data are used to create heating and cooling volume vs. temperature plots. An example plot is shown in Figure 2.3.

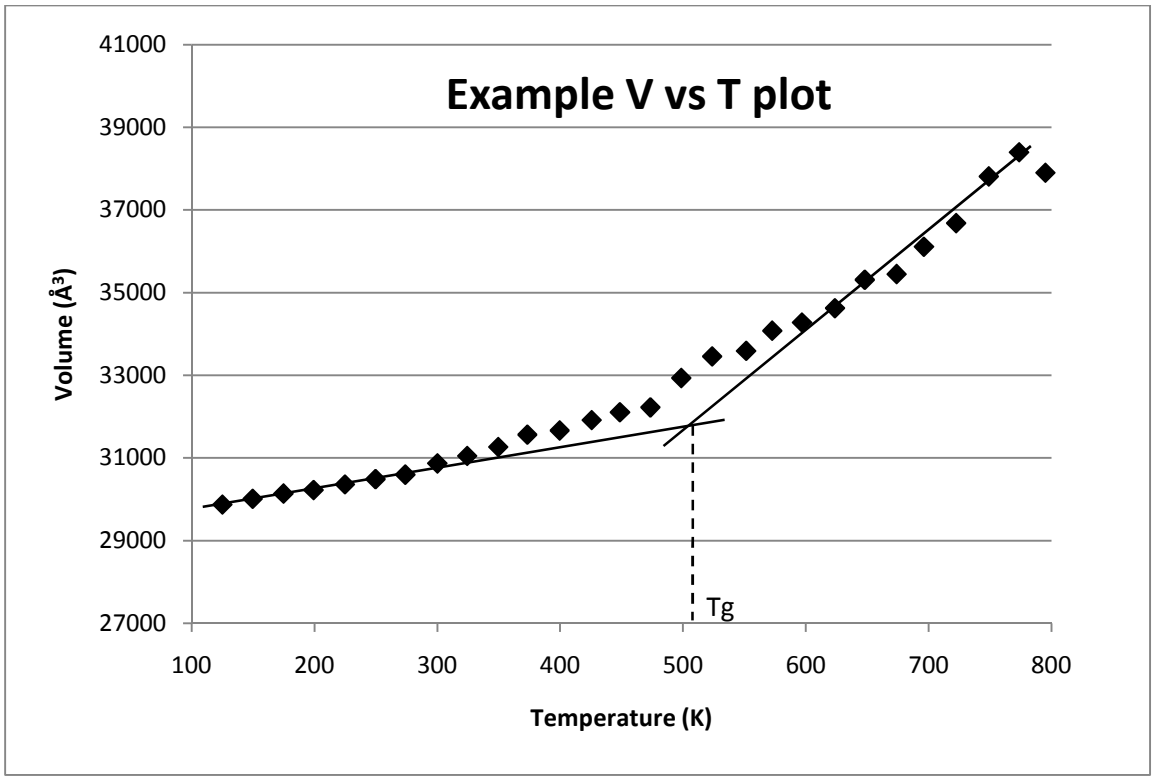

Figure 2.3. Example volume vs. temperature plot.

The slope of the V vs. T line at temperatures above T_g gives the rubbery CTE, while the slope of the plot at temperatures below T_g gives the glassy CTE. The slope is calculated between 100K and 300K to determine the glassy CTE and between 600K and 800K to determine the rubbery CTE. The T_g is determined by extrapolating the two linear curves from which glassy and rubbery CTEs were calculated until these curves intersect. The temperature at the intersection is determined as the T_g. Finally, J_1 is calculated from the average simulated glassy CTE and Tg data according to Equation 2.7.

$$J_1 = \left[\alpha_g\left(T_g - 273\right) + 1\right]^3 - 1$$

Equation 2.7. Determination of J_1.

Results and Discussion

Accuracy of Simulations

To determine the accuracy of simulations, experimental data for 33DDS/DGEBA and 44DDS/DGEBA are compared to simulated values. Table 2.2 details the five thermomechanical properties experimentally obtained, tensile modulus (E), shear modulus (G), glass transition temperature (T_g), density (ρ), and compression yield strain (ε_y). Multiple trials for each experiment were completed, and the average values and standard deviations are reported above the raw data.

By comparing 33DDS to 44DDS, we can observe which simulated properties give accurate values, which simulations show correct trends for comparative purposes, and which simulation procedures need to be altered to yield more accurate results. The 33DDS vs. 44DDS comparison also shows the effect of meta substitution in the polymer backbone on thermomechanical properties of chemically isomeric systems. The experimental data show that tensile modulus, shear modulus, and density are statistically higher in the 33DDS/DGEBA matrix than the 44DDS/DGEBA matrix; however, the glass transition temperature and compression yield strain of 44DDS/DGEBA are significantly higher than the corresponding values for 33DDS/DGEBA.

Table 2.2. Experimental Properties of 44DDS/DGEBA and 33DDS/DGEBA

System	E, GPa	G, GPa	T_g, °C DSC	T_g, °C DMA	ρ, gm/cc	ε_y
44DDS/DGEBA	**2.19**	**0.71**	**217**	**220**	**1.23**	**0.110**
Std. Dev.	*0.31*	*0.05*	*0.4*	*1*	*0.001*	*0.002*
Trial 1	1.85	0.74	217	220	1.24	0.112
Trial 2	2.26	0.70	218	220	1.23	0.109
Trial 3	2.45	0.65	217	221	1.23	
Trial 4		0.75	217		1.23	
Trial 5					1.23	
33DDS/DGEBA	**2.60**	**0.76**	**173**	**186**	**1.24**	**0.095**
Std. Dev.	*0.23*	*0.02*	*0.3*	*1*	*0.003*	*0.001*
Trial 1	2.45	0.73	174	186	1.23	0.094
Trial 2	2.48	0.78	174	187	1.23	0.096
Trial 3	2.86	0.76	174	186	1.24	
Trial 4		0.77	173		1.24	
Trial 5					1.24	

The first set of simulations compares 44DDS to 33DDS and will be used to demonstrate the failures and successes of the simulations in accurately predicting properties and showing trends. Tri-functional versions of the amines are simulated to observe the effect of crosslink density on properties. The structures for the four amines used and the epoxy, DGEBA, are given in Figure 2.4.

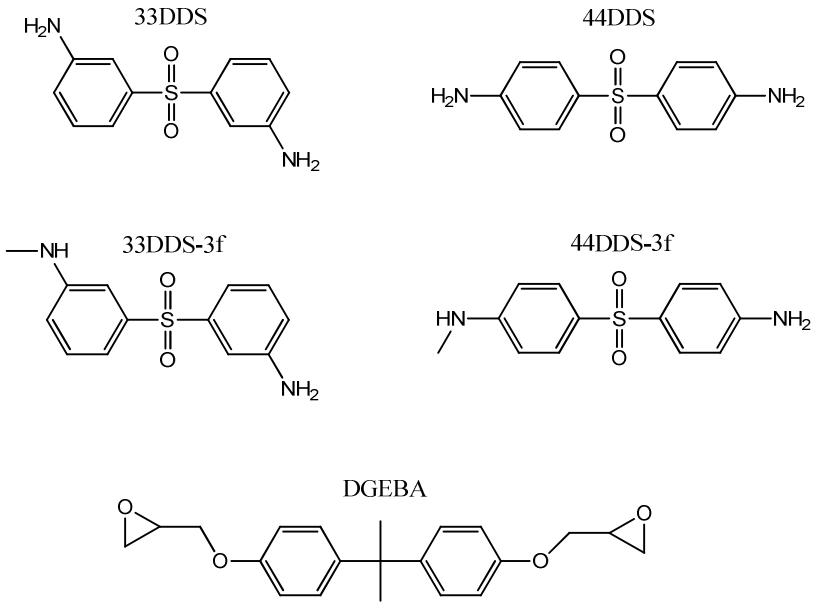

Figure 2.4. Structures of 3f and 4f 33DDS and 44DDS and DGEBA.

Table 2.3 gives the simulation data for these four epoxy systems. All thermomechanical properties are simulated in triplicate for each system, and the average values and standard deviations are recorded above the three trials for each system.

Table 2.3. Simulated Properties for 33DDS/DGEBA and 44DDS/DGEBA

System	E, GPa	G, GPa	ν	α, in/inF x10^{-6}	T_g, °C	ρ, g/cc	J_1	ε_y
44DDS	**5.07**	**1.92**	**0.322**	**32.4**	**202**	**1.196**	**0.031**	**0.14**
Std. Dev.:	*0.18*	*0.08*	*0.007*	*0.7*	*12*	*0.002*	*0.004*	*0.01*
Trial 1	5.26	2.00	0.314	33.2	214	1.198	0.035	0.13
Trial 2	4.91	1.85	0.326	32.2	201	1.195	0.031	0.15
Trial 3	5.04	1.90	0.326	31.8	191	1.195	0.028	0.14
33DDS	**4.42**	**1.68**	**0.317**	**35.1**	**222**	**1.193**	**0.038**	**0.17**
Std. Dev.:	*0.54*	*0.20*	*0.010*	*3.3*	*7*	*0.002*	*0.003*	*0.02*
Trial 1	3.91	1.48	0.318	38.8	223	1.194	0.042	0.18
Trial 2	4.98	1.88	0.327	32.5	229	1.191	0.036	0.15
Trial 3	4.37	1.68	0.307	34.0	215	1.195	0.036	0.19
3f-44DDS	**4.35**	**1.64**	**0.327**	**37.8**	**231**	**1.194**	**0.044**	**0.15**
Std. Dev.:	*0.35*	*0.14*	*0.004*	*3.2*	*30*	*0.010*	*0.009*	*0.01*
Trial 1	4.32	1.62	0.330	35.9	212	1.203	0.040	0.16
Trial 2	4.72	1.78	0.323	35.9	216	1.194	0.038	0.14
Trial 3	4.02	1.51	0.329	41.5	265	1.184	0.055	0.14
3f-33DDS	**4.21**	**1.57**	**0.344**	**35.2**	**194**	**1.203**	**0.033**	**0.14**
Std. Dev.:	*0.30*	*0.13*	*0.017*	*0.7*	*19*	*0.001*	*0.004*	*0.01*
Trial 1	3.90	1.44	0.358	35.8	190	1.203	0.032	0.15
Trial 2	4.50	1.70	0.325	34.5	177	1.202	0.029	0.13
Trial 3	4.24	1.57	0.349	35.4	215	1.203	0.037	0.15

Obtaining accurate densities is considered the first step in determining the validity of molecular dynamics simulations. If the amorphous cell is not relaxed into a structure that possesses a density close to the true density of the material, there is not a good chance the simulations are accurate. The experimental densities for 44DDS/DGEBA and 33DDS/DGEBA are 1.233 and 1.236g/cc, respectively. The simulated densities were a little lower at 1.196 and 1.193g/cc, respectively. This difference in density is not large enough to assume that the simulations are invalid, but it indicates the possibility that the structures did not reach a fully relaxed conformation. The simulations for the 3 functional amines also gave densities a bit low; however, at least these simulations

produced the correct trend: 33DDS/DGEBA having a greater density than 44DDS/DGEBA.

The simulated values for tensile and shear moduli do not show agreement with the experimental data. Firstly, the experimental values are significantly lower than the simulated values. In part, this is explained by the perfect nature of the test specimens in the simulation compared to the experimental test specimens, which possess microscopic defects such as bubbles, voids, microcracks, etc. The larger error is that the simulation fails to show the correct trend between the meta and para amine. Physical properties determined through experimentation clearly show that 33DDS possesses higher E and G than 44DDS. The tri-functional amines show values closer to the experimentally determined values, but the trend is wrong once again.

As is the case with modulus, the simulated T_gs for 33DDS and 44DDS do not give a good estimate of T_g. As determined by DSC and DMA, the T_g of 33DDS/DGEBA should be in the range of 170-190°C, and the T_g of 44DDS/DGEBA in the range of 210-230°C. The simulated values predict a T_g of 222°C for 33DDS/DGEBA and a T_g of 202°C for 44DDS. Interestingly, the tri-functional amines give much more accurate values for the T_gs of 33DDS/DGEBA and 44DDS/DGEBA of 194°C and 231°C, respectively. This result is either indicative of a polymer build that more accurately represents reality when incomplete crosslinking is assumed or a simulation procedure for T_g with too much error. Both of these concerns are addressed in latter simulations summarized in Chapters II and III.

The first invariant of the strain tensor, J_1, gives a measure of the elastic response of the polymer, while von Mises strain ε_{vm} gives an approximation of the distortional

ability of the matrix. J_1 is approximated from the same simulation as T_g, and the same trends are observed: systems with high T_gs also possess high J_1s. We have not determined the J_1 by means of experimental testing; however, since simulated J_1 values came from the same simulation as the T_g, they are likely just as flawed as the simulated T_gs. If a simulation procedure that more accurately predict T_g can be developed, more confidence could be placed in the simulated J_1 values.

The compression strain at yield, ε_y, is used to estimate ε_{vm}. Based on failure theory, increasing the distortional ability of resins is believed to be integral to increasing the failure properties of composites. Before starting this work, our hypothesis was that meta-substituted amines would provide kinks in the backbone that would increase the distortional capability by lowering activation energy for molecular level rearrangements. The simulated results provide support for this hypothesis by showing that the 33DDS matrix possesses a substantially higher compression yield strain than the 44DDS matrix. However, the opposite trend is seen in the experimental data. This result not only debunked our hypothesis, but it also showed a limitation of the simulation procedure.

Effect of Chemical and Structural Design of the Network

In addition to the previous four amines studied, an additional seven amines are combined with DGEBA, and their properties are simulated (Figure 2.5). The structures in Figure 2.5 are chosen in order to study the effects of specific variables in molecular structure on simulated material properties, including, crosslink density, sulfone and aromatic content, and the effect of the amine group's position on the ring (para vs. meta vs. ortho). These simulated results are summarized in Table 2.4

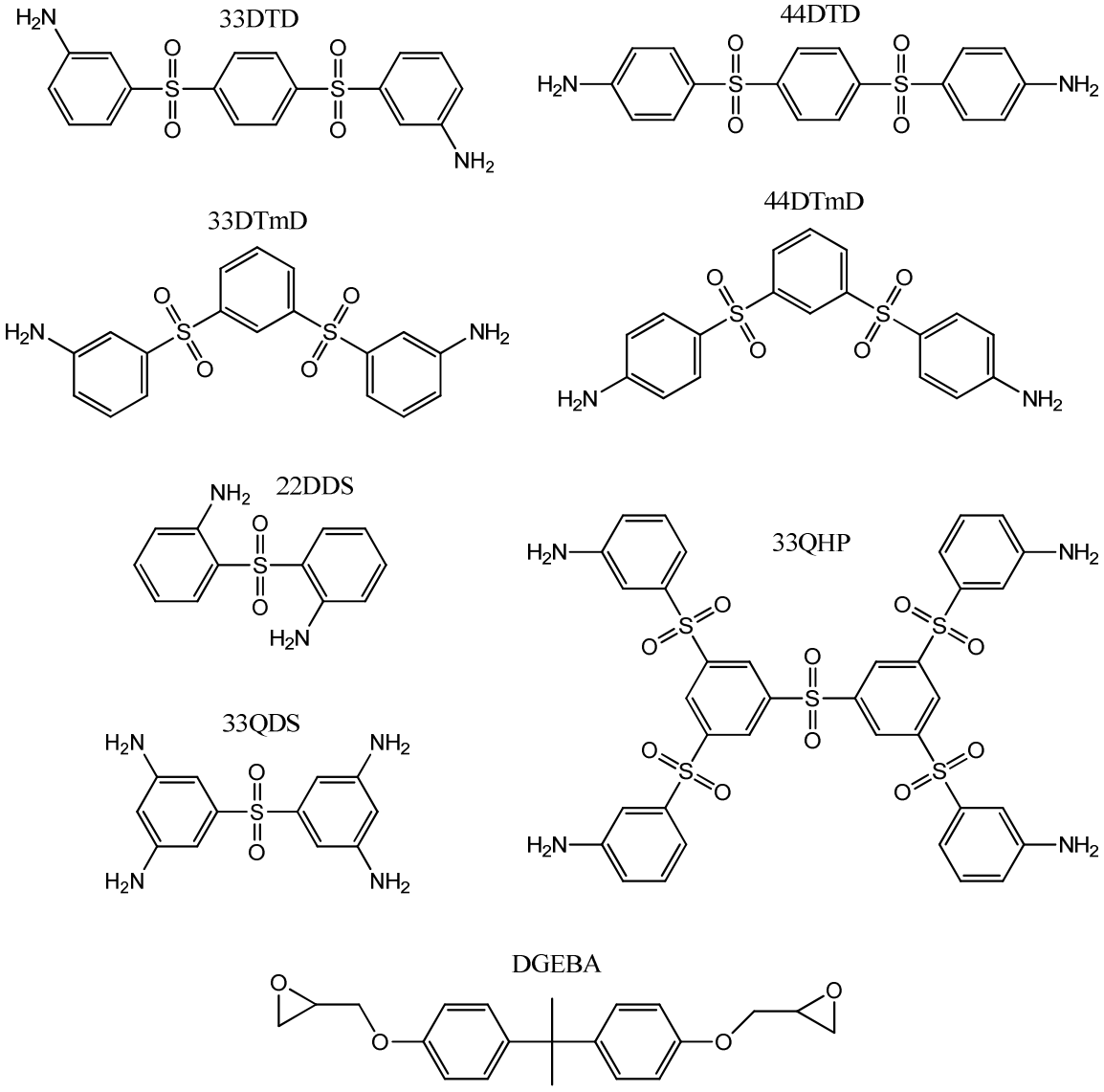

Figure 2.5. Amines simulated to determine effect of chemistry and structure of the network.

Table 2.4. MD Simulation Values for All Amines with DGEBA

System	E, GPa	G, GPa	ν	α, in/inF x10^{-6}	T_g, °C	ρ, g/cc	J_1	ε_y
33-DDS	4.71	1.77	0.330	31.7	197	1.200	0.030	0.17
44-DDS	5.07	1.92	0.324	32.9	202	1.201	0.032	0.14
33-DDS (3f)	4.54	1.71	0.333	31.4	185	1.207	0.028	0.14
44-DDS (3f)	4.76	1.80	0.325	33.1	213	1.202	0.035	0.15
22-DDS	4.85	1.85	0.315	34.4	171	1.195	0.028	0.14
33-DTD	4.17	1.54	0.351	31.5	183	1.220	0.027	0.13
44-DTD	4.03	1.52	0.323	35.1	188	1.222	0.031	0.12
33-DTmD	4.37	1.63	0.336	33.5	165	1.219	0.025	0.13
44-DTmD	4.28	1.59	0.342	33.2	184	1.229	0.030	0.14
33-QDS	4.65	1.74	0.332	33.4	161	1.179	0.025	0.11
33-QHP	4.88	1.84	0.327	33.1	179	1.229	0.028	0.065

Crosslink Density

To study the effect of crosslink density, 33DDS and 44DDS are compared to their tri-functional counterparts, 33DDS-3f and 44DDS-3f. As discussed previously, the tri-functional amines give results more commensurate with experimental findings (Table 2.2). 33DDS is also compared to 33QDS, the octa-functional equivalent of 33DDS. As expected, the higher crosslinked structure possesses a significantly decreased ε_y. Somewhat unexpectedly, it also shows decreased tensile and shear moduli, T_g, and J_1.

Sulfone and Aromatic Content

33DDS and 44DDS are compared to 33DTD and 44DTD, respectively, to show the impact of additional spacer components (sulfones and phenyl rings) between the amines. The addition of sulfones and phenyl rings between amine groups by necessity increases the molecular weight between crosslinks, which decreases the crosslink density. Unfortunately for the purposes of this study, the effect of the change in crosslink density cannot be separated from the effect of additional sulfone groups and phenyl rings. The 33DTD and 44DTD show decreases in E, G, T_g, and ε_y when compared to 33DDS and

44DDS, respectively. It is interesting to see that increasing sulfone content and aromaticity created a decline in all the properties.

33QHP and 33QDS can also be compared to study the effect of sulfone and aromatic content. In this case, the increased aromaticity and sulfone content create a polymer that has greater Young's modulus, shear modulus, and T_g and a lower compression yield strain. These trends indicate a polymer that is more rigid and possesses less distortional capability.

Para vs Meta vs Ortho Substitution

22DDS, 33DDS, and 44DDS can all be compared to show the effects of ortho vs meta vs para substitution of the amine. In this comparison, the 33DDS shows increased ε_y, indicating superior distortional capability. 33DTD and 44DTD can be compared to 33DTmD and 44DTmD, respectively, to determine the effect of meta substitution in the middle of the diamine. As expected, when the middle phenyl group is bonded in the meta as opposed to the para position, the ε_y rises, connecting the presence of meta substitution with distortional capability (Table 2.4). The internal meta substitution also decreases T_g and increases E and G moderately.

Conclusions

Although the fully crosslinked 33DDS and 44DDS show the opposite trend to experimental compression yield data, the tri-functional 33DDS and 44DDS show the correct trend. In fact, across all thermomechanical properties, the tri-functional 33DDS and 44DDS gave simulated values more commensurate with experimentally determined results than the fully crosslinked 33DDS and 44DDS. This result shows the error introduced into simulations by the assumption of 100% conversion. Furthermore, this

result implies experimental matrices (i.e., real polymers, not simulated polymers) possess a substantial amount of unreacted secondary amines. This is a significant piece of evidence in the debate over the percent crosslinking in thermoset matrices due to the difficulty in studying these systems spectroscopically.

Studying the effect of structural and chemical design on network properties shows some interesting trends. However, due to the inconsistencies seen in the comparison between 33DDS and 44DDS simulated vs. experimental data using this simulation procedure, it is difficult to draw too many conclusions when only simulated values are compared. Furthermore, none of the simulated materials shows values significantly greater than 33DDS and 44DDS in the majority of thermomechanical properties, which decreases their appeal for synthesis and experimental testing. In order to make firm conclusions about the effects of structural and chemical design on network properties, a more accurate simulation procedure must be proved.

References

1. *Accelrys Materials Studio 5.0 Help,* Group Based Cutoff.
2. Allen, M.P.; Tildesley, D.J. *Computer simulation of liquids.* New York, NY. Clarendon Pr. (1993).
3. *Accelrys Materials Studio 5.0 Help*. Static Elastic Property Determination.

CHAPTER III

A MOLECULAR DYNAMICS APPROACH TO PREDICTING PROPERTIES OF CROSSLINKED AROMATIC POLYMERS, PART II

Objective

The second chapter closely follows the objectives of the first chapter, and contains two primary objectives. The first objective is to employ a simulation procedure, which has been revised using the lessons learned in the Chapter I, to accomplish simulations more commensurate with experimental results for 33DDS/DGEBA and 44DDS/DGEBA. Once again simulation and experimental data are compared to determine for which physical properties the simulation procedure provides accurate values or trends and for which properties the simulation procedure needs to be further revised.

Secondly, simulations are accomplished to study the effect on thermomechanical properties of two interesting nano-modifiers bonded into a 33DDS/DGEBA matrix at varying weight percents. The first modifier is polyhedral oligomeric silsesquioxane (POSS) which is incorporated into the matrix by a single amine and possesses methyl groups on its other seven corners to help with solubilization. Figure 3.1 shows the Materials Studio structure of the POSS bonded to two DGEBA molecules. For simulations, the POSS/DGEBA structure is bonded into a 33DDS/DGEBA matrix to give different percent weights POSS. This procedure simulates ideal reaction of POSS into a 33DDS/DGEBA matrix as shown in Figure 3.2. The results of these simulations provide data about the effect on physical properties of bulky pendant groups bonded into the matrix.

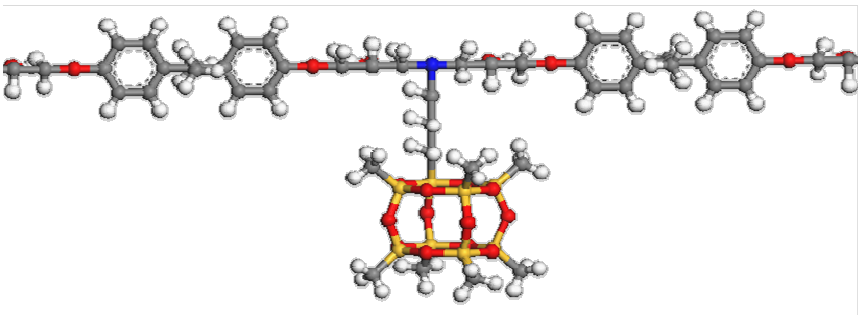

Figure 3.1. Structure for POSS/DGEBA.

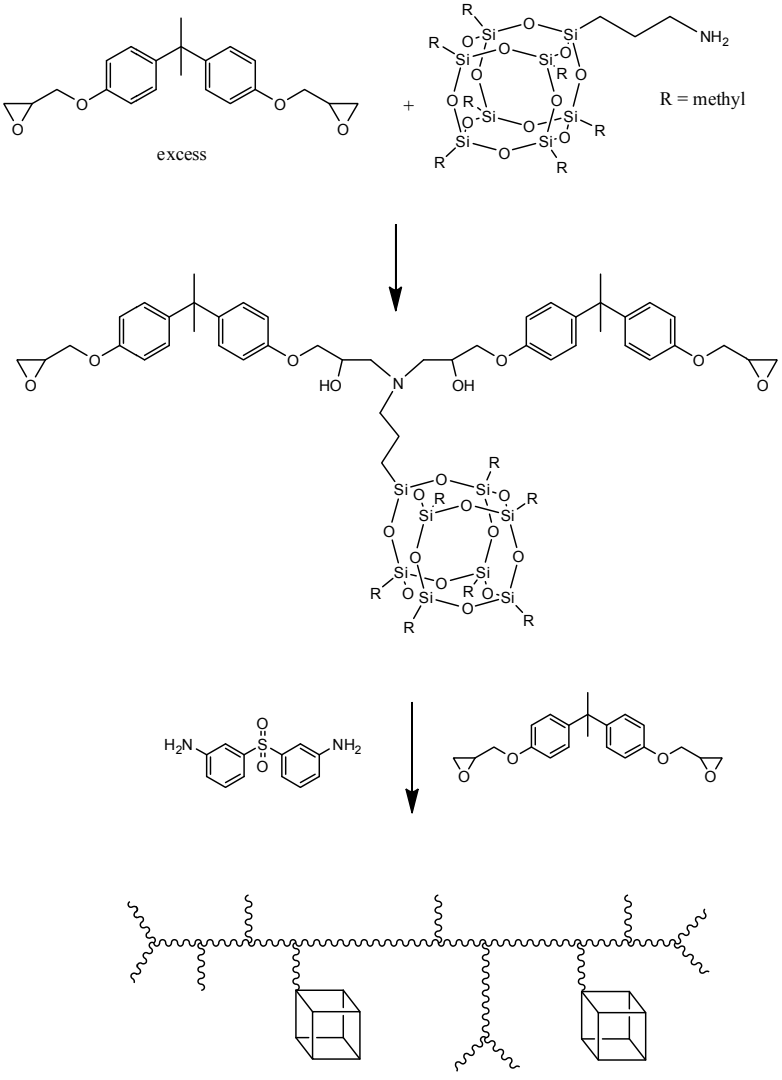

Figure 3.2. Simulated synthesis procedure for making dispersed POSS/33DDS/DGEBA.

The second modifier is a fluorinated pyrene, which has also been bonded into the matrix by an amine. Whereas the POSS molecule is a real molecule that can be synthesized and incorporated into epoxy matrices for evaluation, the F-pyrene is simulated to determine whether the POSS has special properties or will act in the same way as another bulky pendant group. The fluorines are added to make the pyrene less hydrophilic and therefore more capable of pervading free volume. This comparison will help determine whether the mechanism of nano-inclusions by pendant bulky groups is dependent upon the amount of free volume the bulky group creates. Figure 3.3 shows the Materials Studio structure for the F-pyrene/DGEBA, and Figure 3.4 shows the synthetic procedure this simulation models.

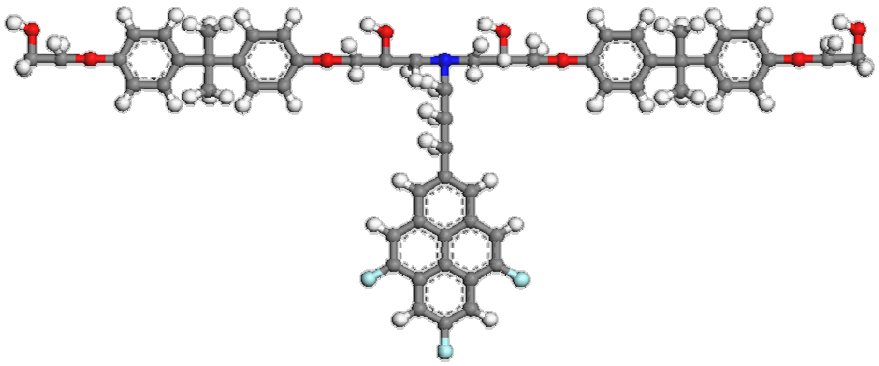

Figure 3.3. Structure for F-pyrene/DGEBA.

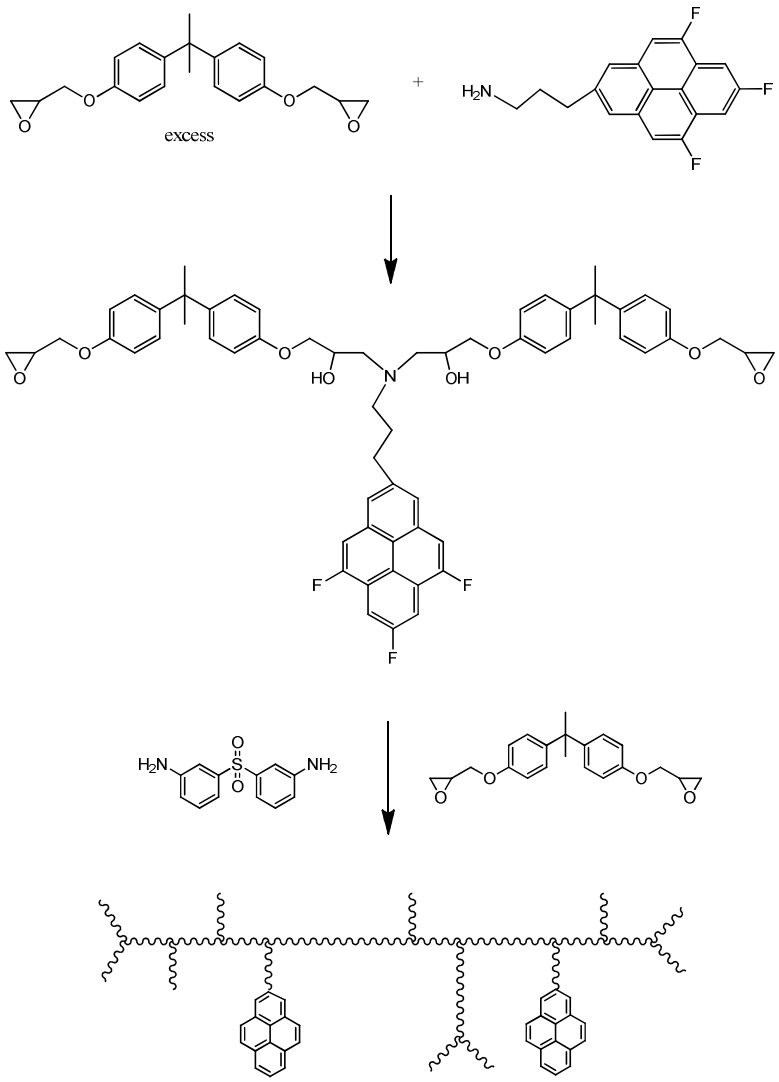

Figure 3.4. Simulated synthesis procedure for making dispersed F-pyrene/ 33DDS/DGEBA.

Methods

MD Simulation Procedure

To reduce some of the error in simulations and create more accurate models, the second round of simulations was accomplished with the same basic method described in the previous chapter, but with a few alterations. First, molecular dynamics calculations were completed in an updated version of Accelrys' software, Materials Studio 4.4. The

Condensed Phase Optimized Molecular Potentials for Atomistic Simulation Studies (COMPASS) forcefield and group-based cutoffs based on user assigned charge groups were still used. The quality used for most of the simulations is still "Medium," but this is increased to "Fine" for the elastic property determination. The "Fine" quality summation sets the cutoff distance at 12.50Å, the spline width at 3.00Å, the buffer width at 1.00Å, and the relative dielectric at 1.00.

Build seed and structures. The Seeds and Structures are built in exactly the same way as described in Chapter I.

Build polymer and amorphous cell. The dendrimer build and amorphous cell construction are accomplished with the same procedure used in Chapter I, with the one alteration that dendrimers are built to ~5,000 atoms as opposed to ~3,500 atoms.

Minimization and equilibration. Minimization, annealing, and equilibration processes are carried out in exactly the same manner as reported in Chapter I.

Calculation of molecular trajectories. The calculation of molecular trajectories is completed in the same manner as stated in Chapter I.

Analysis of molecular trajectories. Tensile modulus (E), shear modulus (G), and Poisson's ratio (ν) are all calculated using the same procedure as recorded in Chapter I, but using the "Fine" quality setting. Compression analysis was completed using the same stress controlled compression script obtained from Boeing.

To determine CTE (α), glass transition temperature (T_g), density (ρ), and the first invariant of the strain tensor (J_1), the temperature cycle in Amorphous Cell Protocols is still employed; however, the process is changed to maximize the number of dynamics steps, thus removing error. In order to accomplish this, the temperature cycle is broken

up into two steps: a heating simulation from 100K to 800K and a cooling simulation from 800K to 100K. Before starting the heating/cooling ramps, additional NPTs are run to equilibrate each cell at both 100K (for heating) and 800K (for cooling). These NPTs are completed at 0.0001GPa (1bar) using 25,000 time steps of 1fs, giving a total dynamics time of 25ps. The final structure generated in this NPT will be the structure for the heating and cooling simulations. In the temperature cycle, one simulation cools the 800K structure down to 100K, while another simulation heats the 100K structure up to 800K. For each process, the number of stages is increased to 71, which will give a simulated volume and density every 10K between 100K and 800K, the stage duration is increased to 100,000fs, and the averaging period is increased to 50,000fs. The number of data points in the V vs. T curve is increased from 28 as seen in Chapter I to 70 as seen in Figure 3.5. Glassy and rubbery CTEs, T_g, and J_1 were all calculated in the same manner as reported in Chapter I. Figure 3.5 shows that despite the more rigorous simulation procedure, the V vs. T curve still fails to show a distinct change in slope at T_g.

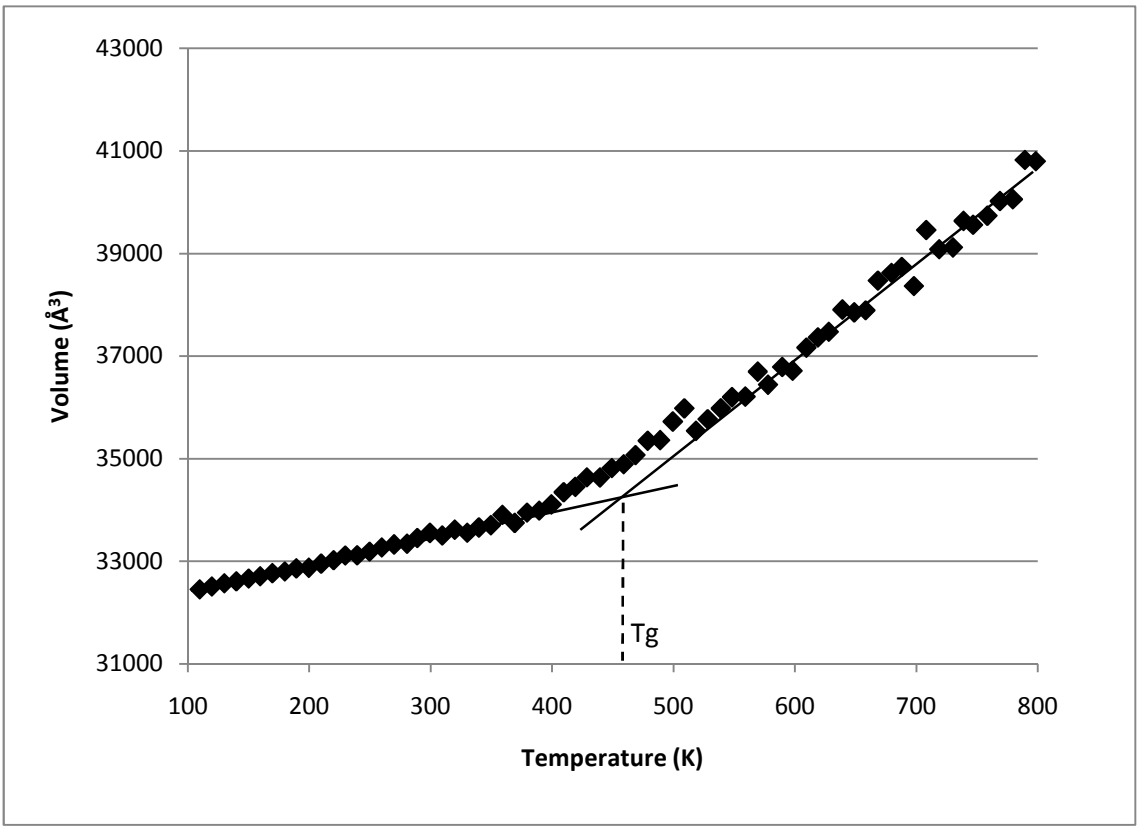

Figure 3.5. Example volume vs. temperature plot, more rigorous cycle.

Results and Discussion

As in Chapter I, to determine the accuracy of simulations, experimental data for 33DDS/DGEBA and 44DDS/DGEBA are compared to simulated values. Table 3.1 details the five thermomechanical properties experimentally obtained, tensile modulus (E), shear modulus (G), glass transition temperature (T_g), density (ρ), and compression yield strain (ε_y). Multiple trials for each experiment were completed, and the average values and standard deviations are reported above the raw data.

Table 3.1. Experimental Properties of 44DDS/DGEBA and 33DDS/DGEBA

System	E, GPa	G, GPa	T_g, °C DSC	T_g, °C DMA	ρ, gm/cc	ε_y
44DDS/DGEBA	**2.19**	**0.71**	**217**	**220**	**1.23**	**0.110**
Std. Dev.	*0.31*	*0.05*	*0.4*	*1*	*0.001*	*0.002*
Trial 1	1.85	0.74	217	220	1.24	0.112
Trial 2	2.26	0.70	218	220	1.23	0.109
Trial 3	2.45	0.65	217	221	1.23	
Trial 4		0.75	217		1.23	
Trial 5					1.23	
33DDS/DGEBA	**2.60**	**0.76**	**173**	**186**	**1.24**	**0.095**
Std. Dev.	*0.23*	*0.02*	*0.3*	*1*	*0.003*	*0.001*
Trial 1	2.45	0.73	174	186	1.23	0.094
Trial 2	2.48	0.78	174	187	1.23	0.096
Trial 3	2.86	0.76	174	186	1.24	
Trial 4		0.77	173		1.24	
Trial 5					1.24	

The comparison of experimental values to simulation values for 44DDS and 33DDS will be used to demonstrate the failures and successes of the revised simulation procedure in accurately predicting properties and showing trends. Tri-functional versions of the amines are simulated to observe the effect of crosslink density on properties. The structures for the four amines used and the epoxy, DGEBA, are given in Figure 3.6.

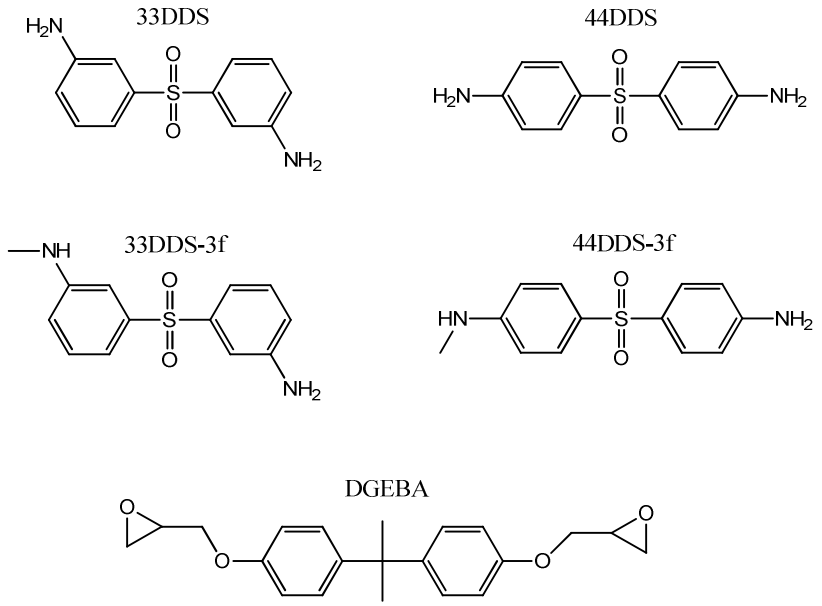

Figure 3.6. Structures of 3f and 4f 33DDS and 44DDS and DGEBA.

Table 3.2 gives the simulation data for these four epoxy systems using the revised simulation procedure. All thermomechanical properties were simulated five times for each system, and the average values and standard deviations are recorded above the five trials for each system. The compression strain at yield is not reported due to a communication problem between software and hardware with the compression analysis at the time these tests were accomplished. The results of the simulations from Chapter I for 33DDS/DGEBA and 44DDS/DGEBA are tabulated in Table 3.3 for comparison to the new simulation technique.

Table 3.2. Simulated Properties for 33DDS/DGEBA and 44DDS/DGEBA

System	E, GPa	G, GPa	ν	α, in/in/F x10^{-6}	T_g, °C	ρ, gm/cc	J_1
44DDS	**5.08**	**1.92**	**0.325**	**33.2**	**202**	**1.202**	**0.032**
Std Dev:	*1.11*	*0.45*	*0.029*	*1.3*	*27*	*0.005*	*0.006*
Trial 1	5.11	1.92	0.329	33.2	232	1.201	0.038
Trial 2	5.14	1.93	0.328	33.8	215	1.200	0.035
Trial 3	5.94	2.28	0.301	33.0	189	1.198	0.030
Trial 4	3.24	1.18	0.369	34.7	212	1.199	0.036
Trial 5	5.97	2.30	0.298	31.3	163	1.211	0.024
33DDS	**4.89**	**1.83**	**0.337**	**29.7**	**181**	**1.203**	**0.026**
Std Dev:	*0.71*	*0.29*	*0.019*	*2.6*	*44*	*0.001*	*0.009*
Trial 1	3.81	1.40	0.366	30.7	206	1.202	0.031
Trial 2	4.86	1.83	0.328	28.6	127	1.204	0.016
Trial 3	5.63	2.14	0.316	27.5	204	1.204	0.027
Trial 4	4.74	1.76	0.345	33.8	227	1.203	0.038
Trial 5	5.40	2.03	0.330	28.0	143	1.204	0.018
3f-44DDS	**5.00**	**1.89**	**0.324**	**30.3**	**202**	**1.207**	**0.030**
Std Dev:	*0.35*	*0.14*	*0.015*	*3.4*	*48*	*0.006*	*0.011*
Trial 1	5.62	2.14	0.314	35.1	260	1.202	0.045
Trial 2	4.82	1.80	0.337	31.9	241	1.203	0.038
Trial 3	4.94	1.89	0.303	26.4	144	1.217	0.017
Trial 4	4.84	1.82	0.332	28.1	169	1.207	0.022
Trial 5	4.79	1.80	0.335	30.1	197	1.207	0.028
3f-33DDS	**4.74**	**1.79**	**0.326**	**29.1**	**180**	**1.210**	**0.025**
Std Dev:	*0.35*	*0.13*	*0.021*	*2.7*	*27*	*0.005*	*0.006*
Trial 1	4.83	1.81	0.336	28.0	195	1.211	0.026
Trial 2	5.27	2.00	0.321	27.6	175	1.215	0.023
Trial 3	4.32	1.67	0.291	26.1	137	1.206	0.016
Trial 4	4.59	1.71	0.346	32.2	181	1.214	0.028
Trial 5	4.70	1.76	0.337	31.8	210	1.205	0.032

Table 3.3. Simulated Properties for 33DDS/DGEBA and 44DDS/DGEBA

System	E, GPa	G, GPa	ν	α, in/inF x10^{-6}	T_g, °C	ρ, g/cc	J_1	ε_y
44DDS	**5.07**	**1.92**	**0.322**	**32.4**	**202**	**1.196**	**0.031**	**0.14**
33DDS	**4.42**	**1.68**	**0.317**	**35.1**	**222**	**1.193**	**0.038**	**0.17**
3f-44DDS	**4.35**	**1.64**	**0.327**	**37.8**	**231**	**1.194**	**0.044**	**0.15**
3f-33DDS	**4.21**	**1.57**	**0.344**	**35.2**	**194**	**1.203**	**0.033**	**0.14**

Simulated densities for 33DDS/DGEBA and 44DDS/DGEBA were 1.203 and 1.202, respectively, a little below the experimentally determined values of 1.236 and 1.233, respectively. These densities indicate structures which are adequately minimized, but are likely not the lowest energy conformers. These densities are marginally closer to experimentally determined densities than those reported in Chapter I, indicating structures which are better minimized. The tri-functional amines showed a further increase in density, once again pointing toward the increased accuracy of simulations in matrices which are not fully crosslinked. The correct trend in density is observed: the 33DDS/DGEBA being slightly denser than 44DDS/DGEBA.

As in Chapter II, the simulated values for tensile and shear moduli do not show agreement with the experimental data. The experimental values are significantly lower than the simulated values, and the simulations fail to show the correct trend between the meta and para amine. Physical properties determined through experimentation clearly show the 33DDS possesses higher E and G than the 44DDS. The tri-functional amines show values closer to the experimentally determined values, but the trend is inaccurate once again.

The simulated T_g for 44DDS/DGEBA is 202°C, a little below the experimentally determined T_g range of 210 - 230°C. However, the simulated T_g for 33DDS/DGEBA is

180°C, right in the middle of the experimentally determined T_g range of 170 - 190°C. These T_gs are in much better agreement with experimental T_gs than those recorded in Chapter I. The tri-functional amines show no difference in T_g, giving values of 181°C and 202°C for 33DDS/DGEBA and 44DDS/DGEBA, respectively. This is a significant departure from simulations in Chapter I in which the tri-functional amines showed T_gs much closer to experimental values. One point for improvement is seen in the high variance within each averaged set. Although the averaged data give good approximations and show the correct trend (44DDS/DGEBA possessing a higher T_g than 33DDS/DGEBA), the variance is cause for some concern about the repeatability of the experiments and will be addressed in Chapter III.

Pendant Bulky Group Simulations

To study the effect of bulky pendant groups reacted into an epoxy matrix, methyl POSS and fluorinated pyrene were incorporated into epoxy matrices. Table 3.4 summarizes the results for incorporation of POSS into a 33DDS/DGEBA matrix at 2.5, 5.0, and 7.5 mole %, corresponding to 5, 13, and 21 wt. %, respectively. At the top of Table 8, the average results for the simulated properties of 33DDS/DGEBA are included; all values reported are from Chapter II simulations, except for ε_y, which is from Chapter I.

Table 3.4. Simulations for 33DDS/DGEBA Matrix with Pendant Methyl POSS

System	E, GPa	G, GPa	ν	α, in/in/F x10^{-6}	T_g, °C	ρ, g/cc	J_1	ε_y
33DDS	**4.89**	**1.83**	**0.337**	**29.7**	**181**	**1.203**	**0.026**	**0.17**
2.5% POSS / 33DDS	**5.55**	**2.14**	**0.302**	**29.6**	**188**	**1.200**	**0.027**	**0.13**
Std Dev:	**1.50**	**0.63**	**0.038**	**0.5**	**42**	**0.005**	**0.006**	**0.03**
Trial 1	4.49	1.69	0.329	29.9	158	1.203	0.022	0.11
Trial 2	6.61	2.59	0.275	29.2	218	1.196	0.031	0.16
5% POSS / 33DDS	**7.01**	**2.71**	**0.292**	**33.7**	**209**	**1.219**	**0.034**	**0.15**
Std Dev:	**0.10**	**0.05**	**0.007**	**2.3**	**25**	**0.003**	**0.003**	**0.02**
Trial 1	7.07	2.75	0.287	32.1	227	1.217	0.036	0.17
Trial 2	6.94	2.68	0.297	35.3	192	1.221	0.032	0.14
7.5% POSS / 33DDS	**10.20**	**4.05**	**0.249**	**30.5**	**217**	**1.224**	**0.032**	**0.17**
Std Dev:	**0.34**	**0.11**	**0.004**	**0.2**	**13**	**0.004**	**0.001**	**0.01**
Trial 1	10.44	4.13	0.246	30.3	226	1.221	0.033	0.16
Trial 2	9.96	3.98	0.252	30.6	207	1.226	0.031	0.18

The simulations for pendant POSS matrices show strong trends of increasing E, G, T_g, ρ, J_1, and ε_y and decreasing ν with increased POSS content. This indicates a matrix which possesses both higher stiffness and greater distortional capability, making it unusual and of significant interest for validation of Onset Theory. The increased T_g, tensile modulus, and shear modulus, with only slight increase in density make this material of interest for a number of applications which demand such performance criteria.

The simulations for pendant F-pyrene matrices do not show the same clear trends as the POSS matrices (Table 3.5). Density increases marginally with increased F-pyrene, but other physical properties do not follow clear trends of increased performance with increased F-pyrene content. E, G, and ε_y reach maximum values for 5% and then drop off at 7.5% F-pyrene. Poisson's ratio, T_g, and J_1 reach minima at 5% and then rebound at

7.5% F-pyrene incorporation. Compared to POSS incorporation, F-pyrene shows a significantly less drastic effect on physical properties.

Table 3.5. Simulations for 33DDS/DGEBA Matrix with Pendant Fluorinated Pyrene

System	E, GPa	G, GPa	N	α, in/in/F x10^{-6}	T_g, °C	ρ, g/cc	J_1	ε_y
33DDS	**4.89**	**1.83**	**0.337**	**29.7**	**181**	**1.203**	**0.026**	**0.17**
2.5% F-py / 33DDS	**4.50**	**1.67**	**0.344**	**30.1**	**208**	**1.197**	**0.030**	**0.14**
Std Dev:	**0.65**	**0.27**	**0.023**	**1.1**	**19**	**0.006**	**0.003**	**0.03**
Trial 1	3.75	1.37	0.371	31.2	211	1.191	0.032	0.11
Trial 2	4.91	1.83	0.334	30.2	188	1.203	0.027	0.16
Trial 3	4.83	1.82	0.328	29.0	226	1.198	0.032	0.16
5% F-py / 33DDS	**4.73**	**1.78**	**0.330**	**31.1**	**180**	**1.204**	**0.026**	**0.17**
Std Dev:	**0.27**	**0.11**	**0.006**	**2.7**	**32**	**0.009**	**0.006**	**0.02**
Trial 1	4.98	1.88	0.326	33.4	157	1.208	0.024	0.18
Trial 2	4.44	1.66	0.336	31.8	216	1.193	0.033	0.15
Trial 3	4.78	1.80	0.327	28.2	168	1.21	0.022	0.16
7.5% F-py / 33DDS	**4.64**	**1.74**	**0.337**	**32.0**	**207**	**1.210**	**0.032**	**0.15**
Std Dev:	**0.36**	**0.15**	**0.009**	**1.2**	**25**	**0.005**	**0.004**	**0.02**
Trial 1	4.37	1.62	0.347	32.5	228	1.204	0.036	0.16
Trial 2	5.05	1.90	0.329	30.6	212	1.214	0.032	0.13
Trial 3	4.51	1.69	0.335	32.8	179	1.212	0.028	0.18

Conclusions

The one major improvement from Chapter I is the increased accuracy for simulated T_g of 33DDS/DGEBA in both the tri-functional and tetra-functional amine simulations. The other noticeably deviation from Chapter I simulations is that the difference in values between the tri-functional and tetra-functional amines is negligible in Chapter II. The tri-functional amines marginally lowered tensile and shear moduli and increased density but showed no other significant changes. Although the simulated T_g for 33DDS/DGEBA is closer to experimental values in Chapter II, the simulated T_g for

44DDS/DGEBA is still low and the variances in T_g values are too high. Additionally, the modulus values still significantly overestimate experimental capability and show the reverse trend, with 44DDS possessing the higher E and G. Although Chapter II simulations are more accurate than Chapter I, the need for an improved simulation procedure is still apparent.

POSS incorporation into a 33DDS/DGEBA matrix as a pendant group showed considerable improvement in physical properties with increased POSS content, while F-pyrene only marginally affected properties. The trends observed with POSS incorporation indicate a matrix material which should be synthesized, and experimentally tested to determine whether the simulated gain in physical properties can be realized. Ongoing work in the Wiggins Research Group is focused on the solubilization and miscibilization of pendant POSS and other bulky groups into epoxy networks.

CHAPTER IV

A MOLECULAR DYNAMICS APPROACH TO PREDICTING PROPERTIES OF CROSSLINKED AROMATIC POLYMERS, PART III

Objective

The third chapter's sole purpose is to improve the simulation procedure such that simulations more accurately match experimentation. Once again 33DDS/DGEBA and 44DDS/DGEBA will be simulated and compared to experimental analysis. Additionally, matrices of hexamethylene diamine (HDA) and bis(hexamethylene)triamine (B-HTA) are simulated with DGEBA (Figure 4.1). The simulation of linear aliphatic amines provides a network with less aromaticity. High phenyl ring content complicates simulations by making the chains more rigid and therefore more difficult to relax energetically. Ring catenation also becomes a problem with such highly aromatic matrices. Additionally, 33DDS and 44DDS possess sulfone groups, which create complexities in the simulation in terms of defining secondary forces, such as hydrogen bonding, and make matrices even more rigid. Our hypothesis was that the HDA/DGEBA and B-HTA/DGEBA matrices would provide more accurate simulations due to their relative simplicity in comparison to 33DDS/DGEBA and 44DDS/DGEBA.

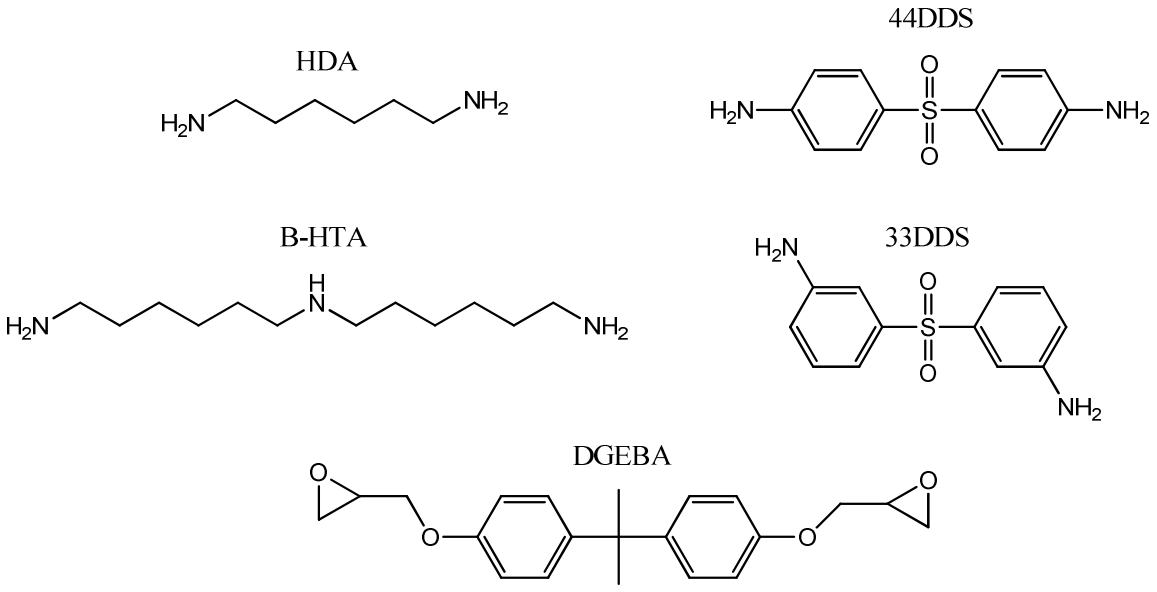

Figure 4.1. Chemical Structures of Amines and DGEBA.

To address the problems remaining in the simulation procedure from Chapter II, in the third round of simulations, specific attention was lent to creating more realistic polymers, performing more realistic simulations, and using more trials to average out error and obtain more accurate results. With these goals in mind, the temperature cycle was once again refined to include more dynamics steps in the temperature range of the glass transition.

Additionally, we had concerns about the dendrimer build we used to create the polymers. In previous simulations, perfect dendrimers were built assuming complete crosslinking until the last addition of epoxy or amine, which would balance stoichiometry. This perfect dendritic growth is likely not the best procedure to simulate molecular weight growth in epoxies. For the work in this section, we use a build script in which amine and epoxy monomer structures are reacted to create a randomized

crosslinked network.[1] The protocol for compression analysis was also altered to a strain-controlled as opposed to stress-controlled compression.[2] Finally, a few other small modifications to the procedure were made to ensure we were minimizing the energy in the system as much as possible.

Methods

MD Simulation Procedure

Molecular dynamics calculations were completed in an updated version of Accelrys' software, Materials Studio 5.0. The Condensed Phase Optimized Molecular Potentials for Atomistic Simulation Studies (COMPASS) forcefield and group based cutoffs based on user assigned charge groups were still used. The quality used for most of the simulations is still "Medium," but this is increased to "Fine" for the elastic property determination.

Build seed and structures. The Seeds and Structures are built in exactly the same way as in Chapter I.

Build polymer and amorphous cell. The polymer build script used in this section directs molecular weight growth through a computer-controlled randomized dendrimer build. Stoichiometry is set to 2:1 epoxies-to-amines, corresponding to 1:1 epoxides-to-reactive amine hydrogens, and the number of atoms is set to 5,000. Based on the stoichiometry and number of atoms, the script determines the number of generations and creates connect points each generation using a random number generator. This simulation polymerization procedure shares commonality with collision theory for chemical reactions. By matching the simulation procedure to our understanding of real

crosslinking polymerizations, we will see an improved accuracy in thermomechanical property prediction.

For each polymer system, ten polymers were built using the build script. Each of these ten polymers was incorporated into an amorphous cell for a total of ten amorphous cells on which the thermomechanical properties will be determined. In previous simulations in Chapters I and II, only one polymer build was accomplished and three amorphous cells were made from this one build. The amorphous cells were constructed in the same manner as in Chapter I, with the exception that the density was increased to $0.5 g/cm^3$.

Minimization and equilibration. The minimization of the ten amorphous cells was made more rigorous by increasing the number of iterations to 200,000 or until convergence was reached. All amorphous cells converged before 200,000 iterations were reached. The annealing process was kept the same as described in Chapter I.

Calculation of molecular trajectories. The calculation of molecular trajectories is completed in the same manner as stated in the Chapter I.

Analysis of molecular trajectories. Tensile modulus (E), shear modulus (G), and Poisson's ratio (v) are all calculated using the same procedure as recorded in Chapter I, but using the "Fine" quality setting.

Compression analysis was completed using a strain-controlled compression script obtained from Boeing. Each of the ten cells is compressed uniaxially the x, y, and z directions in separate simulations. The cells are compressed from 0 to 20% strain, in increments of 0.5% strain. The stress induced in the cells by this straining process is recorded at each of the forty increments. A stress vs. strain curve is approximated by

fitting the data to a second order polynomial. The compression yield point is approximated from the maximum of the second order polynomial curve. Von Mises strain is then approximated by multiplying the compression yield strain by 1.5. Compression modulus is calculated by taking the slope of a linear best fit curve from 0 to 2% strain.

CTE (α), glass transition temperature (T_g), density (ρ), and the first invariant of the strain tensor (J_1) are determined using the temperature cycle in Amorphous Cell Protocols. As in Chapter II, the temperature cycle is broken up into two steps: a heating simulation and a cooling simulation. In order to obtain more accurate T_gs, the temperature cycle was employed in a 200K range, from 100K below the expected T_g (as determined by DSC, DMA) to 100K above T_g. Before starting the heating/cooling ramps, additional NPTs are run to equilibrate each cell at both 100K below expected T_g (for heating) and 100K above expected T_g (for cooling). These NPTs are completed at 0.0001GPa (1bar) using 25,000 time steps of 1fs, giving a total dynamics time of 25ps. The final structure generated in this NPT will be the structure for the heating and cooling simulations.

For both the heating and cooling ramps, the number of stages is 20, which will give a simulated volume and density every 10K, the stage duration is increased to 120,000fs, and the averaging period is increased to 60,000fs. The number of data points in the V vs. T curve is decreased to 19 as seen in Figure 4.2. Glassy and rubbery CTEs, T_g, and J_1 were all calculated in the same manner as reported in Chapter I. Figure 4.2 shows that focusing the simulation in a small temperature window above and below T_g, and increasing the number of time steps in this window yields a V vs. T curve that shows

a much more distinct T_g. If this protocol still gives results with lower accuracy than desired, the stage duration and averaging period can be increased to produce a more accurate V vs. T curve.

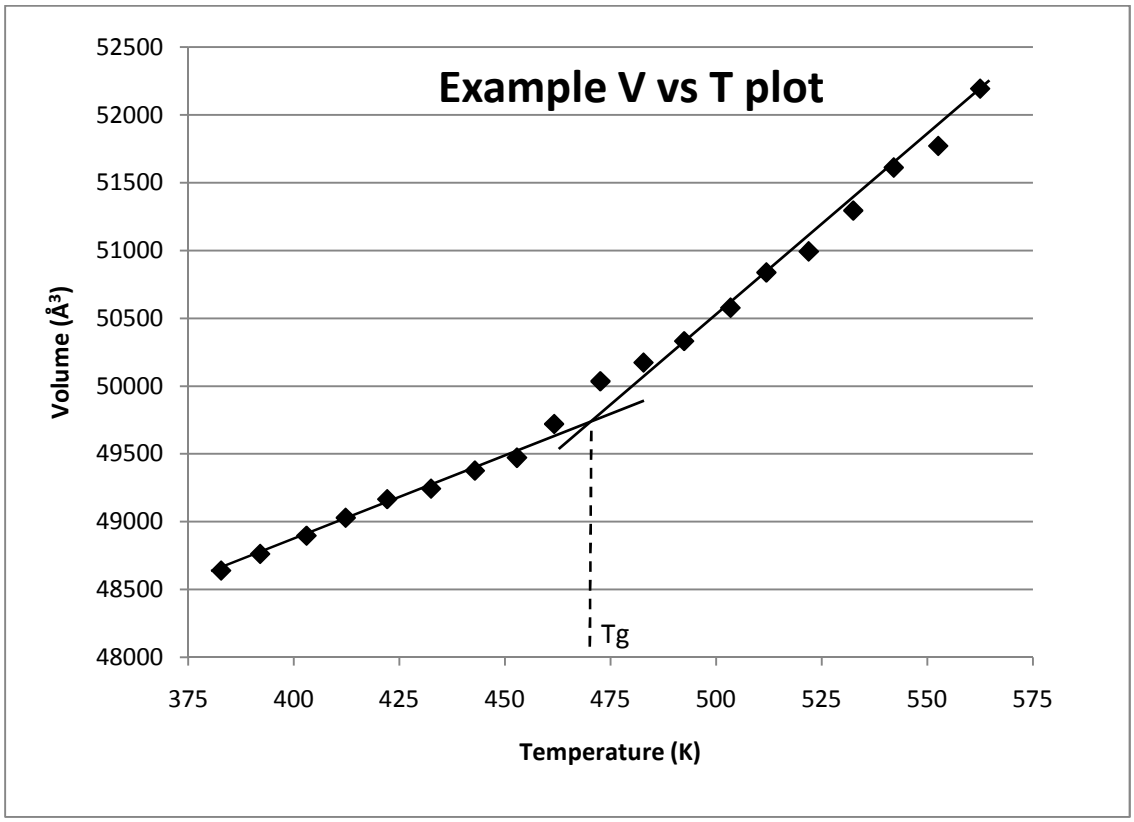

Figure 4.2. Example volume vs. temperature plot, more rigorous cycle.

Results and Discussion

33DDS/DGEBA and 44DDS/DGEBA Experimental vs. Simulation Comparison

Experimentally determined physical properties for 33DDS/DGEBA and 44DDS/DGEBA to be compared to simulation values are summarized in Table 4.1.

Table 4.1. Experimental Properties for 33DDS/DGEBA and 44DDS/DGEBA

System	E, GPa	G, GPa	T_g, °C DSC	T_g, °C DMA	ρ, g/cc	ε_y	σ_y	M, Gpa
44DDS	**2.19**	**0.71**	**217**	**220**	**1.23**	**0.110**	**0.140**	**2.64**
Std. Dev.	*0.31*	*0.05*	*0.4*	*1*	*0.001*	*0.002*	*0.0001*	*0.05*
Trial 1	1.85	0.7412	217	220	1.24	0.112	0.140	2.60
Trial 2	2.26	0.69797	218	220	1.23	0.109	0.140	2.68
Trial 3	2.45	0.65104	217	221	1.23			
Trial 4		0.75179	217		1.23			
Trial 5					1.23			
33DDS	**2.60**	**0.76**	**173**	**186**	**1.24**	**0.095**	**0.143**	**2.85**
Std. Dev.	*0.23*	*0.02*	*0.3*	*1*	*0.003*	*0.001*	*0.0002*	*0.03*
Trial 1	2.45	0.73242	174	186	1.23	0.094	0.143	2.87
Trial 2	2.48	0.77713	174	187	1.23	0.096	0.143	2.83
Trial 3	2.86	0.75513	174	186	1.24			
Trial 4		0.77341	173		1.24			
Trial 5					1.24			

Table 4.2 shows simulated thermomechanical properties for 33DDS/DGEBA and 44DDS/DGEBA matrices. Despite improved simulation procedure, simulated tensile and shear moduli values are still far greater than experimentally determined values, and the trend still incorrectly shows 33DDS/DGEBA to possess lower E and G than 44DDS/DGEBA. Density values are still a little low, but the trend is correct, as in previous simulations. Simulated compression strain at yield is greater for simulated matrices than experiments show, and the trend is backwards.

Table 4.2. Simulated Properties for 33DDS/DGEBA and 44DDS/DGEBA

System	E, GPa	G, GPa	T_g, °C	ρ, g/cc	ε_y	σ_y, GPa	M, GPa
44DDS	**4.85**	**1.83**	**221**	**1.204**	**0.19**	**0.322**	**2.79**
Std Dev:	*0.42*	*0.15*	*15*	*0.007*	*0.04*	*0.032*	*0.46*
Trial 1	4.88	1.85	229	1.200	0.17	0.306	3.32
Trial 2	5.16	1.94	229	1.208	0.17	0.337	2.02
Trial 3	3.89	1.49	217	1.187	0.17	0.294	3.39
Trial 4	4.73	1.78	227	1.203	0.16	0.310	2.87
Trial 5	5.18	1.95	229	1.205	0.21	0.344	2.71
Trial 6	4.58	1.71	212	1.199	0.16	0.276	3.16
Trial 7	5.16	1.95	234	1.206	0.19	0.311	2.66
Trial 8	4.60	1.73	181	1.210	0.18	0.345	2.87
Trial 9	5.17	1.96	224	1.207	0.27	0.310	2.79
Trial 10	5.16	1.95	224	1.212	0.22	0.387	2.10
33DDS	**4.53**	**1.69**	**197**	**1.208**	**0.17**	**0.331**	**3.44**
Std Dev:	*0.36*	*0.14*	*18*	*0.004*	*0.02*	*0.019*	*0.34*
Trial 1	4.36	1.62	206	1.204	0.18	0.309	3.61
Trial 2	4.89	1.85	174	1.215	0.19	0.363	3.28
Trial 3	4.60	1.72	195	1.205	0.15	0.326	3.94
Trial 4	4.76	1.77	234	1.205	0.17	0.315	2.84
Trial 5	4.75	1.77	178	1.210	0.16	0.315	3.22
Trial 6	4.32	1.61	181	1.210	0.14	0.335	3.73
Trial 7	4.32	1.61	196	1.210	0.19	0.357	3.75
Trial 8	3.71	1.37	216	1.211	0.17	0.332	3.57
Trial 9	4.90	1.85	201	1.207	0.20	0.349	3.39
Trial 10	4.65	1.74	186	1.207	0.18	0.313	3.09

However, despite the many inadequacies the simulations still possess, simulated T_gs are close to the experimentally determined range, standard deviations have been reduced, and V vs. T plots show clear T_gs, a feat which had not been accomplished in previous simulations (Figure 4.3).

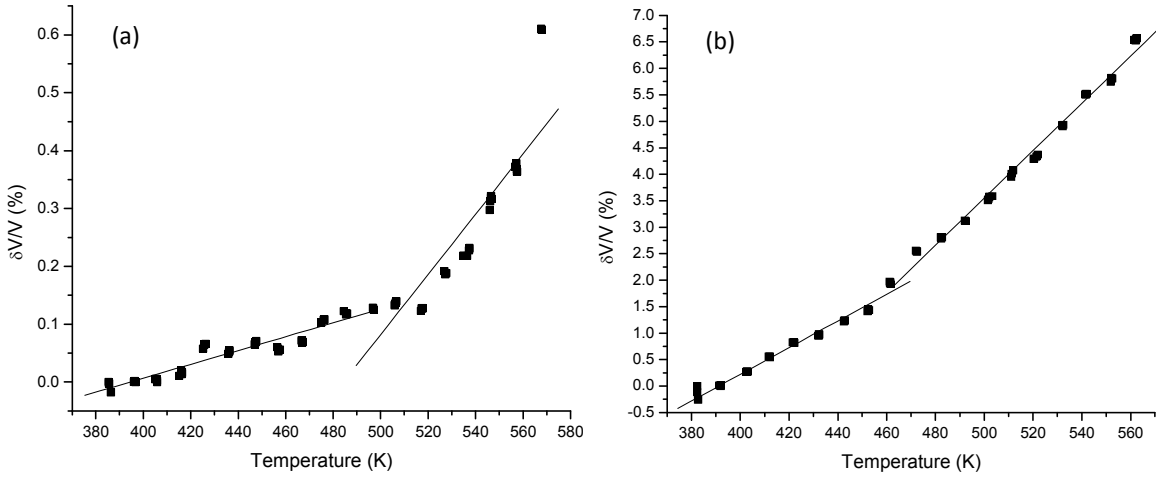

Figure 4.3. Simulated V vs. T plots for 44DDS/DGEBA (a) and 33DDS/DGEBA (b).

Simulated compression analysis was also improved. Although yield strains were still higher than experimental determinations and still showed the incorrect trend of 33DDS/DGEBA possessing lower strain at yield, simulated compression modulus values were fairly accurate and showed the correct trend (Figure 4.4).

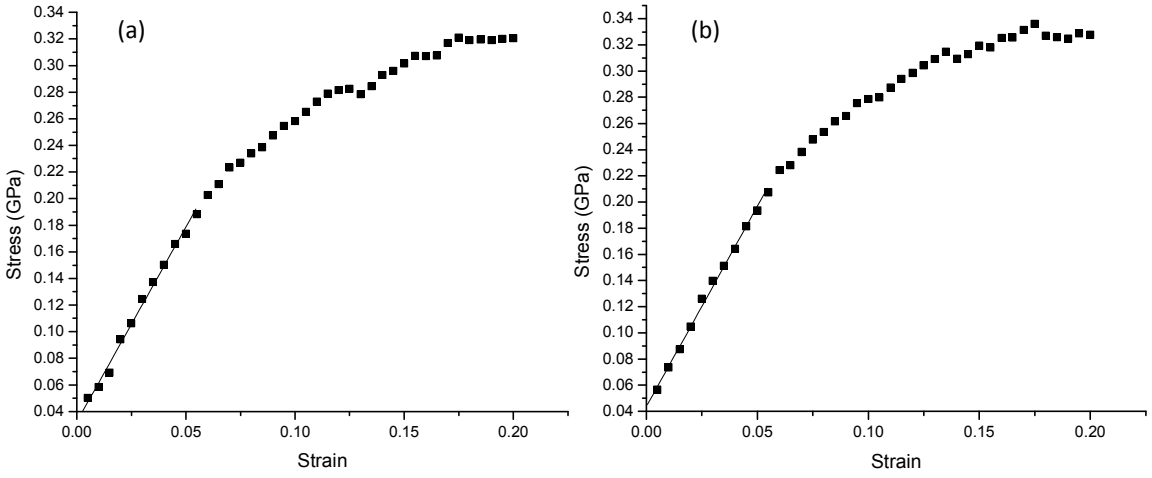

Figure 4.4. Simulated compression for 44DDS/DGEBA (a) and 33DDS/DGEBA (b).

HDA/DGEBA and B-HTA/DGEBA Experimental vs. Simulation Comparison

Tensile Modulus, T_g, and density of HDA/DGEBA and B-HTA/DGEBA matrices were determined experimentally and are summarized in Table 4.3. HDA/DGEBA possessed a higher T_g and density than B-HTA/DGEBA. T_g ranges, as determined by DSC and DMA were equivalent for the two samples. Shear modulus and compression analysis values need to be experimentally determined.

Table 4.3. Experimental Properties for HDA/DGEBA and B-HTA/DGEBA

System	E, GPa	T_g, °C DSC	T_g, °C DMA	ρ, gm/cc
HDA	**2.86**	**100**	**124**	**1.16**
Std. Dev.	*0.69*	*1*	*2*	*0.001*
Trial 1	3.62	100	126	1.16
Trial 2	2.68	101	124	1.16
Trial 3	2.27	100	121	1.16
Trial 4				1.16
Trial 5				1.16
B-HTA	**1.73**	**106**	**118**	**1.16**
Std. Dev.	*0.63*	*3*	*2*	*0.0004*
Trial 1	1.14	106	116	1.16
Trial 2	1.66	109	118	1.15
Trial 3	2.39	102	120	1.16
Trial 4				1.16
Trial 5				1.16

Table 4.4 summarizes properties determined via MD simulations for HDA/DGEBA and B-HTA/DGEBA matrices. Simulated properties of HDA/DGEBA and B-HTA/DGEBA showed values with similar trends as seen in previous simulations, such overestimating E by a large margin and density by a smaller margin. However,

significant improvement on T_g simulation was observed. T_gs for both matrices are within the experimental range, and standard deviations have been significantly reduced.

Table 4.4. Simulated Properties for HDA/DGEBA and B-HTA/DGEBA

System	E, GPa	G, GPa	T_g, °C	ρ, gm/cc	ε_y	σ_y, GPa	M, GPa
HDA	**4.67**	**1.75**	**103**	**1.139**	**0.17**	**0.313**	**3.36**
Std Dev:	*0.39*	*0.16*	*19*	*0.006*	*0.01*	*0.031*	*0.46*
Trial 1	4.50	1.70	100	1.142	0.16	0.297	3.57
Trial 2	5.43	2.08	105	1.145	0.15	0.372	3.09
Trial 3	5.06	1.92	96	1.135	0.18	0.313	4.03
Trial 4	4.46	1.68	78	1.139	0.18	0.318	2.87
Trial 5	4.76	1.79	122	1.149	0.17	0.348	3.10
Trial 6	4.41	1.64	136	1.138	0.17	0.304	3.20
Trial 7	4.14	1.54	120	1.136	0.16	0.291	2.74
Trial 8	5.01	1.88	82	1.147	0.17	0.329	3.95
Trial 9	4.43	1.65	107	1.133	0.18	0.295	3.87
Trial 10	4.48	1.68	82	1.130	0.16	0.262	3.21
B-HTA	**4.29**	**1.61**	**117**	**1.113**	**0.19**	**0.308**	**3.40**
Std Dev:	*0.53*	*0.22*	*8*	*0.006*	*0.03*	*0.055*	*0.77*
Trial 1	4.79	1.81	101	1.124	0.22	0.399	4.54
Trial 2	4.09	1.52	110	1.115	0.15	0.300	3.22
Trial 3	4.33	1.65	120	1.107	0.16	0.179	2.60
Trial 4	4.34	1.65	113	1.103	0.23	0.283	1.87
Trial 5	4.14	1.55	120	1.109	0.20	0.298	3.69
Trial 6	4.99	1.89	117	1.119	0.18	0.337	4.15
Trial 7	4.43	1.66	124	1.113	0.17	0.328	3.09
Trial 8	3.95	1.47	123	1.117	0.18	0.333	3.90
Trial 9	4.75	1.81	131	1.115	0.20	0.310	3.47
Trial 10	3.10	1.13	114	1.112	0.16	0.311	3.44

Additionally, V vs. T plots show distinct at T_gs, a feat which had not been accomplished by previous simulations (Figure 4.5). Oddly, although the B-HTA/DGEBA possesses a lower standard deviation, the V vs. T plot created from the average of the 10 runs does not show a T_g as clearly as the HDA/DGEBA.

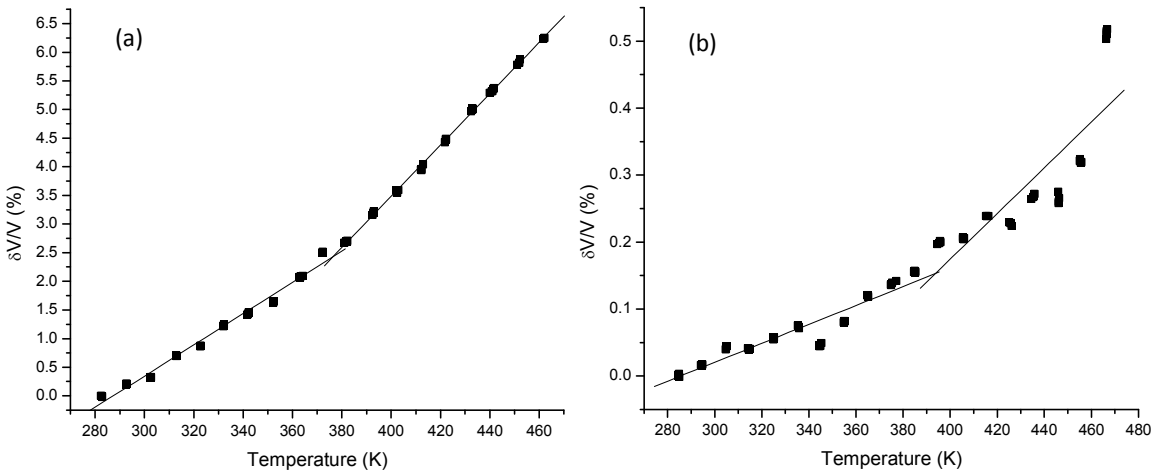

Figure 4.5. Simulated V vs. T plots for HDA/DGEBA (a) and B-HTA/DGEBA (b).

Although experimental compression analysis has not yet been completed for these samples, simulated compression tests show curves that look like compression curves should (Figure 4.6). This had not been accomplished in previous simulation analysis.

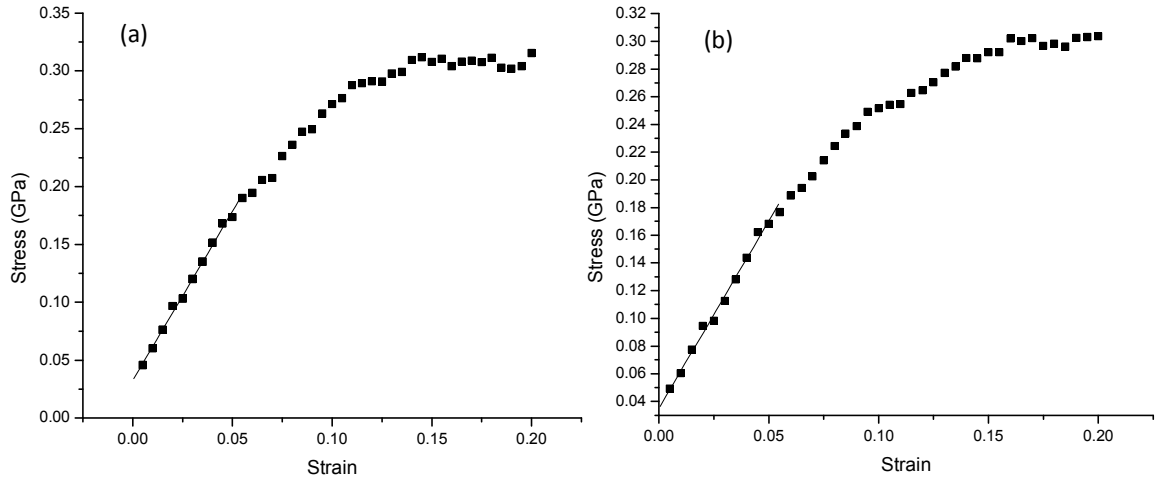

Figure 4.6. Simulated compression for HDA/DGEBA (a) and B-HTA/DGEBA (b).

Conclusions

Thermomechanical property simulations of amorphous networks using molecular dynamics are still in need of improvement. Tensile and shear moduli and compression strain at yield are consistently higher in simulations than experimental determinations. Progress has been made in the simulation of T_g and compression modulus by altering the simulation procedure including using the random dendrimer builder, strain controlled compression analysis, and increasing simulation rigor near T_g in the V vs. T determination. However, research still needs to be accomplished to determine the causes of error and possible solutions to help MD simulations reach their potential of accurately predicting physical properties of crosslinked polymers.

References

1. Stephen Todd,, “Accelrys Build and optimize dendrimer,” 2009, <https://community.accelrys.com/thread/1876>.

2. Andrea Browning, *Strain Controlled True Strain* (Boeing, 2010).

CHAPTER V

INVESTIGATION OF PHENYL RING MOTIONS IN 33DDS/DGEBA AND 44DDS/DGEBA MATRICES BY DEUTERIUM NMR SPECTROSCOPY

Introduction

Nuclear magnetic resonance (NMR) spectroscopy is a sensitive instrumental tool for studying relaxation phenomena in materials. There are numerous relaxation processes within molecules that create fluctuating dipoles, including dipole-dipole, chemical shift anisotropy (CSA), spin rotation, scalar, and quadrupolar relaxations. For polymers, the principle sources of relaxation are dipolar, CSA, and quadrupolar interactions.[1] Quadrupolar relaxations result directly from the quadrupolar moment of the nucleus itself, i.e., the nucleus' unsymmetrical charge. An important advantage of ^{2}H NMR analysis, which requires ^{2}H labeled samples, is that CSA and dipolar mechanisms do not significantly contribute to spin-lattice relaxation or lineshape. Therefore, the spectroscopic behavior of ^{2}H atoms is almost exclusively governed by quadrupolar mechanisms. Relaxation is due to fluctuating fields created by molecular motion, thereby making deuterium NMR spectroscopy a highly sensitive probe of molecular motion. Solid-state deuterium NMR spectroscopy has been used extensively to monitor polymer mobility. The lineshape and spin-lattice relaxation (T_1) times are sensitive to the mode and rate of motion, and these methods have been used to study phenyl ring and methylene motion in polymers.[1,2]

For ^{2}H labeled phenyl rings, a distribution of motions with variability in phenyl ring flip angle and flip rate is observed. Previous work normally employs a stretched exponential, such as the Kohlrausch Williams Watts (KWW) expression, to characterize

this distribution of rates.[3] In addition, a simple Gaussian distribution describing the deviation of the flips from 180° is often used with a very fast librational motion pre-averaged into the simulated lineshape by adjusting the quadrupolar coupling constant, C_Q.[4] This description of ring motions is useful but introduces a higher degree of complexity in the analysis. Here, a simplistic approach was utilized to interpret T_1 and lineshape data.

Objective

The principle objective of this work is to describe the motional behavior of the amine and epoxy aromatic rings in 33DDS/DGEBA and 44DDS/DGEBA. To accomplish this goal, the amine and epoxy phenyl rings have been selectively deuterated, and the motions studied using ^2H spin-lattice relaxation (T_1) studies and lineshape analysis. Spin-lattice relaxation analysis is used to discriminate between ring motions possessing different rates, while lineshape analysis is used to provide information about both the types and rates of phenyl ring motions occurring. Once the basic rates of ring motions have been described using T_1 studies, the contributions of each motion to lineshape can be determined by comparison of the spin-lattice relaxation data to lineshape data. By combining spin-lattice relaxation data with lineshape data, a clear picture of the types and rates of phenyl ring motion can be determined.

In this work deuterium NMR spectroscopy is used to describe the rates and types of motions of selectively labeled aromatic rings. Future work will combine ^2H NMR spectroscopy with simulation results to determine activation energies and their corresponding motional correlation times. Dielectric spectroscopy (DES) and dynamic mechanical analysis (DMA) typically use a constant frequency with the temperature

varied to detect relaxation processes resonant with the predetermined frequency. By combining ^{2}H NMR spectroscopic information with DES and DMA data, the specific moieties within the polymer responsible for sub-T_g relaxations observed in DES and DMA can be determined.[3,4] The relationship of sub-T_g motions to bulk mechanical properties, such as modulus and toughness is well documented.[5,6,7] The ability to connect ^{2}H NMR spectroscopic data to DES and DMA results provides significant potential for understanding the chemistries and structures within polymers that are responsible for mechanical properties.

Materials

Epichlorohydrin (≥99% purity), anhydrous toluene (99.8% purity), anhydrous sodium hydroxide pellets (NaOH, ≥98% purity), toluene (≥99% purity), acetic anhydride (≥98% purity), carbon disulfide (≥99% purity), sulfonyl chloride (≥98% purity), aluminum trichloride (≥98% purity), glacial acetic acid, ammonium chloride (≥99% purity), tetrahydrofuran (THF, ≥99% purity), hydrogen peroxide (≥98% purity), hydrochloric acid (HCl, ≥98% purity), decolorizing carbon, methanol (≥99% purity), potassium nitrate (KNO_3, ≥98% purity), sulfuric acid (H_2SO_4, ≥98% purity), chlorosulfonic acid (≥99% purity), chloroform (≥99% purity), methylene chloride (≥98% purity), dimethyl formamide (DMF, ≥99% purity), palladium-carbon catalyst, 3,3'-diaminodiphenyl sulfone (33DDS, 97% purity), and 4,4'-diaminodiphenyl sulfone (44DDS, 97% purity) were purchased from Sigma Aldrich and used as received. The NaOH pellets were dissolved into deionized water to make a 40%wt. aqueous NaOH solution. Ring deuterated bisphenol A (d8-BPA, 98% purity), ring deuterated aniline (d5-aniline, 98% purity), and deuterated benzene (d6-benzene, 99.5% purity) were

obtained from Cambridge Isotope Laboratories, Inc. and used as received. Hydrogen gas was purchased from Nordan Smith and used as received.

Methods

Ring Deuterated d8-DGEBA Synthesis

Ring deuterated diglycidyl ether of bisphenol A (d8-DGEBA) was synthesized by the reaction of d8-BPA and epichlorohydrin. The synthesis was accomplished in a two-neck flask fitted with reflux condenser; 3.5g (0.015 mol) of D8-BPA and 13.9g (0.15 mol) epichlorohydrin were added and heated to 120^{o}C under magnetic stirring. 3g of 40%wt. aqueous sodium hydroxide (0.03 mol) was added to the boiling reaction mixture and allowed to reflux for 4 hours. The excess epichlorohydrin was then distilled off the reaction product. Toluene was added with stirring to precipitate off the NaCl salt. The precipitate salt was filtered off the filtrate, and additional toluene was used to wash any remaining product off the solid salt. Toluene was then distilled off the filtrate to leave the reaction product d8-DGEBA. The d8-DGEBA was then dried under vacuum at 50^{o}C. The d8-DGEBA showed no indication of impurities using ^{13}C and ^{1}H NMR, indicating the purity is >95% (product1, Scheme 1).

Scheme 5.1. Synthesis of d8-DGEBA

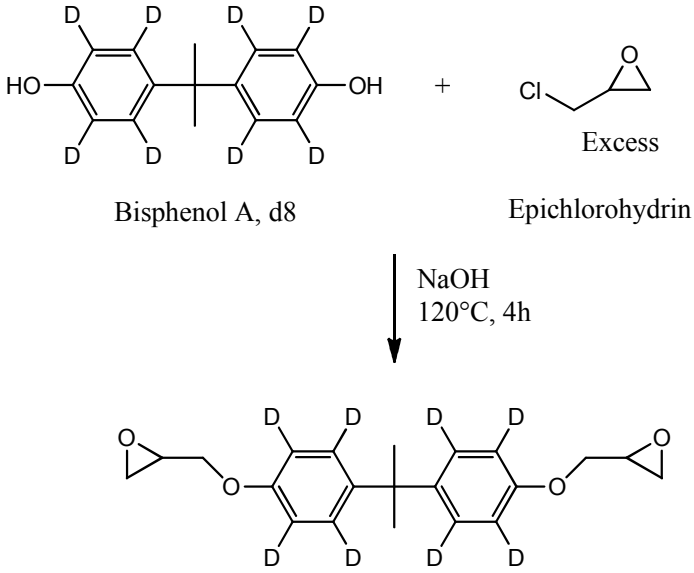

(1) Diglycidyl ether of bisphenol A, d8

Ring Deuterated d8-44DDS Synthesis

Ring deuterated aniline (2g) was added to 20ml acetic anhydride and heated at reflux for 30min. After cooling to room temperature, 25ml water was added and heated at reflux for 10min. The solution was then cooled to room temperature and diluted with water to precipitate the product, N-acetylaniline. The ring deuterated N-acetylaniline was filtered, washed with water, recrystallized from water, and dried (product 1, Scheme 2). The ring deuterated N-acetylaniline was suspended in 80ml carbon disulfide (CS_2), after which 15g aluminum trichloride ($AlCl_3$) and 3ml sulfonyl chloride ($SOCl_2$) were added. After the initial reaction subsided, the mixture was heated at reflux for 6hr, cooled to room temperature, and quenched by the addition of a 10% ammonium chloride solution in water. The mixture was filtered, and the solid was washed with water, dissolved in

THF, filtered, and the filtrate concentrated under vacuum. The product, ring deuterated 4,4'-di-n-acetylaminodiphenyl sulfoxide, was recrystallized with MeOH/H_2O (product 2, Scheme 2)

The ring deuterated 4,4'-di-N-acetylaminodiphenyl sulfoxide was suspended in 100ml glacial acetic acid. 10ml 30% H_2O_2 was added to the suspension, and the mixture was allowed to stand for 3hr at room temperature. The mixture was then heated at 50^oC for 2hr and subsequently refluxed until homogenous. The homogenous mixture was cooled to room temperature, 5ml 30%H_2O_2 was added, and the mixture was stored overnight at 4^oC. The mixture was concentrated under vacuum and then recrystallized with MeOH/H_2O to yield ring deuterated 4,4'-di-n-acetylaminodiphenyl sulfone, (product 3, Scheme 2).

The ring deuterated 4,4'-di-n-acetylaminodiphenyl sulfone was suspended in 60ml 10% HCl, and heated at reflux for 1.5hr. At this point decolorizing carbon was added, and the mixture was refluxed for 1hr, filtered while hot, and cooled to room temperature. A 10% NaOH solution was added to adjust the pH to 14, and the resulting precipitate was isolated by filtration, recrystallized with MeOH/H_2O, and dried in a vacuum oven to yield 0.5g of the final product, ring deuterated 4,4'-diaminodiphenyl sulfone, d8-44DDS (product 4, Scheme 2).

Scheme 5.2. Synthesis of d8-44DDS

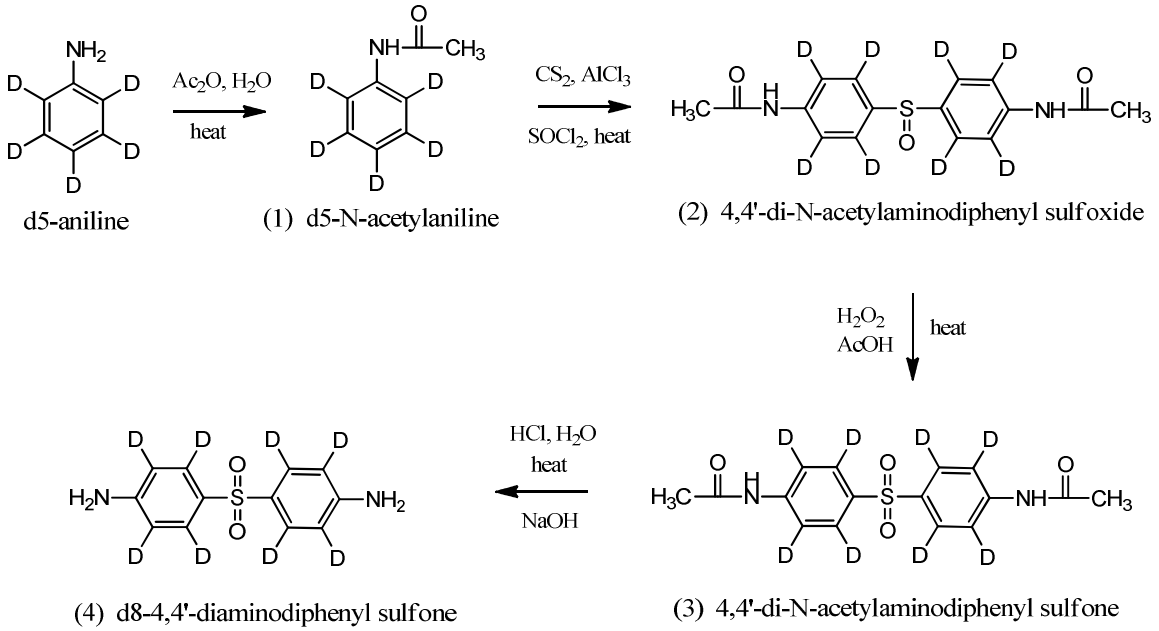

Ring Deuterated d8-33DDS Synthesis

The preparation of 100% nitric acid by the reaction of sulfuric acid with potassium nitrate is accomplished for use later in the synthetic procedure. Vacuum distillation is used to collect the nitric acid (Scheme 3).

Scheme 5.3. Preparation of 100% Nitric Acid Via Vacuum Distillation

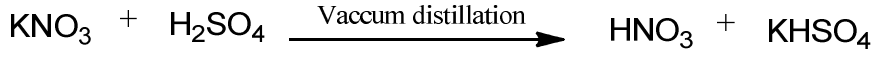

The first step in the synthesis of d8-33DDS is the dropwise addition of chlorosulphonic acid (11.65g, 0.1 mol) to ring deuterated benzene (16.82g, 0.2 mol). The reaction mixture is kept at 20°C and allowed to stir for 30min. This reaction mixture is then poured on ice and extracted with chloroform. The chloroform is distilled off the

reaction mixture under reduced pressure. After distillation, the residue is filtered to leave a filtrate composed of the colorless liquid ring deuterated benzenesulfonyl chloride (product 1, Scheme 4) and a white filter cake, ring deuterated diphenyl sulfone; 75% yield, m.p. 128°C (product 2, Scheme 4).

The deuterated diphenyl sulfone (10.96 g, 0.048 mol) was suspended in 30 ml of methylene chloride and dissolved with the aforementioned 100wt.% nitric acid (7.55g, 0.117mol). 14.8g of 96wt.% sulphuric acid was then added dropwise under reflux with stirring over a period 4 hours at the boiling temperature of the solution (50^{o}C). After cooling to 20^{o}C, the reaction product, ring deuterated 3,3'-dinitrodiphenyl sulfone, precipitated out of solution and was filtered off, washed twice with 100 ml of methylene chloride and then once with water and dried at 100°C. The ring deuterated 3,3'-dinitrodiphenyl sulfone was then purified by recrystallized from DMF; 98% yield, m.p. 203°C (product 3, Scheme 4).

DMF was added dropwise to the ring deuterated 3,3'-dinitrodiphenyl sulfone (14.88g, 0.047mol) until fully dissolved, and 10wt.% palladium catalyst on wet carbon powder (0.74g) was added. This mixture was placed into the hydrogenation flask of a Parr apparatus to reduce the nitro groups. The hydrogenation was carried out under a pressure of 3.5atm at ambient temperature until the reaction mixture would not react further with hydrogen. The catalyst was filtered off, and the filtrate was placed in a vacuum oven at 80°C and reduced pressure to pull off the solvent, DMF. The final product, ring deuterated 3,3'-diaminodiphenyl sulfone, was a yellow solid which was purified by recrystallization from MeOH and charcoal; m.p. 174°C (product 4, Scheme 4).

Scheme 5.4. Synthesis of d8-33DDS

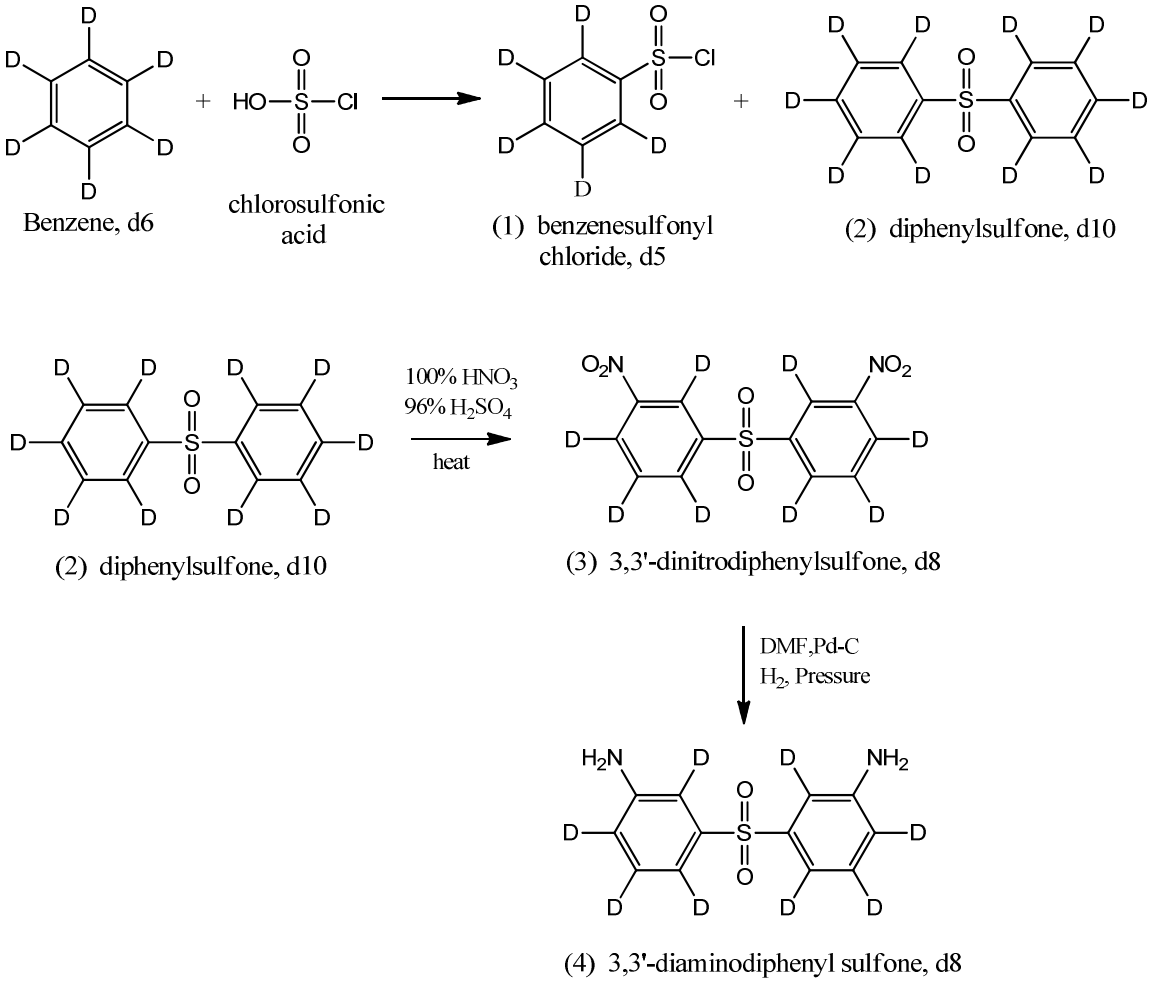

Network Synthesis

Four deuterated resin samples were prepared to selectively study the amine rings and epoxy rings in 33DDS/DGEBA and 44DDS/DGEBA matrices. The d8-DGEBA was reacted with 33DDS and 44DDS to study the effect on epoxy ring motions of the meta vs. para curative. Both of the ring deuterated amines, d8-33DDS and d8-44DDS were reacted with DGEBA to study the motions of the amine rings and compare them to one other and the epoxy rings. Due to the high cost of the deuterated starting materials, the difficulty of the syntheses, and the quantities needed for deuterium NMR analysis, only

300mg of epoxy/amine samples were prepared. Samples were reacted stoichiometrically (2:1 epoxy:amine ratio, equaling a 1:1 functional group ratio) assuming full conversion of the amine. The amines were solubilized into the epoxies using GPC vials as reaction vessels and an oil bath to supply heat. Deuterated amines proved more difficult to solubilize into DGEBA than non-deuterated amines, and the deuterated DGEBA acted as a less efficient solvent for the amines. Thus, temperatures of up to 150°C were required to solubilize the amines.

Once the amines were solubilized into the epoxies, the samples were cured 5 hours at 125°C and 2 hours at 225°C. The deuterated monomers cured more slowly than nondeuterated amines, requiring post cures of multiple days at 200°C and 225°C for fully cured networks. The deuterated amines underwent particularly slow cures, exhibiting changes in deuterium lineshape until fully cured.

Deuterium Solid State Nuclear Magnetic Resonance Methods

Instrumentation and pulse sequences. Solid state NMR spectra were acquired on a Varian ^{UNITY}INOVA NMR spectrometer operating at a frequency of 61.4 MHz for deuterium and equipped with a Tecmag wideline ^{2}H probe. The standard quadrupolar-echo pulse sequence was employed with 90° pulse widths of 2.5μs and a delay of 25μs between pulses. A dwell time of 0.25μs, corresponding to a spectral width of 2.0MHz was used. The number of time domain points sampled during acquisition was 1024, with the data zero-filled to 16,384 points prior to application of Fourier transformation. The number of scans collected for spectra varied depending upon signal strength, which is effected by a number of variables, including temperature and quantity of deuterium present in the sample. The recycle delay between scans was varied from 1-10s,

depending upon the spin-lattice relaxation time of the slowest deuterium motion at that particular temperature. Temperature control was attained by placing a thermocouple directly into the sample chamber and adjusting heater power until the desired temperature was reached.

Solid state deuterium spin-lattice relaxation data was obtained using the saturation-recovery method with a recycle delay of 500ms for all analyses. Here a series of ten 90° pulses separated by 1ms was applied prior to the quadrupolar echo sequence in order to suppress initial magnetization, with signal recovery monitored as a function of time. Spin-lattice relaxation values were obtained by curve fitting the integral areas.

Quadrupolar echo lineshape analysis. Routine spectra were obtained using the standard quadrupolar echo delay sequence.[1] Quadrupolar echo spectra were obtained at 25, 50, 75, 100, 125, 140, 160, 180, and 200°C for all four samples, 33DDS/d8-DGEBA, 44DDS/d8-DGEBA, d8-33DDS/DGEBA, and d8-44DDS/DGEBA. Information concerning type and rate of motion is obtained from the comparison of experimental data to spectral simulation. In this work, simulated lineshapes are calculated using EXPRESS software.[8]

Deuterium NMR spin-lattice relaxation analysis. Spin-lattice relaxation studies were implemented in order to discriminate various motional rates of motion for the selectively deuterated phenyl rings. Experiments were performed at 25, 50, 75, 100, 125, 140, 160, 180, and 200°C for 33DDS/d8-DGEBA, 44DDS/d8-DGEBA, and d8-44DDS/DGEBA. Two experiments were obtained at each temperature for each sample, and the results averaged.

Figure 5.1 shows an example of a saturation recovery experiment for 44DDS/d8-DGEBA at room temperature. For clarity, only 11 delay times are shown; typically 23-24 delay times are measured to ensure a sufficient number of data points for fitting. Note that a distinct lineshape change can also be observed. Initially, only the inner splittings are present at short delay times, with the outer splittings appearing as the delay time increases.

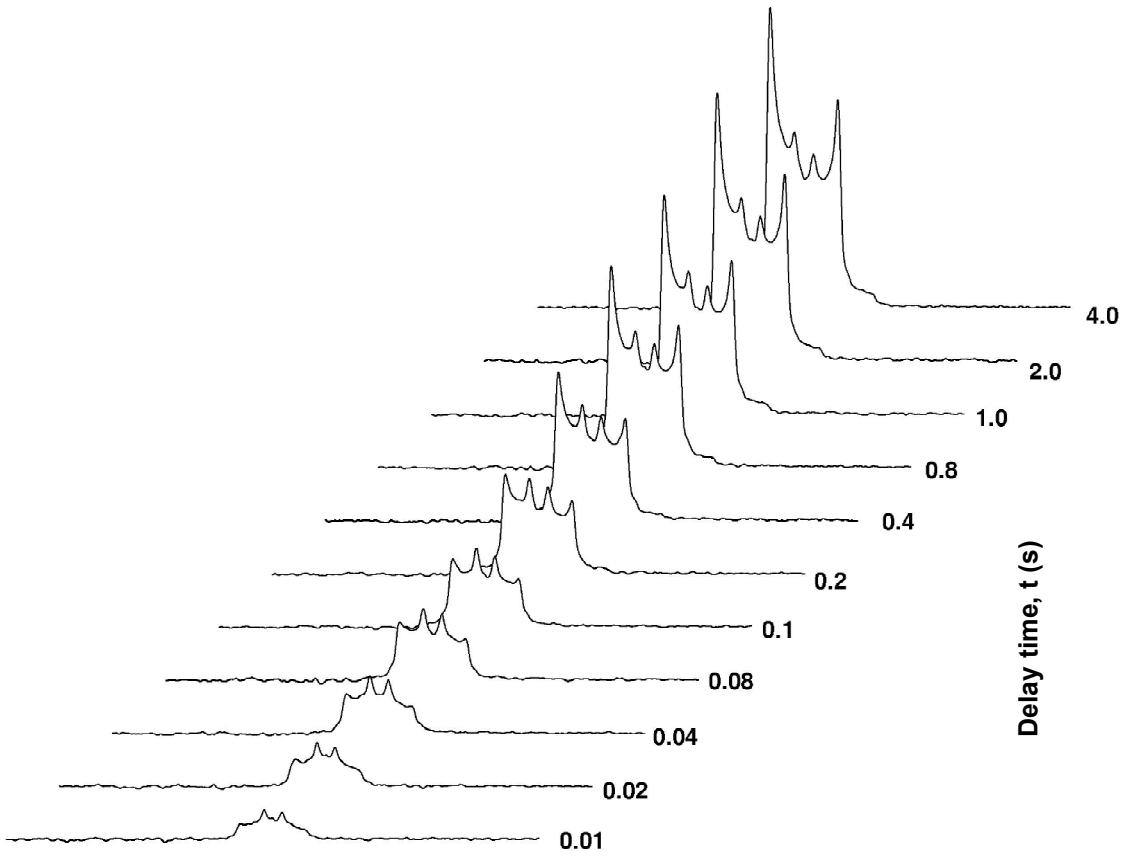

Figure 5.1. 44DDS/ d8-DGEBA saturation recovery spectra.

The data was fitted to an exponential expression in order to determine spin-lattice relaxation times for phenyl ring motion. Equation 5.1 shows the relationship between integral area, delay time, and spin-lattice relaxation time:

$$M(t) = M_0 * (1 - e^{\frac{-t}{T_1}})$$

where: M(t) = signal (or integral area) as a function of delay time, t

M_0 = equilibrium signal at infinite time

t = delay time

T_1 = spin-lattice relaxation time

Equation 5.1. Theoretical exponential equation relating T_1 time to integral area.

Equation 5.1 assumes only one rate of motion, and therefore only one spin-lattice relaxation time. Here the data was fitted to one component, two component, and three component exponentials; it was determined that a two component exponential fit was sufficient to describe spin-lattice relaxation behavior. A modified two component exponential equation used for fitting is shown in Equation 5.2. The red line in Figure 5.2 shows the fit produced by Equation 5.2. Chi squared values were 0.999 – 0.997 for all samples at all temperatures.

$$M(t) = M_1 * \left(e^{\frac{-t}{T_{11}}}\right) + M_2 * \left(e^{\frac{-t}{T_{12}}}\right) + y_0$$

where: M(t) = signal (or integral area) as a function of delay time, t

M_1 = equilibrium signal due to the first motion

M_2 = equilibrium signal due to the second motion

t = delay time

T_{11} = spin-lattice relaxation time of first motion

T_{12} = spin-lattice relaxation time of second motion

y_0 = fitting factor

Equation 5.2. Modified two component exponential equation used for curve fitting.

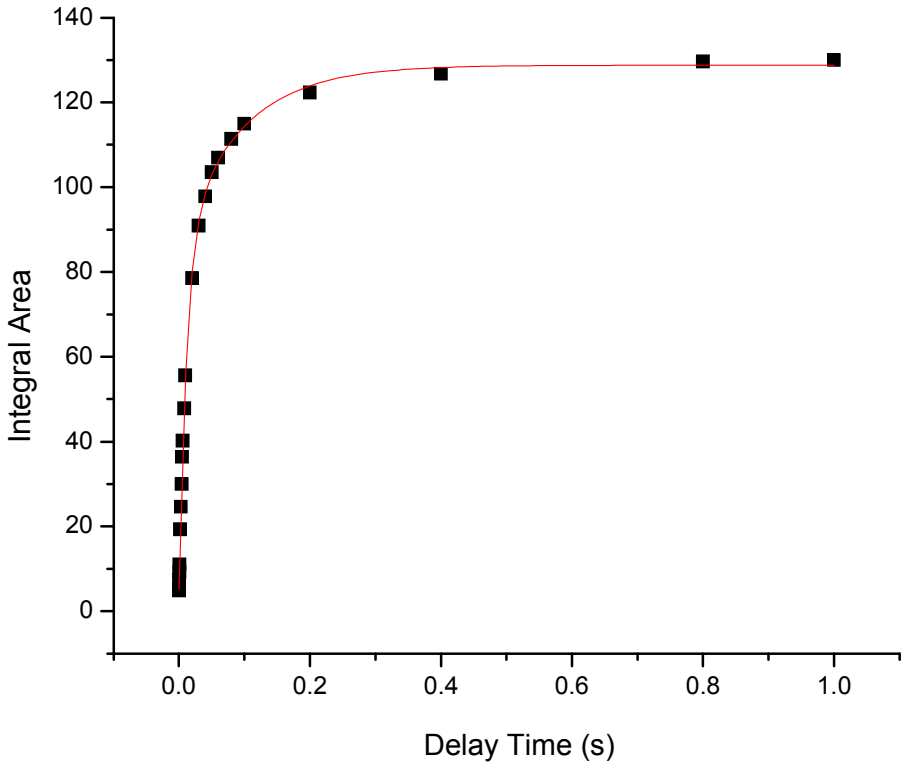

Figure 5.2. Two component curve fitting for saturation recovery experiment.

Results and Discussion

Spin-lattice Relaxation Analysis

Spin-Lattice relaxation (T_1) studies were performed to identify basic motional contributions to lineshape. A two component fit closely matches the spin-lattice experimental data, confirming the presence of two distinct phenyl ring with significantly different rates of motion. These ring motions can be explained in terms of a fast 180° π-flipping motion and a slow or restricted phenyl ring flip motion possessing a small flip angle. The spin-lattice relaxation times are summarized in Table 5.1.

Table 5.1. Spin-Lattice Relaxation Times Calculated from Two Component Fitting for Slow and Fast Phenyl Ring Motions 25 – 200°C

	33DDS/d8-DGEBA		44DDS/d8-DGEBA		d8-44DDS/DGEBA	
T (°C)	**fast**	**slow**	**fast**	**slow**	**fast**	**slow**
25	0.049	0.83	0.059	0.99	0.42	1.95
49	0.026	0.55	0.032	0.69	0.32	1.39
75	0.020	0.38	0.022	0.49	0.14	0.81
100	0.015	0.20	0.016	0.29	0.071	0.58
123	0.012	0.090	0.012	0.13	0.045	0.39
140	0.011	0.042	0.011	0.08	0.039	0.34
160	0.013	N/A	0.013	0.11	0.028	0.31
180	0.011	N/A	0.013	0.12	0.019	0.14
200	0.0087	N/A	0.012	0.14	0.015	0.10

Excluding behavior of the slow motional component above 160°C, the spin-lattice relaxation values indicate that the motion of the epoxy rings is similar regardless of amine. The epoxy rings in the 33DDS/d8-DGEBA sample exhibit slightly faster motions than the 44DDS/d8-DGEBA sample with similar trends for both fast and slow motions. At 160°C, a one component fit is sufficient to characterize T_1 behavior of the 33DDS/d8-

DGEBA sample. At this temperature, all the epoxy rings appear to undergo identical ring motions. Since the T_g of 33DDS/DGEBA is 180°C, it is likely that upon approaching T_g, restriction of ring motion is eliminated.

In the 44DDS/d8-DGEBA sample, the T_1 values of the slow motion display the same behavior observed in 33DDS/d8-DGEBA, decreasing from 25°-140°. However, above 140°C, the spin-lattice relaxation time unexpectedly increases. One possible explanation for this T_1 anomaly is a change in motional mode.

The d8-44DDS/DGEBA sample exhibits two distinct spin-lattice values, i.e., motions, throughout the temperature range analyzed. As expected, the T_1 times of both increase with increasing temperature. It is important to note the relaxation behavior of the 44DDS rings is substantially slower than the DGEBA rings, indicating the amine rings experience more hindrance to bond rotation than the epoxy rings. This is clearly demonstrated by comparing the behavior of the epoxy and amine rings in d8-44DDS/DGEBA and 44DDS/d8-DGEBA. The difference in motional behavior in the epoxy and amine rings is likely due to the presence of ether and quaternary carbon groups adjacent to the DGEBA ring as opposed to amine and sulfone groups adjacent to the 44DDS ring. Ether bonds are well known for allowing facile ring flipping in adjacent phenyl rings.[9 10 11] Additionally, the amine group on 44DDS is most likely a tertiary amine, which increases steric hindrance (Figure 5.3).

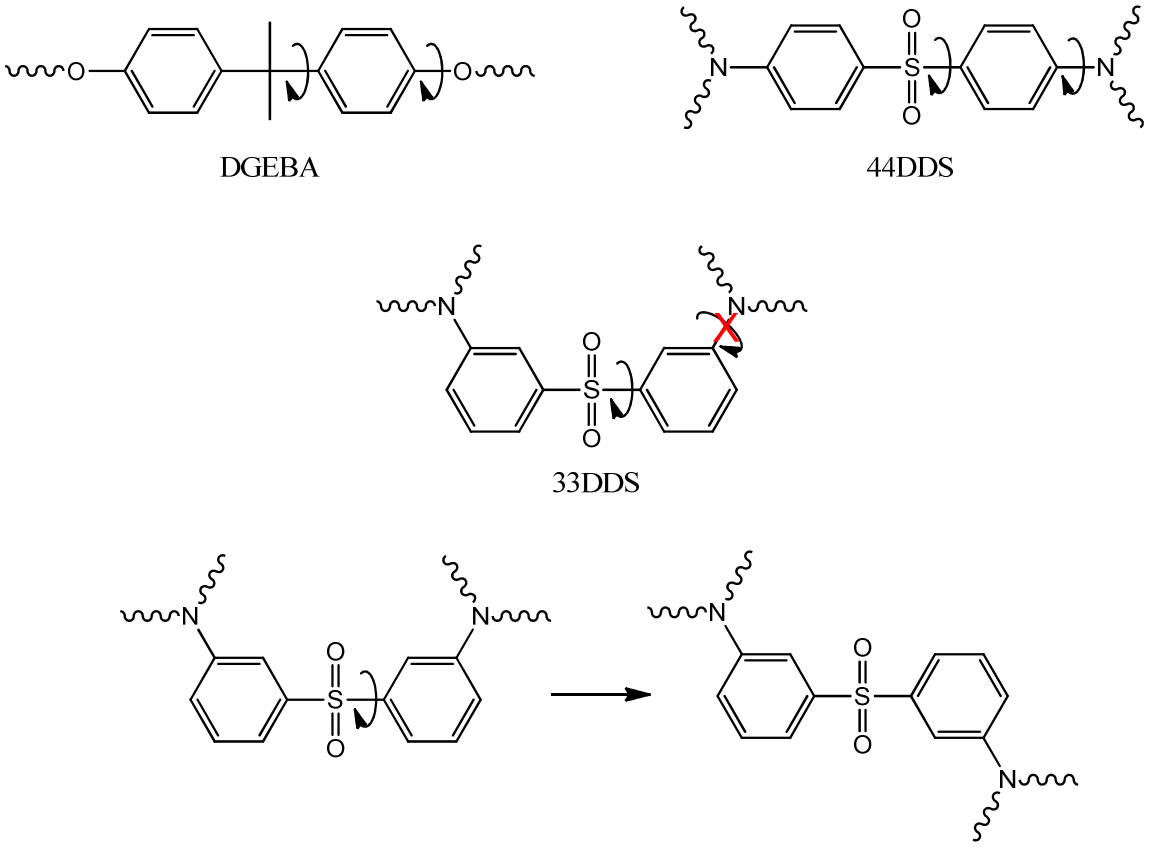

Figure 5.3. DGEBA rings possess more facile phenyl ring π-flipping than 44DDS rings. 33DDS lacks an axis of symmetry making phenyl ring π-flips impossible.

Figures 5, 7, and 9 show plots of log T_1 time vs. inverse temperature. Here linear, i.e., Arrhenius, behavior indicates that no major changes in the type of motion are occurring. In some studies, such as ^{1}H solid state NMR spectroscopy, the activation energy of the motion may be obtained directly from the slope of the log T_1 time vs. 1/T plot.[12] However, in deuterium studies, the actual correlation time, τ_c, obtained with spectral simulation, is necessary to create an Arrhenius plot of log τ_c vs. 1/T. This work is currently underway.

In the log T_1 time vs. 1/T plot for 33DDS/d8-DGEBA (Figure 5.4), the slow motion shows fairly linear behavior at low temperatures (25-75°C), but starts to deviate

at 100°C and disappears by 180°C. The fast motion is linear up to 140°C but shows a slight increase at 160°C, the same temperature at which the slow/restricted motion disappears. This behavior is most likely due to a combination of (1) Decreasing contribution of the slow motional component to the point that it can no longer be accurately determined by data fitting, and (2) The introduction of additional motion as temperature approaches T_g. The decreasing contribution of the slow motional component is shown in Figure 5.5.

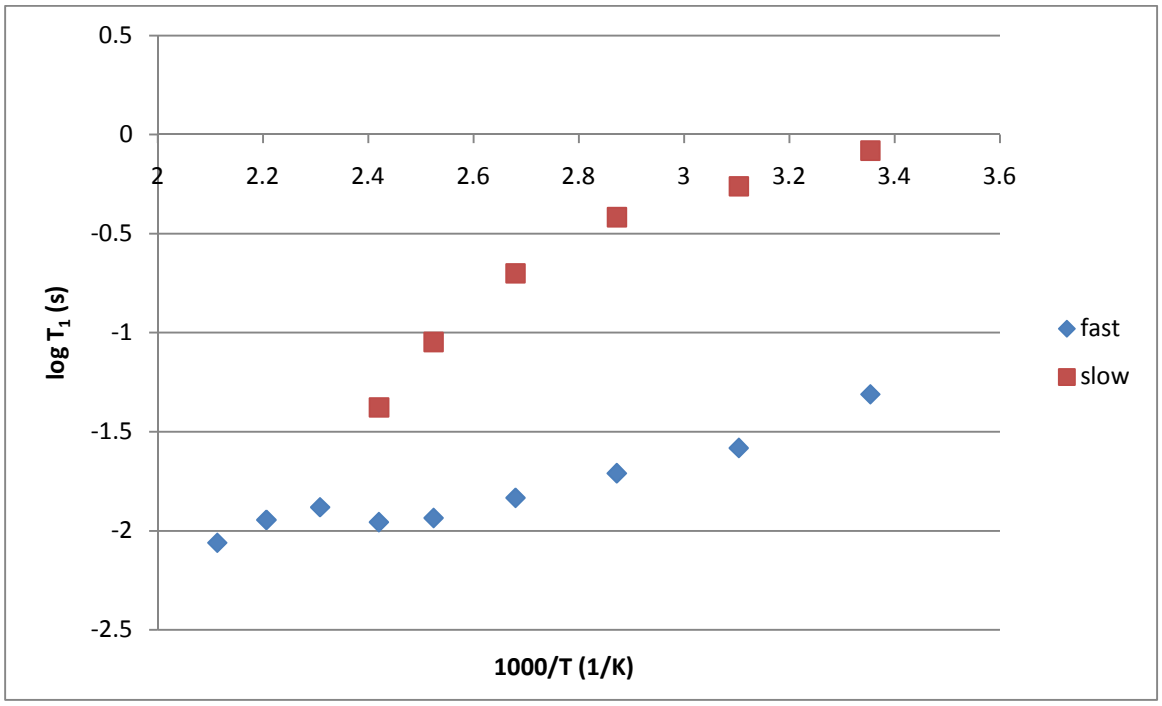

Figure 5.4. Log T_1 time vs. inverse temperature plot for 33DDS/d8-DGEBA.

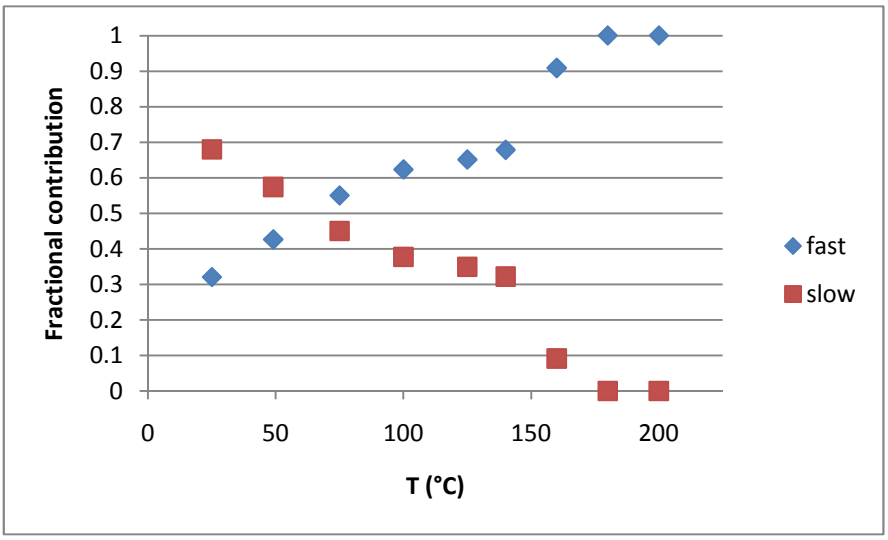

Figure 5.5. Fractional contribution of fast and slow motion in 33DDS/d8-DGEBA.

The log T_1 time vs. 1/T plot of 44DDS/d8-DGEBA is shown in Figure 5.6. The slow component shows similar behavior to the 33DDS/d8-DGEBA sample, decreasing linearly from 25-100°C, then dropping significantly, due to less restricted motion. As noted previously, the slow component exhibits odd behavior above 140°C, with T_1 values increasing with increasing temperature. As previously stated, this anomaly may be due to a change in the motional mode. However, unlike 33DDS/d8-DGEBA, 44DDS/d8-DGEBA is still well below T_g at these temperatures (T_g = 225°C); thus, this behavior cannot be regarded as a T_g effect.

Figure 5.7 shows the fractional contribution of fast and slow motions based on the integral area for 44DDS/d8-DGEBA. As observed in the 33DDS/d8-DGEBA sample, the contribution of the slow motion decreases while the fast motion increases with increasing temperature. However, for 44DDS/d8-DGEBA, the slow motion never completely disappears due to its distance from T_g at 225°C

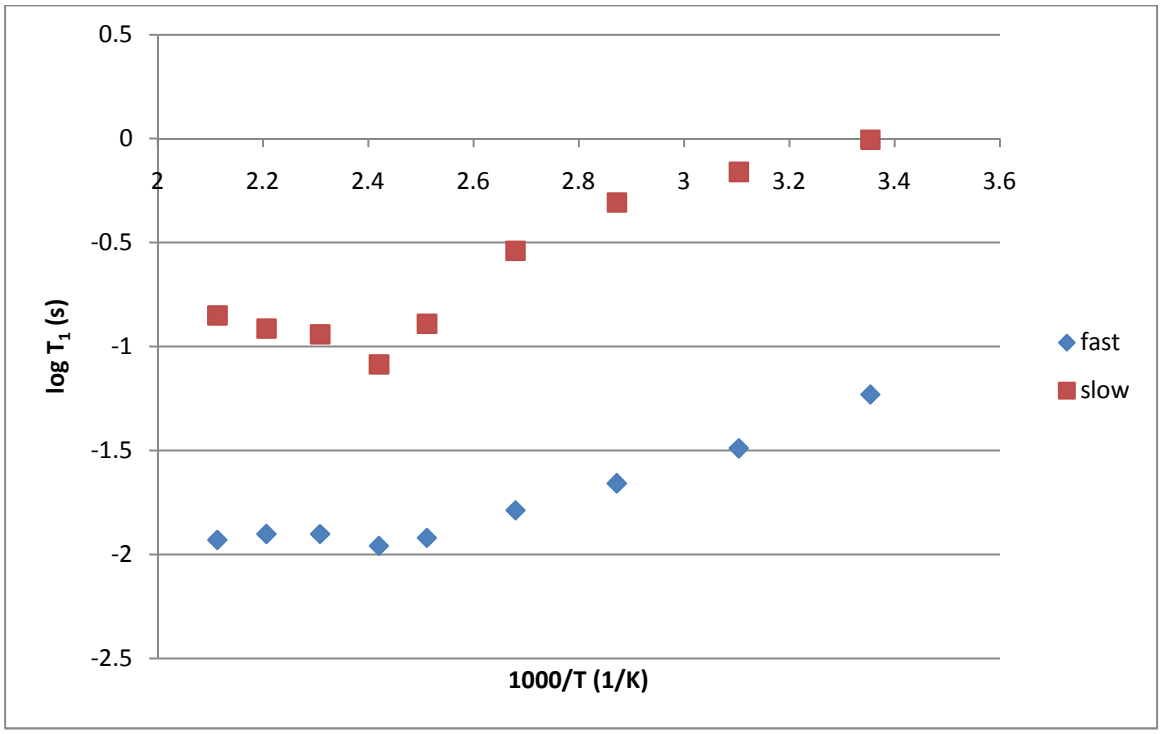

Figure 5.6. Log T_1 time vs. inverse temperature plot for 44DDS/d8-DGEBA.

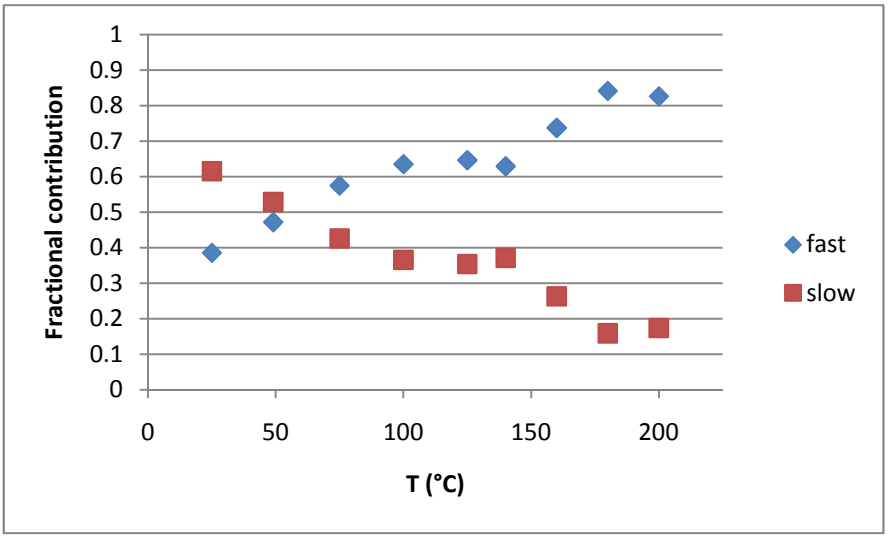

Figure 5.7. Fractional contribution of fast and slow motion in 44DDS/d8-DGEBA.

Figure 5.8 shows the log T_1 time vs. 1/T plot for d8-44DDS/DGEBA. Both fast and slow motional components show Arrhenius behavior throughout the temperature range studied, with the slower component motion remaining linear in the log T_1 time vs. 1/T plot up to 200°C. This is strong evidence that the amine rings are significantly more restricted than the epoxy rings.

The motional contribution of the fast and slow motions based on integral area is seen in Figure 5.9. Although an irregularity exists at 50°C, the trend clearly shows the decrease of the slow motion's contribution as temperature is raised. However, unlike the epoxy rings in which the slow, restricted motion continually decreased as temperature increased, the contribution of the slow motion in the 44DDS rings levels off at 160°C at a level of about 40%. This supports the hypothesis that the amine rings possess greater motional hindrance than the epoxy rings.

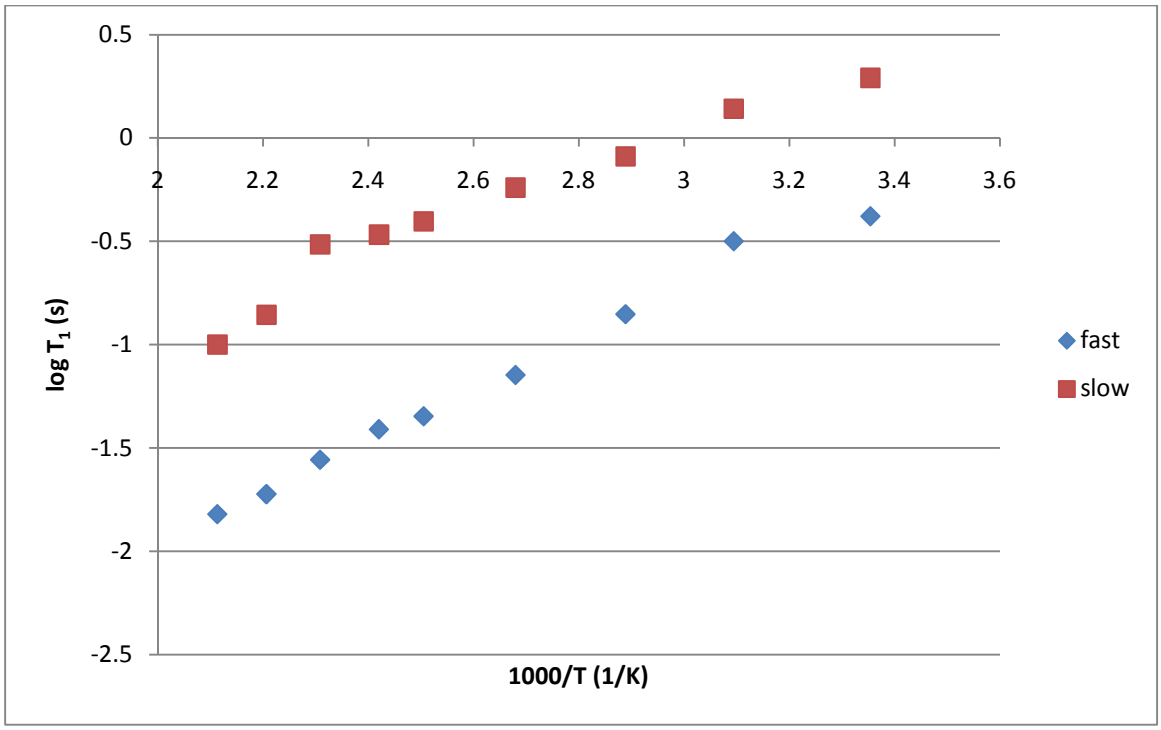

Figure 5.8. Log T_1 time vs. inverse temperature plot for d8-44DDS/DGEBA.

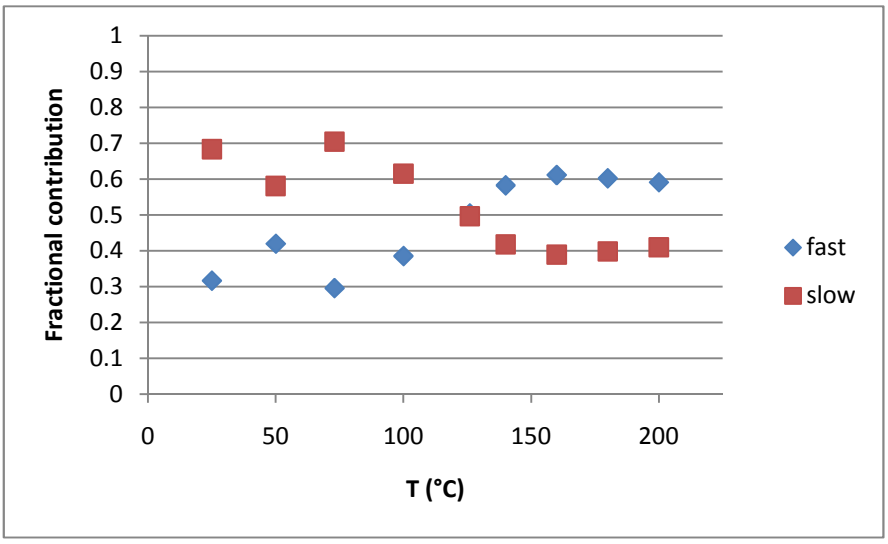

Figure 5.9. Fractional contribution of fast and slow motion in d8-44DDS/DGEBA.

Quadrupolar Echo Lineshape Analysis

Solid state deuterium NMR spectral lineshapes were used to study the motional behavior of d8-33DDS/DGEBA, 33DDS/d8-DGEBA, d8-44DDS/DGEBA, and 44DDS/d8-DGEBA. Deuterium NMR lineshapes provide relevant information concerning the modes and rates of molecular motion present in the matrices. The asymmetry of the lineshapes is due to a distortion caused by the presence of phase transients. However, this distortion is a common spectroscopic artifact in solid state ^2H NMR spectroscopy and does not affect the validity of the results.

In ^2H lineshape analysis, static or restricted phenyl ring motions yield spectra in the form of a Pake doublet; the spectal splitting between the main peaks, or "horns," is ¾ the quadrupolar coupling constant.[3,13,14] The presence of motion will dramatically alter this lineshape, based both on the rate and type of motion. Facile phenyl ring π-flipping is typically observed as a collapsed Pake pattern with closely separated horns located between upfield and downfield shoulders.[3,13,15] A static lineshape is observed in the d8-44DDS/DGEBA sample at 25°C; however, as the temperature increases, both a static and motionally averaged lineshape can be discerned in the spectrum up to 200°C. This overlapping spectral behavior is most clearly observed in the d8-44DDS/DGEBA lineshape at 125°C.

Two other types of motions are also observed. The appearance of a single narrow peak at 0kHz is indicative of a fully motionally averaged system, whereby sufficient mobility exists so that the effective quadrupolar coupling (C_Q) is averaged to approximately zero. This behavior is observed in liquids or polymers at temperatures above glass transition. In addition, a nondescript, "very fast" motion, termed libration, is

also present, which effectively reduces C_Q. In essence, the libration is the summation of all motions in the polymer which affect the phenyl ring other than phenyl ring flipping. Motions that create small amplitude main chain motions, which, in turn, affect phenyl rings, are the main source of libration.

Figure 5.10 compares the ^2H spectra of the ring-deuterated amine (left) and ring-deuterated epoxy (right) in the 33DDS/DGEBA matrix. The deuterated 33DDS cured with DGEBA shows a Pake pattern consistent with restricted ring motion until reaching 180°C (T_g), at which point a narrow peak in the center of the Pake pattern appears. This center peak indicates a small amount of highly mobile rings. The center peak becomes significantly more prominent at 200°C, as the sample is heated to well above T_g. The prominence of the outer splittings above T_g indicates most 33DDS rings remain restricted. 33DDS rings between crosslinks cannot undergo rapid ring flipping due to their meta substitution, which prevents their possessing an axis of symmetry about which to flip. For this reason, even at 200°C, the broad splittings at $\pm$63.5kHz never collapse into narrow splittings. The growth of the center peak above T_g could be indicative of 33DDS molecules on chain ends, which have increased mobility above T_g.

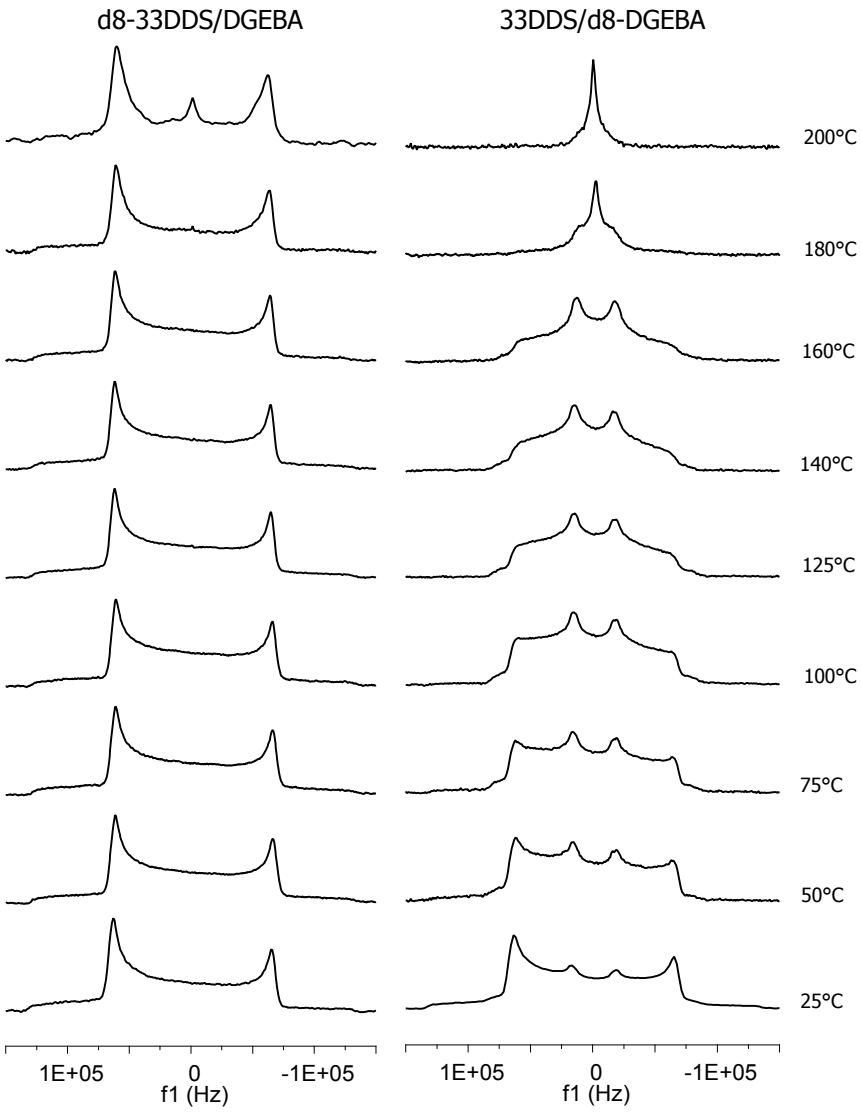

Figure 5.10. ^{2}H NMR spectra of d8-33DDS/DGEBA (left) and 33DDS/d8-DGEBA (right).

Evidence of librational averaging is observed in the d8-33DDS/DGEBA sample by the reduction of the splittings from $\pm$63.5kHz at 25°C to $\pm$61.75kHz at 200°C. Since the d8-33DDS/DGEBA ^{2}H lineshapes do not undergo significant motional averaging throughout the entire temperature range, this sample provides the best opportunity to study libration. The relationship between the quadrupolar coupling constant (C_Q) and the spectral splitting of the Pake doublet is given by Equation 5.3.

$$C_Q = \frac{4}{3} * S$$

where: C_Q = quadrupolar coupling constant

S = the frequency difference between the outer splittings

Equation 5.3. Calculation of quadrupolar coupling constant based on outer splitting.

The theoretical C_Q for a completely static C-D phenyl ring bond is 180kHz, which corresponds to a spectral separation of 135kHz between the outer splittings. At room temperature in the d8-33DDS/DGEBA sample, this spectral separation is 127kHz, indicating a significant amount of libration is occurring at room temperature. The spectral separation between splittings for d8-33DDS/DGEBA decreases from 127kHz to 123.5kHz as temperature is raised from 25°C to 200°C, corresponding to a decrease in C_Q from to 169.5kHz to 164.5kHz. The effective amplitude of the librational motion can be calculated from Equation 5.4.

$$< C_Q >= C_Q * \frac{3cos^2(\theta)}{2}$$

where: $<C_Q>$ = the average quadrupolar coupling constant observed

C_Q = the theoretical coupling constant for static phenyl C-D bonds (180kHz)

θ = librational amplitude

Equation 5.4. Relation of C_Q to librational amplitude.

For d8-33DDS/DGEBA, the librational amplitude changes from 37° to 39° as the temperature changes from 25°C to 200°C. This value is in good agreement with a

librational amplitude of 37° for similar aromatic crosslinked epoxies observed by Ingelfield and coworkers.[3]

It is clear from Figure 5.10 that the epoxy rings in 33DDS/d8-DGEBA display a substantially different behavior than the amine rings of d8-33DDS/DGEBA. At 25°C the outer splittings at ±63kHz and shoulders at ±136kHz are prominent, with the inner splittings at ±18kHz also present at room temperature, indicating some fast 180° ring flips are occurring at 25°C. As temperature is increased, the restricted lineshape diminishes while the fast motion increases until a lineshape indicative of facile ring flipping is observed at 140°C. At 160°C, the lineshape has narrowed even further, and has changed appearance, indicating an additional mode of motion is occurring. At 180°C, a narrow line is observed, and by 200°C, 20°C above T_g, the lineshape has fully collapsed to a single peak attributed to long range cooperative (liquid-like) motions occurring above T_g.

Figure 5.11 shows the deuterium lineshape of the amine rings (left) and epoxy rings (right) for 44DDS/DGEBA. The d8-44DDS rings initially display restricted motional behavior at 25°C, with outer splittings at ±63.5kHz and shoulders at ±140kHz. However, at 50°C, inner peaks at ±19kHz are visible, indicating π-flipping motions. These inner peaks continue to grow while the outer peaks decrease up to 200°C; at this temperature the lineshape is indicative of facile ring flipping motions. It should be noted that 200°C is the upper temperature limit of the NMR probe and is 25°C below the T_g of 44DDS/DGEBA. This prevents studies above T_g whereby liquid-like behavior could be observed.

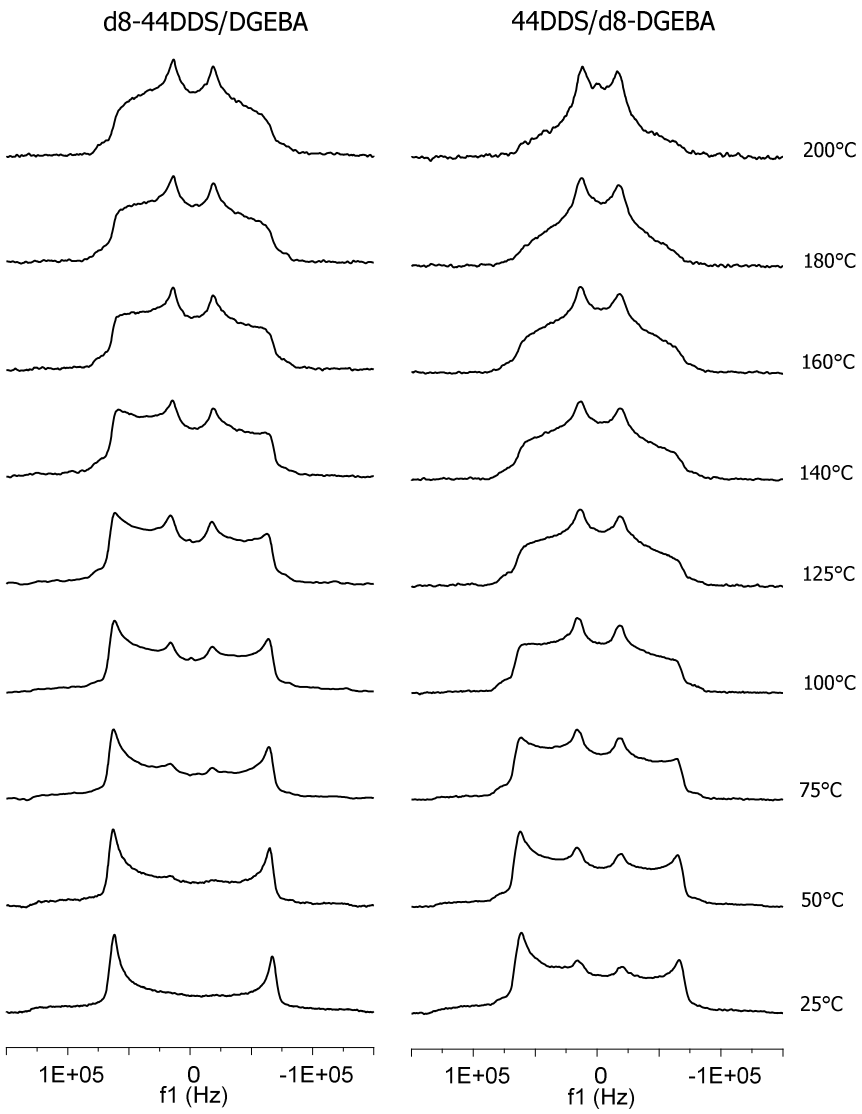

Figure 5.11. ^{2}H NMR spectra of d8-44DDS/DGEBA (left) and 44DDS/d8-DGEBA (right).

The motions of epoxy rings in 44DDS/d8-DGEBA are shown on the right side of Figure 5.11. At 25°C, both outer (±63kHz) and inner (±18kHz) splittings are seen, indicating restricted π-flipping motions are present. The outer splittings and shoulders (± 136kHz) decrease and inner splittings become the dominant lineshape as temperature is increased to 125°C. Above 125°C, additional lineshape changes are observed due to additional modes of motion and increased rate of motion.

Interestingly, the peak shape of the epoxy rings in 44DDS/d8-DGEBA at 25°C closely matches that of the amine rings in d8-44DDS/DGEBA at 100°C. This delta of 75°C between the lineshapes of the epoxy and amine holds throughout the lineshape analysis, such that ring motions in the amine are observed at temperatures 75°C higher than in the epoxy. Since both the epoxy and amine phenyl rings possess an axis of rotation, this increased activation energy for the amine rings is likely due to the sulfone group hindering motion, as evidenced by the T_1 experiments.

Figure 5.12 compares the ^2H spectra of the meta-substituted amine (33DDS) vs. the para-substituted amine (44DDS) when both have been reacted with DGEBA. As observed previously, 33DDS exhibits no ring flipping, but does show the presence of some sites undergoing rapid, isotropic motion, i.e., the narrow center peak, above T_g. The amine rings of 44DDS show phenyl ring flipping, but no evidence of rapid, near isotropic motion since the matrix never reaches T_g.

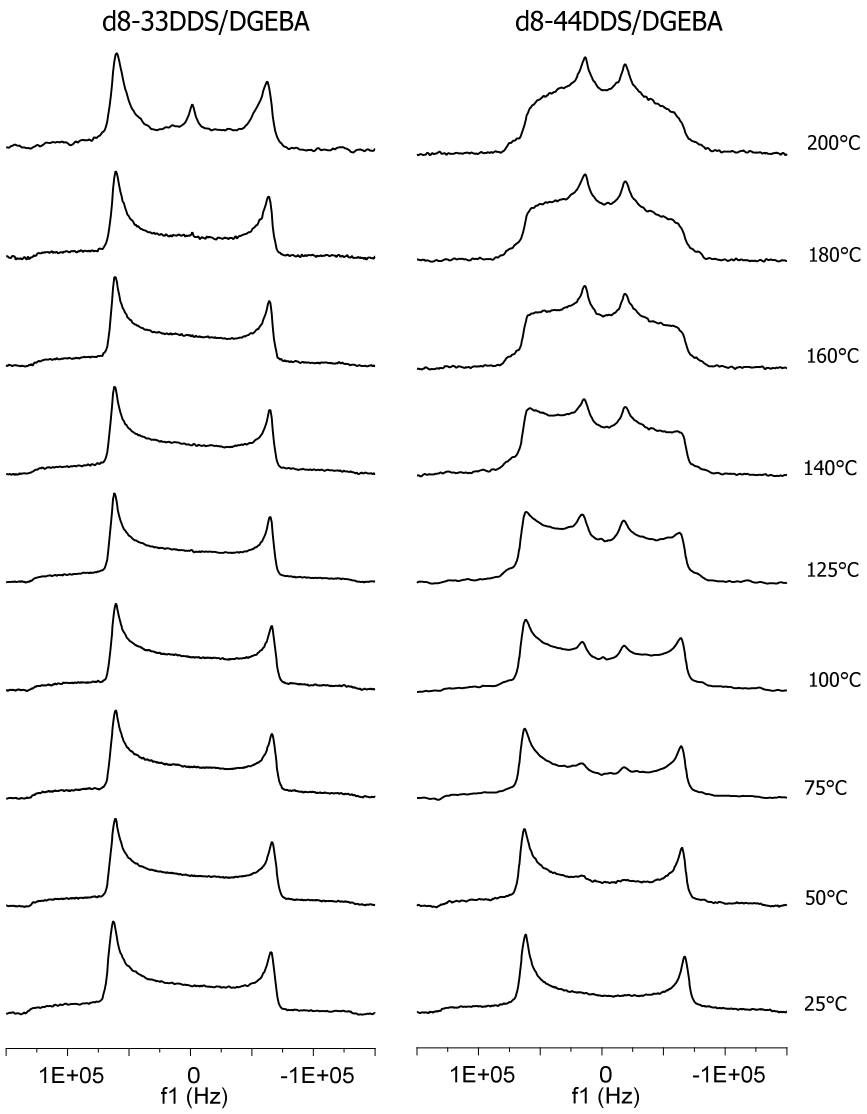

Figure 5.12. ^{2}H NMR spectra of d8-33DDS/DGEBA (left) and d8-44DDS/ DGEBA (right).

The effect of meta vs. para curative substitution on the epoxy ring motions are examined by comparing the solid-state ^{2}H lineshapes of 33DDS/d8-DGEBA (left) vs. 44DDS/d8-DGEBA (right), Figure 5.13. The epoxy lineshapes are almost identical between 25°C and 125°C; however at 140°C, 33DDS/d8-DGEBA begins to show a larger reduction of the outer splittings. This lineshape change is accentuated at 160°C. Above 160°C, the lineshapes for the two epoxies completely differ, with the 33DDS/d8-DGEBA

narrowing into a single peak, while the 44DDS/d8-DGEBA material exhibits a solid-state pattern characteristic of rapid ring motion.

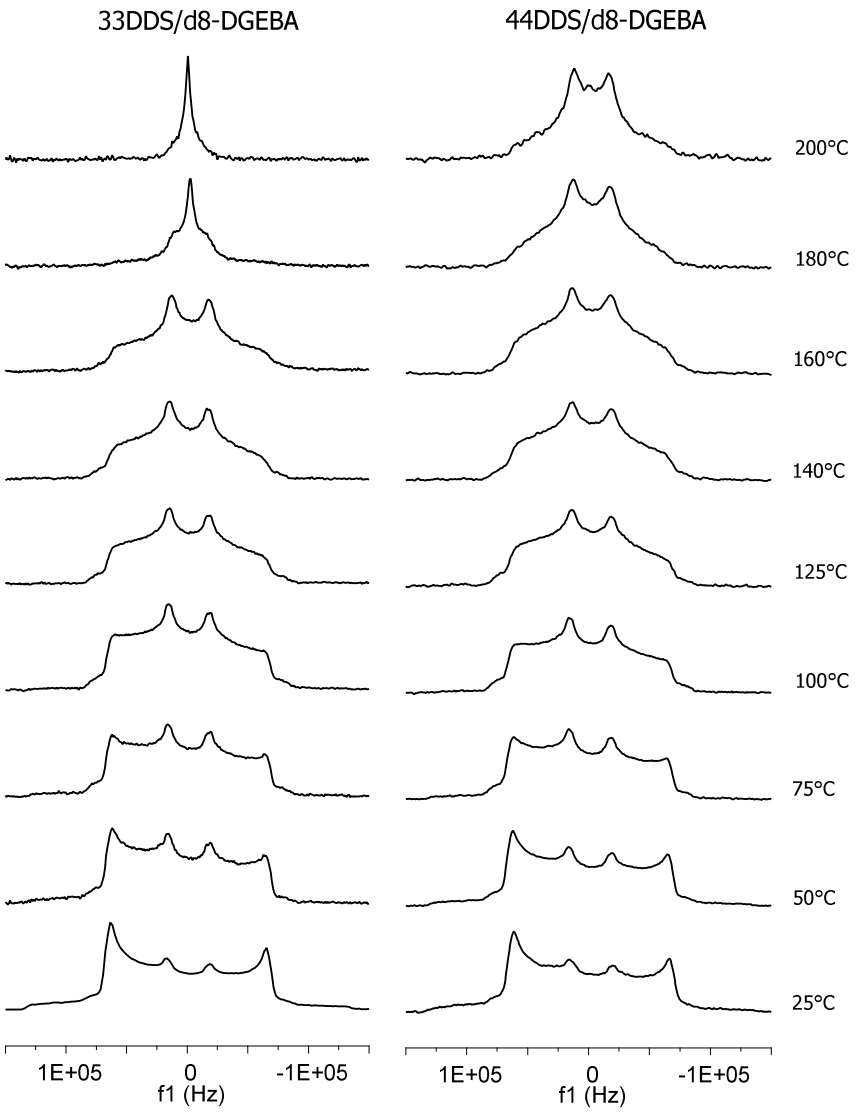

Figure 5.13. ^{2}H NMR spectra of 33DDS/d8-DGEBA (left) and 44DDS/d8-DGEBA (right).

Conclusions

Linear trends in log T_1 time vs. 1/T plots are observed for the fast motional component in all three samples (Figures 5, 7, 9) with the exception of a small deviation

from linearity in the deuterated epoxy ring samples at 160°C. In 33DDS/d8-DGEBA, this is attributed a small contribution of the slow motion being averaged in with the fast component or a change in motional mode due to the proximity to T_g (180°C). In 44DDS/d8-DGEBA, the change in slope of the slow motional component is explained by a change in motional mode; however, as the sample is still well below T_g, the cause of this change is unknown.

Further deuterium NMR experimentation at low temperatures is required to further investigate the motional behavior of these systems. Of particular interest is to determine whether the librational motion can be frozen out such that the theoretical value of $C_Q = 180$ for a static C-D phenyl ring bond is observable. Additionally, spin-lattice relaxation studies for the d8-33DDS/DGEBA should be obtained in the 25-200°C temperature range to compare to data already obtained for the other systems. Due to the highly static nature of the 33DDS rings, we would expect to see evidence of slow, restricted motions for most of the temperature range. Low temperature T_1 analysis on all four samples would provide interesting information on the rate of motions at low temperatures and temperature at which various motions became "frozen out."

In future ^2H lineshape simulation work, ring flipping motions will be more accurately described using a stretched exponential equation (KWW) to account for a range of motional rates and a simple Gaussian distribution of flip angles. Librational motions will be pre-averaged in to the lineshape by adjusting the quadrupolar coupling constant. The completion of these complex simulated lineshapes will allow experimental lineshapes to be accurately replicated, thus describing the complex motions of the phenyl rings.

Additionally, ^{2}H lineshape simulations will provide correlation times for the motions at different temperatures. From this data it is possible to calculate activation energies as well as permit comparison of NMR results to relaxations observed with dynamic mechanical analysis and dielectric spectroscopy. This comparison can provide evidence regarding the correlation between phenyl ring motions and the sub-T_g transitions responsible for bulk mechanical properties of matrices such as modulus, toughness, and strength,[5,6,7] and thus further our understanding of the relationship between chemical composition and mechanical properties in polymers.

References

1. Mirau, P.A. *A practical guide to understanding the NMR of polymers* Wiley-Interscience, New Jersey (2005).
2. Schmidt-Rohr, K.; Spiess, H. W. *Multidimensional Solid-State NMR and Polymers*; Academic Press: San Diego, (1996) Chapters 7 and 8
3. Shi, J.F.; Ingelfield, P.T.; Jones, A.A.; Meadows, M.D.; , *Macromolecules,* **1996**, *29*, 605-609.
4. Vorselaars, B; Lyulin, A.V.; Michels, M.A.J. *Macromolecules,* **2007**, *40*, 6001-6011.
5. Chen, L.P.; Yee, A.F. *Macromolecules,* **1998**, 31, 5371-5382.
6. Sauvant, V.; Halary, J.L. *Journal of Applied Polymer Science,* **2001**, 82, 759-774.
7. Blanco, M.; Ramos, J.A.; Goyanes, S.; Rubiolo, G.; Salgueiro, W.; Somoza, A; Mondragon, I. *Journal of Polymer Science Part B: Polymer Physics,* **2009**, 47, 1240-1252.
8. Vold, R.L.; Hoatson, G.L. *Journal of Magnetic Resonance,* **2009**, 198, 57-72.
9. Roy, A.K.; Jones, A.A., Ingelfield, P.T. *Macromolecules,* **1986** 19, 1356-1362.
10. Schaefer, J.; Stejskal, E.O.; Perchak, D., Skolnick, J.; Yaris, R. *Macromolecules,* **1985**, 18, 368-373.
11. McEachern, D.M.B; Lehmann, P.E.F. *Journal of Molecular Structure,* **1971**, 7, 267-276.
12. Taylor, R.E.; Bacher, A.D.; Dybowski, C. *Journal of Molecular Structure,* **2007**, 846, 147-152.
13. Cholli, A.L.; Dumais, J.J.; Engel, A.K.; Jelinski, L.W. *Macromolecules,* **1984**, 17, 2399-2404.

14. Hiraoki, T.; Kogame, A.; Nishi, N.; Tsutsumi, A. *Journal of Molecular Structure,* **1998**, 441, 243-250.

15. Clayden, N.J. *Polymer,* **2000**, 41, 1167-1174.

CHAPTER VI

INVESTIGATION OF MOLECULAR MOTIONS OF EPOXY NETWORKS VIA ^{13}C NMR SPECTROSCOPY

Introduction

Solid state NMR spin-lattice relaxation studies give ideal opportunity to study molecular motions in crosslinked glassy solids. Carbon spin-lattice relaxation (T_1) times are a function of both the rate and type of motions at the carbon site. Generally in the solid state, T_1 times are directly related to molecular motions, with shorter T_1 times indicating faster motions and longer T_1 times indicating slower motions. Proton spin-lattice relaxation values do not offer information about specific molecular level motions because proton spin diffusion homogenizes T_1 times. However, ^{13}C atoms are isolated from one another due to their 1.1% natural abundance. Since the rate and type of molecular motions influence T_1 values, spin-lattice relaxation experiments should provide information concerning molecular motion at ^{13}C sites.

In deuterium NMR spectroscopy, spin-lattice relaxation is dominated by the quadrupolar moment; however, mechanisms available for spin-lattice relaxation are more numerous in ^{13}C experiments. Dipole-dipole interactions are the largest contributors to ^{13}C spin-lattice relaxation for protonated sites, while chemical shift anisotropy (CSA) contributes substantially to the relaxation mechanism in quaternary aromatic carbon sites. For ^{13}C T_1 studies to provide information on molecular motion, contributions from dipolar and CSA interactions must be separated.

Objective

The goal of this chapter is to determine the molecular mobility of select carbon sites within 33DDS/DGEBA and 44DDS/DGEBA matrices using ^{13}C variable temperature solid state NMR spin-lattice relaxation (T_1) studies. By combining ^{13}C spin-lattice relaxation behavior as a function of temperature with ^{2}H NMR results, it is hoped that processes contributing to sub-T_g transitions will be identified.

Materials

All reagents were used without further purification. 33DDS and 44DDS were purchased from Aldrich. DGEBA resin, EPON 825, was donated by Hexion. 33DDS and 44DDS were solubilized in DGEBA at 110°C, and the resins were cured at 125°C for 5hrs and 225°C for 2hr. Figure 6.1 shows the chemical structures for 33DDS, 44DDS, and DGEBA.

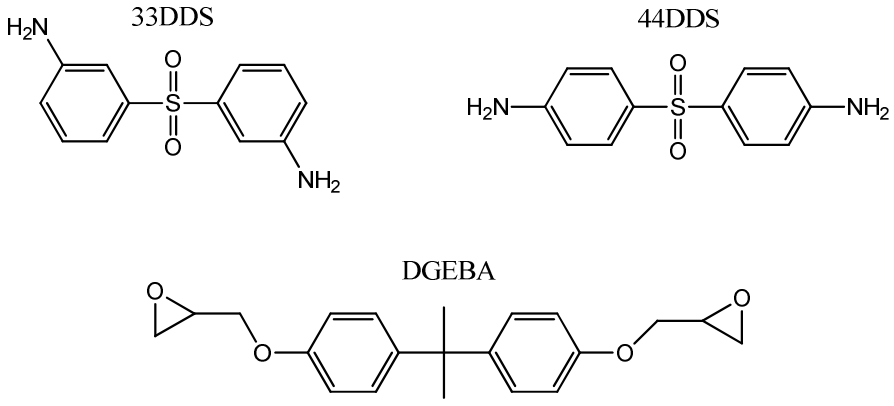

Figure 6.1. Structures of 44DDS, 33DDS, and DGEBA.

Methods

Carbon-13 NMR Spectroscopy

Solid-state NMR spectroscopy was performed on a Varian ^{UNITY}INOVA 400 spectrometer using a standard Chemagnetics 7.5mm PENCIL™-style probe. Samples were loaded into zirconia rotor sleeves, sealed with Teflon™ caps, and spun at rate of 4.0kHz. Carbon spectra were obtained using the standard cross-polarization/magic angle spinning (CP/MAS) technique with high-power proton decoupling implemented during data acquisition.[1] In addition, the TOSS technique was implemented to remove spinning side bands.[2] Acquisition parameters were as follows: The ^{1}H 90° pulse width was 5.5μs, the cross-polarization contact time was 1ms, the dead time delay was 6.4μs, and the acquisition time was 45ms. A recycle delay of 3.0s between scans was utilized. Spectral processing included Gaussian line broadening as well as fitting the baselines to a 20th order polynomial to remove spectral distortion

Spin-lattice relaxation (T_1) inversion recovery experiments were performed by applying a ^{13}C 90° pulse immediately after cross polarization, thereby "flipping" the ^{13}C spins along the -z axis. After a variable delay, another 90° pulse is used to acquire signal, and thus monitor magnetization recovery. Spin-lattice values are calculated by fitting peak values using the Varian VNMR6.1C software.

Results and Discussion

Spectral Assignments

^{13}C CP/MAS solid state spectra were obtained for both the 44DDS/DGEBA and 33DDS/DGEBA samples (Figure 6.2). In addition to literature assignments, small

molecule solution NMR studies, pre-gel melt state NMR studies, and the MNOVA® Modgraph NMRPredict package were used to make spectral assignments.[3]

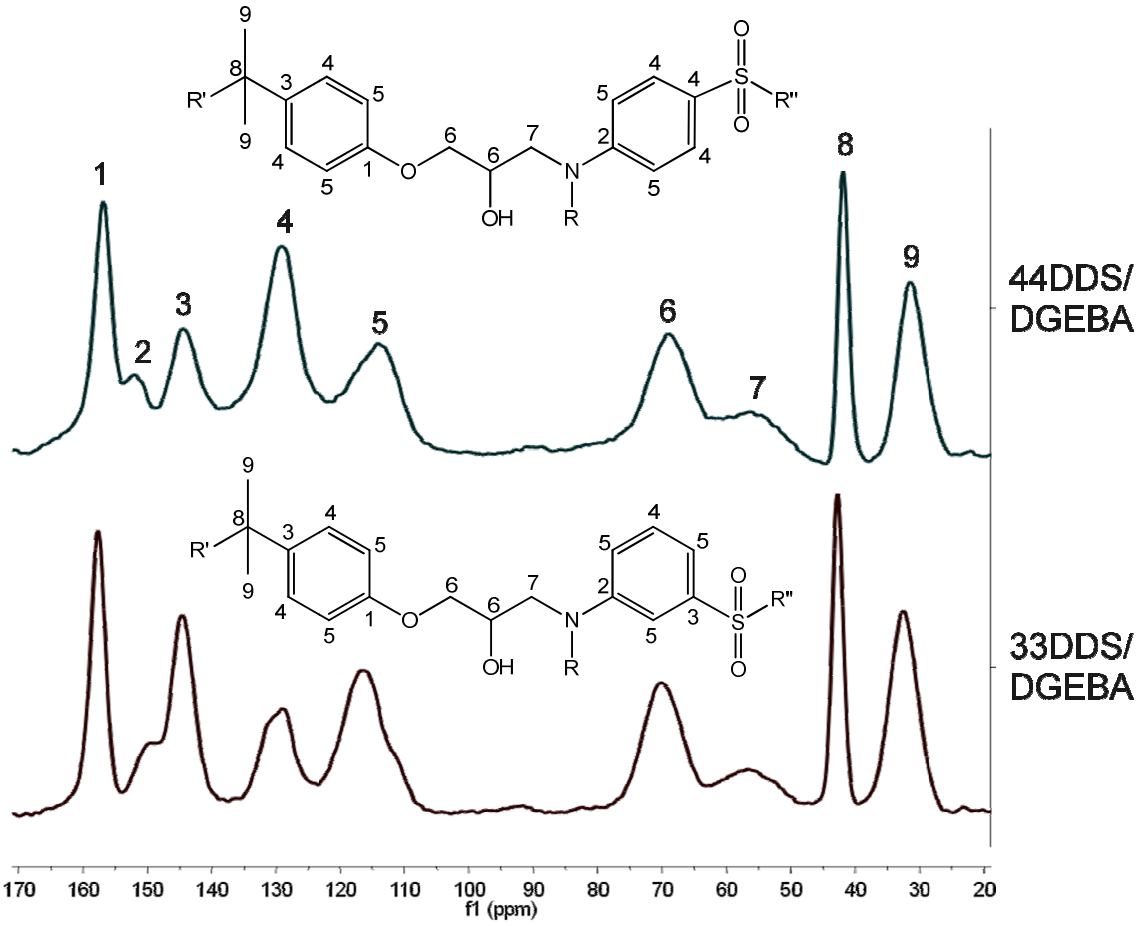

Figure 6.2. Carbon solid state CP/MAS NMR spectra of 44DDS/DGEBA and 33DDS/DGEBA with spectral assignments correlating to the carbon sites labeled.

The upfield shifts, peaks 6-9, are due to aliphatic carbon resonances. Here the shapes and chemical shifts of these peaks are similar for 33DDS and 44DDS systems, since these sites are well removed from the aromatic moieties. The downfield shifts, peaks 1- 4, reflect aromatic carbon resonances. The peaks for DGEBA aromatic carbons are the same in both samples. However, the amine sites, peaks 2-5, are all noticeably different in shape and size due to the differences in meta vs. para connectivity. For

instance, peak 2 appears as a shoulder on the upfield side of peak 1 in the 44DDS/DGEBA sample, but is observed as a downfield shoulder of peak 3 in the 33DDS/DGEBA sample. Peak 4 intensity is greater than peak 5 in the 44DDS/DGEBA sample, while peak 5 is the more intense than peak 4 in the 33DDS/DGEBA sample. It is important to note the resonances of the DDS carbons closest to the sulfone have different shifts. In the 44DDS/DGEBA spectrum, these are three aromatic carbons on the amine ring that contribute to peak 4, while in the 33DDS/DGEBA spectrum, these sites are observed as peaks 3, 4, and 5.

Comparison of T_1 Times between 44DDS/DGEBA and 33DDS/DGEBA

A representative inversion-recovery experiment for 33DDS-DGEBA is shown in Figure 6.3. Spectra have been selected so that the null points for many of these peaks can be examined. At a delay of 0.01s, all peaks are inverted. Peak 9 exhibits its null at about 0.08s, peak 8 at 4s, etc.

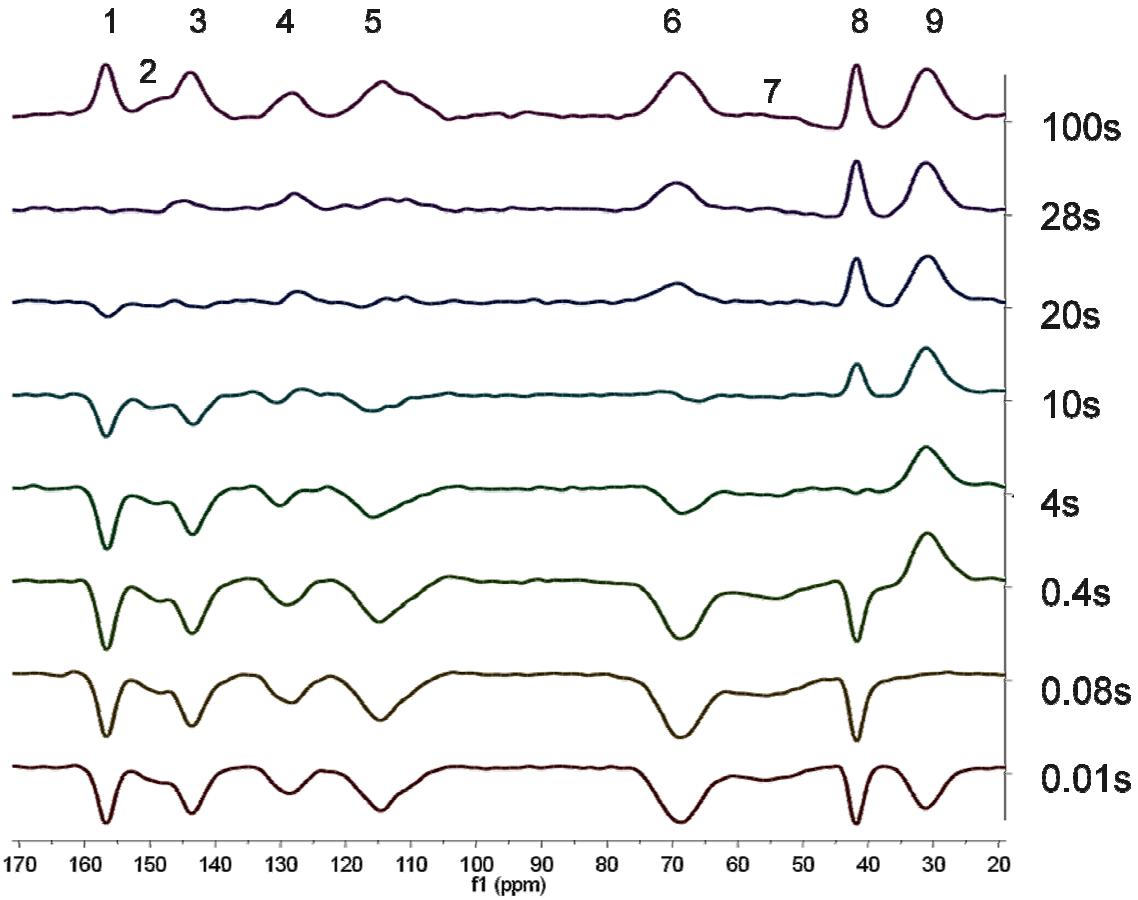

Figure 6.3. Carbon T_1 inversion recovery experiment on 33DDS/DGEBA.

Figure 6.4 is a plot of peak intensity versus delay time for the data presented in Figure 6.3. A one component curve fitting analysis was used to determine T_1 values. Note that peaks 3-6 are composite resonances of two or more different carbon sites, and that differing carbon sites in 44DDS/DGEBA and 33DDS/DGEBA contribute to peaks 3-5. Using a one component curve fit is valid only if all carbon sites responsible for the peak possess the same motional behavior. The odd behavior of peak 9 (the methyl resonance) is due to a transient NOE phenomenon often associated with methyl groups.

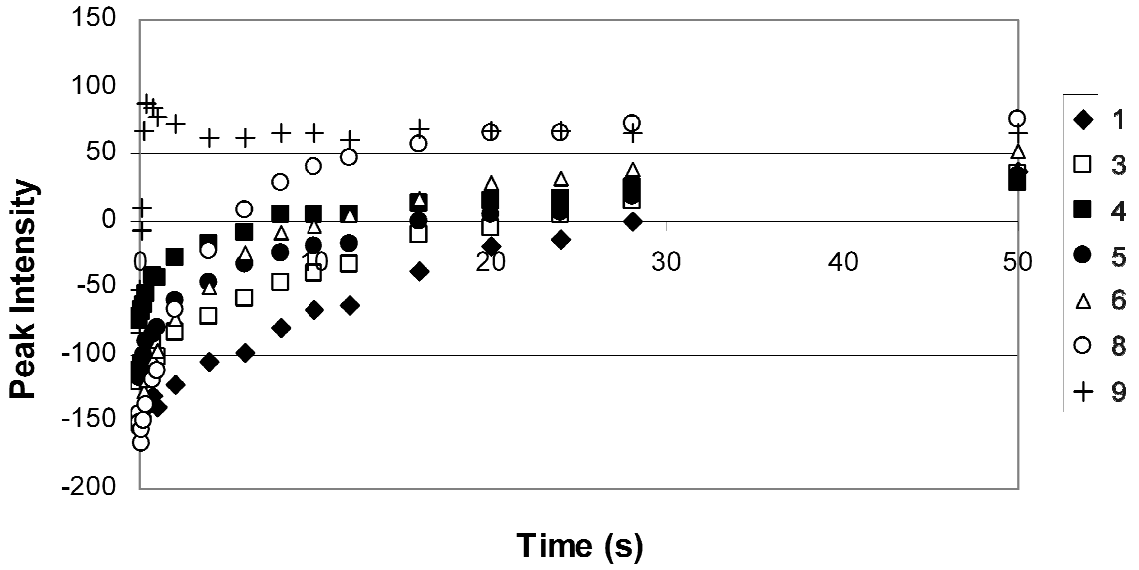

Figure 6.4. Inversion-recovery data for the spectra shown in Figure 6.3.

The tabulated data for variable temperature T_1 analysis of 33DDS/DGEBA and 44DDS/DGEBA is summarized in Table 6.1. The intensities of peaks 2 and 7 were not adequate for accurate fitting. Peaks 1 and 3, the quaternary aromatic sites in DGEBA and the quaternary aromatic site adjacent to the sulfone in 33DDS, possess long T_1 times even at 200°C, 20°C above the T_g of 33DDS/DGEBA. Peaks 8 and 9 show increasing T_1 values as temperature is increased due to the very fast rotation of the methyl group (peak 9), which makes its spin-lattice behavior liquid-like.

Table 6.1. Comparison of ^{13}C T_1 Times for 33DDS/DGEBA and 44DDS/DGEBA

Spin-Lattice Relaxation Times for 33DDS/DGEBA

T (°C)	Peak 1	Peak 3	Peak 4	Peak 5	Peak 6	Peak 8	Peak 9
25	25	19	6.8	12	7.2	4.4	0.076
50	16	12	1.6	5.9	4.3	4.4	0.071
75	19	18	1.8	4.3	4.3	4.7	0.073
100	18	15	1.2	2.4	2.7	5.3	0.084
150	18	19	1.1	1.4	1.5	7.1	0.099
200	16	14	0.70	1.0	1.1	5.5	0.090

Spin-Lattice Relaxation Times for 44DDS/DGEBA

T (°C)	Peak 1	Peak 3	Peak 4	Peak 5	Peak 6	Peak 8	Peak 9
25	22	14	13.0	7	5.9	3.9	0.072
50	18	13	11.0	5.4	5.3	4.0	0.071
75	18	12	8.6	4.6	4.9	4.6	0.076
100	18	14	7.3	3.2	3.5	4.7	0.077
150	15	13	5.5	1.7	2.3	4.8	0.086
200	15	11	1.70	1.1	1.7	5.8	0.098

Figures 6.5 and 6.6 show the log T_1 time vs. 1/T plots for peaks 4, 5, and 6 of 33DDS/DGEBA and 44DDS/DGEBA, respectively. Peaks 1, 3, 8, and 9 were excluded from the plots. For carbon sites 1 and 3, due to the location on the axis of symmetry, only small changes in T_1 time were observed across the temperature range. Peaks 8 and 9 were excluded due to the transient NOE phenomenon associated with methyl groups. Peaks 4 and 5 comprise the sp^2-hybridized phenylene ring carbons. Peak 6 is composed of two of the aliphatic carbons formed by the ring opening of the epoxide group.

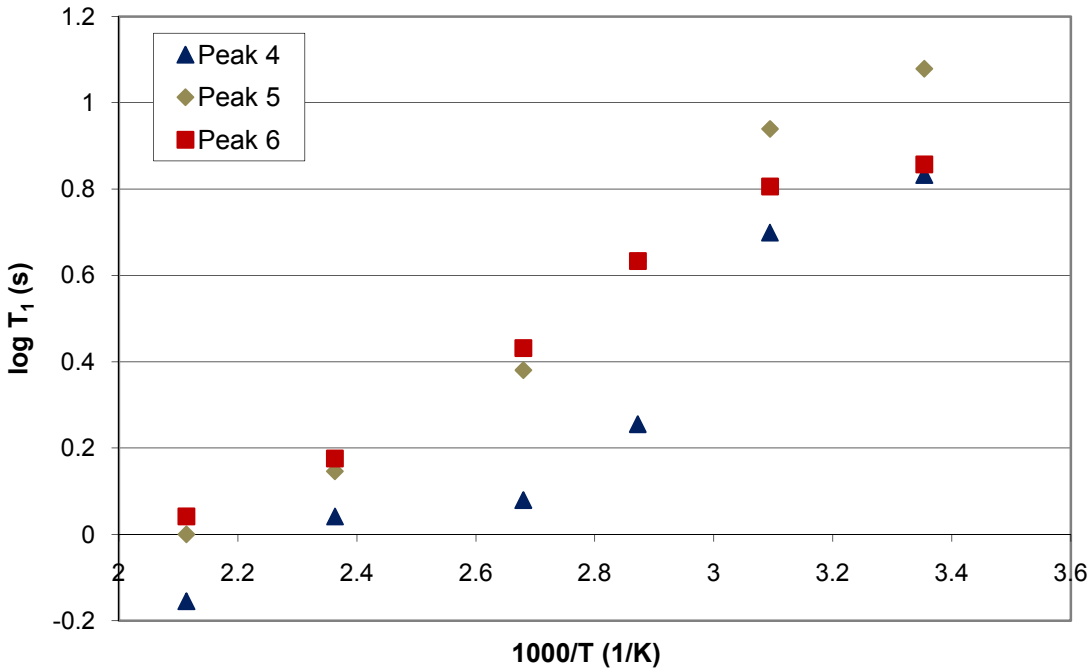

Figure 6.5. Log T_1 time vs. 1/T plot for peaks 4,5, and 6 of 33DDS/DGEBA.

The behavior of peaks 4, 5, and 6 is approximately linear from 25 to 200°C in 33DDS/DGEBA, indicating a single mode of motion, i.e., Arrhenius behavior. The nonlinearity of peak 4 at 75°C and 100°C is not understood at this time. This anomaly may be due to experimental error.

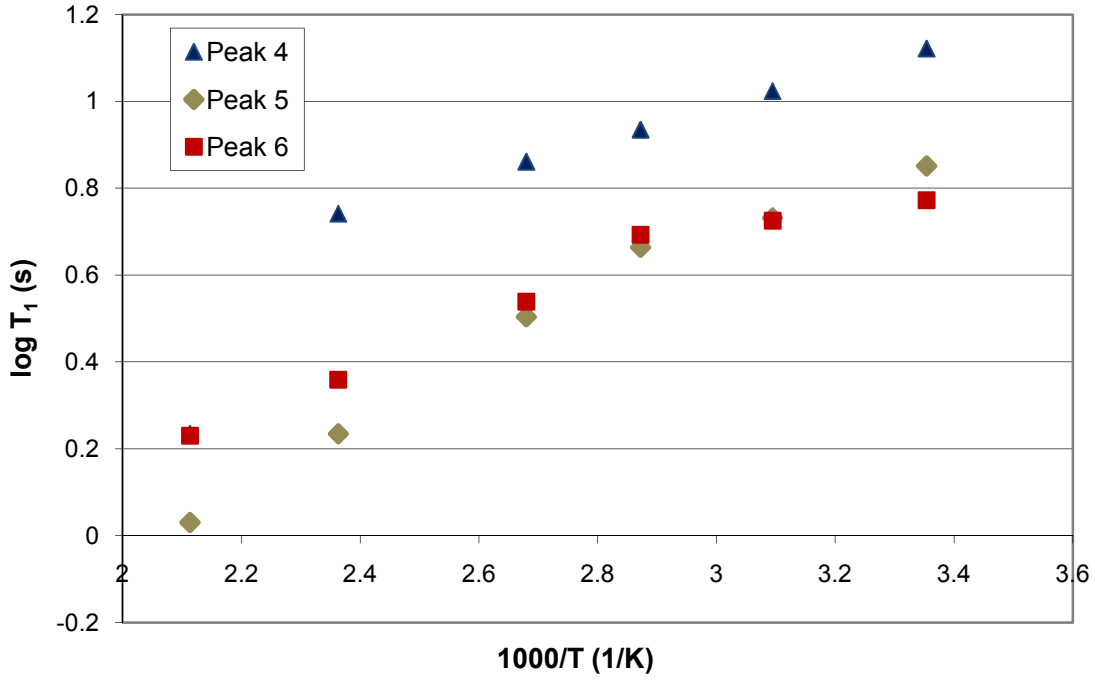

Figure 6.6. Log T_1 time vs. 1/T plot for peaks 4,5, and 6 of 44DDS/DGEBA.

In the 44DDS/DGEBA sample, linearity of the data points indicates the motions follow Arrhenius behavior. Additionally, peak 4 shows a sharp drop in slope at 150°C, around the same temperature as a slope change in the deuterium log T_1 time vs. 1/T plot for the epoxy phenyl rings in that sample is observed. Peak 5 shows the change in T_1 at a lower temperature because the carbons contributing are close to amine and ether linkages, which provide a greater deal of ring flexibility than the sulfone.

Conclusions

Carbon CP/MAS T_1 experiments were largely inconclusive due to broad peaks, resonances shifting in the 33DDS vs. 44DDS samples, and multiple modes of relaxation which contribute to T_1 behavior, including dipolar effects and chemical shift anisotropy. However, some interesting information could still be gleaned. Quaternary aromatic sites, peaks 1 and 3, exhibited small changes in T_1 values with increasing temperature due to their location on the axis of symmetry. At this location, even when phenyl rings are moving, these atoms are remaining in the same place. Peaks 4, 5, and 6 display generally Arrhenius behavior in the log T_1 time vs. 1/T plots. Peak 4 in 44DDS/DGEBA shows a discontinuity in Arrhenius behavior at 150°C, approximately the same temperature this same phenomenon is seen in the ^{2}H NMR log T_1 time vs. 1/T plot. The proximity of aromatic carbons to the sulfone group appears to increase spin-lattice relaxation times of the carbon sites. This evidence supports the hypothesis proposed in Chapter IV that the sulfone limits phenyl ring mobility. Future work should include multi-component fitting to separate carbon sites resonating in the same peaks and to determine if multiple modes of relaxation can be observed.

References

1. Schaefer, J.; Stejskal, E.O.; Buchdahl, R. *Macromolecules,* **1977**, 10, 384-405.

2. Dixon, W.T. *The Journal of Chemical Physics,* **1982**, 77 1800.

3. Harris, R.K.; Yeung, R.R.; Johncock, P.; Jones, D. *Polymer,* **1996**, 37, 721-727.

CHAPTER VII

CHAIN DYNAMICS OF EPOXY-BASED COMPOSITES AS INVESTIGATED BY BROADBAND DIELECTRIC SPECTROSCOPY

Introduction

Polymer networks based DGEBA cured by the simple aromatic amines 33DDS and 44DDS were considered good model systems for studying epoxy networks since investigation of the chemistry of reactions and side reactions had been carefully established, structural models of networks in the rubbery state were produced, and polymers showed a high level of mechanical properties in the glassy state.[1] These properties facilitate understanding important aspects of structural-properties relationship of the polymers when compared to more complex epoxy systems.[1]

Generally, many aspects of glassy network cannot be understood without considering the chemistry of their formation, degree of crosslinking and behavior in the rubbery state. Crosslink density has a significant effect on behaviors of a network. In general, a higher density of crosslinks, which means a "tighter" network, results in a higher modulus of a material.[2] The crosslink density of a network is dependent upon the molecular weight between crosslinks and the extent of reaction as a higher conversion results in higher crosslink density. Full conversion of functional groups in an epoxy network is usually unattainable due to network vitrification, and the final structure is a combination of a majority of tertiary amines and a small amount of secondary amines. Meanwhile, the molecular weight of the monomers determines the molecular weight between crosslinks. At a theoretically full conversion, the crosslink density of a network is inversely proportional to the average molecular weight of segments between junctions,

M_c. Longer segments, due to less constraint of junctions, display more mobility and flexibility, which leads to a network with a smaller modulus.[3]

The work here investigates the dynamics of the glass transitions (T_g) and secondary relaxations of epoxy networks formed from the reaction of diglycidyl ether of bisphenol A (DGEBA) with the 4,4′-diaminodiphenyl sulfone (44DDS) vs. 3,3′-diaminodiphenyl sulfone (33DDS) curatives. Although secondary and T_g related motions for 44DDS/DGEBA networks were studied in details by other researchers,[1,4-12] to the best of our knowledge, no reports mention the use of 33DDS/DGEBA networks.

Here, modern broadband dielectric spectroscopy (DES) was used to interrogate the molecular dynamics of these resin networks. Recently, Mauritz et al. used DES to characterize chemical degradation in polylactides[13] and Nafion ionomers[14] as well as to accurately define and confirm the true glass transition temperature of Nafion membranes.[15]

Dielectric spectroscopy is a powerful tool because information over a broad frequency range is attainable,[16] so motional processes that occur over broad time and distance scales can be investigated vs. temperature. In addition to polymer relaxations, significant differences in dielectric permittivity and/or electrical conductivity across phase boundaries can cause fluctuating interfacial polarization that manifest at low frequency (f) on loss permittivity (ε'') vs. f plots.[17]

Dielectric spectroscopy deals with the interaction of an applied alternating electric field with the orientable dipoles on a polymer that account for overall polarizability. Conformational fluctuations on different distance scales affect dipole reorientation and the long range chain segmental mobility that is affected at the glass transition is a

cooperative process. The dielectric spectrum of an amorphous polymer generally shows multiple relaxations at different temperatures, where each relaxation is indicated by a peak in loss permittivity ε'' and an associated step decrease in storage permittivity (ε') versus frequency at a fixed temperature.

Objective

The principle goal of this work is to study the dynamics of the secondary (sub-T_g) and glass transition relaxations of 33DDS/DGEBA and 44DDS/DGEBA using broadband dielectric spectroscopy (DES). To determine the polymeric chemical structures responsible for sub-T_g relaxations, relationships between dielectric relaxations and molecular motions observed with deuterium NMR spectroscopy can be established. Firstly, the temperature at which a motion of a certain frequency occurs in DES can be related to a calculated temperature from deuterium NMR Arrhenius plots. Next, correlation times of the dielectric relaxations and motions observed with ^{2}H NMR can be compared. Finally, if sub-T_g dielectric relaxations are small scale motions, Arrhenius plots of the LOG correlation time versus inverse temperature can be created and activation energy can be calculated. This activation energy can be compared to activation energies determined by ^{2}H NMR lineshape simulations. In this work, the temperatures, correlation times, and activation energies of sub-T_g relaxations are determined via dielectric spectroscopy.

Materials

Preparation of Cured Epoxy Resins

All reagents were used without further purification. 33DDS and 44DDS were purchased from Aldrich. EPON 825, DGEBA resin, was donated by Hexion. 33DDS

and 44DDS were solubilized in DGEBA at 110°C under vacuum, and the resins were cured at 125°C for 5hrs and 225°C for 2hrs (Figure 7.1).

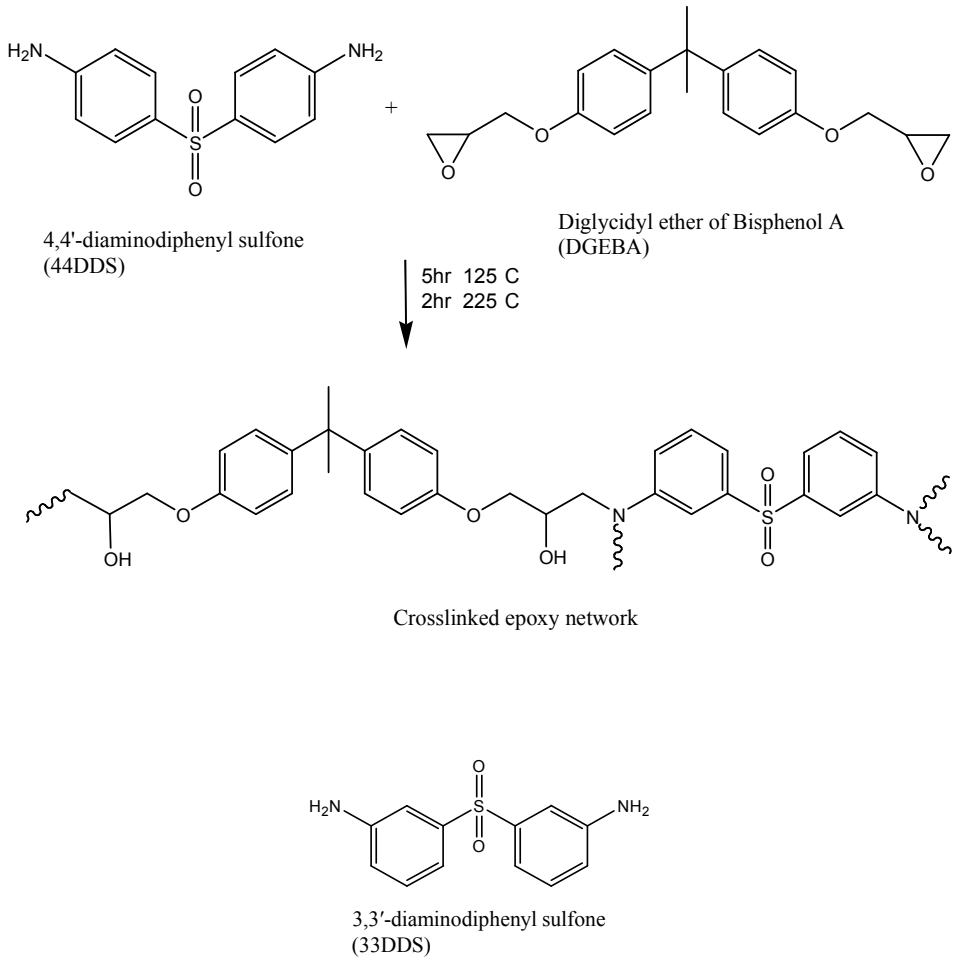

Figure 7.1. Reaction between DGEBA and 44DDS. 33DDS is reacted in the same manner.

Methods

Dynamic Mechanical Analysis (DMA)

The dynamic storage modulus (E′) and tan δ = E″/E′ vs. temperature (T) curves for samples were generated using a DMA Thermal Analysis Q800 instrument. All samples were run in tensile mode with a frequency of 1 Hz and oscillation amplitude of

20 μm. The experiments were performed over the temperature range of -120 to 300°C at a heating rate of 2°C/min.

Broadband Dielectric Spectroscopy (DES) Measurements

Dielectric spectra were collected isothermally using a Novocontrol GmbH Concept 80 Broadband Dielectric Spectrometer over the frequency range 0.1 Hz - 3 MHz and temperature range of -80 - +300°C. Temperature stability was controlled to within ±0.2° C. Resin sample was cured between two stainless steel discs with the lower one of 4 cm diameter and the upper one of 2 cm diameter. Thickness of both discs was determined before and after enclosure of the resin to determine the thickness of each sample. Those discs with samples were preconditioned in a humidity chamber with controlled 19% RH for one week before performing DES experiments. Electrodes with sample were then transferred to the instrument for data collection.

Results and Discussion

Dynamic Mechanical Analysis (DMA)

Figure 7.2a shows the dynamic loss tangent (tan δ) vs. temperature for 33DDS/DGEBA and 44DDS/DGEBA. Molecular motions in networks are shown by three distinct peaks, with different intensities and degrees of broadening. The first transition is broad with a peak maximum at ≈ -50°C for both samples and will be called the γ-transition. The second transition is a weak one with peak maxima at ≈ 40°C and will be called β-transition. The third transition represents the glass transition temperatures (T_g) of the networks and will be called α-transition.

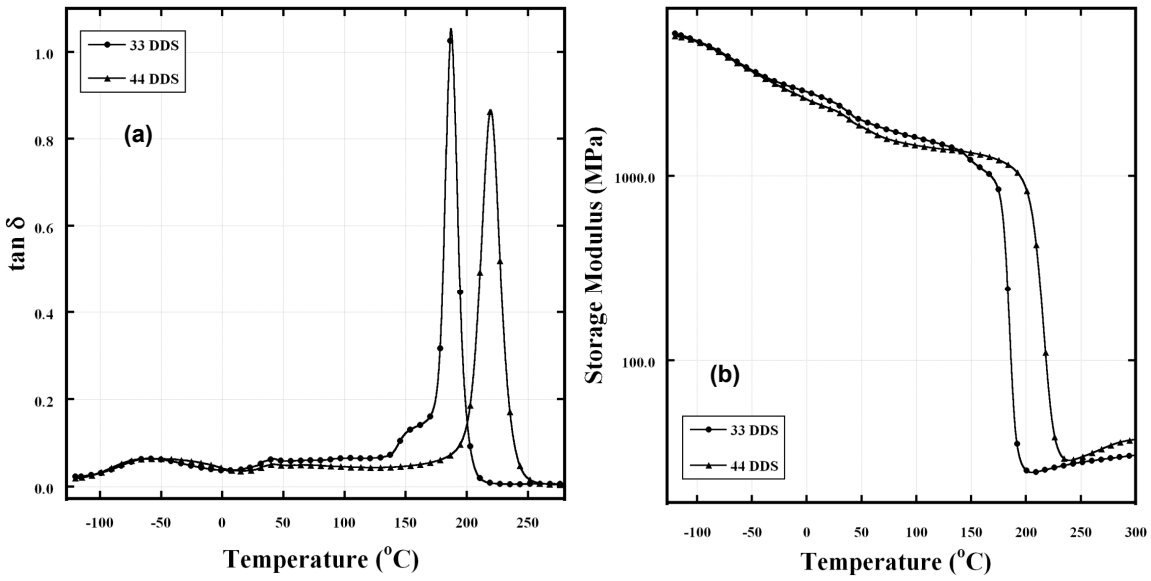

Figure 7.2. DMA curves showing tan δ (a) and storage modulus (b) vs. temperature at 1 Hz for 33DDS/DGEBA and 44DDS/DGEBA.

Assignments of the γ and β-transitions will be discussed in detail in the next section. The T_g peak is clearly higher for the 44DDS/DGEBA sample comparing to the 33DDS/DGEBA by about 50°C. Interestingly, as shown in Figure 7.2a, the 33DDS/DGEBA network shows a shoulder at the lower temperature part of the tan δ curve for the T_g. Keenan et al. reported a split in the tan δ vs. temperature curve for networks formed by curing tetraglycidyl 4,4′-diaminodiphenyl methane epoxy with small amounts of 4,4′-diaminodiphenyl sulfone.[11] This split was thought to result from additional cure in the sample occurring during the DMA run. This additional cure was evidenced by an increase in storage modulus vs. temperature curves around the same range of the glass transition splitting. The storage modulus vs. temperature curve for sample shown in Figure 7.2b, however, did not show any increase around the temperature of the T_g shoulder but only a two stage drop. This would reflect inhomogeneous

crosslinking or differences in the molecular weight of chains between crosslinks (M_c) rather than additional cure during the DMA run.

Analysis of the Dielectric Spectra

Secondary relaxations in cured networks. Figure 7.3 shows change in tan δ (ε″/ε′) and the dielectric loss permittivity (ε″) vs. temperature at different frequencies for 33DDS/DGEBA and 44DDS/DGEBA. The tan δ vs. temperature curves show two distinct transitions. As depicted in the DMA curves in Figure 7.2a; two secondary relaxations, named γ- and β-peaks plus the glass transition were observed in the dielectric tan δ vs. temperature curves. A detailed explanation of the assignment of these peaks and the effect of variation in the crosslink structure on the motions associated with them will be given in this section.

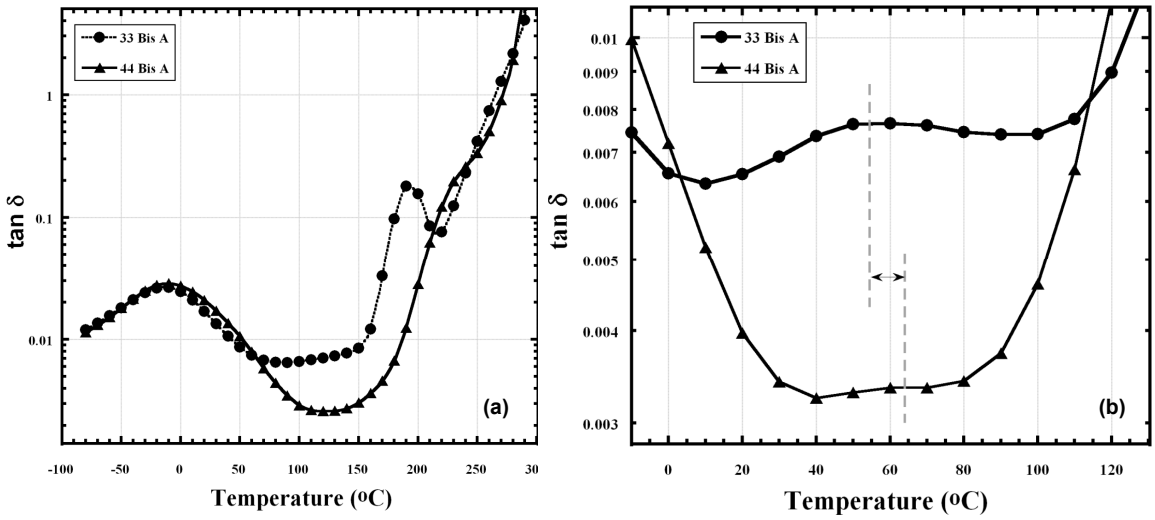

Figure 7.3. Dielectric tan δ vs. temperature at (a) 1 kHz and (b) 1 Hz, to show the β relaxation, for 33DDS/DGEBA and 44DDS/DGEBA. Dashed lines in (b) are used to show the β relaxation peak maxima.

The γ-Peak

The γ-transition peak was observed in cured epoxy networks having similar structures to those reported in previous work.[4-12] Johari and Mangion assigned this peak to be due to local motions of dipoles that remain as the unreacted components during the curing of the thermosets. The dipoles may be parts of the DGEBA polymer chain including the unreacted epoxy groups and/or free amino-diphenyl or primary amine groups. Ochi et al. proposed the mechanically observed γ transition to be due to the local motion of polymer segments consists of at least four carbon atoms.[6]

For the epoxy samples reported here, well-resolved γ-transition peaks for both the 33DDS and 44DDS crosslinkers are clearly shown. To characterize these transitions to the type of molecular motion and the chemical moieties responsible for this motion, static deuterium NMR (^{2}H) experiments were conducted at different temperatures on selectively deuterated phenyl rings in the polymer. The necessary information to relate ^{2}H NMR spectroscopy to DES includes the correlation time, from which Arrhenius plots can be created and activation energies and temperatures of 1Hz frequency motions can be calculated. This work involves complex simulated lineshape studies and is currently underway.

The same relative intensities of tan δ curves for both 33DDS/DGEBA and 44DDS/DGEBA could indicate that the flexible fragments of these polymers even in the glassy state have an equilibrium conformational structure. Thus, chains might exist in the form of an unperturbed coil in a densely crosslinked epoxy-aromatic amine glasses.[19,20] Therefore, high packing density is determined by the aromatic fragments of the polymer and the flexible aliphatic chains, created during the glycidyl rings opening during the cure

process, helping the network realize the highest possible packing density.[1] To extract relaxation parameters of the γ-transition peaks, the Havriliak-Negami (HN) equation[21-23] was fitted to experimental data (Equation 7.1):

$$\varepsilon^*(\omega) = \varepsilon' - i\varepsilon'' = -i\left(\frac{\sigma_{dc}}{\varepsilon_0 \omega}\right)^N + \sum_{k=1}^{3}\left[\frac{\Delta\varepsilon_k}{\left(1+(i\omega\tau_{HN})^{\alpha_k}\right)^{\beta_k}} + \varepsilon_{\infty k}\right]$$

where: ε_0 = vacuum permittivity and $\omega = 2\pi f$

The three relaxation terms in the sum and the term on the left account for D.C. conductivity. For each relaxation term k, $\Delta\varepsilon_k = (\varepsilon_R - \varepsilon_\infty)_k$, the dielectric strength, is the difference between ε' at very low and very high frequencies, respectively. In the first term σ_{dc} is the D.C. conductivity and the exponent N characterizes conduction in terms of the nature of charge hopping pathways and mobility constraints. α and β characterize the breadth and degree of asymmetry, respectively, of ε″ vs. ω peaks. $\tau_{HN,}$ is the Havriliak-Negami (HN) relaxation time.

Equation 7.1. Havriliak-Negami expression.

The Havriliak-Negami (HN) relaxation (τ_{HN}) is related to the actual relaxation time at loss peak maximum at f_{max}, i.e., τ_{max}, by Equation 7.2: [16, p 64]

$$\tau_{\max} = \tau_{HN}\left[\frac{\sin\left(\frac{\pi\alpha\beta}{2(\beta+1)}\right)}{\sin\left(\frac{\pi\alpha}{2(\beta+1)}\right)}\right]^{\frac{1}{\alpha}}$$

Equation 7.2. Relation of τ_{HN} to τ_{max}.

The D.C. term accounts for inherent or unintended charge (impurity) migration that is often subtracted to uncover loss peaks or make them more distinct. The Havriliak-Negami (HN) equation was fitted to the data in Figure 7.4 and the relaxation time at peak maximum (τ_{max}) extracted at each temperature. As shown in Figure 7.4, the frequency at loss permittivity (ε'') peak maximum, f_{max}, shifts to higher values with increasing temperature in the usual fashion reflecting faster motions and smaller relaxation times, relaxation time $\tau = 1/(2\pi f_{max})$.

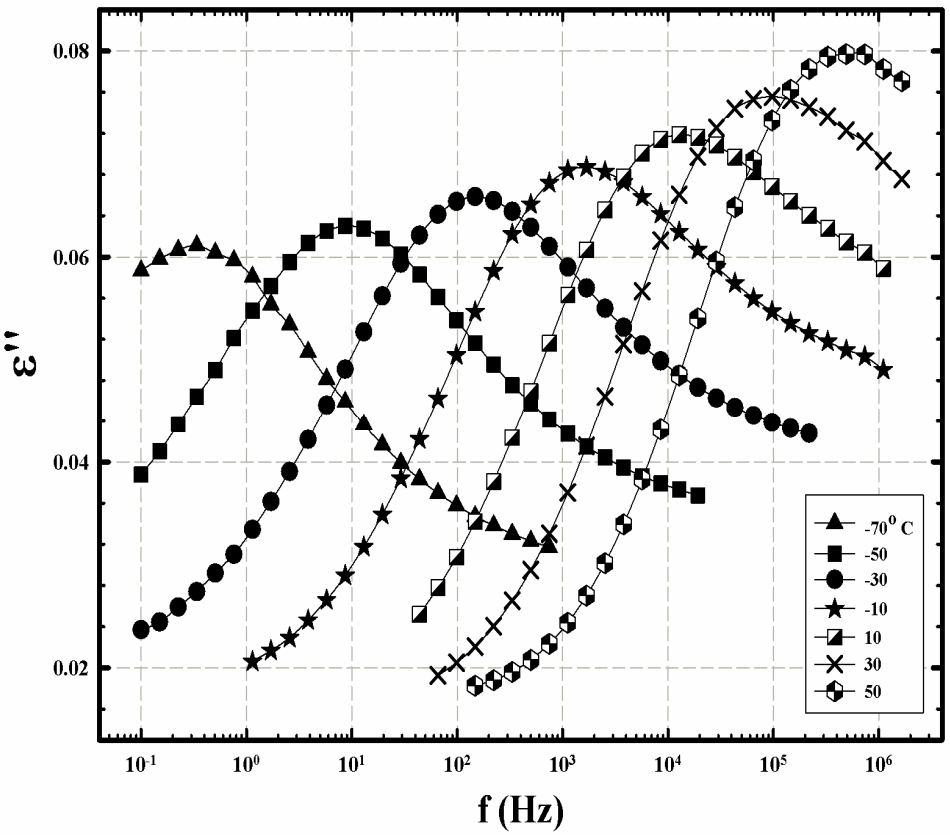

Figure 7.4. ε″ vs. frequency for different temperatures for 33DDS/DGEBA.

The τ_{max} was then plotted against temperature (T) to show Arrhenius behavior for the γ-transition (Equation 7.3):

$$\tau(T) = \tau_0 \exp\left(\frac{E_a}{RT}\right)$$

where: τ_0 is the pre-exponential factor, R is the universal gas constant, and E_a is the activation energy for this transition.

Equation 7.3. Arrhenius expression for calculation activation energy.

The analysis of this local motion shows that it has an Arrhenius type behavior with the same value of activation energy, 24.5 kJ/mol, for both 33DDS/DGEBA and 44DDS/DGEBA samples, as depicted in Figure 7.5. This fact strongly supports the idea that the internal rotation barriers in the considered fragments local motions are not sensitive to the presence of crosslinks in the polymer structure.

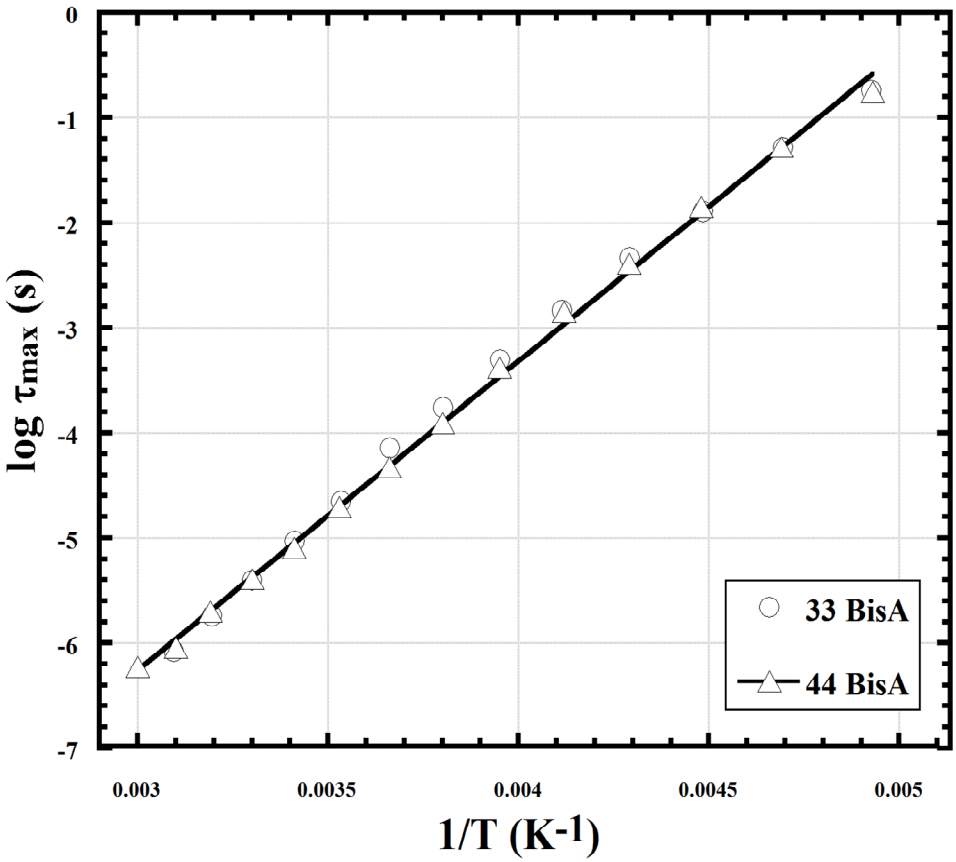

Figure 7.5. Arrhenius plots for 33DDS/DGEBA and 44DDS/DGEBA.

The β-Peak

The β relaxation peak was assigned to the local motion of the dipolar groups which are created during the crosslinking reactions as previously reported.[4-9] Those

groups include the hydroxyl ether and the secondary or tertiary amine groups. β relaxation peaks for the 33DDS/DGEBA and 44DDS/DGEBA networks are shown in Figure 7.3b. The comparison of tan δ vs. temperature curves had to be made at 1 Hz instead of at 1 kHz, the frequency used to clearly show the trends of the α and γ relaxations. Perhaps this is related the nature of the dynamics of each of the three motions.

Two features can be clearly observed for the β relaxation peaks in Figure 7.3b, peak position and resolution. β relaxation peak strength, or resolution, is related to the number of active molecules or dipoles contributing to the relaxation. Therefore, the strength of this relaxation is affected by the nature of molecular packing in glassy state as well as nature of disorder in its rigid matrix.[9,12] Johari and Mangion reported that the rate of the β relaxation (its peak position) is less affected by the growth of a polymer chain or of a polymer network during first step of curing than is the rate of the α relaxation; however, the strength of the β relaxation is more affected. As a consequence, the β relaxation becomes more prominent as the number of crosslinks and chain length increases during the curing process.[9,12] This conclusion suggests that 33DDS/DGEBA networks have higher number of crosslinks; consequently higher number of hydroxyl groups formed, and increased chain length compared to 44DDS/DGEBA.

Although it is difficult to compare both peak positions because of peak broadening and lower resolution in case of the 44DDS/DGEBA networks as shown in Figure 7.3b, peak position seems to shifts to *somewhat* lower temperature for 33DDS/DGEBA comparing to 44DDS/DGEBA networks. The β relaxation peak position is more sensitive to difference in distribution of local volume within the network

or the local space surrounding the mobile dipolar segments. Thus, different distributions of local volume within the network formed from 33DDS/DGEBA compared to 44DDS/DGEBA are apparent.

Glass Transition Dynamics in Cured Networks

The glass transition or α relaxation is associated with long range chain segmental mobility. T_g is closely related to the structure and crosslink density of the cured epoxy resins. The frequency at loss permittivity (ε″) peak maximum (f_{max}) for the 33DDS/DGEBA sample shifts to higher values with increasing temperature in the usual non-Arrhenius fashion, as shown in Figure 7.6.

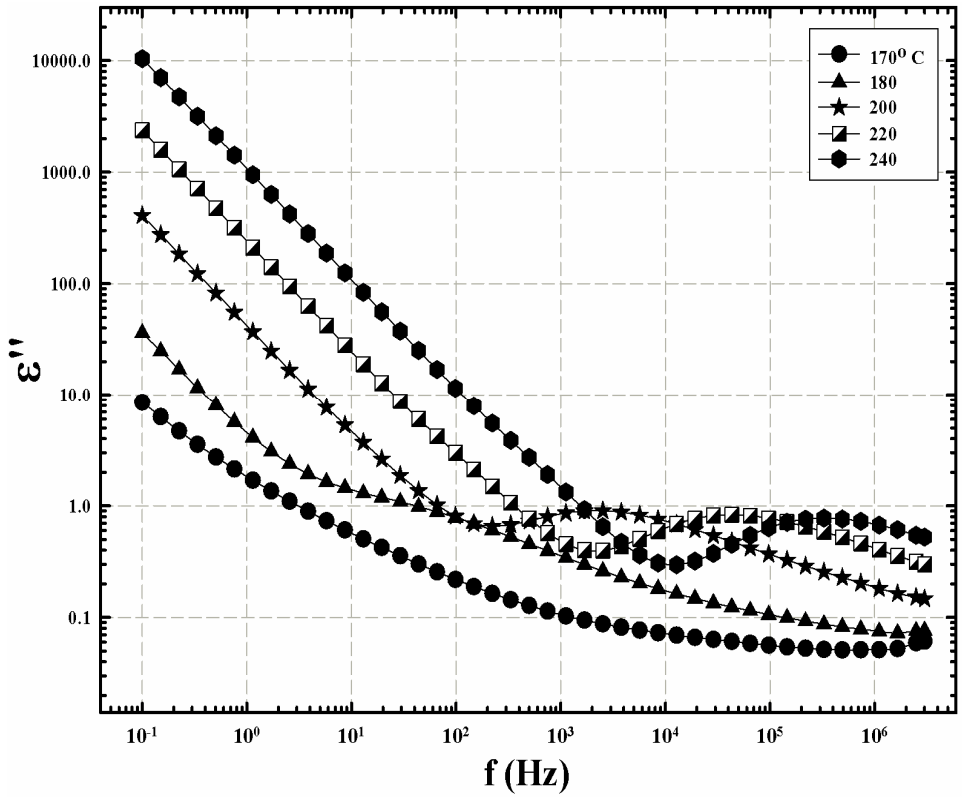

Figure 7.6. ε″ vs. frequency at different temperatures for 33DDS/DGEBA showing the glass transition related peak (α-transition).

The upswing in ε'' at low f region of Figure 7.6 accounts for the presence of electrode polarization and D.C. conduction processes effects. The electrode polarization effect arises in resins from the ionic conductivity resulting from either intrinsic ions or residual impurity ions. When those ions become relatively mobile, due to larger chain mobility at the onset of the T_g, they have enough time to accumulate at the electrode-resin interface during one-half cycle of applied electric field at low frequencies.[24-26] The accumulated ion layers produce charged layers at both electrodes. The ion layers can have much greater charge per unit area than those produced from the actual material dipole orientation. Therefore, the measured sample capacitance becomes much greater than that produced by material dipoles and thus the dielectric storage permittivity (ε') becomes much greater than the actual bulk permittivity. A large increase in ε' values starting at 220°C is clearly seen in Figure 7.7 for the 33DDS/DGEBA sample. This increase is also observed for 44DDS/DGEBA.

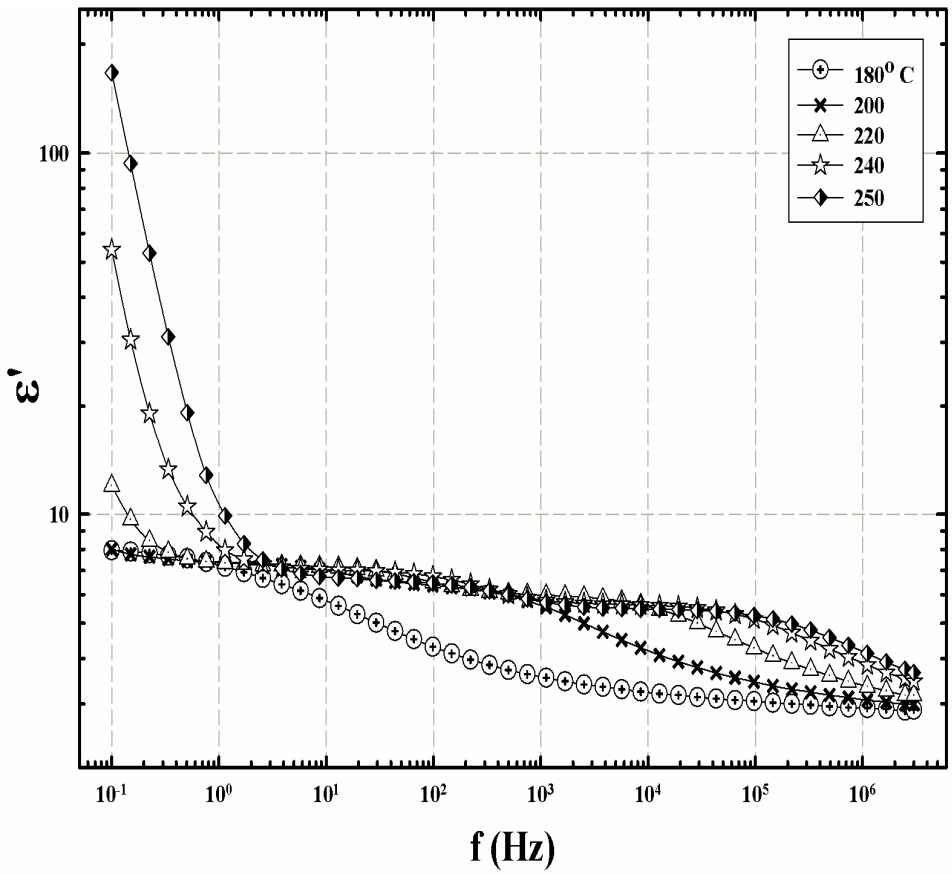

Figure 7.7. ε′ vs. frequency at different temperatures for 33DDS/DGEBA showing the electrode polarization effects at high temperatures.

The second effect accounting for the upswing in ε'' at the low f region is the D.C. conduction effect which is expressed by the first term of the right side of the HN equation (Equation 7.1). D.C. conductivity in this context involves the instrumental sampling of charge hopping pathways that become progressively longer at increasingly lower frequencies. As the experimental time scale, or half period of oscillation = $(2f)^{-1}$, increases, charge carriers, likely intrinsic ions or residual impurity ions in this case, can execute more elementary hops before the applied field reverses. In this frequency region

for $T > T_g$, LOG ε'' vs. LOG f plots are linear such that the slopes are slightly less than 1.0.[27]

Figure 7.8 shows ε'' vs. f at 250°C for 44DDS/DGEBA and 33DDS/DGEBA, showing the glass transition related peak. Dashed lines and the arrow are used to show the shift in relaxation peaks maxima. The α relaxation peak maxima, although very broad, for the 44DDS/DGEBA sample shifts downward compared to 33DDS/DGEBA. This indicates a slower chain motion in the case of 44DDS/DGEBA, thus higher relaxation time (relaxation time $\tau = 1/2\pi f_{max}$). This result confirms the DMA results shown earlier in which the T_g is almost 50°C higher for 44DDS/DGEBA than 33DDS/DGEBA. Also, this same conclusion can be seen when comparing the dielectrically measured tan δ at 1 kHz shown in Figure 7.3a.

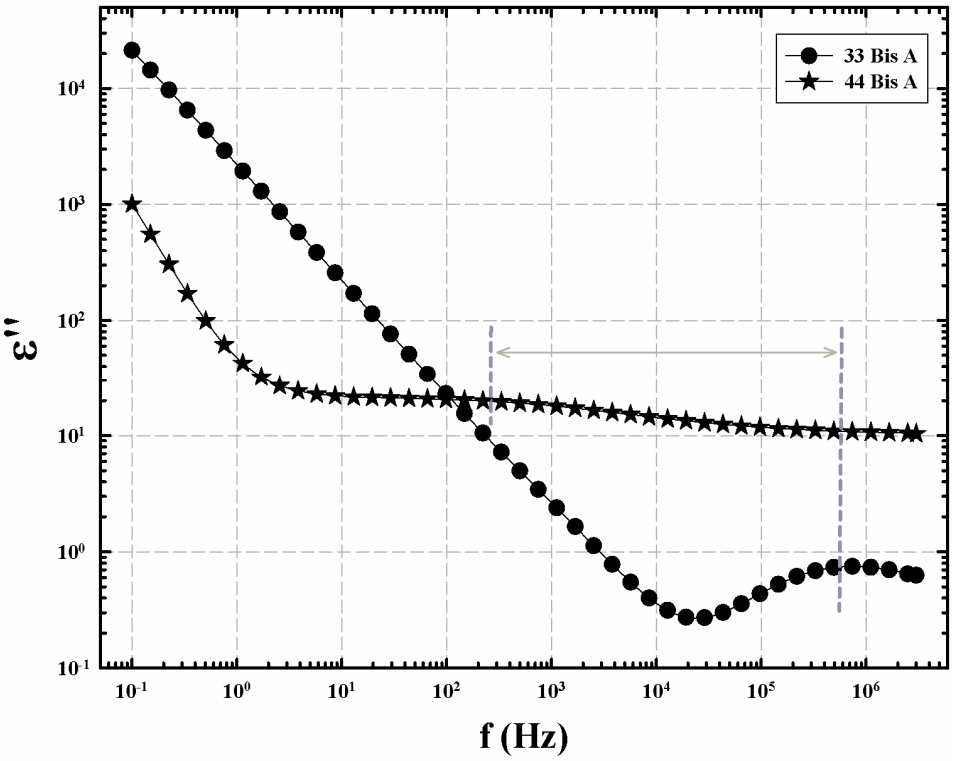

Figure 7.8. Comparison of ε″ vs. frequency curves at 250°C for 33DDS/DGEBA and 44DDS/DGEBA, showing the glass transition related peak (α-transition). Dashed lines and the arrow to show the shift in relaxation maxima.

The T_g related relaxation spectra at different temperatures for the 33DDS/DGEBA and 44DDS/DGEBA samples were fitted to the HN equation. Then, the D.C. conductivity term was subtracted for the purpose of uncovering loss peaks corresponding to macromolecular motions. D.C. - subtracted loss spectra at 250°C for 33DDS/DGEBA and 44DDS/DGEBA are shown in Figure 7.9. Subtraction of the D.C. contribution causes the peaks to be more distinct and their shifts to higher or lower frequencies (shorter relaxation times) are more clearly seen. The nature of the T_g peak for the 33DDS/DGEBA network is bimodal, while the 44DDS/DGEBA glass transition appears as a very broad peak.

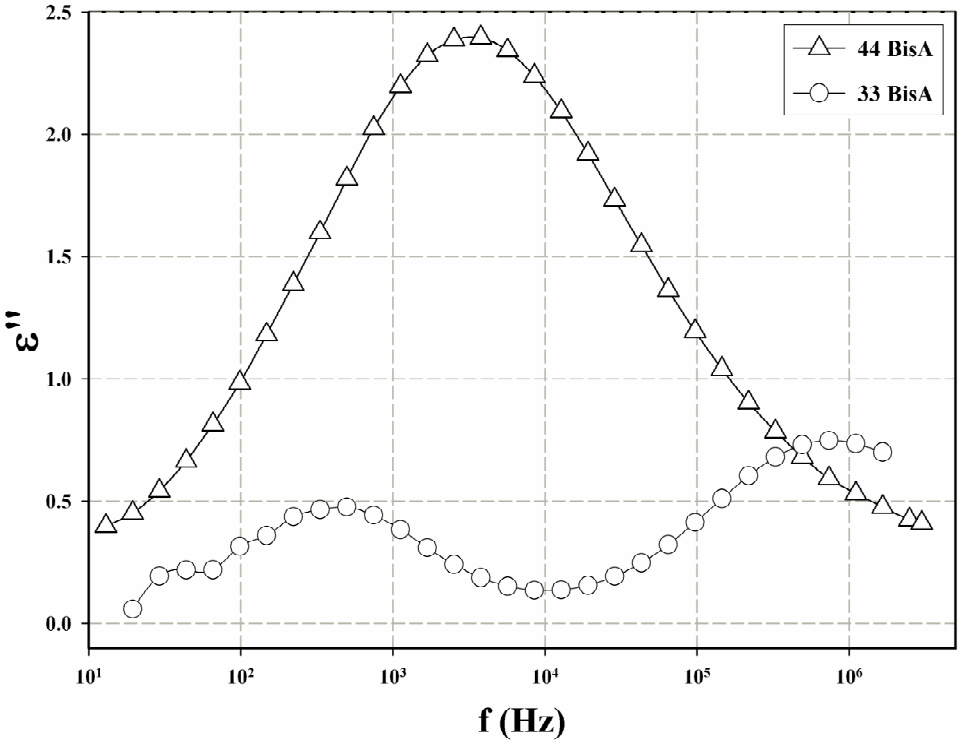

Figure 7.9. Comparison of ε″ vs. frequency curves at 250°C for 33DDS/DGEBA and 44DDS/DGEBA. The dc-conductivity term in eq. 1 is subtracted to resolve the T_g related relaxation peak.

The peak maximum for the 44DDS/DGEBA sample is shifted to lower frequency, indicating slower chain motion, when compared to one of the two peaks that appear for 33DDS/DGEBA. To further understand the nature of this bimodal T_g peak of the 33DDS/DGEBA sample, D.C. conductivity subtracted spectra at different temperatures are shown in Figure 7.10. T_g related transition shows two peaks, the first peak has its onset at 180°C, and peak maximum shifts to higher frequencies as temperature increases. The second peak has an onset at about 200°C and tracks with the aforementioned peak in moving to higher frequencies as temperature is increased. This behavior typically reflects an inhomogeneous network structure or differences in molecular weight of chains between crosslinks.

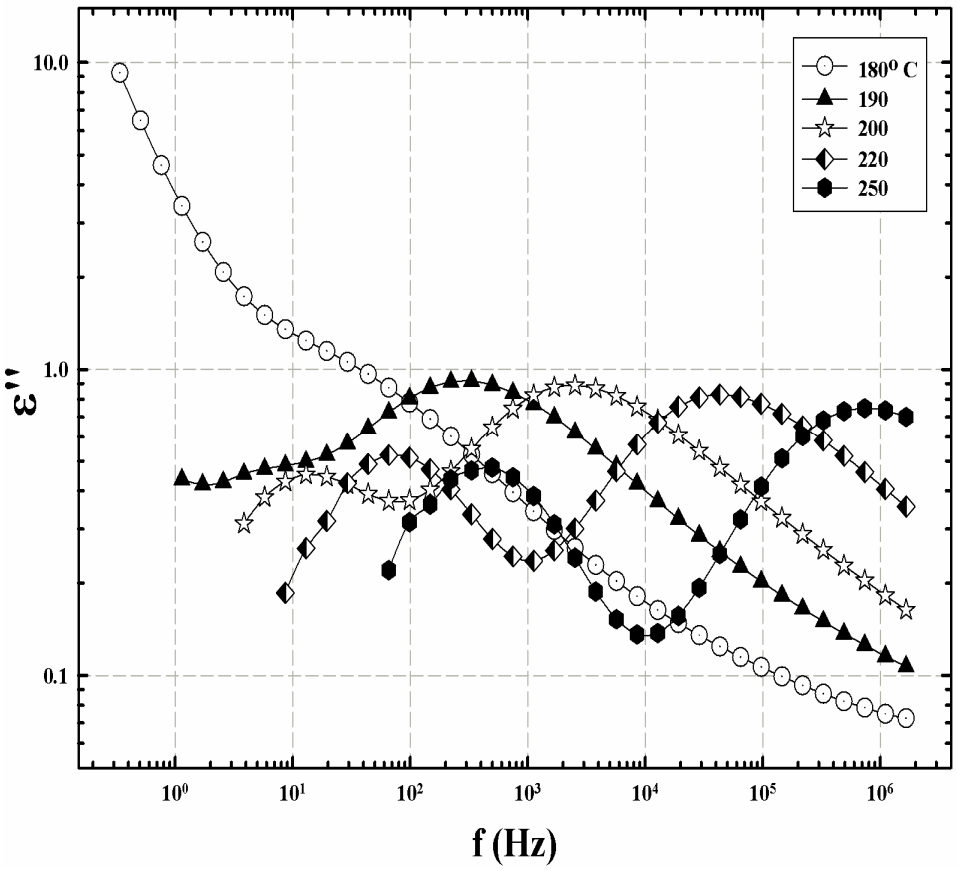

Figure 7.10. D.C. - conductivity subtracted spectra at different temperatures of T_g related relaxation peak for the 33DDS/DGEBA.

The HN equation was fitted to the data for both networks and the relaxation time at peak maximum extracted. The Vogel-Fulcher-Tammann-Hesse (VFTH) equation was then fitted to τ_{max} vs. temperature (T) data[28] as shown in Equation 7.4:

$$\tau(T) = \tau_0 \exp\left(\frac{E_a}{k_B(T - T_V)}\right)$$

where: k_B is the Boltzmann constant, τ_0 is a hypothetical relaxation time at infinite temperature. E_a, while having units of energy, is a ubiquitous quantity that it is not associated with an activated process in the usual sense. T_V, the Vogel temperature, is the temperature at which chain segments become frozen in a hypothetical situation in which a polymer is cooled quasi-statically from the rubbery state.

Equation 7.4. Vogel-Fulcher-Tammann-Hesse (VFTH) expression.

Figure 7.11 shows VFTH plots for networks of the two isomers, but each of the two peaks observed for the 33DDS/DGEBA sample, as shown in Figure 7.10, were fitted separately. The plots are quite nonlinear which implies that this is not a relaxation that can be described in terms of activated rate theory but is related to glass formation. The curve for the mean peak of the T_g of 33DDS/DGEBA is significantly vertically down-shifted relative to the 44DDS/DGEBA, indicating that chain motions become faster, and T_g is decreased in the 33DDS/DGEBA. It is interesting to note that the second T_g related peak for the 33DDS/DGEBA moves a little faster than the 44DDS/DGEBA peak until 230°C when they cross. This behavior is not clear at this point.

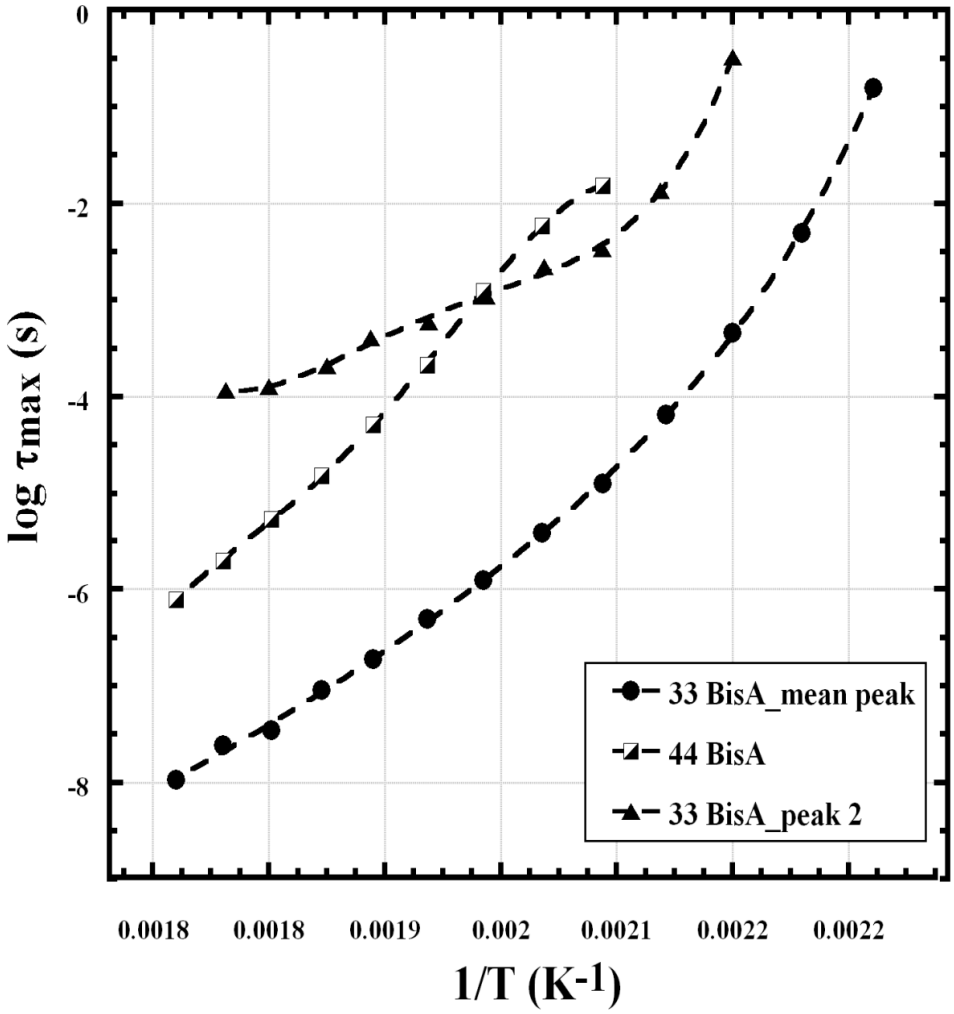

Figure 7.11. VFTH plots for the high temperature glass transition peaks of 33DDS/DGEBA and 44DDS/DGEBA.

Vogel temperature (T_V) values were extracted from the curve-fitted VFTH data and were found to be 349 and 370K for the 44DDS/DGEBA and 33DDS/DGEBA (mean peak) samples, respectively. Thus, T_V increases for the 33DDS/DGEBA relative to the 44DDS/DGEBA, which suggests more restricted chain mobility for the 33DDS/DGEBA sample. Also, increased T_V suggests lower free volume per mass for the 33DDS/DGEBA sample, or more efficient packing of the local space surrounding the mobile dipolar segments. This result confirms free volume work conducted in the Nazarenko research

group, clearly showing 33DDS-epoxies to possess lower free volume than 44DDS-epoxies.[29]

While this appears contradictory to the observed lower T_g of the 33DDS/DGEBA samples, this phenomenon can be explained by considering conformational entropy. The higher degree of chain packing in 33DDS is due to the conformational freedom given to 33DDS/DGEBA by the meta-substituted amine, which gives chains the flexibility to rearrange into better packed network. Interestingly, the increased conformational entropy of 33DDS which creates better chain packing and an increased T_v is the same property which lowers the T_g by allowing chains the flexibility to access more conformations at a lower temperature as the sample cools. Hence, 33DDS/DGEBA requires a greater amount of cooling to eliminate the configuration entropy than 44DDS/DGEBA and therefore has a lower T_g.

In the Havriliak-Negami equation, α and β determine the distribution of relaxation times, $G(\tau)$ such that α characterizes the distribution breadth and β, by its deviation from unity, characterizes the degree of curve asymmetry [22]. $G(\tau)$ is given by Equation 7.5:

$$G(\tau) = \frac{\left(\frac{\tau}{\tau_{0i}}\right)^{\beta_i \alpha_i} \sin(\beta_i \Theta_i)}{\pi\tau\left(\left(\frac{\tau}{\tau_{0i}}\right)^{2\alpha_i} + 2\left(\frac{\tau}{\tau_{0i}}\right)^{\alpha_i} \cos(\pi\alpha_i) + 1\right)^{\frac{\beta_i}{2}}}$$

where: $\Theta_i = \arctan\left(\frac{\sin(\pi\alpha_1)}{\left(\frac{\tau}{\tau_{0i}}\right)^{\alpha_i} + \cos(\pi\alpha_i)}\right)$

The angular quantity Θ_i has units in radians such that ($0 \leq \Theta_i \leq \pi$).

Equation 7.5. Distribution of relaxation times from HN equation.

G(τ) plots at 250°C for 33DDS/DGEBA vs. 44DDS/DGEBA are shown in Figure 7.12. A bimodal curve is clearly observed for the 33DDS/DGEBA sample, while the 44DDS/DGEBA shows a much broader distribution of relaxation times. This could indicate broad distribution of molecular weight between crosslinks for the 44DDS/DGEBA while the 33DDS/DGEBA sample has an inhomogeneous network structure as discussed earlier. The shift in the distribution peak of 44DDS/DGEBA to longer relaxation times as compared to the mean T_g peak of the 33DDS/DGEBA sample, seen on the left side of the *G(τ)* plot of 33DDS/DGEBA, supports the observed higher T_g of 44DDS/DGEBA.

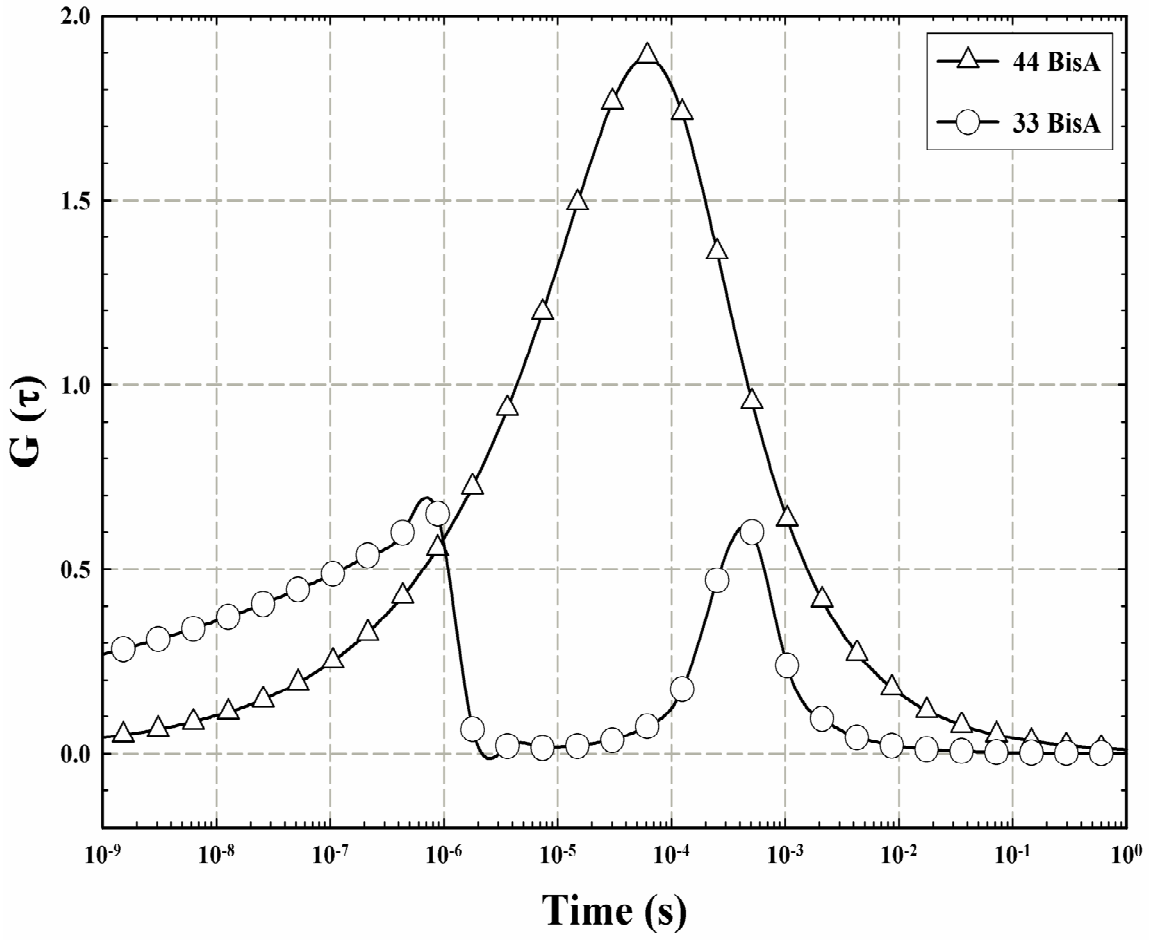

Figure 7.12. Distribution of relaxation times G(τ) plots at 250°C for 33DDS/DGEBA and 44DDS/DGEBA.

Conclusions

In summary, broadband dielectric spectroscopy was used to examine macromolecular motions in epoxy networks formed from diglycidyl ether of bisphenol A and 3,3′ vs. 4,4′- diaminodiphenyl sulfone isomers as crosslinkers. Dynamics of the secondary and glass transition related relaxation of the fully cured networks were analyzed and fitted to the Havriliak-Negami equation. The sub-T_g γ relaxation peak maximum, f_{max}, shifts to higher values with increasing temperature in an Arrhenius

fashion with similar activation energies for the two crosslinker isomers. This result supports the proposed assignment of the γ relaxation to account for the phenyl rings flipping in the main DGEBA chain facilitated by the presence of adjacent flexible ether linkage. 44DDS/DGEBA networks exhibited higher T_g relative 33DDS/DGEBA networks as indicated by both dynamic mechanical analysis and broadband dielectric spectroscopy results.

T_g related relaxations spectra fitted to the Havriliak-Negami equation for networks of both isomers showed evidences for the higher Tg of 44DDS/DGEBA. This was clearly seen in D.C. subtracted ε'' vs. f spectra and the VFTH plots of samples of both isomers.

Vogel temperature showed an increase for the 33DDS/DGEBA network relative 44DDS/DGEBA, suggesting lower free volume per mass or more efficient packing of the local space surrounding the mobile dipolar segments. The distribution of relaxation times, $G(\tau)$, curves showed a bi-modal network structure for the 33DDS/DGEBA, suggesting microstructural heterogeneity in this sample or heterogeneity in its crosslink density.

References

1. Oleinik EF. *Epoxy-aromatic amine networks in the glassy state: structure and properties. In: Dušek K. Advances in Polymer Science: Epoxy Resins and Composites* IV, Vol. 80. Verlag Berlin Heidelberg: Springer, 1986. pp. 49-99.
2. Hiemenz PC, Lodge, TP. *Polymer Chemistry*, 2nd ed. Boca Raton, FL: CRC Press, 2007. p. 404.
3. Tucker SJ, Fu B, Kara S, Heinz S, Wiggins JS. *Composites Part A Appl Sci Manufact,* **2010**, 1441-1446.
4. Shimbo M, Ochi M, Iesako H. *J Polym Sci Part B Polym Phys,* **1984**, 1461-1470.
5. Ochi M, Yoshizumi, M, Shimbo M. *J Polym Sci Part B Polym Phys,* **1987**, 25, 1817-1827.
6. Ochi M, Okazaki, M, Shimbo M. *J Polym Sci Part B Polym Phys,* **1982,** 689-699.
7. Ochi M, Iesako H, Shimbo M. *J Polym Sci Part B Polym Phys,* **1986**, 1271-1282.
8. Ochi M, Shimbo M, Saga M, Takashima, N. *J Polym Sci Part B Polym Phys,* **1986**, 2185-2195.
9. Mangion MBM, Johari GP. *J Polym Sci Part B Polym Phys,* **1990**, 71-83.
10. Mikolajczak G, Cavaille JY, Johari GP. *Polymer* **1987**, 2023-2031.
11. Keenan JD, Seferis JC, Quinlivan JT. *J Appl Polym Sci,* **1979**, 2375-2387.
12. Mangion MBM. PhD Thesis, McMaster University, 1990.
13. Wiggins JS, Hassan MK, Mauritz KA, Storey RF. *Polymer,* **2006**, 1960–1969.
14. Rhoades DW, Hassan MK, Osborn SJ, Moore RB, Mauritz KA. *J Power Sources,* **2007**, 72–77.

15. Osborn SJ, Hassan MK, Divoux GM, Rhoades DW, Mauritz KA, Moore RB. *Macromolecules,* **2007**, 3886-3890.

16. Kremer F, Schönhals A. Broadband Dielectric Spectroscopy, Berlin: Springer, 2003. p 225.

17. Mauritz KA, Stefanithis ID. *Macromolecules,* **1990**, 1380.

18. Tucker SJ. PhD Thesis, The University of Southern Mississippi, 2010.

19. Flory PJ. J Macromol Sci Part B Phys, **1976**, 1-11.

20. Fischer EW, Strobl GR, Dettenmaier M, Stamm M, Steidle N. *Faraday Discuss Chem Soc.,* **1979**, 26-45.

21. Havriliak S, Negami S. *J Polym Sci Polym Symp,* **1966**, 99.

22. Havriliak S, Negami S. *Polymer,* **1967**, 161.

23. Negami S, Ruch RJ, Myers RR. *J Colloid Interface Sci,* **1982**, 117.

24. Day DR, Lewis TJ, Lee HL, Senturia SD. *J Adhesion,* **1985**, 73-90.

25. Schultz JW, Chartoff RP. *J Coat Tech,* **1996**, 97-106.

26. Senturia SD, Sheppard NF. *Dielectric analysis of thermoset cure. In: Dušek K. Advances in Polymer Science: Epoxy Resins and Composites IV*, Vol. 80. Verlag Berlin Heidelberg: Springer, 1986. pp. 1-47.

27. McCrum NG, Read BE, Williams, G. *Anelastic and Dielectric Effects in Polymeric Solids.* New York: Dover, 1991.

28. Vogel H. *Phys Z* **1921**, 645; Fulcher GS. *J Am Ceram Soc,* **1923**, 339; Tammann G, Hesse W. Z *Anorg Allgem Chem,* **1926**, 245.

29. Kaushik M, Jackson M, Heinz S, Wiggins J, Nazarenko S. *Proc. from SAMPE I'nat. Conf.* Wichita, KS. 2009.

CHAPTER VIII

REACTION KINETICS OF PRE-GEL CROSSLINKED EPOXIES BY SOLID STATE NMR SPECTROSCOPY

Objective

To improve multiscale models and the distortional deformation capabilities of composite networks, a comprehensive understanding of the true network chemical topology is required. A number of solid state NMR techniques can be employed to accomplish this research goal, aided by synthesizing networks with isotopically labeled monomers to augment or identify spectroscopic signals at specific sites. Networks consisting of 44DDS/DGEBA and 33DDS/DGEBA have been selected to provide molecular-level geometrical models to properly evaluate and improve understanding of the effect para vs. meta substituted amines on crosslink formation in epoxies.

In this chapter, variable temperature in situ NMR spectroscopy (VT-NMR) is used to study the kinetics of network formation of two amine/epoxy matrices. The kinetics of the meta amine curative 3,3'-diaminodiphenyl sulfone (33DDS) and epoxy diglycidyl ether of bisphenol A (DGEBA) are probed with ^{13}C VT-NMR spectroscopy. DGEBA is also reacted with a ^{15}N-labeled para amine 4,4'-diaminodiphenyl sulfone (44DDS), and ^{15}N VT-NMR is used to track the kinetics of cure. The monomers used are shown in Figure 8.1.

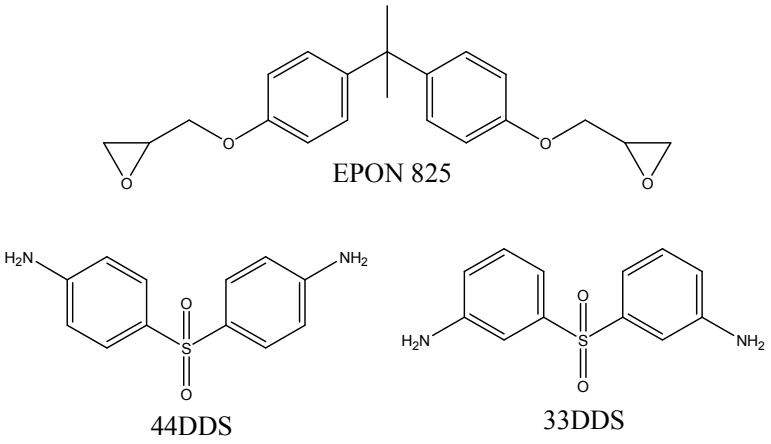

Figure 8.1. DGEBA, 44DDS, and 33DDS.

Materials

Anhydrous sodium hydroxide pellets (NaOH, ≥98% purity), toluene (≥99% purity), acetic anhydride (≥98% purity), carbon disulfide (≥99% purity), sulfonyl chloride (≥98% purity), aluminum trichloride (≥98% purity), glacial acetic acid, ammonium chloride (≥99% purity), tetrahydrofuran (THF, ≥99% purity), hydrogen peroxide (≥98% purity), hydrochloric acid (HCl, ≥98% purity), and decolorizing carbon, methanol (≥99% purity) were purchased from Sigma Aldrich and used as received. The NaOH pellets were dissolved into deionized water to make a 40%wt. aqueous NaOH solution. ^{15}N-labeled aniline, 98% purity was obtained from Cambridge Isotope Laboratories, Inc. and used as received.

Methods

NMR studies for the solid-state require benchmark control (non-labeled) studies to optimize the spectrometer for each resin system. As necessary, isotope-labeled networks are synthesized as model compounds to fully resolve resonance shifting patterns for a specific matrix and NMR technique. For the ^{13}C study, 33DDS was chosen

due to its greater solubility in DGEBA. For the ^{15}N study, ^{15}N-labeled 44DDS was chosen due to its ease of synthesis in comparison to 33DDS. The detailed synthetic procedure for creating ^{15}N labeled 44DDS is included below. The ^{13}C VT-NMR study accomplished on 33DDS/DGEBA did not require isotope-labeled synthesis as signal-to-noise was acceptable.

Synthesis of ^{15}N Labeled 4,4'-Diaminodiphenyl Sulfone (44DDS)

The natural abundance of ^{15}N is 0.4%, making facile NMR studies difficult. In order to obtain higher signal-to-noise (S/N) ^{15}N NMR spectra, labeling samples with ^{15}N is often required. In this work, 44DDS/DGEBA samples were cured with ^{15}N-labeled 44DDS incorporated into the matrix at a level of ~5% enrichment.

Scheme 8.1. Synthesis of ^{15}N 44DDS

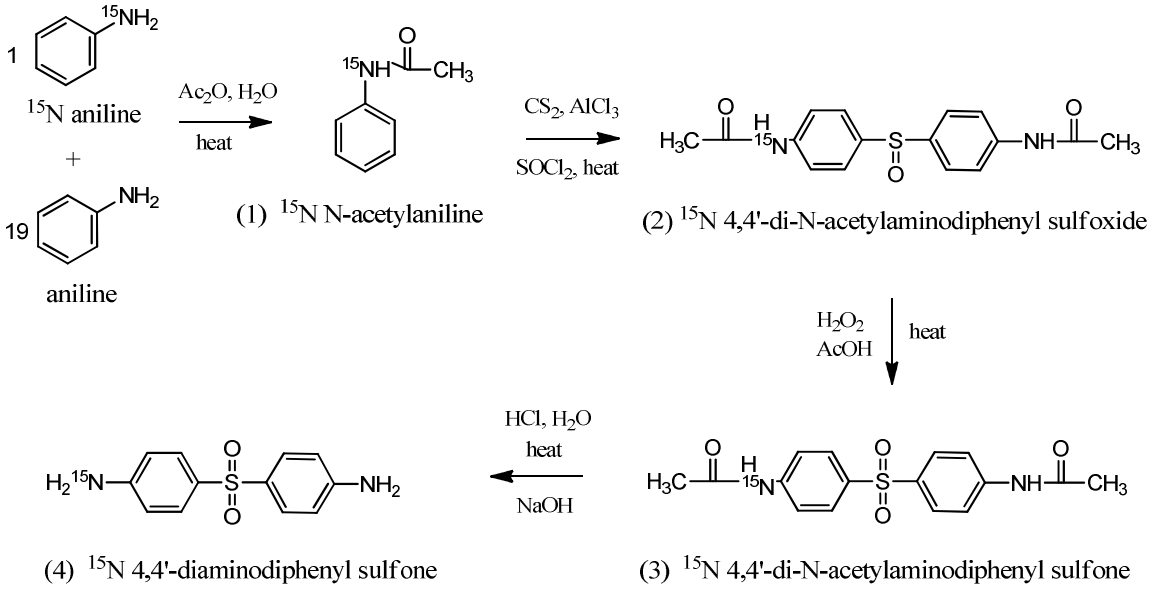

N-acetylaniline

Aniline (6g ^{15}N-labeled + 54g unlabeled) was added to 150ml acetic anhydride and heated at reflux for 30min. After cooling to room temperature, 180ml water was added and heated at reflux for 10min. The solution was then cooled to room temperature and diluted with water to precipitate the product, N-acetylaniline. The N-acetylaniline was filtered, washed with water, recrystallized from water, and dried to yield 45 g; mp: 109-111^{o}C (Figure 8.2).

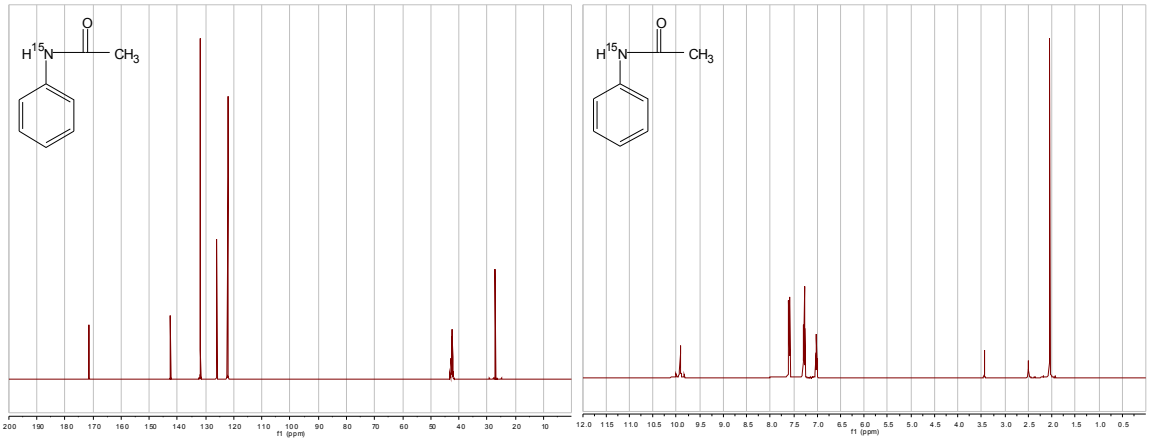

Figure 8.2. ^{1}H and ^{13}C NMR spectra of ^{15}N-labeled N-acetylaniline.

4,4'-Di-N-acetylaminodiphenyl Sulfoxide

43g N-acetylaniline was suspended in 437ml CS_2, after which 80g $AlCl_3$ and 17.5ml $SOCl_2$ were added. After the initial reaction subsided, the mixture was heated at reflux for 6hr, cooled to room temperature, and quenched by the addition of a 10% ammonium chloride solution in water. The mixture was filtered, and the filter cake was washed with water. The filter cake was then dissolved in THF, filtered, and the filtrate

concentrated under vacuum to yield 42g of product. The product, 4,4'-di-n-acetylaminodiphenyl sulfoxide, was recrystallized with MeOH/H_2O; mp: 304^oC (Figure 8.3).

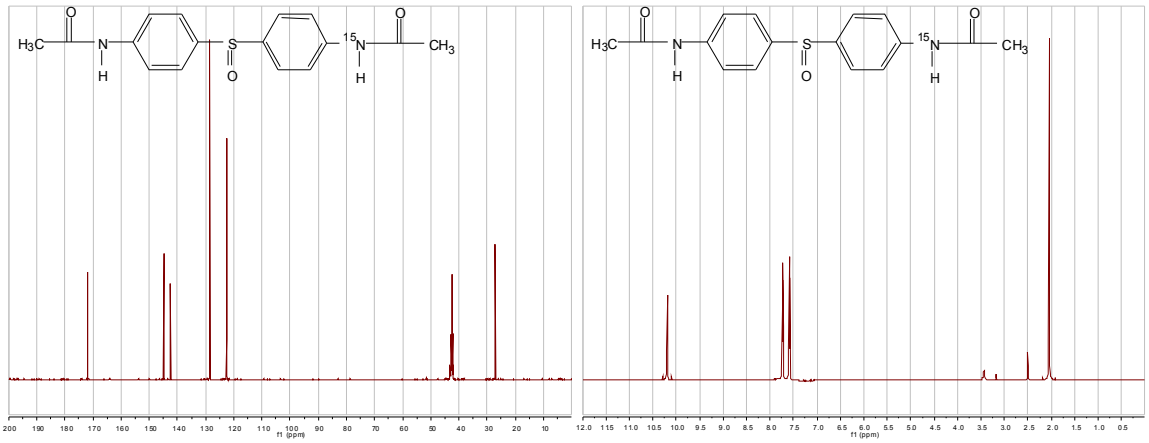

Figure 8.3. ^1H and ^{13}C NMR of ^{15}N 4,4'-di-n-acetylaminodiphenyl sulfoxide.

4,4'-Di-N-acetylaminodiphenyl Sulfone

41g 4,4'-di-N-acetylaminodiphenyl sulfoxide was suspended in 525ml glacial acetic acid. 52.5ml 30% H_2O_2 was added to the suspension, and the mixture was allowed to stand for 3hr at room temperature. The mixture was then heated at 50^oC for 2hr and subsequently refluxed until homogenous. The homogenous mixture was cooled to room temperature, 31.5ml 30%H_2O_2 was added, and the mixture was stored overnight at 4^oC. The mixture was concentrated under vacuum to yield 38g and then recrystallized with MeOH/H_2O to yield 37g 4,4'-di-n-acetylaminodiphenyl sulfone; mp: 281^oC (Figure 8.4).

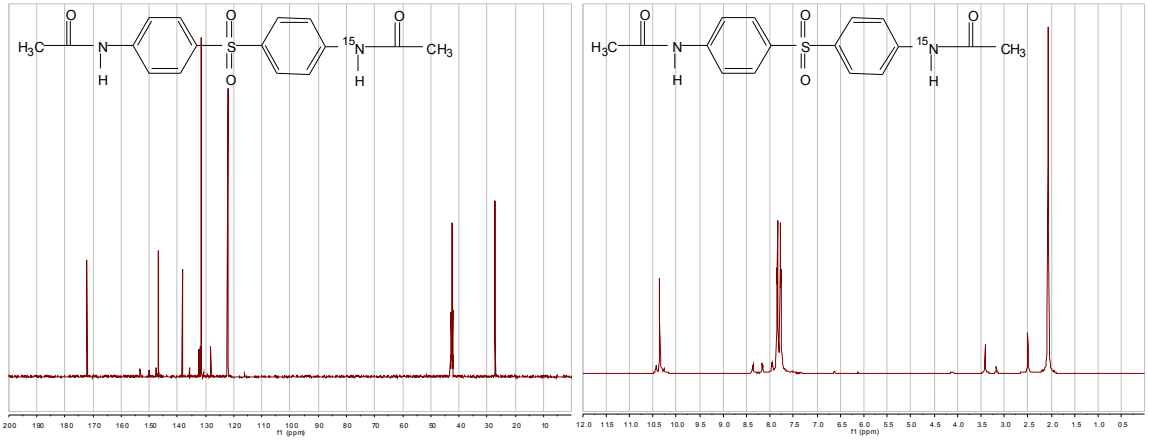

Figure 8.4. ^{1}H and ^{13}C NMR of ^{15}N 4,4'-di-n-acetylaminodiphenyl sulfone.

4,4'-Diaminodiphenyl Sulfone

36g 4,4'-di-n-acetylaminodiphenyl sulfone was suspended in 360ml 10% HCl, and heated at reflux for 1.5hr. At this point decolorizing carbon was added, and the mixture was refluxed for 1hr, filtered while hot, and cooled to room temperature. 10% NaOH was added to adjust the pH to 14, and the resulting precipitate was isolated by filtration, recrystallized with MeOH/H_2O, and dried in a vacuum oven to yield 15g of the final product, ^{15}N labeled 44DDS; mp: 178°C (Figure 8.5).

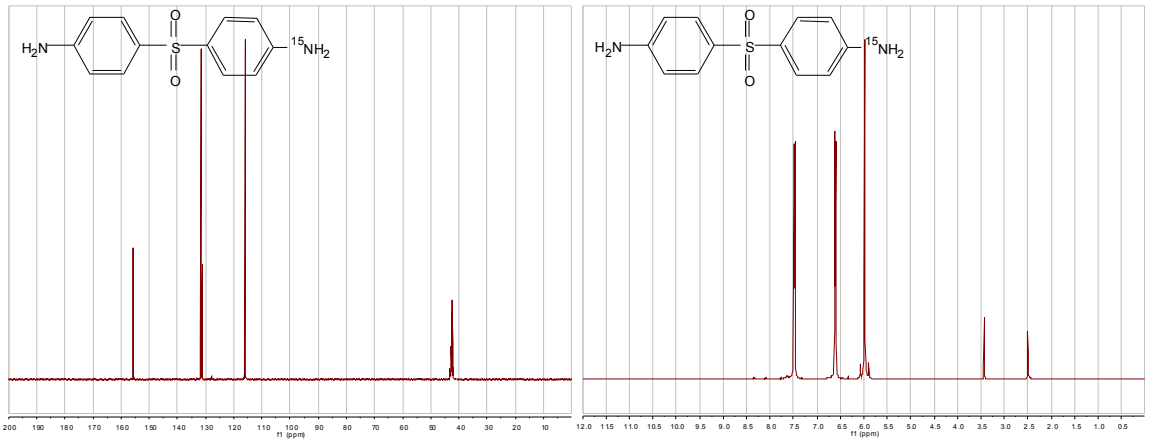

Figure 8.5. ^{1}H and ^{13}C NMR of ^{15}N 4,4'-diaminodiphenyl sulfone.

NMR Analysis

Solid-state NMR spectroscopy was performed on a Varian ^{UNITY}INOVA 400 spectrometer using a standard Chemagnetics 7.5 mm PENCIL™-style probe. Samples were loaded into zirconia rotor sleeves and sealed with Teflon™ caps. The standard solid state magic angle spinning (MAS) technique was used with high-power proton decoupling implemented during data acquisition.[1] In addition, the TOSS technique was implemented on the ^{13}C data acquisition to remove spinning side bands.[2]

For liquid conditions, a modified Bloch decay sequence was used. Here instead of a simple 90° pulse acquisition, a DEPTH sequence was implemented in order to reduce background ^{13}C signal. For vitrified samples, a standard cross-polarization / magic angle spinning (CP/MAS) sequence was used, with a cross polarization pulse of 1ms. High-power proton decoupling during acquisition was employed in both sequences.

Sample Preparation

33DDS and 44DDS are crystalline solids with melting temperatures of 170-173°C and 175-177°C, respectively. DGEBA is a viscous liquid in which both 33DDS and 44DDS are marginally soluble. VT-NMR samples are prepared by sonicating the amine and the epoxy together for 20 minutes at 50°C. This amount of heat does not initiate reaction but does solubilize some amine into the epoxy. The sample is then placed in a solid state NMR rotor and data acquisition using Bloch decay is started. Samples are prepared stoichiometrically assuming full reaction of the amine and epoxy. Since each amine can react twice, once to form a secondary amine and a second time to form a tertiary amine, samples are prepared at a 2:1 epoxy:amine molar ratio (corresponding to a 1:1 ratio of reactive groups).

Variable Temperature NMR (VT-NMR)

Variable temperature experiments were performed by obtaining a room temperature spectrum for the unreacted specimen, then heating to 125°C and obtaining spectra via Bloch decay until the signal broadened and resolution was lost. At this point, cross polarization was employed. After this, the samples were heated up to 200°C and spectra were obtained using cross polarization. Samples were then cooled to 25°C to obtain a final CP spectrum. For ^{13}C data, previously reported spectral assignments, in addition to small molecule solution NMR studies and the MNOVA® Modgraph NMRPredict package were used to make validated spectral assignments.[3]

Carbon Acquisition Parameters

The ^{1}H 90° pulse width was 5.25 μs, the cross-polarization contact time was 1 ms, the dead time delay was 6.4 μs, and the acquisition time was 45 ms. A recycle delay of 3 seconds between scans was utilized.

Nitrogen Acquisition Parameters

The ^{1}H 90° pulse width was 6.5 μs, the cross-polarization time was 2 ms, the dead time delay was 6.4 μs, and the acquisition time was 45 ms. The recycle delay was 3 or 5 seconds, and a ^{1}H decoupling field of 61.9 kHz was implemented during data acquisition.

Results and Discussion

Carbon VT-NMR Analysis of 33DDS/DGEBA

The ^{13}C VT-NMR Bloch decay spectra of the 33DDS/DGEBA system consists of narrow line widths, with new resonances appearing upon heating to 125°C. These can be integratedwhich can be integrated in order to identify the kinetics of the cure (Figure 8.6).

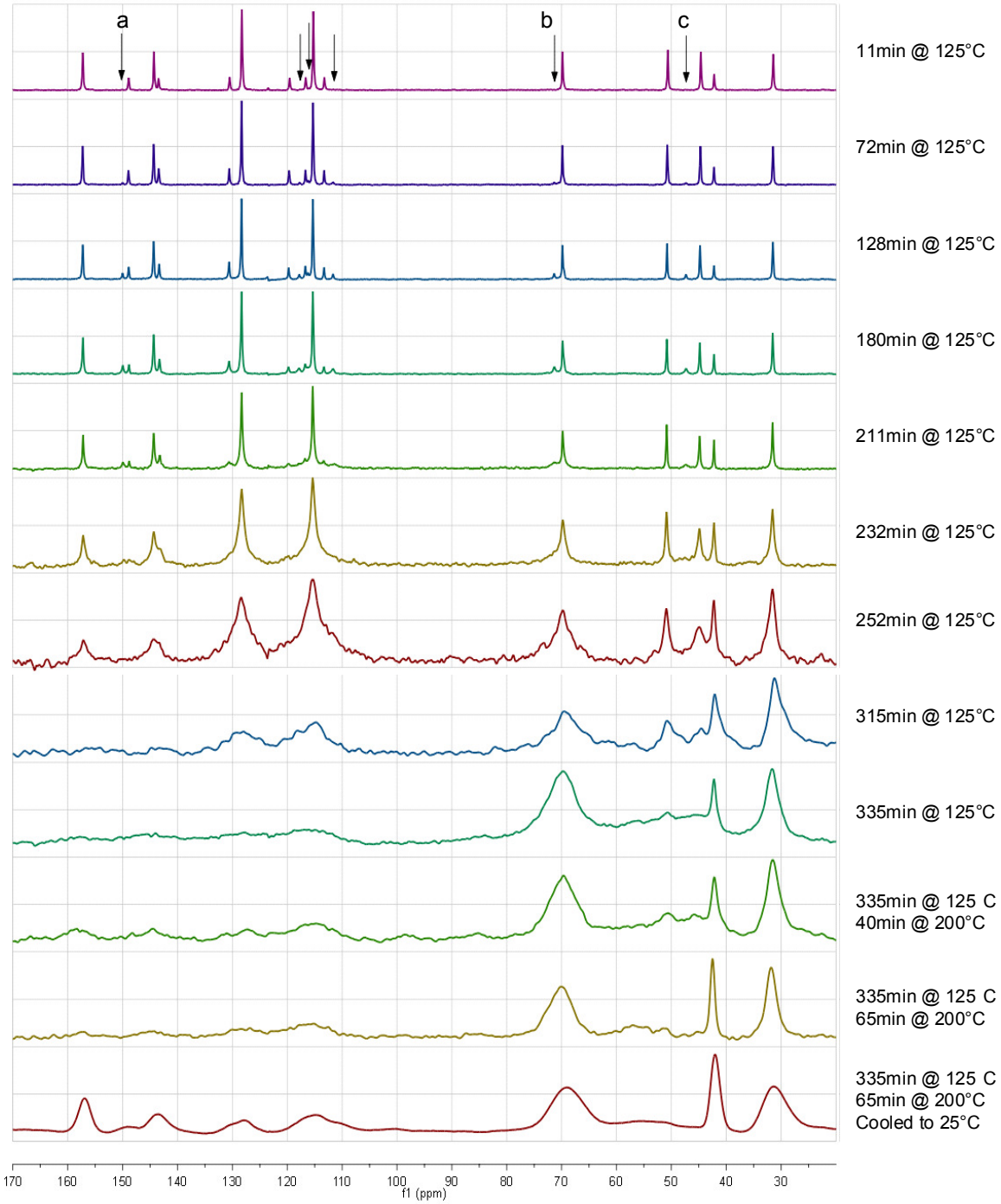

Figure 8.6. Variable temperature ^{13}C NMR spectra of 33DDS/DGEBA cure.

The resonances of interest are labeled (a), (b), and (c) at 150, 71.5, and 47.5ppm, respectively (Figure 8.6). Site (a) exhibits a new peak for the aromatic carbon on 33DDS

adjacent to the amine as the amine reacts and becomes secondary and/or tertiary. Sites (b) and (c) represent the carbon on DGEBA adjacent to the ether and the reactive epoxy carbon, respectively, and confirm reaction of the epoxide group. Sites (A), (B), and (C) correspond to the same carbons as (a), (b), and (c) before the amine and epoxide react (Figure 8.7).

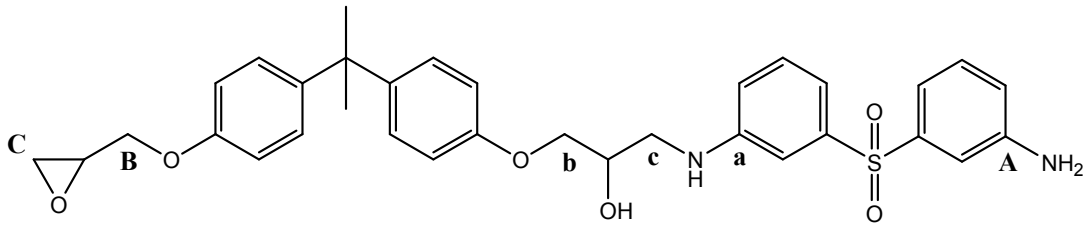

Figure 8.7. Partially reacted 33DDS and DGEBA.

The spectrum at 252min was the last obtained without cross polarization . The broadening of the peaks shows the sample is becoming a solid, making accurate integrations impossible for the spectra acquired after 180min. Figures 10-13 show the reduction in intensity of peaks A, B, and C and the growth in intensity of peaks a, b, and c at 11min, 72min, 128min, and 180min after reaching 125°C. These peaks are integrated to provide kinetics information.

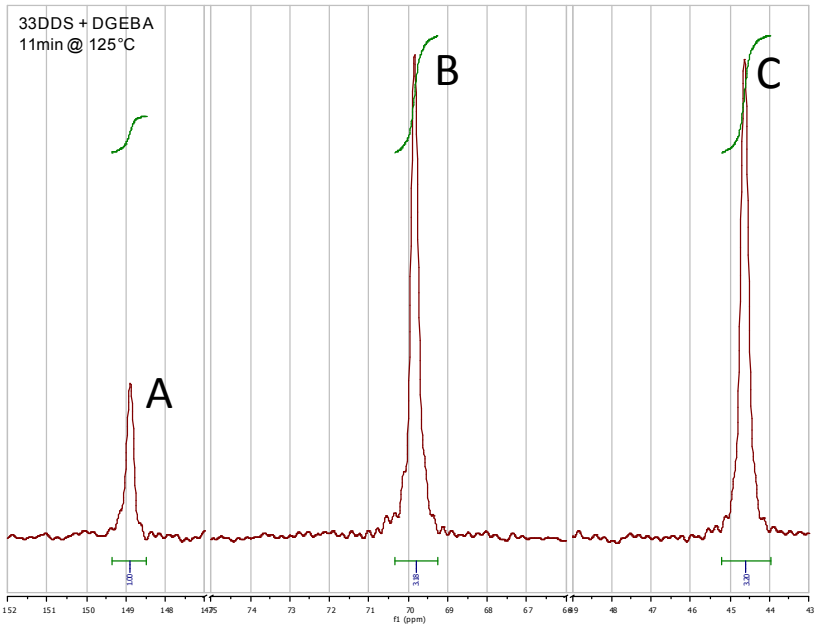

Figure 8.8. 33DDS and DGEBA after 11min at 125°C; no observable reaction.

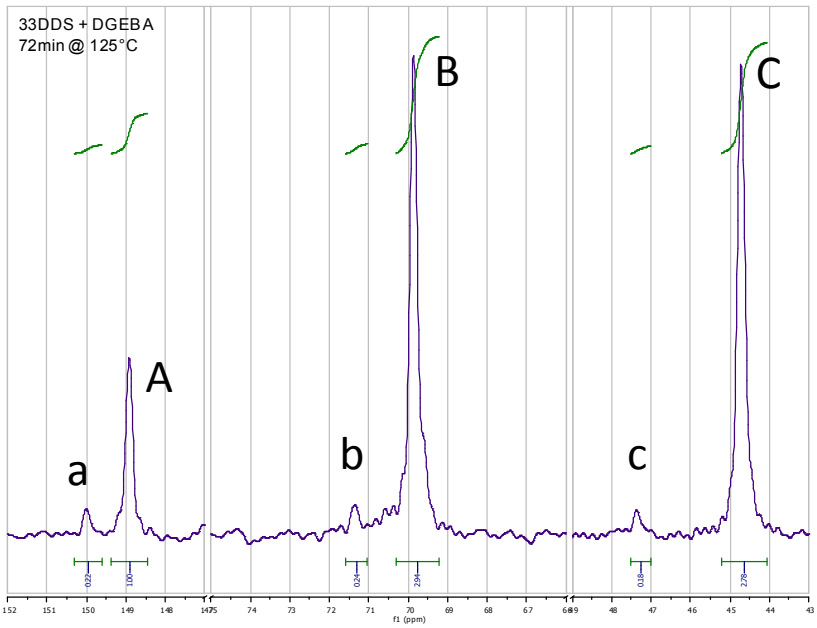

Figure 8.9. 33DDS and DGEBA after 72min at 125°C.

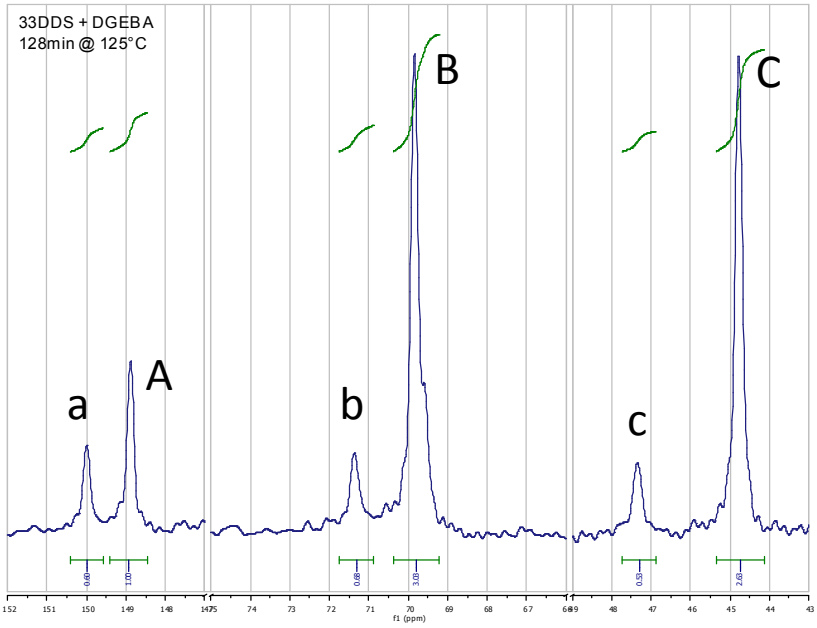

Figure 8.10. 33DDS and DGEBA after 128min at 125°C.

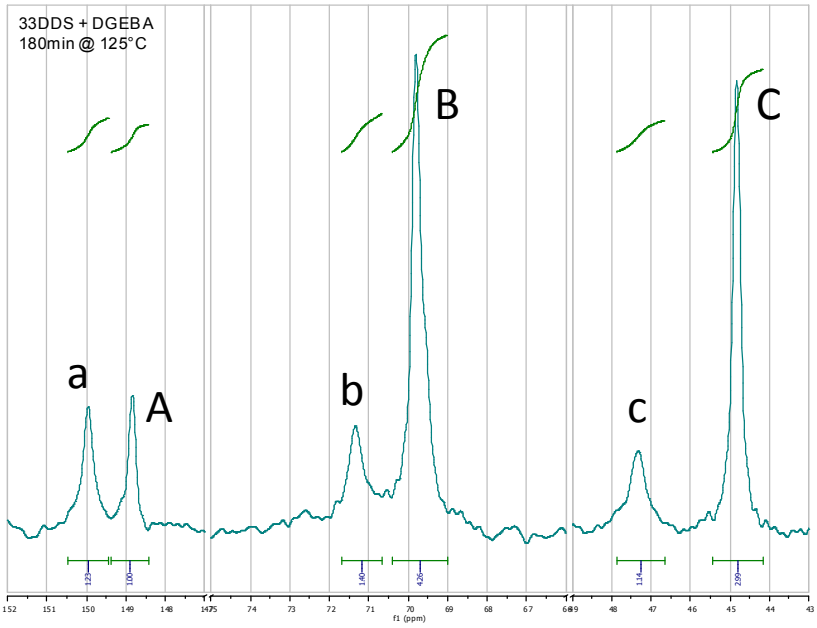

Figure 8.11. 33DDS and DGEBA after 180min at 125°C.

The peaks corresponding to the reacted species, (a), (b), and (c), can be compared to those corresponding to the unreacted species, (A), (B), and (C) to determine percent conversion of epoxide and amine (Table 8.1).

Table 8.1. Reaction of 33DDS and DGEBA as Shown by NMR

Time at 125°C (min)	**Conversion** (A→a)	**Conversion** (B→b)	**Conversion** (C→c)
11	0%	0%	0%
72	18%	8%	6%
128	37%	18%	17%
180	55%	25%	27%

Table 8.1 summarizes the conversion by showing four snapshots along the cure pathway; however, between 0min and 180min after reaching 125°C, 11 spectra were taken and integrated. The complete data is shown in a conversion versus time plot in Figure 8.12.

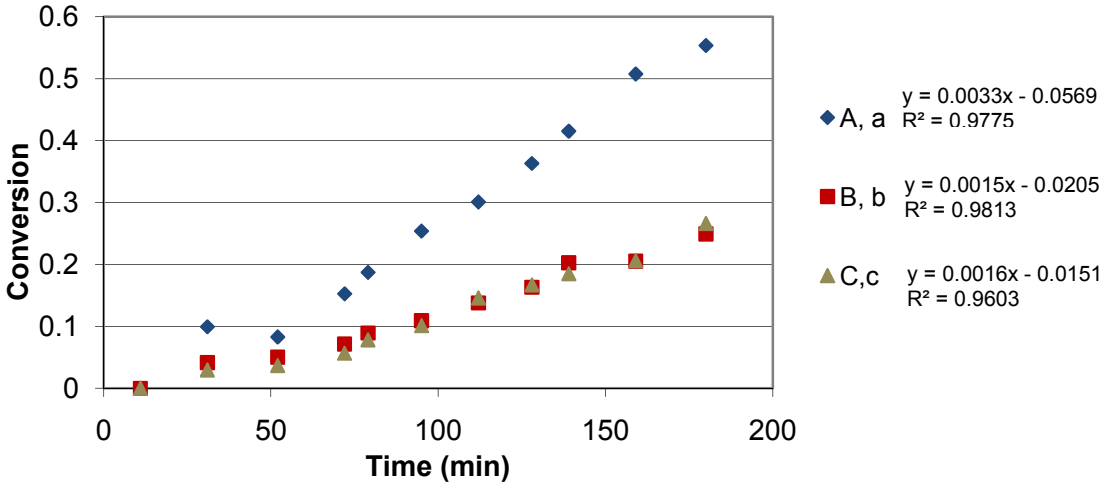

Figure 8.12. ^{13}C VT-NMR results of 33DDS/DGEBA conversion vs. time plot.

Figure 8.12 shows all three conversions plotted linearly versus time. The plot for the amine carbon possesses a slope approximately twice that of the two epoxide carbon sites. Therefore, approximately twice as much amine as epoxide is being consumed during the reaction. The stoichiometry in the reaction is set at two epoxides for every amine so that at 100% conversion all epoxide rings have reacted once and all amines have reacted twice to form secondary amines. Making the assumptions that epoxides are only consumed by amines and primary amines only react with epoxides, the data shows that virtually no tertiary amines are being formed while the matrix has sufficient mobility to be effectively probed by Bloch decay techniques. This explains why only two amine peaks are observed.

Oddly, the reaction rates are slower than expected based on near IR measurements.[4] This is likely because of difficulties in fully solubilizing the 33DDS deu to the centrifugal force of sample spinning. To address this issue, the amine was further

solubilized before acquiring spectra in later experimentation. However, the window of opportunity before peaks broaden is narrow, and further solubilization results in further reaction, and no useful kinetic data could be obtained.

^{15}N NMR Analysis of 44DDS/DGEBA

A sample incorporating 5% ^{15}N-labeled material was used for ^{15}N NMR VT analysis of 44DDS/DGEBA. The top two spectra in Figure 8.13 show the solution ^{15}N NMR of unlabeled 44DDS (red) and 5% labeled ^{15}N 44DDS (green), illustrating the significant S/N increase obtained via isotopic labeling.

An amine peak in addition to the primary amine was observed at 256min at 125°C, obtained using the CP/MAS method (Figure 8.13). Although the spectrum possesses poor S/N two peaks are nevertheless clearly observed. Spectra taken after 256min only showed one broad peak. It is likely that the peak forming at 256min is the secondary amine appearing, while the broad peak observed after 1hr at 200°C is due to the formation of tertiary amine. This is consistent with the ^{13}C data, which indicates that secondary amines do not form until after all primary amines have been consumed. At this point, peaks are too broad to resolve secondary/tertiary amine sites.

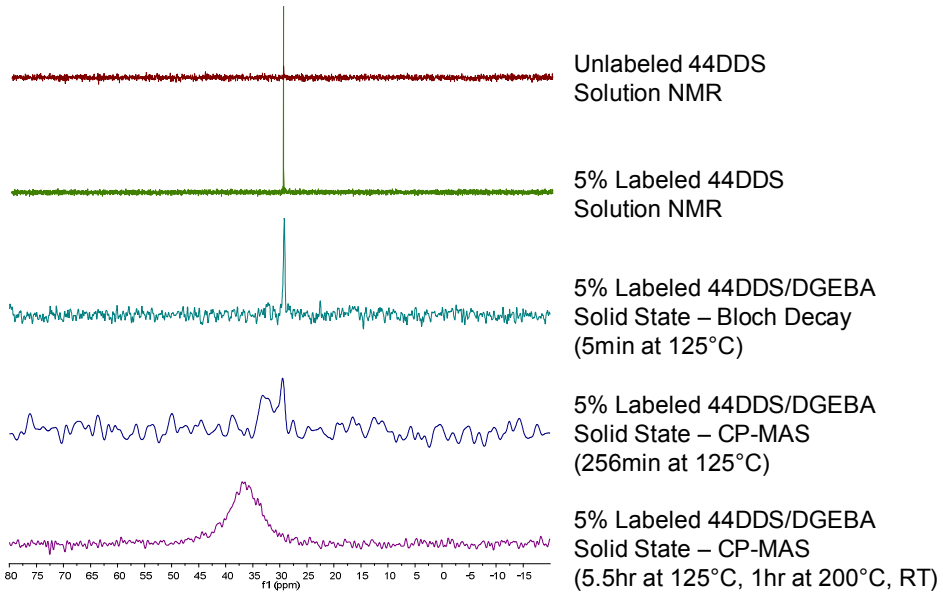

Figure 8.13. Variable temperature ^{15}N NMR study of 33DDS/DGEBA cure.

Unfortunately, this work suffered the same problem with amine solubility during magic angle spinning as in the ^{13}C work, and further solubilization once again resulted in the inability to acquire kinetic data. Additionally, these experiments, 5% ^{15}N labeling was not sufficient to see the appearance of an integratable secondary or tertiary amine peak appear using the Bloch decay sequence.

Conclusions

Solid state magic angle spinning NMR spectroscopy does not provide a facile and accurate method for determining reaction kinetics of 33DSS/DGEBA or 44DDS/DGEBA. Spectral distances between resonances of unreacted and reacted species are not sufficient to be individually integrated after the sample begins to gel and peaks broaden. Additionally, the magic angle spinning technique appears to centrifuge the amine out of the epoxy, thus artificially slowing reaction kinetics.

References

1. Schaefer, J.; Stejskal, E.O.; Buchdahl, R. *Macromolecules,* **1977**, 10, 384-405.

2. Dixon, W.T. *The Journal of Chemical Physics,* **1982**, 77 1800.

3. Harris, R.K.; Yeung, R.R.; Johncock, P.; Jones, D. *Polymer,* **1996**, 37, 721-727.

4. Jeremy Swanson, Dissertation. Hattiesburg, MS: University of Southern Mississippi, 2010.

CHAPTER IX

AMBIENT CURE POSS-EPOXY MATRICES FOR MARINE COMPOSITES

Introduction

The marine composites industry has evolved over the last decade with the implementation of numerous polymer matrix and fiber-reinforced structures being manufactured through a variety of composite fabrication techniques. While glass-fiber reinforced isophthalic polyester and vinylester composites have been utilized extensively in the manufacturing of pleasure craft and fishing boats, they have only recently been incorporated into more advanced naval applications including sonar domes, submarine masts, and mine-hunters.[1] Weight reduction, longevity, maintenance, corrosion resistance, zero magnetic signature, and design flexibility are important driving forces for replacing aluminum and steel in marine applications. However, polyester matrix composites are inherently limited in the marine industry due to degradations at the fiber-matrix interface.

The fiber-matrix interface can be weakened over time as a result of the relatively high CTE differences between polyester and glass.[1] Expansion and contraction of these dissimilar materials during the service life of a structure can weaken interfacial adhesion due to abnormal stresses placed at the interface. In addition, polyester matrices suffer long-term degradations of the interface associated with the hydrolysis of ester linkages within the matrix.[1,2] Prolonged exposure of structure to seawater decreases strength and toughness over extended periods of time.[3] Seawater wicks along fiber surfaces resulting in debonding of the interface leading to a reduction in the mechanical properties of the structure.[4]

When considering long-term hydrolytic stability, CTE/shrinkage, fracture toughness, mechanical properties, thermal properties, and fiber-matrix interfacial strength/stability, epoxy resins are superior to polyesters. Despite these advantages, epoxies have found restricted use in large primary structure marine applications due to limited thermomechanical performance with low viscosity room temperature cure formulations. Large primary structure marine applications require epoxy formulations that balance low viscosity with long gel-times and elevated temperature thermomechanical properties. High T_g ambient cure epoxies have relatively short gel-times and rely upon a kinetically controlled exotherm to drive network vitrification. Slowing the kinetics of epoxies to extend the gel-time reduces the exotherm and vitrified state of the network yielding low T_g and low elevated temperature mechanical properties. It is impractical to post-cure large marine primary structure in ovens or autoclaves to drive vitrification of long gel-time formulations, so this paradox has prevented traditional epoxy chemistries from finding utility in these applications.

We are incorporating functionalized polyhedral oligomeric silsesquioxane (POSS) to advance desirable properties of ambient cure epoxies designed for marine applications. The POSS chemical moiety is an ideal building block for synthesis of new organic-inorganic polymers as it resembles a nano-sized particle of SiO_2 and provides molecular level elevated temperature thermomechanical reinforcement[5]. Proper solubilization and functionalization of POSS cages into epoxy networks will result in strong POSS-polymer chemical interactions and provide an increase in desirable properties.[6] The inorganic cage structure of POSS can be glycidyl functionalized to achieve a high degree of crosslinking in epoxies to significantly improve elevated temperature performance of the

matrix. In a stoichiometric equivalent system (one epoxy per amine hydrogen), formulations possessing octa-functional monomers will vitrify at lower temperatures. POSS units tend to aggregate within crosslinked networks to provide physical crosslinks which improve mechanical properties at elevated temperatures.[7] Therefore, POSS-POSS interactions have a dominant role in controlling elevated temperature physical properties of modified polymers.[8] Mechanical properties such as modulus are enhanced at elevated temperatures from the formation of a physical network of POSS within the network architecture.

Materials

Derakane 510A-40 brominated bisphenol-A based vinylester (Ashland), EPON 862 bisphenol-F based diglycidyl ether (FW=338 g/mol; eqW=169 g/mol; Hexion), diethylenetriamine (DETA; FW=103.17 g/mol; eqW=20.63 g/mol; Aldrich), 2-butanone peroxide (Luperox DDM-9) 35 wt% in 2,2,4-trimethyl-1,3-pentanediol diisobutyrate composition (MEKP, Aldrich), 6 wt% cobalt naphthenate in mineral spirits (Aldrich), and EP0409 octaglycidyl polyhedral oligomeric silsesquioxane (gly-POSS) (FW=1337.88 g/mol; eqW=167.24 g/mol; Hybrid Plastics) were used as received. For composite fabrication, 10 oz e-glass plain weave fabric (FG-C1038), vacuum bag sealant tape (VB-BT25), polyethylene tubing (3/4" O.D., ½" I.D.), spiral cut polyethylene tubing (3/4" O.D., ½" I.D.), polyester peel ply release fabric (VB-P56150), nylon mesh distribution medium, and nylon vacuum bagging film (VB-VF02110), (all U.S. Composites) were used as received. Chemical structures of monomers are shown in Scheme 1.

Scheme 9.1. Chemical Structures of Monomers

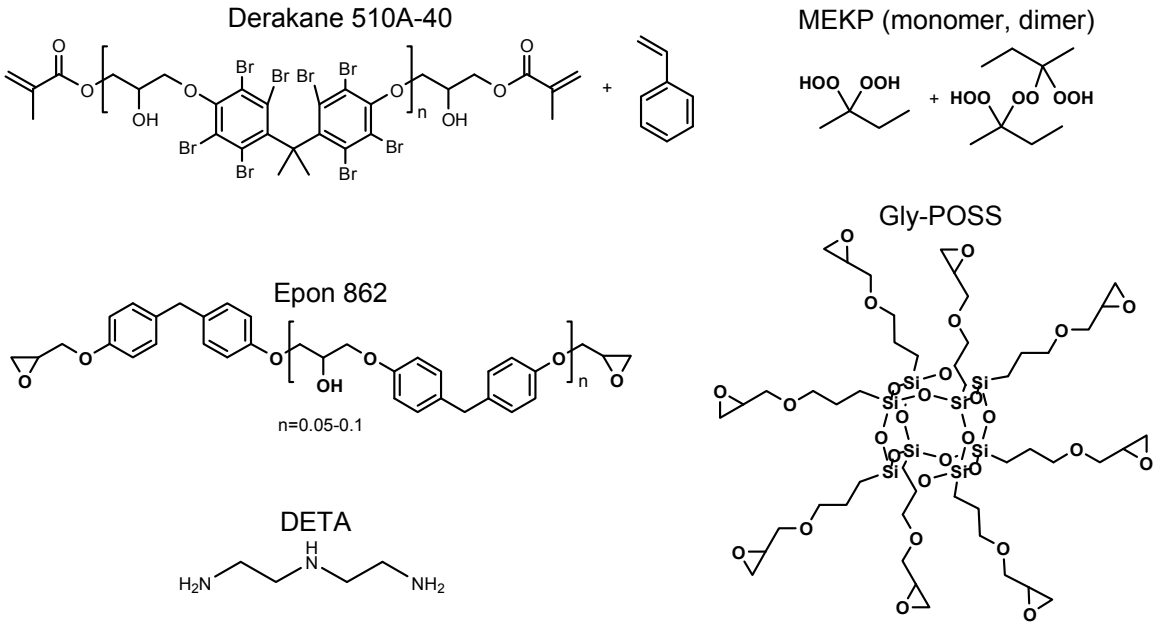

Methods

Preparation of Vinylester Matrix Formulations

Derakane 510A-40 vinylester matrices used to fabricate 3-ply composite panels were prepared in 300g batches. In a typical formulation 300.0 g Derakane 510A-40 and 0.60g (0.20 wt%) of 6% cobalt naphthenate solution were charged to a dry aluminum can. The mixture was stirred with a wooden tongue depressor for approximately 5 min until a homogenous mixture was observed. 3.0g (1.0 wt%) of 35% MEKP solution was then charged into the vinylester / cobalt naphthenate mixture and stirred for an additional 5 min until a homogenous mixture was observed.

Preparation of Epoxy Matrix Formulations

Epoxy matrices used to fabricate 3-ply composite panels were prepared in 300g batches. All epoxy formulations were based on total epoxide concentration cured by DETA in 1:1 stoichiometric ratio (oxirane to active hydrogen). In a typical formulation

267.4g EPON 862 (1.58 moles eqW) and 32.64g DETA (1.58 moles eqW) were charged into a dry aluminum can. The mixture was stirred for approximately 5 min until a homogenous mixture was observed. POSS modified epoxies were formulated at gly-POSS concentrations of 26.5 wt% and 62.5 wt% of the formulation. In a 26.5 wt% gly-POSS modified formulation 187.8g EPON 862 (1.11 moles eqW) and 79.5g EP0409 (0.48 moles eqW) were charged into a dry aluminum can. The mixture was stirred for approximately 5 min until a homogenous mixture was observed. 32.73 DETA (1.59 moles eqW) was then charged into the mixture and stirred for approximately 5 minutes. Matrix nomenclature for materials contained within this manuscript is provided in Table 9.1.

Table 9.1. Matrix Nomenclature

Sample	Formulation
VE	Derakane 510A-40 (benchmark vinylester)
E	DETA + DGEBF (control epoxy)
E27P	DETA + DGEBF + 26.5 wt% gly-POSS
E63P	DETA + DGEBF + 62.5 wt% gly-POSS

VARTM

Figure 9.1 depicts the vacuum assist resin transfer molding (VARTM) procedure employed for fabrication of composite panels. The fiber lay-up packages contained three plies of 24" x 24" 10oz. e-glass plain weave fabric stacked in 0/90 orientation on a freshly waxed flat aluminum tool. Two 24" length ¾" spiral cut polyethylene tubes adhered to the aluminum tool with vacuum bag sealant tape were used for matrix inlet and outlet channels. The matrix inlet tube was placed adjacent to an edge of the fiber

stack and the matrix outlet tube was placed under the fiber stack at the opposite edge as shown in Figure 9.1. A 24" x 24" polyester peel ply was placed over the fiber stack. A 24" x 22" nylon distribution medium was placed from the top of the matrix inlet tube to the resin outlet tube as depicted in Figure 9.1.

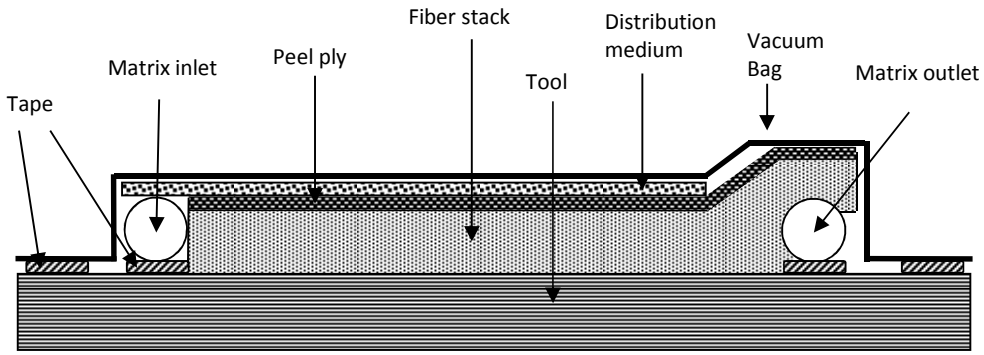

Figure 9.1. VARTM process illustration.

For transfer of the matrix from the aluminum mixing can to the inlet channel and from the outlet channel to the waste collection, polyethylene tubes, approximately 36" to 48" in length were used. The transfer tubes were inserted approximately 1" into the spiral cut inlet and outlet channels and secured in place with vacuum bag sealant tape. We then placed an approximate 28" x 28" vacuum bag sealant tape square border onto the aluminum tool which surrounded the entire lay-up, taking special care to properly seal the transfer tubes. Vacuum bagging film was then adhered to the taped border, again, taking special care to minimize any discontinuities that could lead to a vacuum leak. The inlet transfer tube was sealed using locking pliers and the outlet transfer tube was connected to air aspirator. Vacuum was applied to the dry laminate and the seal checked

for leaks. Once a complete vacuum was achieved, the matrix was mixed, and the inlet tube seal removed and immersed immediately into the matrix.

Typical infusions for the 24" x 24" panels were conducted over a 20-30 minute period, and full vacuum was maintained until the matrix gelled. Composite panels were cured in ambient conditions for 24h after vacuum was released and removed from the VARTM apparatus. Panels were post-cured an additional 6 days in ambient conditions prior to testing. Panels with useful dimensions of approximately 22" x 20" were obtained from this procedure and cut into test specimens using a diamond edge tile-saw.

Instrumental Analysis

Viscosity measurements of vinylester and epoxy-amine matrices were analyzed with a cone and plate Brookfield CAP 2000+ viscometer. Isothermal measurements were taken at 25°C, and the cone was rotated at 10 s^{-1} using spindle #1.

Rheology measurements used to determine gel-times of the matrices were analyzed on an TA Instruments ARES G2 Rheometer using 25 mm diameter plates at a gap of 1 mm. Isothermal time sweep measurements at 25°C were run for 3.5h in dynamic-state oscillatory shear mode at a frequency of 6.28 rad/s with measurement intervals of 5s at a strain of 0.005%.

Dynamic Mechanical Analysis (DMA) measurements were performed on a TA Instruments RSA III Solid State Rheometer using a three point bending method. Measurements were taken using composite samples fabricated with three plain weave fabric plies; approximate dimensions were 50.0mm x 5.0mm x 1.7mm. Samples were tested between 25°C – 160°C at a ramp rate of 2°C/min.

Heat Distortion Temperature (HDT) was measured on a Rheometric Scientific DMTA V in three point bending mode. Measurements were taken using composite samples fabricated with three woven roving plies; approximate dimensions were 40mm x 6.0mm x 1.7mm mounted to 22mm span lengths. DMTA samples were placed under a stress of 1.8 MPa and heated 5°C/min from -80°C to 200°C. Heat distortion temperature is determined at the point where the flexural strain reaches 0.121% in compliance with ASTM D648.

Mechanical Testing was measured on an MTS Model 810 servo-hydraulic test frame at a test rate of 4.0mm/min. Measurements were taken using composite samples fabricated with three woven roving plies. Tensile test sample dimensions were 120mm x 15.0mm x 1.7mm with a measurement gauge length of 80.0mm. Flexural test sample dimensions were 40mm x 12.7mm x 1.7mm mounted to 28.0mm span lengths. Reported values are an average of three measurements.

Results and Discussion

In order for room-temperature cured matrices to be useful in the marine industry, the useful working time or "pot-life" of the matrix must be carefully controlled through reaction kinetics. Common marine composite fabrication techniques such as VARTM require a minimum 2-3h working time prior to significant increased viscosity. Vinylester matrices have been the benchmark resin in marine composites because of their combined viscosity, kinetic, and thermomechanical property profiles for ambient cure fabrications. Vinylester reaction kinetics are readily controlled through summer to winter ambient temperature variations through well-established adjustments to promoter and initiator concentrations in matrix formulations.

Viscometry

Initial catalyzed matrix viscosity is the starting point for determining the utility of a resin in application, and we have utilized a Brookfield cone and plate viscometer to compare our formulations to a vinylester standard. Table 9.2 provides initial viscosity data for the matrices. These measurements show that the initial viscosities for our epoxy control, 26.5 wt% gly-POSS, and 62.5 wt% gly-POSS matrices were approximately 55%, 51% and 18% less than the VE benchmark, respectively. Generally, matrix formulations under 1.20 Pa*s are considered to be "VARTMable," so each of these formulations was advanced for composite fabrication and testing.

Table 9.2. Initial Viscosity Data

Sample	**Viscosity (Pa*s)**
VE	0.489
E	0.219
E27P	0.242
E63P	0.402

Epoxy Selection and Processability

Literature review and preliminary evaluation of numerous commercial epoxy formulations led to the selection of DGEBF/DETA as the ambient cure epoxy control matrix for our research. Although we do not present data in this manuscript, it is noteworthy to mention epoxy formulation viscosities have been further reduced with a reactive diluent, such as butyl glycidyl ether, and we did not observe a significant influence on the key composite properties below 8-10 wt% loading levels.

Each of the matrices had excellent processability, flowed easily within the VARTM apparatus, fully encapsulated fiber packages, and demonstrated excellent curing kinetics verified by rigid, non-tacky cured panels removed from the VARTM tooling without difficulty 24 h after mixing. Matrix flow behavior and flow patterns observed during the VARTM infusion were similar for each of the matrices, and the fill-out times for all panels were consistently in the 25-30 min timeframe. Laminates were free of observable voids in all panels and displayed consistent visual appearance when considering complete flow-out and fiber wetting/infusion. Fully cured laminates also displayed excellent cutting characteristics and machined well without "fuzzy edges," which we use as an indicator of wet-out and cure.

Rheology

Isothermal parallel-plate rheological measurements performed on the matrices at 25°C as a function of time are shown in Figure 9.2. A significant difference in shear deformation viscosity between vinylester and all epoxy formulations is illustrated highlighting viscosity for the vinylester increases at a faster rate. Viscosity behavior of each epoxy formulation is similar up to around 170 min when the E63P begins to gel.

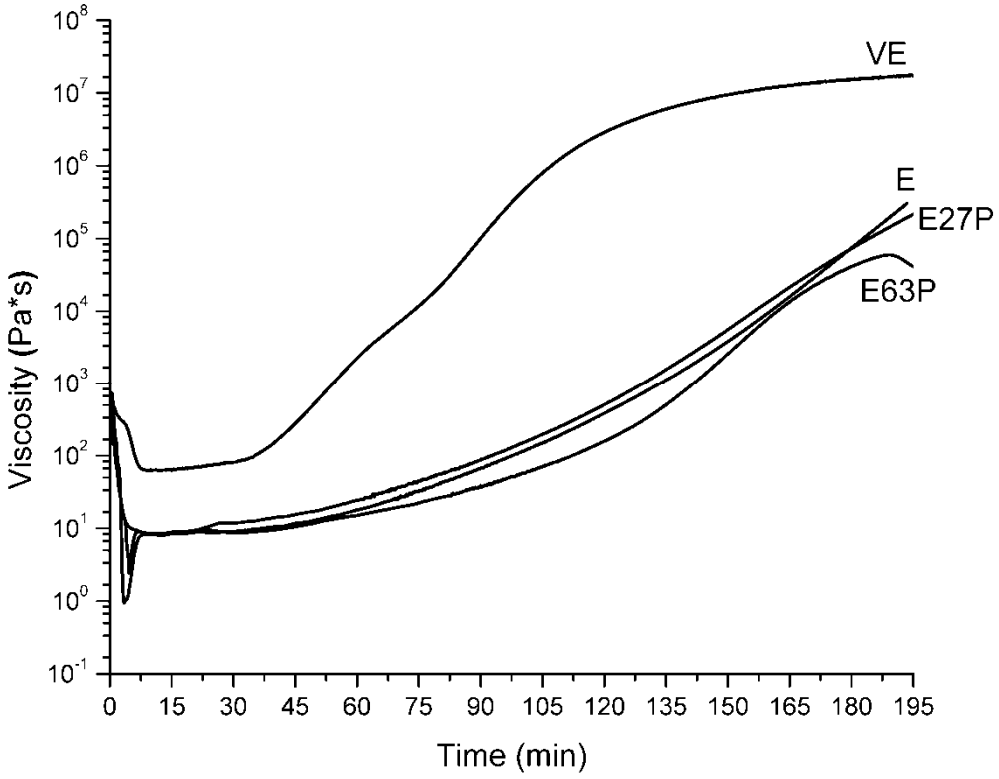

Figure 9.2. 25°C isothermal viscosity vs. time curves.

Dynamic Mechanical Analysis

To further probe the rheological behavior of the matrices in the solid-state, we performed a series of DMA measurements on composite samples to gain insights on the relationship between glass transition temperature (T_g) and storage modulus (E'). T_g is often viewed as the most critical property for measuring the mechanical limitations for a room-temperature (RT) cured matrix. Epoxies with adequate working times for marine applications do not provide the kinetic exotherm necessary to drive vitrification and T_g beyond that of vinylester. As a result, T_gs for RT cure epoxies are inferior to vinylesters creating the perception that epoxy matrix composites have lower thermomechanical performance at elevated temperatures.

We believe storage modulus is a more appropriate indicator of matrix performance than T_g since it quantifies mechanical performance at elevated temperatures. Figure 9.3 shows the dynamic mechanical behavior for composite samples fabricated from each of our matrix chemistries. All composites show similar room temperature moduli at ~10 GPa up to ~55-60°C where each sample drops in modulus. Composite samples VE, E27P, and E63P plateau around 3 GPa at 75-80°C. The epoxy control composite, E, displays a more significant drop in modulus between 55-80°C to ~1 GPa.

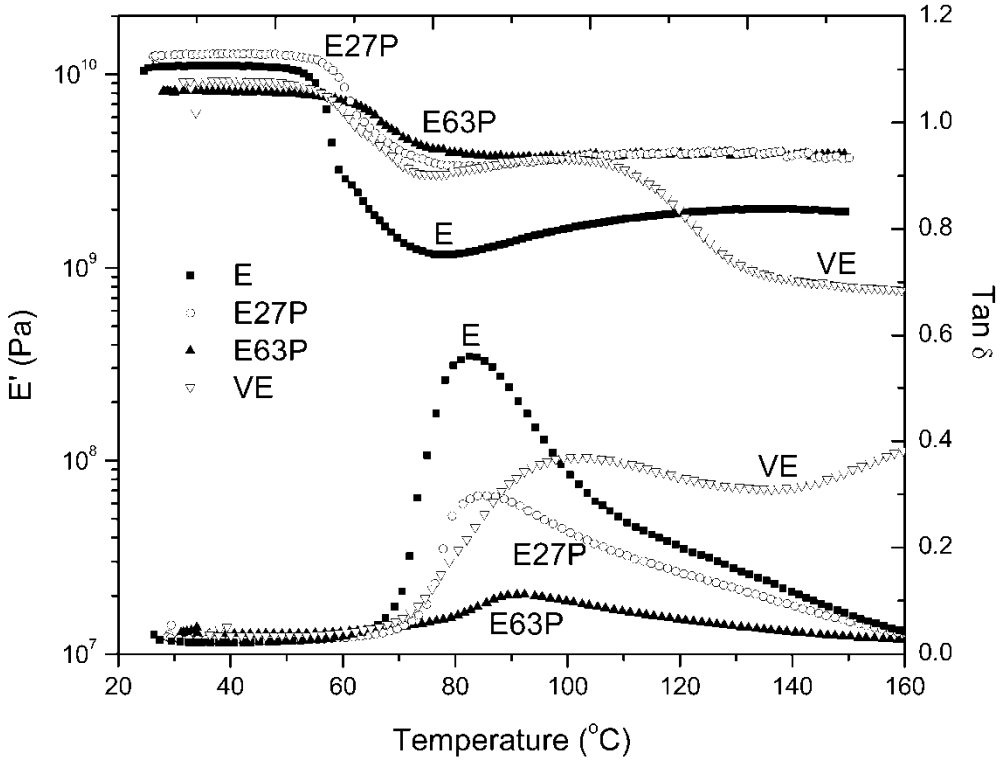

Figure 9.3. Storage modulus and Tan δ behavior of composites.

It is important to note the modulus drop of sample E is significantly greater than VE in the temperature range of 55-80°C; sample E is indeed inferior in storage modulus

below T_g of the vinylester. However, sample E shows a modest increase in modulus between 80°C and 150°C suggesting continued curing as the sample is heated. As temperature is increased above 80°C, composite samples VE, E27P, and E63P maintain a stable storage modulus up to 105°C when a second sharp reduction of VE storage modulus is observed. This second drop in modulus to a level of ~0.75 GPa coincides with the T_g of the vinylester matrix and is the only reduction in storage modulus observed for any of the composite samples above 80°C. At ~120°C, E' for VE crosses below E' for E at ~2 GPa, showing VE has a lower storage modulus than any of the epoxy matrices above 120°C.

Samples E27P and E63P maintain plateau moduli of ~3 GPa, well beyond their T_gs, to above 150°C without a secondary drop. This result is significant. Clearly, the POSS modified epoxy matrix composites display superior mechanical performance at elevated temperatures above the other matrices assessed. This result suggests T_g and mechanical behaviors for POSS-epoxy networks do not follow behaviors observed for vinylester matrix composites. The significant drop in modulus we observed for the VE above T_g justifies concern regarding mechanical performance at elevated temperatures for vinylester matrices. Our results show E27P and E63P composites preserve moduli of 3 GPa to temperatures of 150^{o}C, while VE modulus drops well below 3 GPa at 105°C. It is our position that T_g is not a sufficient indicator of elevated temperature mechanical performance for POSS modified epoxy matrix composites.

DMA Tan δ curves provide valuable insights regarding the relationships between T_g, crosslink density/morphology, and mechanical response. VE had the highest Tan δ T_g of 102°C, and all epoxy matrices were 10-20°C below this value. When comparing the

various epoxy based matrices, we observed a modest increase in T_g through incorporating POSS compared to the unmodified epoxy control. POSS increases T_g in epoxy networks due to POSS-chain and POSS-POSS interactions as discussed by Fu et al.[9] When comparing DMA behaviors, we observed the Tan δ of VE to be much broader than those for the three epoxy systems. This suggests the cured vinylester morphology is less homogenous than the epoxies, which is expected for a free-radical chain growth copolymerization product of vinylester and styrene.

Increasing POSS content within epoxy matrices showed an inverse relationship to Tan δ peak height. Incorporating POSS into epoxy networks enhances storage modulus at elevated temperatures since the octafunctional gly-POSS creates polyhedral hubs of more highly crosslinked network architecture leading to a loss of chain mobility.[10,11] This response is further enhanced by the tendency for POSS moieties to aggregate locally creating additional physical crosslink sites within epoxy networks.[12,13] DMA results for the composite samples are summarized in Table 9.3 and show POSS modified matrices maintain higher storage moduli across a broad temperature range.

Table 9.3. DMA Moduli and T_gs for Composite Samples

Sample	**T_g** (°C)	**E' @ 25°C** (GPa)	**E' @ 100°C** (GPa)	**E' @ 150°C** (GPa)
VE	102	9.3	3.7	0.8
E	83	11.1	1.6	2.0
E27P	85	12.8	3.7	3.7
E63P	89	8.2	3.8	3.9

Heat Distortion Temperature

Elevated temperature mechanical responses for our composite materials have also been evaluated through heat distortion temperature (HDT) measurements. HDT measurements are similar to 3-point bending tests but apply a constant force of 1.8MPa to the sample during a thermal sweep. The HDT is assigned as the temperature where flexural strain reaches 0.121% under the applied stress according to ASTM D648. Figure 9.4 shows the HDT results of the four composite samples. Epoxy control sample E had the lowest HDT of 80°C, which correlates with the DMA results. The VE composite also showed an onset transition at ~80°C, but did not drop as sharply as sample E and had an HDT of 91°C.

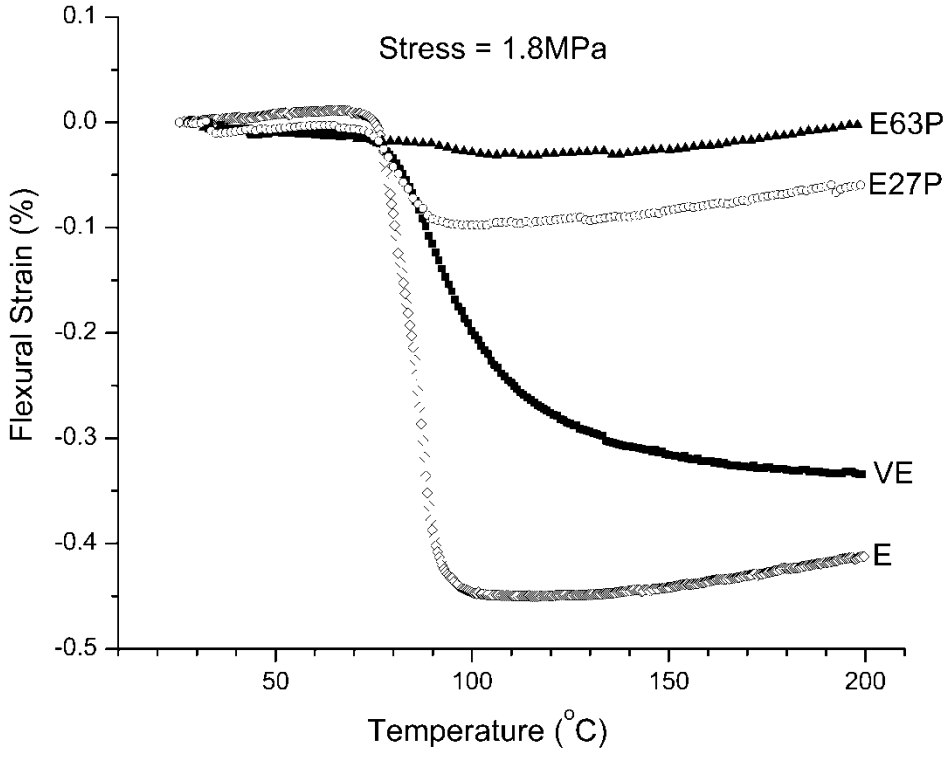

Figure 9.4. Heat distortion temperature behavior of composites.

It is interesting to note the deformation behavior for the VE sample displayed a more gradual deflection with temperature up to ~200°C. We were surprised to see the significant improvements in HDT for the E27P and E63P samples which did not deflect to 0.121% at any temperature up to 200°C. Sample E27P displayed a nominal level of distortion at an onset of ~80°C; however, the deformation was less significant than samples VE and E, and the flexural strain never exceeded 0.1% up to 200°C. Sample E63P exhibited even less distortion, showing minimal deflection at temperatures up to 200°C. The HDT data is in agreement with DMA results and indicates E27P and E63P have enhanced elevated temperature stabilities; the incorporation of POSS has significantly raised the storage modulus of the matrix to maintain stiffness of the composite above T_g. The HDT results further suggest highly functionalized POSS molecules act as crosslinking hubs and significantly restrict local chain mobility in crosslinked epoxy matrices. DMA and HDT data provide evidence that POSS modification is useful for obtaining higher performance properties in epoxies, making them desirable for fabricating high temperature resistant composites cured in ambient conditions.

Mechanical Testing

Flexural and tensile properties for the composite samples were analyzed to determine room temperature mechanical behavior of the composites fabricated from the four matrix chemistries. Although our research is primarily concerned with elevated temperature properties, we feel it is instructive to present mechanical data in order to provide insights on ambient performance. Figure 9.5 shows the flexural stress vs. strain curves for the composites obtained by averaging three flexural tests for each sample.

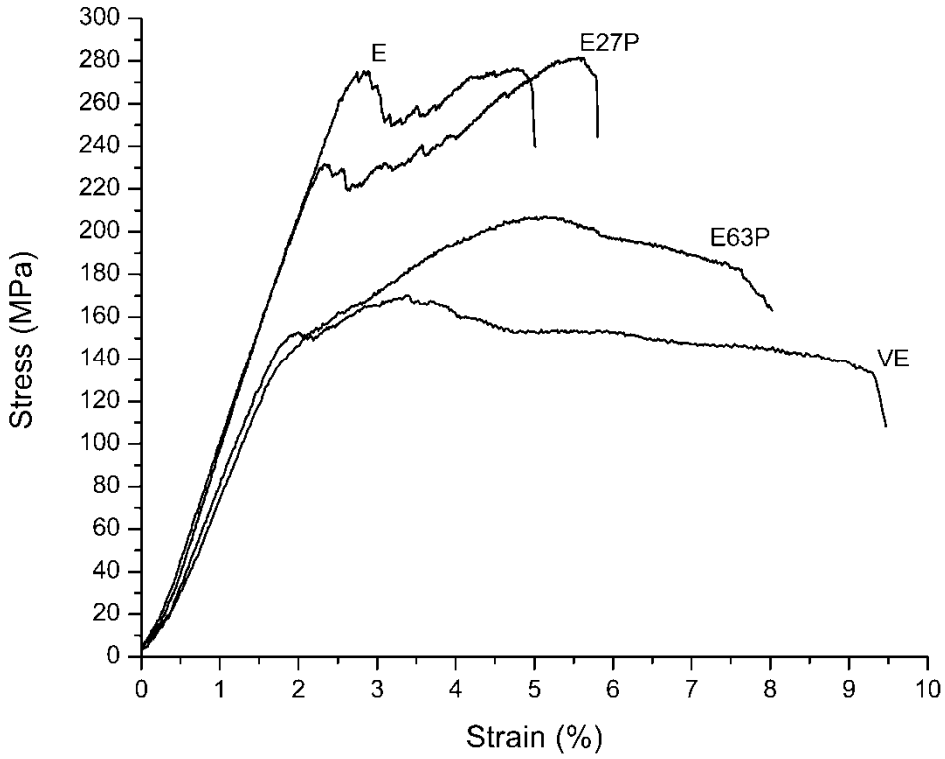

Figure 9.5. 3-Point bend flexural behavior of composites.

Samples E and E27P have higher ultimate strengths and moduli, but lower ultimate strains. The POSS modified samples distinguish themselves by displaying higher load bearing capabilities after initial fracture, with E27P showing an increase from 231 MPa to ultimate failure at 281 MPa and E63P increasing from 153 MPa to ultimate failure at 207 MPa. This response is likely due to toughening of the epoxy matrix through POSS-POSS and POSS-matrix interactions. Samples VE and E63P possess substantially lower strengths and moduli than E and E27P, but maintain higher ultimate strains around 8-9%. Due to the high level of octafunctional POSS in E63P, room temperature kinetics create a matrix that has vitrified before reaching a high degree of

crosslinking. This creates large numbers of unreacted chain ends and significantly lowers the modulus of E63P as compared to E and E27P. The flexural properties for the composites are summarized in Table 9.4.

Table 9.4. 3-Point Bend Flexural Properties of Composites

Sample	**Modulus** (MPa)	**Failure Onset Strain** (%)	**Failure Onset Stress** (MPa)
VE	70 ± 10	2.1 ± 0.2	150 ± 5
E	95 ± 6	2.8 ± 0.2	275 ± 11
E27P	96 ± 3	2.3 ± 0.1	231 ± 17
E63P	78 ± 5	2.0 ± 0.1	153 ± 6

Samples E and E27P had the highest tensile moduli and ultimate strengths, and sample VE had the highest ultimate strain. The tensile modulus and strength of E63P lag behind E and E27P due to the inadequate network formation of E63P at room temperature. Figure 9.6 shows tensile stress vs. strain curves for the composite samples obtained by averaging three tensile tests for each sample. The corresponding data is summarized in Table 9.5. Sample E27P displays a good balance of maintaining the strength and modulus properties of the control epoxy while showing a modest increase in failure strain.

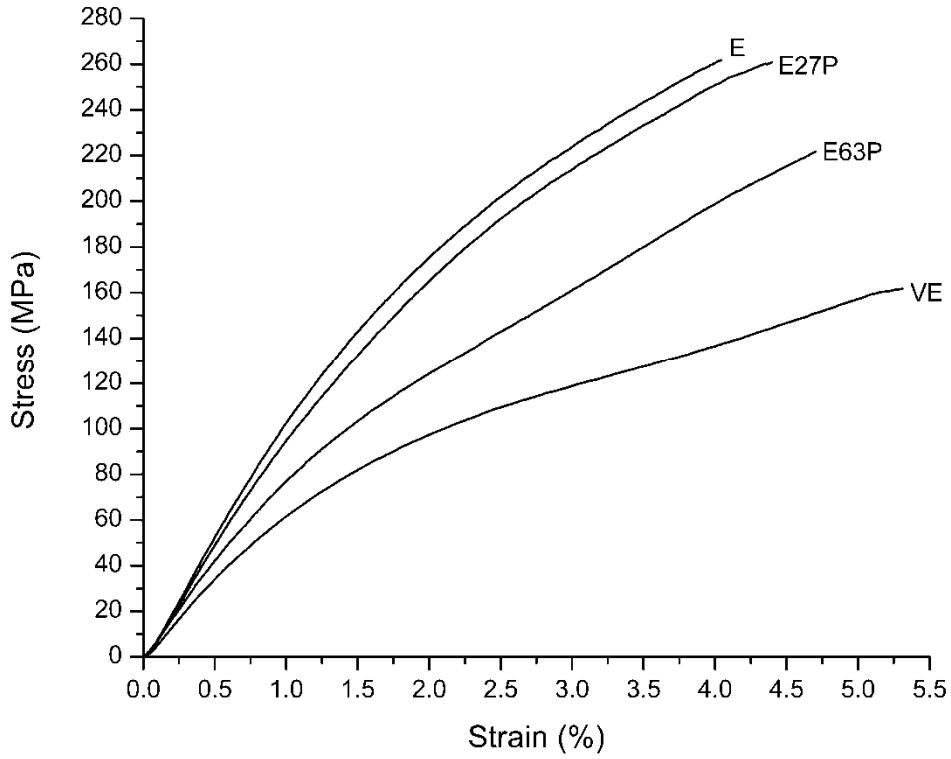

Figure 9.6. Tensile stress vs. strain behavior of composites.

Table 9.5. Tensile Properties of Composites

Sample	**Modulus** (GPa)	**UTS** (MPa)	**Strain At Break** (%)
VE	6.1 ± 0.2	163 ± 2	5.3 ± 0.2
E	10.2 ± 0.2	262 ± 9	4.1 ± 0.2
E27P	9.5 ± 0.2	264 ± 8	4.4 ± 0.3
E63P	7.7 ± 0.1	222 ± 10	4.7 ± 0.5

Conclusions

A room temperature cure epoxy with substantial improvement in elevated temperature properties was developed by reacting octafunctional glycidyl POSS with

DGEBF and DETA. Composites fabricated from these matrices had excellent VARTM processability and enhanced thermomechanical properties as compared to vinylester and epoxy controls. The 26.5 wt% gly-POSS modified epoxy showed an excellent balance of desirable properties with improvements in elevated temperature and ambient mechanical properties. The formulations and results provided from this research will provide the marine composites community with an epoxy matrix possessing a combination of properties which exceed requirements for utility in large primary structure marine applications.

References

1. Xia Cao, Dissertation. Ohio State, 2002.
2. Kootsookos, A.; Mouritz, A.P. *Comp Sci and Tech*, **2004**, 64, 1503.
3. Veazie, D.R.; Robinson, K.R.; Shivakumar, K. *Composites Part B*, **2004**, 35, 461-466.
4. Miyano, Y.; Nakada, M.; Sekine, N. *Composites Part B*, **2004**, 35, 497-502.
5. Romo-Uribe, A.; Mather, P.T., Haddad, T.S., Lichtenhan, J.D.; *J Poly Sci Part B: Poly Phys*, **1998**, 36, 1857-1872.
6. Phillips, S.H.; Blanski, R.L.; Svejda, S.A.; Haddad, T.S.; Lee, A.; Lichtenhan, J.D.; Feher, F.J.; Mather, P.T.; Hsiao, B.S. **2000**; MRS 628: CC4.6.1-CC4.6.10.
7. Zheng, L.; Waddon, A.J.; Farris, R.J.; Coughlin, E. Macromolecules, **2002**; 35, 2375-2379.
8. Lichtenhan, J.D.; Haddad, T.S.; Schwab, J.J.; Carr, M.J.; Chaffee, K.P.; Mather, P.T. *Polym. Prepr*, **1998**, 39, 489- 490.
9. Fu, B.X.; Gelfer, M.Y.; Hsiao, B.S.; Phillips, S.; Viers, B.; Blanski, R.; Ruth, P. *Polymer*, **2003**, 44, 1499-1506.
10. Sellinger, A.; Laine, R.M. *Macromolecules*, **1996**, 29, 2327-2330.
11. Crivello, J.V.; Malik, R. *J Poly Sci, Part A: Poly Chem*, **1997**, 35, 407-425.
12. Kim, G.K. *Journal of Polymer Science Part B: Polymer Physics*, **2003**, 41, 3299-3313.

13. Strachota, A.; *Macromolecules*, **2004**, 37, 9457-9464.

CHAPTER X

SURFACE ANALYSIS OF HIGH PERFORMANCE EPOXY/CARBON FIBER COMPOSITES FOR BONDING APPLICATIONS

Introduction

One challenge for the application of composite materials into large aerospace structures, i.e., commercial jets, satellites, rockets, etc., is the ability to bond component parts into the final structure. Failure of final structures is usually caused by insufficient joining of component parts. The number and diversity of reports on interfacial adhesive failure reflects the fundamental importance of this aspect for composites in general. In one such report, Qiao and Xu reported interfacial failures of common epoxy resin/carbon fiber fabric composites bonded to concrete.[1] Observations on this type of failure were related to temperature effects ranging from relatively low temperatures (-34.4ºC) to elevated temperatures (+71.1ºC).

It is also known that uniaxial compression can lead to failure in epoxy composites at the bonding interface.[2,3] Another example shows physical impact resistance is connected to aging phenomena and failure at the bonding interface.[4] To avoid failures at the bonding interface, great effort to enhance interfacial stability in epoxy/carbon composites is undertaken. Common methods to enhance surface energy at composite surfaces include physical techniques, such as plasma application: Kim reported on this particular technique in a series of publications.[5,6,7,8] Other physical treatments expose composites to UV radiation,[9] cryogenic temperatures, electrochemical modification, and chemical treatments.[10] A more common method, scientifically based on the formation of

covalent bonds between fiber and epoxy matrix is the usage of adhesion promoters to enhance bonding between epoxy and carbon fibers.[11]

Given the well documented problems with composite bonding and the inadequacy of current methods to promote bonding, a surprisingly limited number of reports relate potential bonding failure to specific processing conditions of the materials.[8,12] This research provides analytical evidence that relates specific composite fabrication techniques to the surface chemistry and consequently bonding behavior of epoxy composites.

To take advantage of strength while minimizing weight, fiber reinforced composites are most often fabricated into thin parts, i.e., panels, cylinders, or other primarily two dimensional geometries. When applying external pressure, such as in an autoclave or through a vacuum assisted resin transfer molding (VARTM) process, this creates a composite part which must be released on two surfaces: one released from a tool (tool side) and one released from a polymeric film or bag material (bag side). Therefore the fabrication process creates two individual composite surfaces each specifically affected by the surface from which it is released. Figure 10.1 illustrates a typical lay-up procedure for the epoxy/carbon fiber composites studied in this report. The tool side (TS) of the composite is exposed a lubricant on top of a thin PET (Mylar®) film, which covers the Invar 36 tool (Figure 10.1). The bag side (BS) is exposed to a polymeric release film, which will contour to the composite's surface (Figure 10.1).

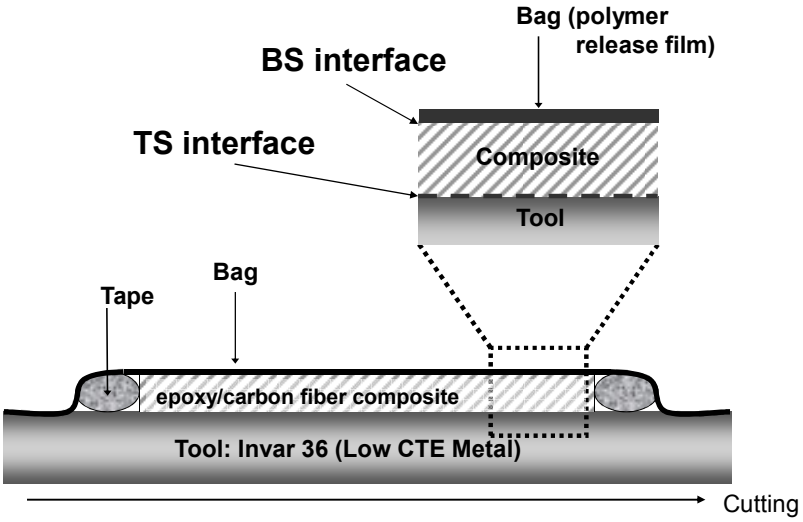

Figure 10.1. Schematic process conditions of epoxy carbon fiber composite material. Fabrication interfaces TS and BS are individually defined by process conditions.

The chemical and morphological properties of the TS and BS surfaces will be focus of this report. Specifically, the effect that different polymer release films and lubricant have on the tool and bag sides of composites is studied. The chemical properties of these two composite surfaces will give a strong indication of the ultimate bonding properties of the composite. The following analytical techniques were used to analyze the composite surfaces:

1. SEM imaging will be used to describe morphology of composite surfaces.

2. Contact angle measurements, attenuated total reflectance fourier transformed infrared (ATR FT-IR) spectroscopy and energy dispersive x-ray (EDX) spectroscopy will be employed to analyze chemical properties at composite surfaces. Furthermore, variable

angle ATR FT-IR will be used to gain information on migration of processing components into the depth of the composite surfaces.

Materials

Sample #1: DEN431/33DDS with T40-800 carbon fibers; delaminated to study inner (virgin) surface.

Sample #2: DEN431/33DDS with T40-800 carbon fibers; released with Mylar film.

Sample #3: DEN431/33DDS with T40-800 carbon fibers; released with FEP film.

The toolsides of Samples 1, 2, and 3 were composed of a thin Mylar film which had been sprayed with the siloxane lubricant. The Mylar film was placed on top of an Invar 36 tool to minimize the tool's coefficient of thermal expansion.

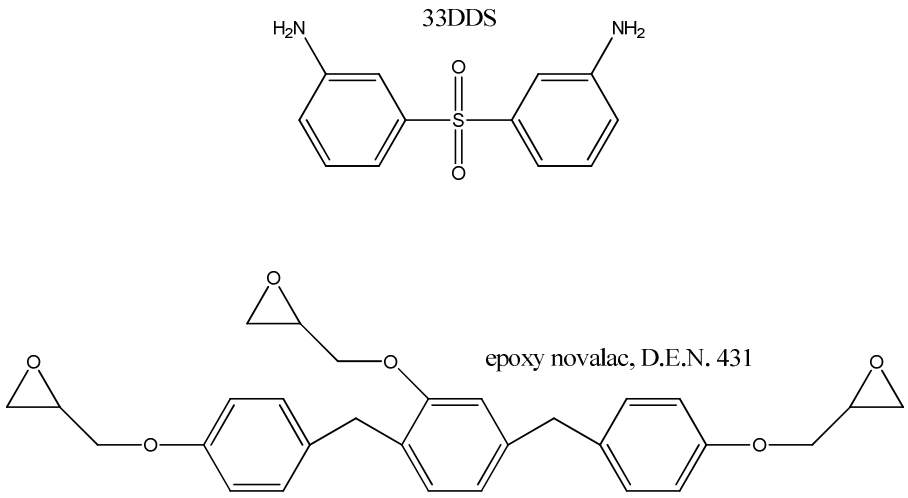

Figure 10.2. Chemical structures for composite resin monomers.

Three carbon fiber/epoxy panels consisting of a low molecular weight epoxy novalac resin (Dow's D.E.N.™ 431) cured with 3,3'-diaminodiphenyl sulfone (33DDS) into Cytec's THORNEL® T40/800 carbon fibers were analyzed as received from the Boeing Company (Figure 10.2). The two flat sides of each panel are defined as tool side (TS) and bag side (BS) to specify whether the composite surface was cured against the tool or a bagging material as shown in Figure 10.1. The edges of the panels were not analyzed.

The first of the three samples was delaminated approximately half way into the thickness of the sample to yield a virgin surface, which had no contact with any release films or other release agents. The virgin surface of sample 1 (1Vir) is used as a control in ATR FT-IR experiments. The other two samples received from Boeing were manufactured using two different polymer release films. Biaxially oriented polyethylene terephthalate, PET (Mylar®) was used as the bag material in sample 2. Sample 3 was bagged with a tetrafluoroethylene/hexafluoropropylene copolymer, also referred to as a fluorinated ethylene propylene (FEP) film. Additional reference samples were neat polymer films of PET and FEP. All three composite samples were fabricated at Boeing on an Invar 36 tool with a 0.005in PET (Mylar®) film covering the tool. The tool was sprayed with FREKOTE® 710-NC, a siloxane-based tool release agent produced by Henkel.

The contact angle measurements were completed using deionized water. Acetone was purchased from Fisher-Scientific (ACS grade) and dried with molecular sieves before rinsing the composite surfaces.

Methods

Sample Preparation

After the sample panels were received from Boeing, $1in^2$ panel sections were covered with a protective cap, sealed, and cut with care taken that the samples were not touched or exposed to any lubricant or particulates due to the cutting procedure. To prevent analysis techniques from altering the sample, separate samples from the same panels were used for analysis by SEM/EDX, ATR FT-IR, and contact angle.

Surface energies of the composite samples were measured qualitatively with contact angle measurements conducted using an FTA200 dynamic contact angle analyzer and a KRUESS K12 process tensiometer. Four 1.0μL water droplets were analyzed and averaged per sample (Table 10.1). Contact angles were measured before and after the surfaces had been rinsed with acetone. After solvent application the samples were dried under a stream of dry air with a blow-gun.

Table 10.1. Contact Angle Measurements Before and After Acetone Rinse

Sample #2 – Bag Side				Sample #3 – Bag Side			
	Left	Right	Mean		Left	Right	Mean
Test 1	85.7	88.1	86.9	Test 1	92.7	94.8	93.7
Test 2	87.4	94.2	90.8	Test 2	93.7	98.0	95.8
Test 3	85.1	91.2	88.2	Test 3	90.5	96.0	93.3
Test 4	89.1	91.9	90.5	Test 4	90.0	96.4	93.2
Average	86.8	91.4	89.1	Average	91.7	96.3	94.0
Sample #2 – Bag Side (After Acetone Wash)				Sample #3 – Bag Side (After Acetone Wash)			
	Left	Right	Mean		Left	Right	Mean
Test 1	82.5	83.1	82.8	Test 1	93.2	92.7	92.9
Test 2	82.4	82.5	82.4	Test 2	85.6	87.8	86.7
Test 3	78.5	78.3	78.4	Test 3	91.2	87.4	89.3
Test 4	81.9	81.9	81.9	Test 4	89.4	88.5	89.0
Average	81.3	81.5	81.4	Average	89.9	89.1	89.5
Sample #2 – Tool Side				Sample #3 – Tool Side			
	Left	Right	Mean		Left	Right	Mean
Test 1	87.9	89.2	88.6	Test 1	101.5	102.6	102.0
Test 2	89.5	87.1	88.3	Test 2	104.2	106.4	105.3
Test 3	89.8	87.5	88.6	Test 3	102.5	101.5	102.0
Test 4	87.4	87.0	87.5	Test 4	102.7	104.4	103.6
Average	88.7	87.7	88.3	Average	102.7	103.7	103.2
Sample #2 – Tool Side (After Acetone Wash)				Sample #3 – Tool Side (After Acetone Wash)			
	Left	Right	Mean		Left	Right	Mean
Test 1	76.9	76.5	76.7	Test 1	91.3	92.1	91.7
Test 2	72.4	74.0	73.2	Test 2	90.9	89.7	90.3
Test 3	74.1	75.7	74.9	Test 3	88.5	88.0	88.2
Test 4	81.8	82.8	82.3	Test 4	88.5	89.4	89.0
Average	76.3	77.3	76.8	Average	89.8	89.8	89.8

To describe the morphology of the samples' surfaces, scanning electron microscopy (SEM) images were acquired under high vacuum conditions on a FEI Quanta FEG 200 SEM. Images were acquired from all parts of each sample. Once an image was acquired with SEM, energy dispersive x-ray (EDX) spectroscopy measurements were taken with a Noran Advantage controller to determine the elemental composition of the surfaces. Ten EDX scans were completed for each of the four samples: 2BS, 2TS, 3BS, 3TS. EDX analysis was applied to areas of the composite surface approximately 0.25mm^2.

Fourier transformed infrared (FT-IR) spectra were collected on a Digilab FTS 2000 FT-IR single beam spectrometer at 4cm^{-1} resolution under attenuated total reflectance (ATR) conditions. Zinc selenide (ZnSe) was used as the ATR crystal. The ZnSe crystal

possesses a face angle of 45º, dimensions of 80x10x4mm, and is set into a horizontal ATR stage. To resolve chemical composition into the samples' depths, variable angle ATR FT-IR was employed. Spectra were collected on a Bio-Rad FTS 6000 FT-IR single beam spectrometer at 4cm^{-1} resolution. A Germanium (Ge) ATR crystal with dimensions 50x20x3mm and face angle of 45° was used. The IR beam was set at angles of incidence 60°, 50°, and 45°. Each of the IR spectra obtained represents 100 coadded scans rationed to 100 scans collected on an empty ATR cell. Spectra were corrected for optical effects and distortions using Digilab Merlin software 3.3.0.036 and Digilab Win IR Pro software 3.4, respectively.

Results and Discussion

SEM Analysis

To determine the effect tool release agents and bagging materials have on the surface morphology of the composite, SEM images were acquired. Figure 10.3 shows the SEM images of epoxy/carbon composite surfaces found for the tool side and bag side of samples 2 and 3. Figures 2A and 2B depict TS and BS surfaces for sample 2, while Figures 2C and 2D show the TS and BS surfaces of sample 3. The parallel striations seen in Figures 2B, 2C, and 2D are the result of the imbedded carbon fibers. It is interesting that only sample 2TS shows a resin rich surface in which no carbon fibers are seen. Since the tools and composite precursors used in the preparation of both samples 2 and 3 were the same, this may be indicative of nothing more than large-scale regional differences in the samples. The tool sides and bag sides of both samples are fairly smooth on the μm scale, contain a number of <1μm-sized holes, and often show the outline of the impregnated carbon fiber. Increasing the roughness of the surface by

chemical or physical means would increase the ability of the composites to form high strength bonds.

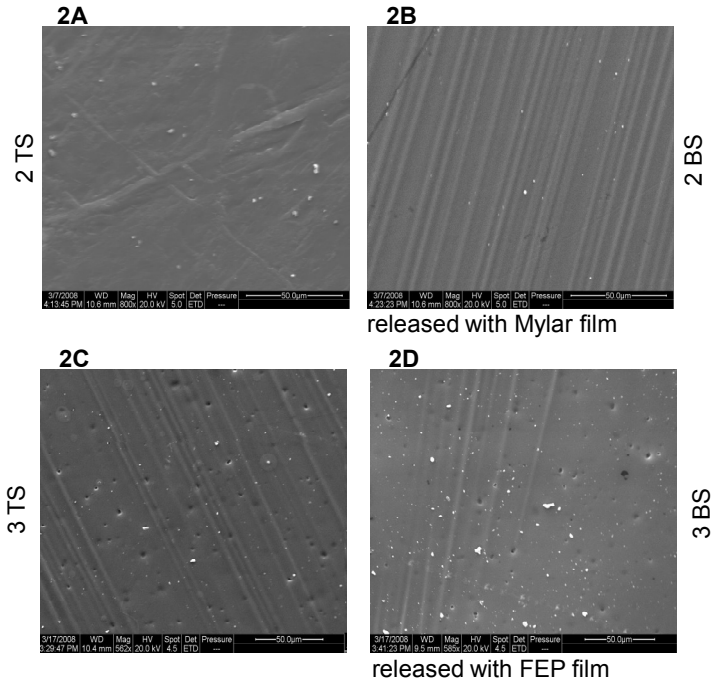

Figure 10.3. SEM images and morphology of TS and BS interfaces from processed epoxy composite materials. BS interfaces after release of polymer bag.

Contact Angle Analysis

Contact angle measurements were completed to qualitatively determine the surface energy of the surfaces. Ideally, the composites will have high surface energy to enable stronger bonding, but the presence of release agents or films remaining from manufacturing will lower that surface energy. To give an approximation of the area of sample analyzed by this technique, the 1.0μL drop of water covers an area of 4.8mm^2 when the contact angle is 90°. As the contact angle increases, this area will decrease, and as the contact angle decreases, this area will increase. Samples studied stayed fairly close to 90°, varying from 77° to 103°.

Figure 10.3a illustrates the contact angles for samples 2 and 3 taken on the tool side and bag side surfaces before and after an acetone rinse. Higher contact angles are indicative of lower surface energies. Before the solvent treatment, the surface energies of samples 3TS and 3BS are significantly lower than 2TS and 2BS, with 3TS possessing the highest contact angle (Figure 10.3a). This result supports the presence of silicon release agent present on the tool sides in high enough quantities to affect contact angle measurements. The difference in surface energies between 2BS and 3BS is likely caused by the presence of trace amounts of FEP on the surface of Sample 3BS. Cohesive failure of the FEP bagging material leaving a thin layer of FEP on the composite surface explains these results. The PET bagging material is also believed to fail cohesively; however, PET does not have a surface energy nearly as high as FEP, so the contact angle measurement did not change as significantly.

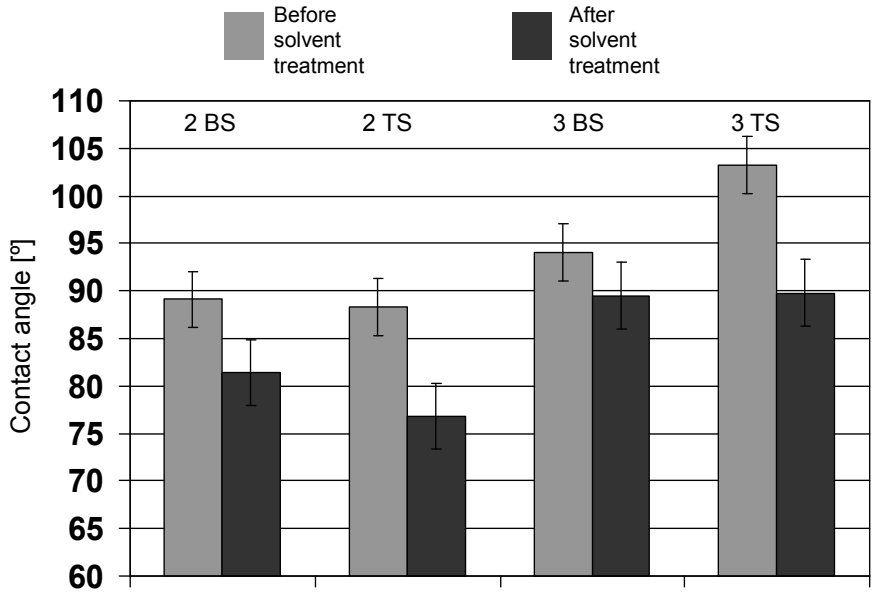

Figure 10.4a. Contact angles at processed epoxy composite interfaces TS and BS for samples 2 and 3 before and after treatment with solvent.

After the initial contact angle measurements were completed, each surface was rinsed with acetone, and contact angles were taken again. In all samples, the contact angle dropped after the acetone rinse indicating the presence of small molecule contaminants on the unwashed surfaces. As seen in Figure 10.4a, contact angles for all samples are higher before solvent rinsing; however, Figure 10.4b illustrates that the tool sides of both samples show a drop in surface energy substantially greater than the bag sides. The drop in surface energies seen on the bag sides of the samples was likely due to a smaller amount of tool release agent being rinsed off, not removal of the bagging film. Since the silicone-based lubricant used to spray the tool is an aerosol, it is likely to become dispersed throughout the building and deposit on many manufacturing surfaces. Since the tool sides had been directly sprayed with release agent, they had more siloxane before the rinse, and showed a more significant decrease in surface energy after the rinse.

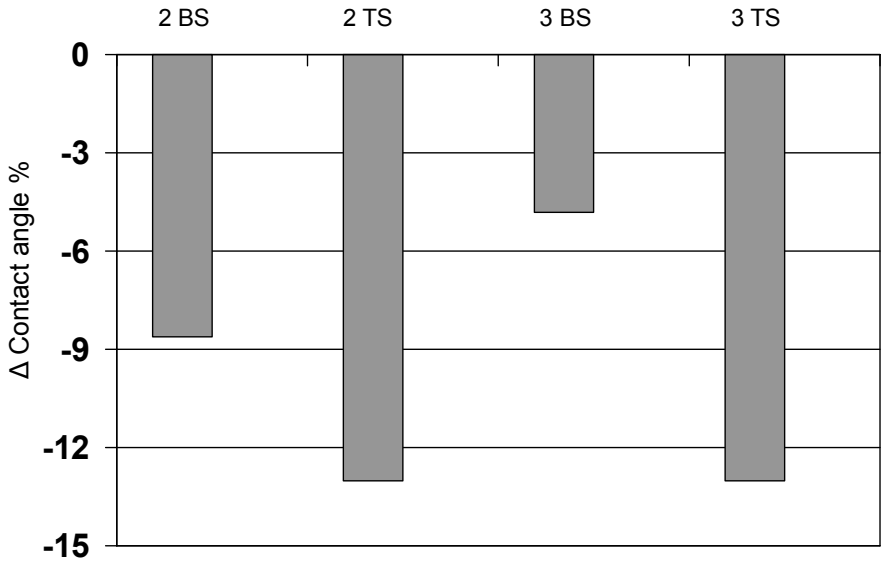

Figure 10.4b. % drop in contact angle at interfaces TS and BS for samples 2 and 3 after solvent treatment.

Cohesive failure of the FEP is further supported by the finding that the contact angle of 3BS remained higher than samples 2TS or 2BS after rinsing (Figure 4a). We believe the fluorinated polymer still present on the surface acts to lower surface energy and provides the explanation for these results.

EDX Spectroscopy

EDX analysis was completed on the tool sides and bag sides of samples 2 and 3 using 0.25mm^2 areas. The four samples were predictably composed of over 99% carbon, oxygen, and sulfur, which comprise the backbone of the resin. However, surface contamination accounts for the last 0.5-0.8 elemental weight %. Most of this surface contamination consists of aluminum, and a very small amount of sodium and chlorine are also seen. The aluminum is likely due to shavings and small particles

created when aluminum is machined in the facility. However, the aluminum, sodium, and chlorine contaminants are not as interesting for this study as the discovery of silicon and fluorine on the surfaces.

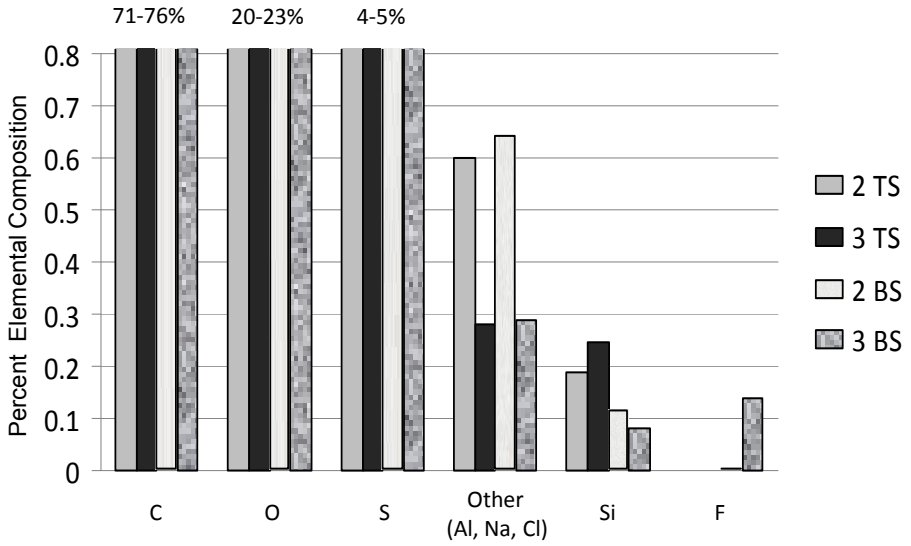

Figure 10.5. EDX analysis of processed epoxy composite materials. Spectra taken at BS interfaces of samples 2 and 3 after release of polymer bag film.

Silicon is present on all four composite surfaces analyzed, ranging from 0.08-0.25 elemental weight % (Figure 10.5). Sample 3TS showed the highest levels of silicon, which agrees well with the contact angle findings. Sample 2TS also shows a significant amount of Si, substantially greater than the amount seen on either bag side. Sample 3BS has the least amount of silicon, which would explain that sample showing the smallest change in contact angle before and after the acetone rinse (Figure 10.4b). Sample 3BS, the sample bagged with FEP, is the only sample that shows a significant amount of fluorine (0.14 elemental weight %).

FT-IR Spectroscopy

Finally, characterization of the surfaces was completed using FT-IR spectroscopy techniques. ATR FT-IR spectra of 1TS and 1Vir were obtained and normalized against the epoxy peak appearing at 1235cm^{-1} (Figure 10.6).

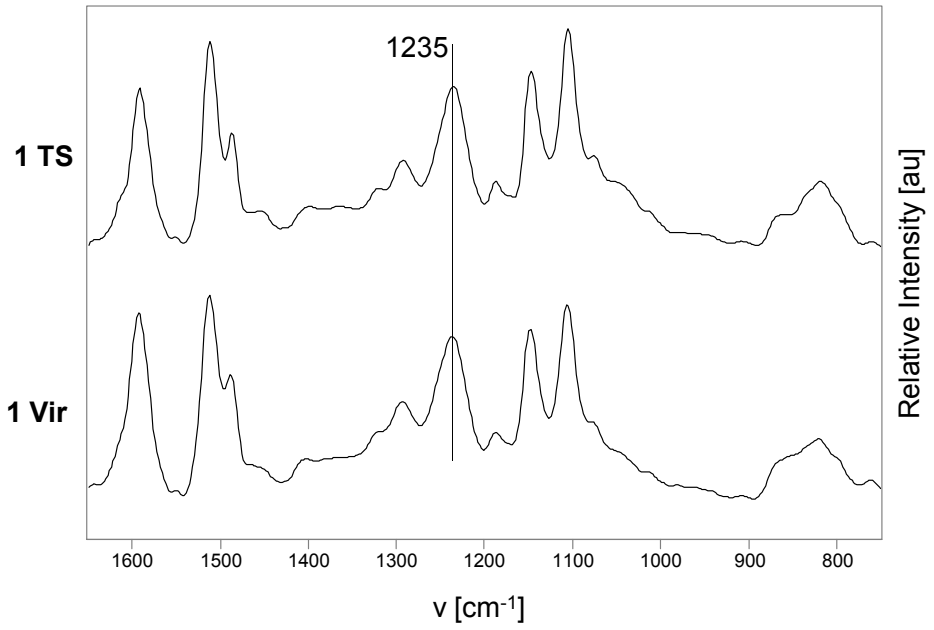

Figure 10.6. ATR FT-IR spectra of epoxy composite reference sample 1 at process defined interfaces TS, uBS (uncoated Bag Side).

Figure 10.7 illustrates the difference spectrum obtained by subtracting the spectrum of 1Vir from 1TS. The positive bands obtained from this spectral normalization are indicative of regions of much higher signal given by the tool side than the virgin surface. Indicated in the difference spectrum of Figure 10.7 are bands A at

1230cm^{-1}, B at 1139cm^{-1}, C at 1105cm^{-1} and D at 805cm^{-1}. These bands support the presence of resonances resulting from silane/siloxane molecules[13]:

→A, 1230cm^{-1}: Si-CH_2-R / Si-CH_3

→B, 1139cm^{-1}: Si-O-CH_3 / Si-Phenyl

→C, 1105cm^{-1}: Si-O-Aliphatic / Si-O-Si

→D, 805cm^{-1}: Si-CH_3 / $(SiO)_n$

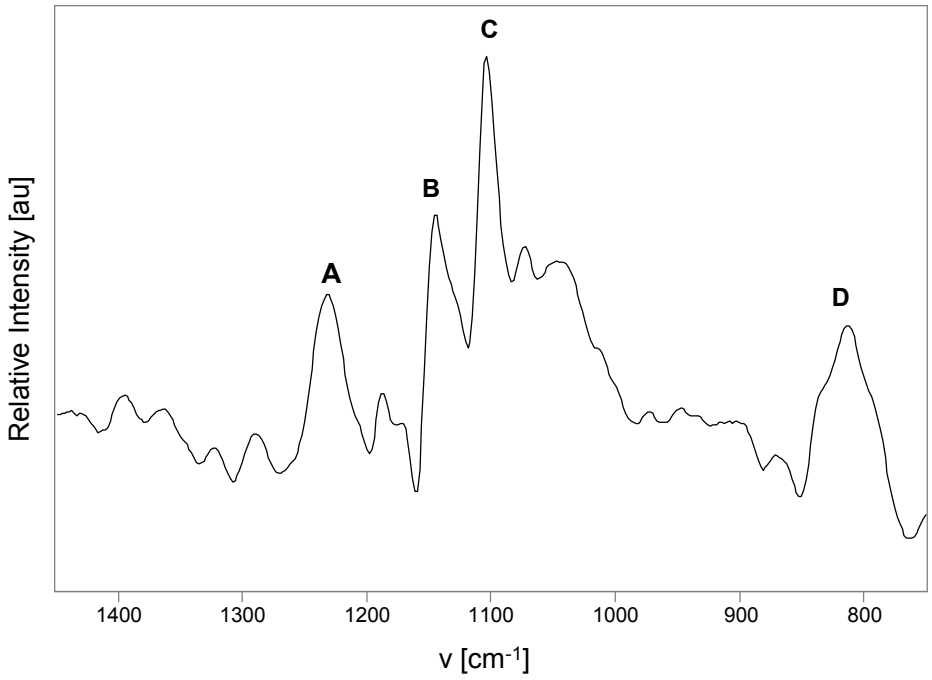

Figure 10.7. ATR FT-IR difference spectrum taken from interfaces TS – BS of reference epoxy composite.

The results displayed in Figure 10.7 were obtained by comparison of the tool side of a composite surface with a virgin surface and are used to interpret findings from ATR FT-IR spectra for the tool sides of samples 2 and 3.

Depth Profiling

From the difference spectrum of sample 1, resonances were identified as silanes/siloxanes. The resonances at 1230cm^{-1}, 1105cm^{-1}, and 805cm^{-1} were further studied with variable angle ATR FT-IR. This technique enables depth profiling to monitor the penetration of lubricant into the depth of the surface by applying different angles of incidence to the samples. The angle of incidence is directly related to the depth of penetration and can be used to quantitatively calculate the depth being probed (Equation 10.1). In this case, 45°, 50°, and 60° and were used to study the tool sides of samples 2 and 3. Figure 10.8a shows the depth profiling of 2TS, and Figure 10.8b shows 3TS. Since the depth of penetration is determined by the wavelength in addition to angle of incidence (Equation 10.1), using set angles of incidence probes each resonant peak (1230cm^{-1}, 1105cm^{-1}, and 805cm^{-1}) to different depths. The numbers given under each peak in Figures 8 show the depth probed in μm. The bold numbers above each peak give the integrated intensity of the resonance. This data is also presented in tabular form (Tables 2a and 2b).

$$d_P = \frac{\lambda_0}{2\prod n_1(\sin^2\theta - n_{21}^2)^{1/2}}$$

where: d_P: depth of penetration

λ_0: IR wavelength in the internal reflection crystal

θ: angle of incidence

n_1: refractive index of the ATR crystal

n_{21}: refractive index ratio sample/crystal.

Equation 10.1. Relationship of depth of penetration to angle of incidence in ATR.

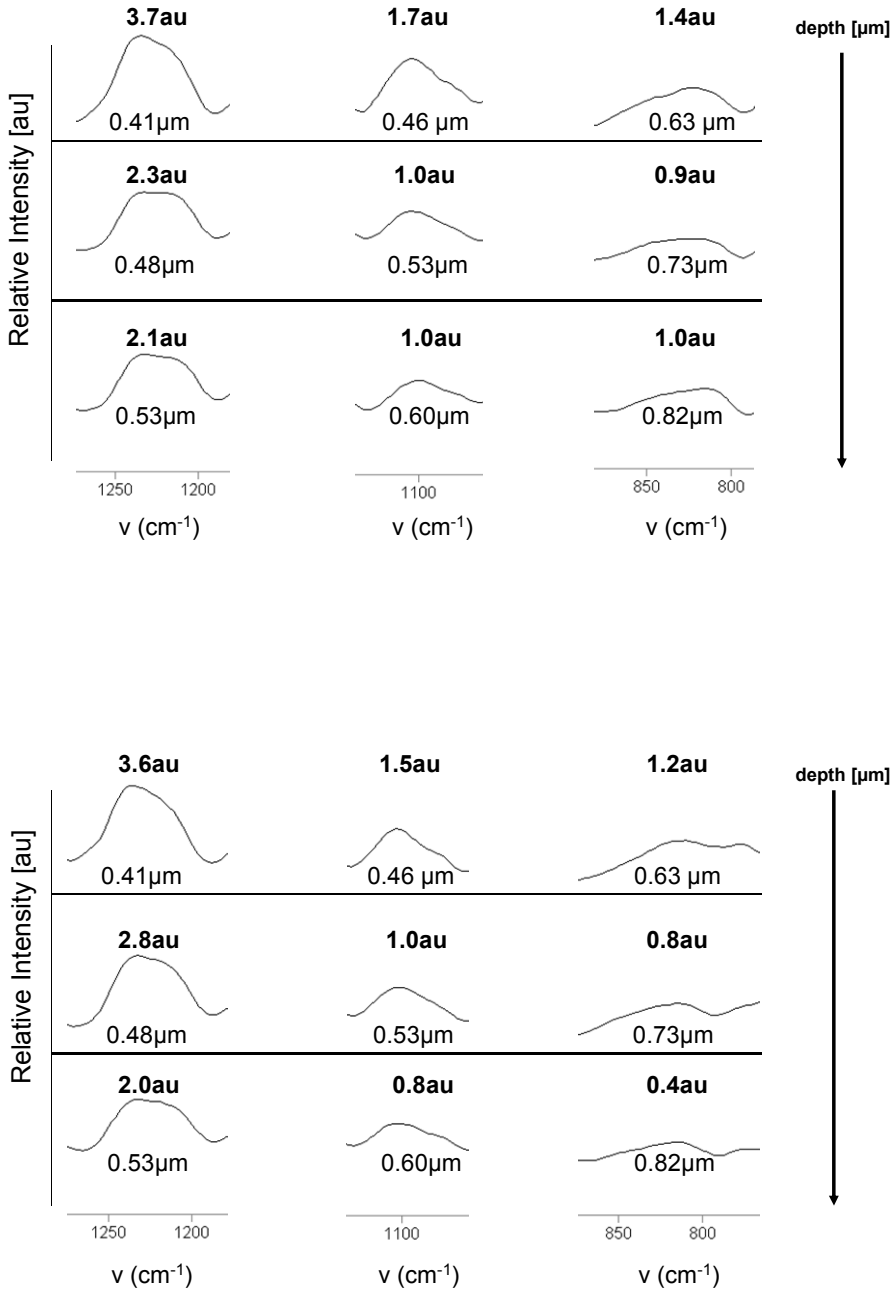

Figure 10.8. Variable angle ATR FT-IR spectra at TS of samples 2 and 3.
8a: silane relevant bands for sample 2 TS. 8b: silane relevant bands for sample 3 TS.

As seen in Table 10.2 and Figure 10.8, the largest drop in peak intensity occurs between the shallowest and the second shallowest penetration. This finding indicates that silane/siloxane concentration is highest on the surface but does penetrate into the bulk in lesser amounts.

Table 10.2a. TS Interface/Sample 2. Depth of Penetration/Band Areas (au) for Silane-Related Wavenumbers Used in Variable Angle ATR FT-IR

1230 cm^{-1}		**1105 cm^{-1}**		**805 cm^{-1}**	
Depth [μm]	Intensity [au]	Depth [μm]	Intensity [au]	Depth [μm]	Intensity [au]
0.41	3.7	0.46	1.7	0.63	1.4
0.48	2.3	0.53	1.0	0.73	0.9
0.53	2.1	0.60	1.0	0.82	1.0

Table 10.2b. TS Interface/Sample 3. Depth of Penetration/Band Areas (au) for Silane-Related Wavenumbers Used in Variable Angle ATR FT-IR

1230 cm^{-1}		**1105 cm^{-1}**		**805 cm^{-1}**	
Depth [μm]	Intensity [au]	Depth [μm]	Intensity [au]	Depth [μm]	Intensity [au]
0.41	3.6	0.46	1.5	0.63	1.2
0.48	2.8	0.53	1.0	0.73	0.8
0.53	2.0	0.60	0.8	0.82	0.4

Additional FT-IR analysis was necessary to reveal more conclusive information on polymer bag residues. ATR FT-IR spectra of samples 2BS, 2TS, 3BS, and 3TS were

normalized with the epoxy resonance at 1235cm^{-1} and compared with the spectrum of 1Vir and the appropriate bagging material (Figures 9 and 10).

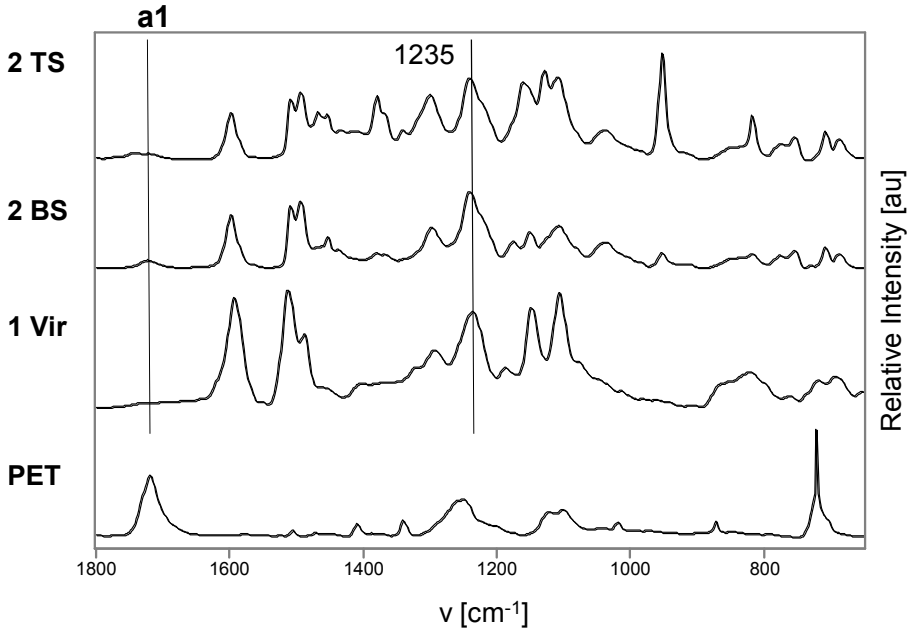

Figure 10.9. ATR FT-IR spectra of sample 2 interfaces TS and BS of epoxy composite with Mylar release film. Reference 2 ATR FT-IR spectrum of neat Mylar film. Normalization band at 1235 cm^{-1}.

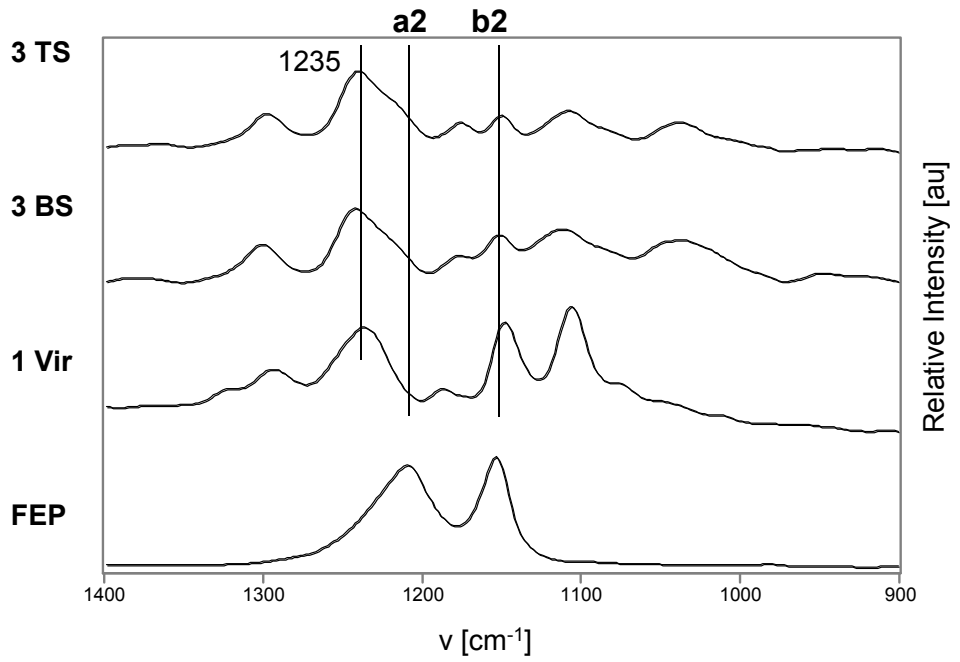

Figure 10.10. ATR FT-IR spectra of sample 3 interfaces TS and BS of epoxy composite with FEP release film. Reference 3 ATR FT-IR spectrum of neat FEP film. Normalization band at 1235 cm^{-1}.

Figure 10.9 displays the bag side and tool side of sample 2 stacked against 1Vir and neat PET (Mylar®) film. Resonance a1 at 1720 cm^{-1} represents the carbonyl stretch [13] present in the ester of PET but not present in the epoxy resin. The C=O resonance is very strong in the PET, vanishingly small in 1Vir, weak in 2TS, and clearly prevalent in 2BS. Both bag side and tool side surfaces of sample 2 were exposed to PET film in the fabrication process. Sample 2BS was directly exposed to PET as the release film, while 2TS was exposed to a lubricated PET film. The data matches expectations as 2BS would have a greater amount of PET film present after cohesive failure than would 2TS due to lubrication, and that 1Vir would show no spectroscopic evidence of PET. These

findings are illustrated more quantitatively in Table 10.3, which shows integrated peak intensities of a1 from 1Vir, 2TS, and 2BS. As seen in Table 10.3, band intensity a1 is higher by factor a factor of 3.5 on sample 2's bag side compared to tool side, and only trace amounts are observed on the virgin surface of sample 1.

Table 10.3. Band Intensities (au) at Process Defined Interfaces TS and BS for Important Bands at Bag Film Polymers of Sample 2 and 3

Peak Integral (au)	**1 Vir**	**2 TS**	**2 BS**	**3 TS**	**3 BS**
a1	0.019	0.055	0.18	-	-
a2	N/A	-	-	N/A	N/A
b2	0	-	-	0.30	0.42

A similar analysis comparing the ATR FT-IR spectra of the bag and tool sides of sample 3 against the virgin surface and a neat FEP film is shown in Figure 10.10. The peaks a2 and b2 at 1208 and 1155cm^{-1}, respectively, represent the C-F stretches of CF_2/CF_3 entities in FEP. Considering the strong intensity of these C-F bands,[13] they should be suitable IR indicators; however, quantitative interpretation of these peaks in 1Vir, 3TS, and 3BS is limited due to overlap in the spectral region for both peaks a2 and b2 (Figure 10.10). The overlap where band a2 occurs makes the integration of a2 impossible. Peak b2 was integrated for samples 3TS and 3BS. Sample 1Vir displays a large peak close to 1155cm^{-1}, but it was determined that this peak is due to an overlapping resonance and not FEP. The integration of band b2 seen in Table 10.3

shows a higher concentration of FEP residue on 3BS as compared to 3TS. However, as shown in the EDX data (Figure 10.5), there is no FEP present on the tool side of sample 3. The peak seen around 1155cm^{-1} in 3TS and 1Vir is an overlapping resonance. The increase in intensity seen in 3BS as compared to 3TS may be due to the addition of the FEP resonance to the already existent resonance from the composite.

Conclusions

Carbon fiber/epoxy composites were analyzed by SEM, contact angle, EDX, and FT-IR techniques to determine the morphology, surface energy, and chemical composition of composite surfaces exposed to different local fabrication conditions. SEM gives clear images of the bag and tool sides of composite samples, and shows a rather smooth morphology with some small holes and ridges caused by carbon fibers present. The bulk of analysis focused on the chemical composition of the surface and the surface energy as a result of chemistry. The effects of materials coming directly in contact with the composite at the time of curing (tool lubricant and polymeric bagging and tooling films) are analyzed.

In the tool lubricant analysis, the contact angle and EDX data fit together nicely, both indicating the presence of some amount of lubricant on all samples. The difference spectrum created by comparing the samples before and after an acetone rinse shows the highest concentrations of lubricant are present on the tool sides of samples 2 and 3. EDX clarifies the source of this lubricant as silicon-based and confirms that the tool sides show the highest concentrations of lubricant. ATR FT-IR analyses further identify this lubricant as a siloxane/silane, very similar to the highly used commercial tool release, polydimethylsiloxane (PDMS). Variable angle infrared spectra indicate siloxane/silane penetration of the surface of the composite at the near micron scale. The identification of a

siloxane/silane lubricant on and into the surface of the composite is indicated by contact angle, EDX, and IR measurements.

The chemical analysis of the bagging and tooling film surface contamination was less straightforward but gave convincing results nonetheless. In contact angle measurements, sample 3BS had a substantially lower surface energy than 2BS, likely due to a cohesive failure of the FEP bagging film that left a thin layer of FEP on the composite surface. Cohesive failure of the PET bag would not leave a surface energy significantly different from the epoxy as PET and epoxy possess similar hydrophilic nature. ATR FT-IR spectroscopy indicates cohesive failure of both the FEP and PET bagging films. Spectroscopic overlap in the IR data makes quantitative measurements impossible on the FEP film, but the carbonyl peak clearly shows the presence of PET on the bag side and trace amounts of PET on the tool side of sample 2. The intensity of the carbonyl peak is much less on the tool side due to the presence of lubricant, which allowed a better release with less cohesive failure. Since PET is composed of carbon, oxygen, and hydrogen, the same elemental components as the epoxy resin, EDX cannot be used to show the existence of PET on the bag or tool sides of composite samples. However, EDX gives clear indication of fluorine only on sample 3BS, the sample released with FEP. Contact angles, EDX, and ATR FT-IR give compelling evidence for the presence of bagging films FEP and PET and tool release film PET on the composite surfaces.

The importance of reliable methods for bonding composites is paramount to the long term success of composites as construction materials. Obtaining clean, chemically and morphologically favorable surfaces for bonding is essential to achieve this goal. Present methods of composite fabrication produce surfaces which mirror the surfaces in contact with

the composite at the time of curing, i.e., surfaces made to release rather than adhere. New fabrication materials and methods or post-fabrication processing are necessary to create reliably bondable composite surfaces.

References

1. Qiao, P.; Xu, Y. *Journal of Advanced Materials*, **2005**, 37, 56-62.
2. Kumar, S.B.; Sivashanker, S.; Bag, A; Sridhar, I. *Materials Science and Engineering: A*, **2005**, 412, 117-122.
3. Kumar, S.B.; Sridhar, I.; Sivashanker, S.; Osiyemi, S.O.; Bag, A. *Materials Science and Engineering: B*, **2006**, 132, 113-120.
4. Mendelsy, D.A; Leterrier, Y.; Manson, J.A.E.; Nairn, J.A. *Journal of Composite Materials*, **2002**, 36, 1655 -1676.
5. Kim, J.K.; Kim, H.S.; Lee, D.G. *Journal of Adhesion Science and Technology*, **2003**, 17, 1751-1771.
6. Kim, J.K.; Lee, D.G. *Journal of Adhesion Science and Technology*, **2004**, 18, 473-494.
7. Kim, J.K.; Kim, H.S.; Lee, D.G. *Journal of Adhesion Science and Technology*, **2003**, 17, 329-352.
8. Kim, J.K.; Lee, D.G, *Composite Structures*, **2002**, 57, 37-46.
9. Kim, J.K.; Kim, H.S.; Lee, D.G. *Journal of Adhesion Science and Technology*, **2003**, 17, 1523-1542.
10. Rashkovan, I.A.; Korabel'nikov, Y.K. *Composites Science and Technology*, **1997**, 57, 1017-1022.
11. Lee, J.Y. *Journal of Applied Polymer Science*, **2006**, 102, 684-689.
12. Cherian, J.T.; Castner, D.G. *Surface and Interface Analysis*, **2000**, 29, 729-734.

13. Lin-Vien, D.; Colthup, N.B.; Fateley, W.G.; Grasselli, J.G. *The handbook of infrared and Raman characteristic frequencies of organic molecules,* Academic Press Boston, (1991).